Utah State University

DigitalCommons@USU

All Graduate Theses and Dissertations | Graduate Studies

5-2016

Benchmark Experiments for Natural Convection in Nuclear Fuel Rod Bundles

Kyle L. Jones
Utah State University

Follow this and additional works at: https://digitalcommons.usu.edu/etd

Part of the Aerospace Engineering Commons

Recommended Citation

Jones, Kyle L., "Benchmark Experiments for Natural Convection in Nuclear Fuel Rod Bundles" (2016). *All Graduate Theses and Dissertations*. 4942.
https://digitalcommons.usu.edu/etd/4942

This Dissertation is brought to you for free and open access by the Graduate Studies at DigitalCommons@USU. It has been accepted for inclusion in All Graduate Theses and Dissertations by an authorized administrator of DigitalCommons@USU. For more information, please contact digitalcommons@usu.edu.

UtahStateUniversity
MERRILL-CAZIER LIBRARY

BENCHMARK EXPERIMENTS FOR NATURAL CONVECTION IN NUCLEAR FUEL ROD BUNDLES

by

Kyle L. Jones

A dissertation submitted in partial fulfillment
of the requirements for the degree

of

DOCTOR OF PHILOSOPHY

in

Mechanical Engineering

Approved:

Dr. Barton L. Smith Major Professor	Dr. Robert E. Spall Committee Member
Dr. Aaron Katz Committee Member	Dr. Heng Ban Committee Member
Dr. David W. Britt Committee Member	Dr. Mark R. McLellan Vice President for Research and Dean of the School of Graduate Studies

UTAH STATE UNIVERSITY
Logan, Utah

2016

Copyright © Kyle L. Jones 2016

All Rights Reserved

ABSTRACT

Benchmark Experiments for Natural Convection in Nuclear Fuel Rod Bundles

by

Kyle L. Jones, Doctor of Philosophy

Utah State University, 2016

Major Professor: Dr. Barton L. Smith
Department: Mechanical and Aerospace Engineering

Natural convection is a phenomenon in which a flow of the fluid surrounding a body is induced by a change in density due to the temperature difference between the body and the fluid. This flow can be highly non-linear and turbulent, generating eddies. The complex interaction between the convective, viscous and buoyant forces requires the use of modern turbulent simulation tools for simulation. The accuracy of these tools, due to non-linearity, is difficult to assess. The present study investigates natural convection in nuclear fuel rod bundles using heated rods to simulate the storage of spent fuel in dry casks as a benchmark for simulation validation. Four heated, aluminum cylinders are instrumented and suspended in a rotatable, open-circuit wind tunnel. Particle Image Velocimetry (PIV) is used to non-obtrusively measure the velocity fields for various heating and flow conditions. The system response quantities (SRQs) and inflow conditions are acquired using PIV for use in validation of Computational Fluid Dynamics (CFD) models. All measurements are reported with uncertainties and are repeated for multiple flow conditions and heating scenarios. The boundary conditions, initial conditions and SRQs are compiled and made available for public use in validating CFD models.

(180 pages)

PUBLIC ABSTRACT

Benchmark Experiments for Natural Convection in Nuclear Fuel Rod Bundles

Kyle L. Jones

Buoyancy is the mechanism through which heated air causes fluid motion due to a difference in temperature between a body and the surrounding fluid. This fluid motion can be very erratic and unstable, which creates a difficult problem when attempting to simulate this fluid motion. Using high performance computational power the capability of simulating these complex interactions is available but requires assessment to determine the accuracy of these difficult flow scenarios. This study provides experimental data that can be used to assess the simulation's accuracy and to ensure the computational models are achieving the correct solution. The Rotatable Buoyancy Tunnel (RoBuT) has been designed for this caliber of experiments known as "validation experiments" and will serve as the framework for the present study.

Four heated aluminum rods are suspended in the test section portion of the wind tunnel to model the physics present in a Pressurized Water Ractor (PWR) fuel rod bundle after it has been removed from the spent fuel pool and placed in dry storage. Boundary conditions that will be used as inputs to the computation fluid dynamics (CFD) model are measured with great detail along with their estimated uncertainties. Particle Image Velocimetry (PIV) is the method used to optically measure fluid velocity without interrupting the flow by insertion of a probe giving a truer assessment of the flow. Thermocouples are embedded in the surfaces of the model to measure temperature boundary conditions. The system response quantities (SRQs) are outputs from the system as a result of the boundary conditions applied. Fuel and wall temperatures as well as velocity profiles are the SRQs for this study. After completion, all data acquired will be made available for public use in CFD model validation.

To my wife Chelsi
for her enduring support and encouragement.

To my sons, Asher and Lennox
whose cheerful smiles each day kept me moving forward.

To my parents and parents-in-law
for always asking me to dumb this stuff down so that they could understand it.

ACKNOWLEDGMENTS

First and foremost, I would like to thank Dr. Barton L. Smith for "giving me a chance" 6 years ago as a measly undergraduate and never growing impatient with my endless questions. Without his guidance and encouragement, I never would have made it this far. I would also like to acknowledge the assistance of my colleagues at the Experimental Fluid Dynamics Laboratory who were always willing to allow me to probe their brains for ideas on how to overcome the many obstacles that surfaced over the years.

I am most indebted to my family for their love, support and encouragement throughout my education. My wife Chelsi always had my back and knew how to cheer me up when I was discouraged. My two boys, Asher and Lennox, who always wanted to know how my day was and always smothered me with hugs, kisses and laughter. My parents, Lenny and Mary Ann, who always taught me to do my absolute best in every aspect of my life, especially in education. My parents-in-law, Jeff and Kathy, who essentially became a second set of parents for me after I got married and loved me as one of their own.

And finally, I would like to thank the U.S. Department of Energy's Nuclear Engineering University Program for providing funding for this study.

Kyle L. Jones

CONTENTS

Page

ABSTRACT iii

PUBLIC ABSTRACT iv

ACKNOWLEDGMENTS vi

LIST OF TABLES ix

LIST OF FIGURES x

NOTATION xv

ACRONYMS xix

1 INTRODUCTION 1
- 1.1 Natural and Forced Convection 1
- 1.2 Nuclear Fuel Rod Bundles 3
- 1.3 Validation of CFD Simulations 6
  - 1.3.1 Validation of Natural Convection Flows 7
  - 1.3.2 Validation in Nuclear Fuel 9

2 OBJECTIVES 12

3 FACILITY AND EQUIPMENT 14
- 3.1 Rotatable Buoyancy Tunnel 14
- 3.2 Test Section 16
  - 3.2.1 Fuel Rods 16
- 3.3 Instrumentation 20
  - 3.3.1 Wind Tunnel Inlet 22
  - 3.3.2 Test Section 23
  - 3.3.3 Fuel Model 23
  - 3.3.4 Particle Image Velocimetry 25

4 APPROACH 35
- 4.1 Parameter Space 35
- 4.2 Coordinate System and Data Acquisition Locations 35
- 4.3 Boundary Conditions 36
- 4.4 System Response Quantities 36
- 4.5 Measurement Uncertainty Quantification 40
  - 4.5.1 Stereoscopic PIV Uncertainty 41
  - 4.5.2 Thermocouple Uncertainty 41
  - 4.5.3 Pressure Measurement Uncertainty 42
  - 4.5.4 Taylor Series Method for Uncertainty Propagation 42

4.5.5 Effect of Seed . . . 43
4.6 Sampling Parameters . . . 44
4.7 Turbulence Quantities . . . 45
4.8 Heat Transfer Coefficient . . . 48

5 RESULTS . . . 49
5.1 Boundary Conditions . . . 49
5.1.1 Inflow . . . 49
5.1.2 Power Input . . . 52
5.1.3 Surface Treatment . . . 52
5.2 System Response Quantities . . . 54
5.2.1 Heat Transfer Coefficient . . . 54
5.2.2 Grashof and Rayleigh Number . . . 56
5.2.3 Rod and Wall Temperature Distribution . . . 58
5.2.4 Outlet Fluid Temperature . . . 59
5.2.5 Radiation Heat Transfer . . . 63
5.2.6 Wall Heat Loss . . . 63
5.2.7 Velocity Profiles . . . 64
5.2.8 Autocorrelation . . . 66

6 CONCLUSION . . . 69

REFERENCES . . . 71

APPENDICES . . . 78
A Data Download Information . . . 79
B Velocity Results . . . 82
B.1 Inlet Velocity Fields and Profiles . . . 82
B.2 SRQ Velocity Profiles . . . 85
C Uncertainties . . . 90
D Uncertainty Analysis . . . 91
E Codes . . . 95
E.1 Air Properties and Uncertainty Code . . . 95
E.2 Mass Flow Rate and Reynolds Number Code . . . 97
F Drawings and Schematics . . . 104
F.1 Fuel Rod Drawings . . . 105
F.2 Grid Spacer Drawings . . . 109
F.3 Test Section Drawings . . . 112

CURRICULUM VITAE . . . 157

LIST OF TABLES

Table Page

2.1 Parameter space for the present study. 13

3.1 Volume flow rate, pressure drop and loss coefficient across the inlet flow conditioning for each test case in order of increasing volume flow rate. 23

3.2 PIV acquisition parameters for the test section inlet velocity and SRQ velocity measurements. The Forced, Mixed400 and Mixed700 parameters were combined due to similarity while the Natural400 and Natural700 cases are listed separately. Ranges listed for the Forced/Mixed cases at the inlet indicate the range for the different flow heating cases, while the ranges for the SRQ velocity measurements indicate variation due to different stream-wise SRQ locations. Particle diameter listed here is approximately twice the diameter described above after [1]. Density is listed as particles per pixel or ppp. 34

5.1 Test section inflow average turbulence quantities for each flow case. 50

5.2 Break down of mass flow rate, $\dot{m}$, Reynolds number, Re, and Richardson number, Ri, for each test case based on the integrated velocity profile at the test section inlet with Re calculated according to Eq. 5.3. The Richardson number was calculated using the Grashof number based on the average rod temperature for each case. . . . 51

5.3 Power input to the rod bundles at each rod section level for heated each flow case. . 52

5.4 Estimated heat loss from rods due to radiation heat transfer. 63

5.5 Estimated wall heat loss due to test section wall heating for each of the heated cases. 65

LIST OF FIGURES

Figure Page

1.1 An example of a split vane grid spacer design as shown in [2, 3]. 5

1.2 The validation hierarchy and their descriptions as presented in [4]. 8

1.3 Spectrum of difficulty to measure or acquire an arbitrary SRQ, $y(x)$, after [5]. . . . 8

3.1 (a) An overview of the Rotatable Buoyancy Tunnel (RoBuT) facility. (b) The wind tunnel portion of the facility with key components labeled. 15

3.2 Placement of optical windows for PIV data acquisition. Laser sheets for the inflow velocity acquisition and SRQ velocity acquisition are also shown. 17

3.3 Inlet flow conditioning including PVC seeding array attached upstream of the heat exchanger and inlet contraction. 18

3.4 Step-by-step progression of building the fuel rod sections. Steps are as follows: 1) Machine internal portion of rod halves from aluminum barstock, 2) Bolt two rectangular halves together, 3) Machine block into cylinder roughly larger than final diameter then separate the halves and glue thermocouples in place, 4) Bolt rod halves together and insert plugs into bolt head counterbore locations and fix in place with machineable aluminum epoxy, 5) Machine cylinder to final diameter, and 6) Use chemical deposit nickel plating to treat surface that will be in contact with fluid. 19

3.5 (a) Drawing of the grid spacer placement with respect to the rod bundle. (b) A photograph of the actual grid spacers in the fuel rod bundle. 21

3.6 Thermocopules (brown wires shown) placed on the honeycomb flow straightener to measure the inlet air temperature profile. 22

3.7 Instrumentation used to acquire rod and wall temperatures during data acquisition. Each brown wire corresponds to a single thermocouple. The thermocouples are connected to National Instruments NI-9123 thermocouple modules and cDAQ-9188 chassis on the rear side of the aluminum test section wall. 24

3.8 Close-up of the conduit used to route thermocouple wires from the rod centers to the data acqusition system outside the test section. 26

3.9 Two Laskin nozzle seeders use compressed air to turn olive oil into a fine mist which is injected into the flow domain for PIV measurements. 27

3.10 An example of a raw 2 component PIV image. 28

3.11 An example of a processed 2-component vector field image. 28

3.12 An example of a 3-component vector field resulting from two 2-component vector fields. 28

3.13 (a) The two-plane calibration plate (not to scale) used for the inflow velocity measurements. (b) The Max Levy calibration plate (not to scale) used for acquiring SRQ data. The plate is a single plane which was mounted to a traverse and moved through the laser sheet for calibration. 30

3.14 Calibration setup used for acquiring the test section inlet velocity profile. 30

3.15 Calibration setup used for acquiring the SRQ velocity data. 31

3.16 The setup used to acquire the inlet velocity profile using stereo-PIV. Note that the laser sheet is aligned horizontally such that the stream-wise velocity component passes through the thickness of the laser sheet. 32

3.17 The setup used to acquire the SRQ velocity profile using stereo-PIV. Note that the laser sheet is aligned vertically such that the stream-wise velocity component is aligned with the laser sheet. 33

4.1 Test section inlet views of coordinate system. (a) xz-plane with y-axis leaving the page. (b) yz-plane with x-axis leaving the page. (c) Isometric view of coordinate system. 37

4.2 Locations of the PIV viewing windows for SRQ data acquisition. (a) The cameras for these fields of view (FOVs) were positioned on the left of the figure looking towards the rod bundle. The red line represents the top edge of the camera FOV for the $x = 0$ m dataset for a given z-position. The blue and green lines represent the top edge of the two FOVs taken on the $x = -0.06$ m plane for a given z-position. The dataset for the blue and green FOVs were stitched together after processing to form a single time-averaged velocity field. Each FOV is 45 mm wide. The coordinate system shown is for directional reference only and does not correspond to the actual origin location. (b)The location of the velocity profiles for each z-position. The blue line represents the length of the velocity profile for the $x = 0$ m plane. Combining the blue and green profiles together forms the complete time-averaged velocity profile for the $x = -0.06$ m plane. 38

4.3 Measurement of the test section after construction. From the “as-built” measurements a 3D model is constructed for use in CFD simulations. 39

4.4 Autocorrelations for preliminary dataset to test for sample independence and determine PIV sampling rate. Figure (a) shows the autocorrelation for a sample natural convection dataset acquired at 1 Hz indicating sample dependence. Integrating $\rho(\tau)$ from 0 to the zero-crossing indicated that the sampling rate should be reduced to 0.1 Hz. Figure (b) shows the autocorrelation of the same natural convection case acquired at 0.1 Hz and indicates statistical sample independence. 46

5.1 Test section inflow velocity measurements for the Natural700 case. (a) Contour plot of the through plane velocity component. The first contour level begins at 0 m/s and the increment is 0.0175 m/s. The arrow indicates increasing contour levels and the dashed line represents the location of the line profile. (a) Velocity profiles of the centerline ($x = 0$ m). The velocity used for calculating turbulence intensity was 0.2584 m/s. 50

5.2 Dimensions of the heated and unheated sections of the rod bundle. Uncertainty for lengths are ± 0.001 m. 53

5.3 Surface treatment of the fuel rod assembly. Blue surfaces represent polished aluminum and green surfaces represent nickel plating. (b) Close up of leading edge of fuel rods. (c) Close up of trailing edge of fuel rods. (a) Overview of full fuel rod assembly. 55

5.4 Sketch of the control volume used to determine mean fluid temperature along rods in the z-direction. The dashed line represents the boundaries of the control volume. The control volume extends to the z-position of each axial rod thermocouple position. 57

5.5 Local heat transfer coefficient, h, versus z-location for each rod thermocouple position. 57

5.6 Local Rayleigh number for heated flow cases. 59

5.7 Rod surface temperature distribution in flow-wise direction for (a) the Mixed400 case, (b) the Mixed700 case, (c) the Natural400 case, and (d) the Natural700 case. . 60

5.8 Test section wall temperature distribution in flow-wise direction for (a) the Mixed400 case, (b) the Mixed700 case, (c) the Natural400 case, and (d) the Natural700 case. . 61

5.9 Outlet fluid temperature contour (at $z = 2$ m) for (a) the Mixed400 case, (b) the Mixed700 case, (c) the Natural400 case, and (d) the Natural700 case. The contour scale begins at $\theta = 0$ and has an increment of 0.008. The arrow indicates the direction of increasing temperature. The thermocouples were arranged in a 4×4 square grid and were evenly spaced across the test section outlet (61 mm apart in the x and y directions). 62

5.10 Autocorrelation of time-series velocity fluctuations in the stream-wise direction. Location 1 corresponds to ($x = -0.06$ m, $y = 0.152$ m, $z = 0.476$ m) and Location 2 corresponds to ($x = -0.06$ m, $y = 0.197$ m, $z = 0.476$ m). 67

5.11 Velocity profile along y-direction for (a) $x = 0$ m and (b) $x = -0.06$ m at four z-positions indicated on each plot for the Natural700 case. The inner edges of the fuel rods are aligned with the y-axes on the $x = 0$ m. The relative locations of the swirl elements in the y-position (not to scale in z) are shown in the background of the $x = -0.06$ m figure. 68

B.1 Test section inflow velocity measurements for the Forced case. (a) Contour plot of the through plane velocity component. The first contour level begins at 0 m/s and the increment is 0.075 m/s. The arrow indicates increasing contour levels and the dashed line represents the location of the line profile. (a) Velocity profiles of the centerline ($x = 0$ m). The velocity used for calculating turbulence intensity was 1.3188 m/s. 82

B.2 Test section inflow velocity measurements for the Mixed400 case. (a) Contour plot of the through plane velocity component. The first contour level begins at 0 m/s and the increment is 0.075 m/s. The arrow indicates increasing contour levels and the dashed line represents the location of the line profile. (a) Velocity profiles of the centerline ($x = 0$ m). The velocity used for calculating turbulence intensity was 1.3239 m/s. 83

B.3 Test section inflow velocity measurements for the Mixed700 case. (a) Contour plot of the through plane velocity component. The first contour level begins at 0 m/s and the increment is 0.075 m/s. The arrow indicates increasing contour levels and the dashed line represents the location of the line profile. (a) Velocity profiles of the centerline ($x = 0$ m). The velocity used for calculating turbulence intensity was 1.3564 m/s. 83

B.4 Test section inflow velocity measurements for the Natural400 case. (a) Contour plot of the through plane velocity component. The first contour level begins at 0 m/s and the increment is 0.0125 m/s. The arrow indicates increasing contour levels and the dashed line represents the location of the line profile. (a) Velocity profiles of the centerline ($x = 0$ m). The velocity used for calculating turbulence intensity was 0.1956 m/s. 84

B.5 Velocity profile along y-direction for (a) $x = 0$ m and (b) $x = -0.06$ m at four z-positions indicated on each plot for the forced case. The inner edges of the fuel rods are aligned with the y-axes on the $x = 0$ m. The relative locations of the swirl elements in the y-position (not to scale in z) are shown in the background of the $x = -0.06$ m figure. 86

B.6 Velocity profile along y-direction for (a) $x = 0$ m and (b) $x = -0.06$ m at four z-positions indicated on each plot for the Mixed400 case. The inner edges of the fuel rods are aligned with the y-axes on the $x = 0$ m. The relative locations of the swirl elements in the y-position (not to scale in z) are shown in the background of the $x = -0.06$ m figure. 87

B.7 Velocity profile along y-direction for (a) $x = 0$ m and (b) $x = -0.06$ m at four z-positions indicated on each plot for the Mixed700 case. The inner edges of the fuel rods are aligned with the y-axes on the $x = 0$ m. The relative locations of the swirl elements in the y-position (not to scale in z) are shown in the background of the $x = -0.06$ m figure. 88

B.8 Velocity profile along y-direction for (a) $x = 0$ m and (b) $x = -0.06$ m at four z-positions indicated on each plot for the Natural400 case. The inner edges of the fuel rods are aligned with the y-axes on the $x = 0$ m. The relative locations of the swirl elements in the y-position (not to scale in z) are shown in the background of the $x = -0.06$ m figure. 89

NOTATION

Variables

A	Cross-sectional area
A_s	Surface area
Bi	Biot number
B_r	Bias uncertainty of variable r
C_μ	Turbulence model constant
c_p	Specific heat
D	Experimental result
D_h	Hydraulic diameter
d_p	Particle diameter
E	Validation error or Voltage
E_{g}	Energy generated
E_{in}	Energy input
E_{out}	Energy output
$f\#$	Camera aperture setting
Gr	Grashof number
g	Acceleration due to gravity
h	Heat transfer coefficient
I	Turbulence intensity or Current
k	Turbulence kinetic energy
k_f	Thermal conductivity of the fluid
k_s	Thermal conductivity of the solid
L	Characteristic length for dimensionless variables
L_c	Characteristic length, $L_c \equiv V / A_s$
ℓ	Mixing length
$\dot{m}$	Mass flow rate

Nu	Nusselt number
P	Perimeter
P_{atm}	Atmospheric Pressure
P_d	Partial pressure of dry air
P_{rod}	Power input to the fuel rods
P_{sat}	Water vapor saturation pressure
P_v	Partial pressure of water vapor
Pr	Prandtl number
Q	Volume flow rate
q	Total heat transfer
R_d	Gas constant for dry air
R_v	Gas constant for water vapor
Ra	Rayleigh number
Re	Reynolds number
Ri	Richardson number
S	Simulation result
S_T	Sutherland's temperature
S_r	Random uncertainty of variable r
s_{ij}	Fluctuating strain rate tensor
T	Temperature measurement
T_{amb}	Ambient temperature
T_i	Inlet fluid temperature
T_m	Mixed mean fluid temperature
T_s	Surface temperature
T_∞	Freestream temperature or ambient temperature
t	Time
U	Uncertainty, subscript indicates corresponding variable
U_∞	Freestream velocity

u	Velocity component in x-direction
$u(t)$	Instantaneous velocity measurement
V	Fluid velocity
v	Velocity component in y-direction
w	Velocity component in z-direction
w_{bulk}	Bulk velocity in the z-direction
x	Cartesian coordinate
y	Cartesian coordinate
z	Cartesian coordinate
α	Thermal diffusivity
β	Thermal expansion coefficient
β^*	Turbulence modeling constant
ΔE_{st}	Change in stored energy
ΔP	Pressure difference
ϵ	Turbulence dissipation
ϵ_s	Total hemispherical emissivity
θ	Dimensionless temperature
μ	Absolute viscosity
ν	Kinematic viscosity
ρ	Density
$\rho(\tau)$	Correlation magnitude
σ^2	Statistical variance
σ_x	Standard deviation of variable x
τ	Time lag in autocorrelation
$\overline{\tau}$	Turbulent shear stress
τ_{ij}	Reynolds stress tensor
ω	Specific turbulence dissipation rate

Symbol Modifiers

$\overline{x}$	An averaging operation
$\hat{x}$	Component of turbulence intensity
x'	The fluctuating portion of a Reynolds decomposition

Subscripts

q_{cond}	Heat transfer due to conduction
q_{conv}	Heat transfer due to convection
q_{loss}	Heat loss from a surface
q_{rad}	Heat transfer due to radiation
q_{total}	Total heat transfer
U_{D}	Experimental data uncertainty
U_{input}	Simulation uncertainty due to input uncertainty
U_{num}	Numeric uncertainty
U_{val}	Validation uncertainty
x_i or x_j	Vector component in index notation
x_i or $x_{,i}$	Property at the inlet
x_{ij}	Tensor component in index notation
x_o or $x_{,o}$	Property at the outlet
x_s	Property at the surface

ACRONYMS

AIAA	American Institute of Aeronautics and Astronautics
ASME	American Society of Mechanical Engineers
BC	Boundary Condition
CFD	Computational Fluid Dynamics
CJC	Cold Junction Compensation
DAQ	Data Acquisiton
DIC	Direct Image Correlation
DNS	Direct Numerical Simulation
DoD	The U.S. Department of Defense
DoE	The U.S. Department of Energy
DRE	Data Reduction Equation
FOV	Field of View
HTGR	High Temperature Gas-cooled Reactor
IC	Initial Condition
LDV	Laser Doppler Velocimetry
LES	Large-Eddy Simulation
LWR	Light Water Reactor
M&S	Modeling and Simulation
NI	National Instruments
NRSE	Non-Referenced Single Ended
ppp	Units of particle density, particles per pixel
PIV	Particle Image Velocimetry
PLIF	Planar Laser-Induced Fluorescence
PWR	Pressurized Water Reactor
RANS	Reynolds-Averaged Navier-Stokes
RoBuT	Rotatable Buoyancy Tunnel
RST	Reynolds Stress Tensor

SLE	Special Limits of Error
SRQ	System Response Quantity
TSM	Taylor Series Method for uncertainty propagation
VI	Virtual Instrument
V&V	Verification and Validation
VV&A	Verification, Validation and Accreditation

CHAPTER 1

INTRODUCTION

Research in all aspects of the reactor fuel life cycle is being performed. Many reactors that have been in service for the last 30+ years are now being considered for retirement and the fuel inside must be disposed of properly. Long-term storage of the reactor fuel is a critical step in the fuel's life cycle for which little research has been performed when compared to other stages in the fuel life cycle. To date, simulations with simplified calculations have been performed to determine the storage parameters. Computational fluid dynamics (CFD) simulations are the primary method for determining the amount of decay heat removed from bundles in dry storage. The solutions from these simulations, however, have not been tested in all applications to determine the validity of the solution. Solution validation is the comparison of the results of a simulation to experimental data to determine the accuracy of the numerical model. A validation experiment should capture all essential physics of interest that are present in the full-scale application, thus a single validation study cannot be applied to all CFD simulations [5]. The inability to apply single validation cases to a wide spectrum of applications requires individual validation level studies to be performed on a case-by-case basis. To date no validation data are available for single-phase natural convection heat transfer in vertical fuel rod bundles. This study will fill this gap in validation data.

1.1 Natural and Forced Convection

In fluid dynamics, the Reynolds number,

$$\mathrm{Re} = \frac{VL}{\nu}, \tag{1.1}$$

provides a measure of the relative importance of inertial and viscous forces. It is well known that Reynolds number is the primary dimensionless parameter that governs transition from laminar to turbulent flow. The flow is often assumed fully turbulent for Reynolds numbers larger than 5×10^5

for zero pressure gradient external flow and larger than $2,300$ for flow in round smooth pipes. This non-dimensional parameter is not appropriate, however, in the case of natural convection where fluid motion is not imposed. In convection, fluid flow around a body is induced by buoyancy forces caused by density changes due to heating or cooling of the fluid. According to Incropera, *et al.* [6], Rayleigh number is customary for determining transition to turbulence under convection. Rayleigh number defined as

$$\mathrm{Ra} = \frac{g\,\beta\,(T_s - T_\infty)\,L^3}{\nu\alpha}. \tag{1.2}$$

where g is the gravitational constant, β is the coefficient of thermal expansion, T_s is the surface temperature of the body, T_∞ is the bulk fluid temperature, L is the characteristic length and α is the thermal diffusivity. The Rayleigh number represents the relationship of buoyancy and viscosity in the fluid due to convection. Similar to the Rayleigh number, the Grashof number (Gr) approximates the ratio of buoyancy to viscous forces and is defined as

$$\mathrm{Gr} = \frac{\mathrm{Ra}}{\mathrm{Pr}} = \frac{g\,\beta\,(T_s - T_\infty)\,L^3}{\nu^2}. \tag{1.3}$$

For flow over vertical plates, Rayleigh numbers larger than 10^9 are considered fully turbulent [6]. In the case of mixed convection where both forced fluid flow and heating/cooling are present, the relative effects of each are determined using the Richardson number $\mathrm{Ri} = \mathrm{Gr}/\mathrm{Re}^2$. Natural convection is considered negligible when $\mathrm{Ri} < 0.3$, forced convection is negligible when $\mathrm{Ri} > 16$, and relative impacts of both are non-negligible when $0.3 < \mathrm{Ri} < 16$ [7].

The total heat transfer from a surface is represented by Newton's law of cooling and is expressed as

$$q = hA_s(T_s - T_\infty) \tag{1.4}$$

where h is the heat transfer coefficient and A_s is the surface area. The convection coefficient is dependent on flow conditions and is generally low for free convection and much higher for forced convection. This coefficient is also larger for liquid flows compared to gaseous flows and can be very large for boiling. Likewise, the convection coefficient is generally low for laminar flow regimes and high for turbulent regimes due to increased boundary layer mixing. Determining the heat transfer

coefficient in Eq. 1.4 is not trivial. In many cases, large sets of experimental results are described through the use of the dimensionless heat transfer coefficient or the Nusselt number

$$\begin{aligned} \mathrm{Nu} = \frac{hL}{k_f} &= f(\mathrm{Re}, \mathrm{Pr}) \text{ for forced convection} \\ &= g(\mathrm{Ra}, \mathrm{Pr}) \text{ for natural convection} \end{aligned} \tag{1.5}$$

where k_f is the thermal conductivity of the fluid [6]. The functions $f(\mathrm{Re}, \mathrm{Pr})$ and $g(\mathrm{Ra}, \mathrm{Pr})$ represent Nusselt number correlations based on experiments. When the Nusselt number cannot be determined analytically, experiments are performed in order to determine the Nusselt number empirically. Using these empirical correlations, the convection coefficient can be determined for application to cases where the flow conditions cannot be easily measured. In many cases when the flow geometry is complex, the only practical approach is to determine the Nusselt number experimentally [7].

In nuclear reactor accident scenarios, such as the loss of off-site power at the Fukushima Daiichi plant in 2011 which resulted in failure of the circulation pumps in the spent fuel pools, the water removing heat from the fuel was reported to have boiled away leaving naturally convecting air surrounding the rods as the only cooling source. Due to the complex geometry of fuel rod bundles and interaction of multiple rods in a confined space, traditional convection correlations for simple geometries do not apply. Research has provided convection correlations to determine the heat transfer coefficient for rod bundles and will be discussed later.

1.2 Nuclear Fuel Rod Bundles

Light water reactors (LWRs) are nuclear reactors that use normal water as both the coolant and the neutron moderator. One such reactor design, the pressurized water reactor (PWR), uses uranium ore which is manufactured in pellet form and inserted into zirconium alloy tubes as the fission source. These tubes are then assembled as bundles with a grid spacer that ensures proper spacing between the rods. Once the rod bundles have been placed in the reactor, water is pumped through the bundles and heated as a by-product of the fission reaction occurring between the rods. The water is superheated as it passes the bundles and this thermal energy is transferred to a secondary water loop where the heat is extracted through rotating turbines which generates electricity.

Heat transfer in rod bundles is improved through the use of mixing vanes or swirl elements on the grid spacers. Swirl elements are designed to increase mixing in the flow and improve heat transfer. An example of a split vane swirl element is shown in Fig. 1.1. Rigorous investigation of the shape of these swirl elements has been performed in order to optimize the rod bundle performance in the reactor.

After the fuel has reached the end of its cycle inside the reactor, it is moved to a spent fuel pool where decay heat is removed until a sufficient level is reached that it may be removed and placed in dry storage. The rods continue to produce decay heat at an exponentially decreasing rate after being placed in dry storage. Sufficient heat must still be removed from the rods to prevent the cladding from melting while in dry storage.

Much of the experimental research in fuel rod bundles that is currently available attempts to determine Nusselt number correlations for specific rod bundle applications. Davis and Perona [8] used an open tube bundle immersed in fluid to determine Nusselt number correlations for two different pitch-to-diameter ratios and compared their result to theoretical results, assuming the flow was stable and laminar. Keyhani, *et al.* used a 3×3 and a 5×5 rod bundle to determine Nusselt number correlations in helium or air-filled canisters under pressurized conditions from 1 to 5 atm and compared these results with rod temperatures of an actual fuel rod bundle and found good agreement [9]. Arya and Keyhani used a one-twelfth scaled model of a sealed storage cask containing 12 heated rods to determine the Nusselt number correlation for the rod bundle under dry storage conditions [10]. Heat transfer correlations in fuel rod bundles have been investigated by Canaan for application of rod bundles in transport and dry storage in the horizontal orientation [11]. While determining the convection correlations for rod bundles is useful for empirical models, it does not provide sufficient information to be used for CFD model validation.

Other attempts have been made to simplify the models needed to approximate the flow and heat transfer characteristics through rod bundles. It has been suggested that a porous media model be used to approximate the flow through rod bundles which simplifies the fluid flow to a discharge rate and pressure drop across the bundle, greatly reducing the mesh size/complexity and computation time. Haldar, *et al.* investigated the application of a Darcy porous media model for use in a 7-

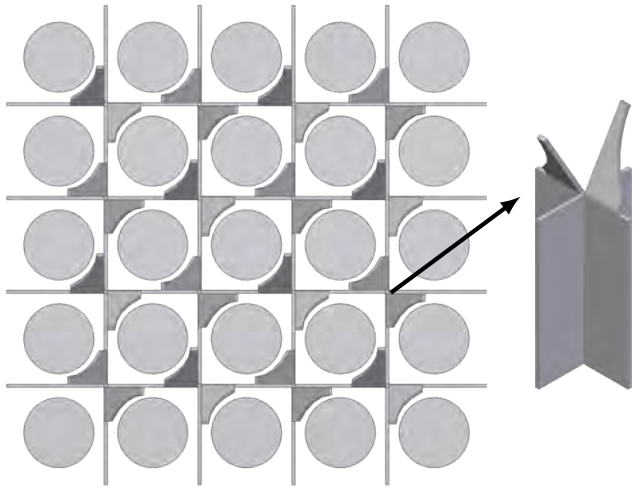

Fig. 1.1: An example of a split vane grid spacer design as shown in [2, 3].

rod fuel assembly and found good agreement with experimental measurements [12]. Krishna, *et al.* suggested using a non-Darcy porous media model and is compared to experimental results. The authors stated that the non-Darcy model provides insight into flow behavior and heat transfer mechanisms inside fuel assemblies while greatly simplifying the model [13].

Grid spacer swirl elements can greatly improve heat transfer from fuel rod assemblies by enhancing swirl and mixing. Yao, *et al.* investigated the impact of swirl elements on the Nusselt number correlation. It was found that the increased blockage ratio had the greatest impact on heat transfer [14]. Karoutas, *et al.* used CFD and simple experimental measurements to determine whether the CFD results could be used to optimize grid spacer design [2]. This work is frequently used for CFD validation and will be further discussed below. Durbin, *et al.* performed laser dopler velocimetry (LDV) measurements on a prototypical fuel rod bundle under laminar flow conditions and found that the presence of mixing vanes induced long time scale wake disturbances that would be more aptly described by turbulent CFD models [15]. Hille, *et al.* performed Particle Image Velocimetry (PIV) and LDV measurements on an unheated 5×5 rod bundle to determine the cross flow distribution or mixing behavior of three different grid spacer designs [16]. Flow mixing experiments performed by Ylönen and Prasser used CFD optimized grid spacer elements and wire mesh sensors to determine mixing downstream of the spacers [17]. Hutli, *et al.* used a combination of PIV and Planar Laser-Induced Fluorescence (PLIF) to measure the coolant flow and mixing

characteristics of a rod bundle used in a PWR and investigate the uncertainty associated with PLIF measurements [18]. Song, *et al.* tested the design of new PWR mixing vanes using a combination of mechanical and thermal-hydraulic tests and simulations to compare their mixing and structural capabilities [19].

1.3 Validation of CFD Simulations

With the exponential increase in computing power over the last 30 years, research groups are relying heavily on the results of simulation to influence the design and decision making processes. In order to ensure that the solutions provided by these simulations are accurate, it is necessary that the models be validated to determine its uncertainty. The U.S. Department of Defense (DoD) released a recommended practices guide for the Verification, Validation and Accreditation (VV&A) of Models and Simulations (M&S) for more informed judgment and assessment [20]. In 1998 the American Institute for Aeronautics and Astronautics (AIAA) published a standard to be used for the verification and validation of CFD models [4]. The American Society of Mechanical Engineers (ASME) also published a standard for Verification and Validation (V&V) of CFD and heat transfer in 2009 called V&V-20 which has been extended from the AIAA standard to include heat transfer problems [21]. Verification and validation is a critical part of model development and application in simulation use.

Using these standards, one can ensure that the simulation results are accurate. According to Oberkampf and Smith [22], “Validation assesses the accuracy of the mathematical model by comparing simulation results to experimentally measured quantities of interest." In contrast to discovery experiments where the experimentalist is attempting to discover or understand more about a certain physical phenomenon, *validation experiments simply look to measure the physical nature of a system for the purpose of providing a complete description of the system which can be used to test the validity of a model* [23].

Validation of complete, large-scale systems is generally not feasible to perform. Methodology for a hierarchical approach to validation has been outlined in [22, 24–26]. Figure 1.2 shows the validation hierarchy for the complete systems which are broken down into smaller subsystems for

validation purposes. According to this hierarchy, the present work is considered a Benchmark-Level case due to the high level of coupling between fluid flow and heat transfer occurring in the flow domain.

When performing a validation experiment, careful documentation of all *boundary conditions* (BCs), *initial conditions* (ICs) and *system response quantities* (SRQs) and their associated uncertainties is vital. Examples of boundary conditions may be locations of physical walls/geometries or the temperature distribution of a surface. Initial conditions are similar to boundary conditions but exist at the start of an experiment and change over time, for example, the temperature response of a body after starting an electric heater. System response quantities are the outputs of the system that are recorded for comparison to the output of a simulation such as a velocity profile in the fluid domain or wall shear density at a boundary. System response quantities are provided to the analyst *after* performing the simulations in order to ensure that the data are used for validation rather than model calibration [5].

Careful experimental design is needed in order to have sufficient insight to plan for SRQs to be measured. Modelers and experimentalists should be involved through all aspects of the design and execution of a validation experiment for optimum success. Knowledge of the relative difficulty of specific SRQs will aid both parties in exercising the limits of the CFD model especially in cases of complex physics. Figure 1.3 shows the spectrum of SRQs and their relative difficulty to both measure and predict. Using this spectrum in the planning stages of a validation study will allow for more rigorous testing of the models applied.

1.3.1 Validation of Natural Convection Flows

Few validation studies exist for buoyantly driven flows. De Vahl Davis [27] and De Vahl Davis and Jones [27] were among the first to perform benchmark studies for natural convection in an enclosure, although these benchmarks were using CFD simulations only on uniform meshes of up to 81×81 cells due to limited computational resources at the time and were compared to analytical solutions for the laminar flow regime.

The first full validation experiment of this type was performed in 1998 by Leong, *et al.* for

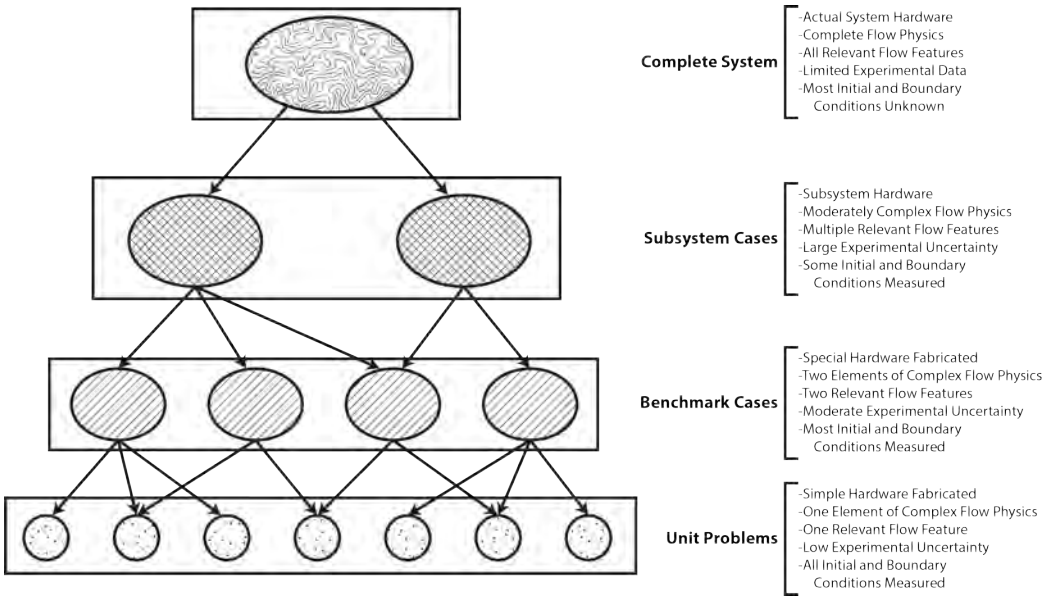

Fig. 1.2: The validation hierarchy and their descriptions as presented in [4].

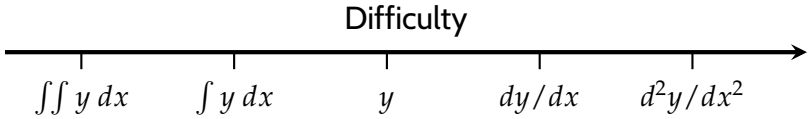

Fig. 1.3: Spectrum of difficulty to measure or acquire an arbitrary SRQ, $y(x)$, after [5].

natural convection in a cubical cavity with opposing faces at different temperatures. The authors report Nusselt numbers accurate to 1% for Rayleigh numbers in the laminar flow regime [28]. The experimental results were compared to CFD for $\mathrm{Ra} = 4 \times 10^4$ and found to be accurate to within 0.3%. Later, Leong, *et al.* also performed benchmark experiments using the same apparatus for a wider range of Rayleigh numbers up to 10^8 in order to determine Nusselt numbers for the cavity at different tilt angles [29].

Other variations of validation experiments for natural convection in cavities were later performed. Mamun, *et al.* provide an extension of Leong's previous publications by using a "double inclined" cubical cavity for Rayleigh numbers ranging from 10^3 to 3×10^8 [30]. Ampofo and Karayiannis performed validation experiments for turbulent natural convection in a square cavity ($\mathrm{Ra} > 10^9$) [31].

Betts and Bokhari have provided a detailed validation study for turbulent natural convection in an enclosed tall cavity [32]. This study not only provides integral quantities such as the Nusselt number and heat transfer coefficient but also temperature and velocity profiles through the vertical direction of the experiment. The experiment presented is very extensive and provides substantial detail for use in CFD validation. Tian and Karayiannis also performed a turbulence validation benchmark experiment for a square cavity providing both velocity and temperature profiles within the cavity for use in validation [33]. These two studies have provided high-quality validation data for naturally convecting flows. However, they are only applicable to recirculating cavity flow. Natural convection open channel flow can be a much more difficult problem to simulate due to tight coupling of fluid flow with fluid properties where slight variations in boundary conditions can dramatically affect the solution.

1.3.2 Validation in Nuclear Fuel

Many studies have been performed using CFD to improve the design process in fuel rod bundles. In the work by In, *et al.*, CFD simulations were used to improve coolant mixing in fuel rod bundles by comparing different grid spacer swirl element shapes [34]. Cui and Kim have investigated the impact of mixing vane shape on the heat transfer to reactor coolant using CFD and found

that swirl element twist angle must be larger than 25° to be effective and larger twist angles increase heat transfer from the rods [35]. Liu, *et al.* used five different CFD approaches to determine the average heat transfer coefficient for different subchannel models using CFD results as the basis for comparison [36]. Navarro and Santos analyzed the influence of vane arrangement on the heat transfer characteristics of a 5×5 prototypical PWR fuel rod bundle in order to determine which configurations provide the best mixing in the fluid [3]. Tiftikçi, *et al.* used the Lattice-Boltzmann method to simulate the mixing induced by flow through a 2×2 PWR grid spacer with vanes [37].

Significant effort has also been made to acquire Benchmark-level validation data for fuel rod bundles in the horizontal orientation. Bundles may be placed in the horizontal position during transport and potentially during dry storage. Keyhani and Lo performed a numerical analysis of fuel rod bundles of size $N\times N$ for $N = 3, 5, 7, 9$ with pitch-to-diameter ratio of 1.33 using a finite element code in order to determine Nusselt number correlations for horizontal rod bundles [38]. Later, Keyhani and Dalton determined Nusselt number correlations experimentally for the same rod bundles but with pitch-to-diameter ratio of 1.35 [39].

Increased computing power has allowed for use of multi-phase flow models in CFD codes. Many researchers are focusing on providing validation for two-phase boiling flow inside rod bundles. Ustinenko, *et al.* and Tentner, *et al.* performed a detailed analysis of multi-phase and bubbly flow in BWR fuel bundles using commercially available CFD software in a staged approach with experiments of increasing difficulty to model [40, 41]. While high quality validation experiments, these cannot be applied to single-phase, naturally convecting flow.

The work of Karoutas, *et al.* was originally carried out to determine if using CFD can improve the design process of rod bundles and grid spacers. While often cited as a validation exercise, the detail necessary for complete validation is lacking [2]. Extensive work at Westinghouse has been performed to determine the effects of grid spacers on heat transfer for both single-phase and two-phase flow in PWR bundles [42–49]. These investigations have provided significant advancement in the amount of validation data available for forced flow through rod bundles.

Many Benchmark-level validation studies are available for different flow regimes in LWR fuel rod assemblies, but there are currently no validation quality experiments for single-phase natural

convection flow through vertical fuel rod bundles. This work will provide much needed validation data.

CHAPTER 2

OBJECTIVES

The purpose of this work is to provide experimental data for validating single-phase, strongly heated internal gas flows around vertical spent nuclear fuel rod bundles *under steady-state conditions*. The objectives to achieve this purpose are:

1. Design and construct a fuel rod model that is compatible with the Rotatable Buoyancy Tunnel (RoBuT) for CFD validation.
2. Carry out validation experiments for forced unheated, mixed convection and natural convection flow cases.
3. Compile boundary conditions and system response quantities and make available for public use.

In order to acheive these objectives, the following tasks were performed:

- Design and construct an experiment according to the methodology presented in Oberkampf and Smith [22].
- Write control system in LabView [50] to control the experiment and room conditions.
- After constructing the test section, acquire all boundary conditions and SRQ data with associated uncertainties for test cases shown in Table 2.1.
  - Boundary Conditions
    - Measure geometry and reconstruct a 3D solid based on measurements.
    - Measure ambient and atmospheric conditions.
    - Measure inflow temperature and inlet velocity profile.
    - Calculate turbulence quantities for inputs to CFD simulations.
    - Measure power input to fuel rods.
  - System Response Quantities
    - Wall and rod temperatures
    - Velocity profiles at various locations in rod bundle

  - Outlet temperature profile of fluid

- Calculate heat transfer coefficient and Nusselt number and compare to empirical correlations for rod bundles from [8–10].
- Compile boundary conditions and system response quantities and make available for use in future validation exercises.

Table 2.1: Parameter space for the present study.

Case No.	Case Name	Heat Flux [W/m^2]	Re	Gr	Blower Freq. [Hz]
1	Forced	Unheated	23,300	N/A	5
2	Mixed400	400	23,400	5.86×10^9	5
3	Mixed700	700	23,200	1.01×10^{10}	5
4	Natural400	400	3,450	6.44×10^9	0
5	Natural700	700	4,600	7.87×10^9	0

CHAPTER 3
FACILITY AND EQUIPMENT

3.1 Rotatable Buoyancy Tunnel

Under a previous grant from the U.S. Department of Energy (DoE), the wind tunnel was designed by Engineering Laboratory Design, Inc. for the purpose of CFD validation. The wind tunnel is mounted to a rotational frame, allowing it to be rotated and change the acting direction of gravity for mixed convection experiments. For the purpose of this work, the buoyancy-aided flow configuration will be the only orientation used. Figure 3.1a shows the complete facility used for validation experiments and Fig. 3.1b shows the wind tunnel portion of the facility. Two other validation studies have been performed in this facility with a test section containing a single heated wall and no fuel rod model intended for flow physics validation in High Temperature Gas-cooled Reactor (HTGR) cores [51, 52].

Olive oil seed is dispersed into the air entering the flow conditioning portion of the wind tunnel through a series of $1/4$ in., Schedule 40 PVC pipe with $\varnothing$ 3.2 mm holes spaced 25.4 mm apart. The fluid then passes through a copper-tube/aluminum-fin heat exchanger (Super Radiator Coils Model 30x30-01R-0.625/048), which was unused for this study, and through a 100 mm settling region before passing through a precision aluminum honeycomb flow straightener and finally two high porosity mesh screen. The seeding array and honey comb flow straightener are shown in Fig. 3.3. Fig. 3.6 shows the downstream side of the honeycomb flow straightener as well as the thermocouples used to measure the incoming fluid temperature. The fluid is then accelerated uniformly through the 6.25:1 area-ratio inlet contraction 0.914m in length constructed of fiberglass with a glossy gel-coat finish before entering the test section described in Section 3.2.

After leaving the test section, the fluid passes through a transformation 0.686 m in length which is attached to the outlet of the test section for connecting it to a blower. The transformation converts the square cross-section (304.8 mm $\times$ 304.8 mm) of the wind tunnel to the circular cross-section

(a)

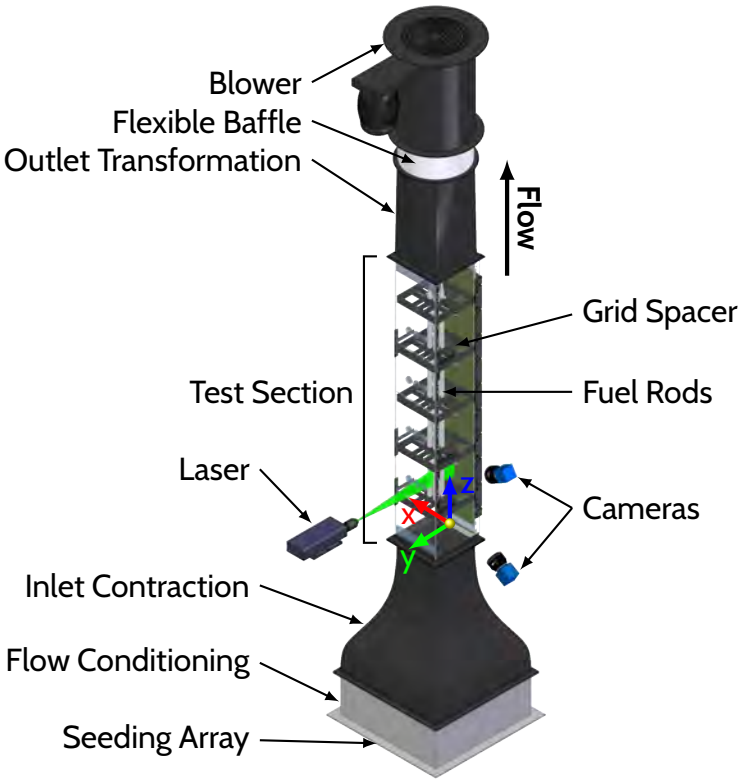

(b)

Fig. 3.1: (a) An overview of the Rotatable Buoyancy Tunnel (RoBuT) facility. (b) The wind tunnel portion of the facility with key components labeled.

(∅ 102 mm) of the blower and is constructed of four sections of fiberglass with a gel-coat finish that are bolted together. A flexible baffle was placed between the outlet transformation and the blower for the forced and mixed cases, allowing the fluid to be drawn through the test section by the blower, and removed for the natural convection cases, allowing the fluid to freely leave the test section. The blower was an inline centrifugal fan (TCF Aerovent Company Model 14-CBD-3767-5) that was belt driven by a 5 HP, TEFC, 230-460 VAC induction motor. The blower speed was controlled by a Toshiba 3-phase variable frequency inverter (VF-S11). The blower frequency was set to 5 Hz for the forced and mixed cases as this was the lowest usable output possible by this system. For drawings of the facility refer to Harris [51].

3.2 Test Section

The dimensions of the wind tunnel walls are fixed in order to be able to mount in the facility. The test section has a 304.8 mm × 304.8 mm (12 in. × 12 in.) internal cross-section and is 2 m in length. Three of the four walls are constructed of Lexan™ polycarbonate and are 12.7 mm (0.5 in.) thick. The fourth wall is constructed of a 12.7 mm thick Aluminum 6061-T6 plate for structural rigidity and has been painted flat black and coated with a rhodamine fluorescent die for filtering reflections during PIV data acquisition. Each wall is divided into four interlocking sections for ease of manufacturing, assembly and maintenance. The panels of the wall opposite the aluminum wall are easily removed for internal cleaning as well as for PIV calibration. Rectangular optical windows are placed at the inlet and outlet of the test section for PIV measurements to reduce the amount of refraction inside the polycarbonate walls during inflow measurement. Circular optical windows are placed at the midpoint between each grid spacer for PIV measurements in the flow-wise direction. Optical window placement is shown in Fig. 3.2.

3.2.1 Fuel Rods

Four 1.58-m-long fuel rods of ∅ 31.75 mm are each divided into four interlocking sections for a total of 16 rod sections. Each section contains a 20 W split-sheath cartridge heater that is powered electrically by two Model 9174 programmable power supplies from BK Precision. Voltage is controlled in order to match a specified rod surface heat flux. Each of the interlocking rod sections

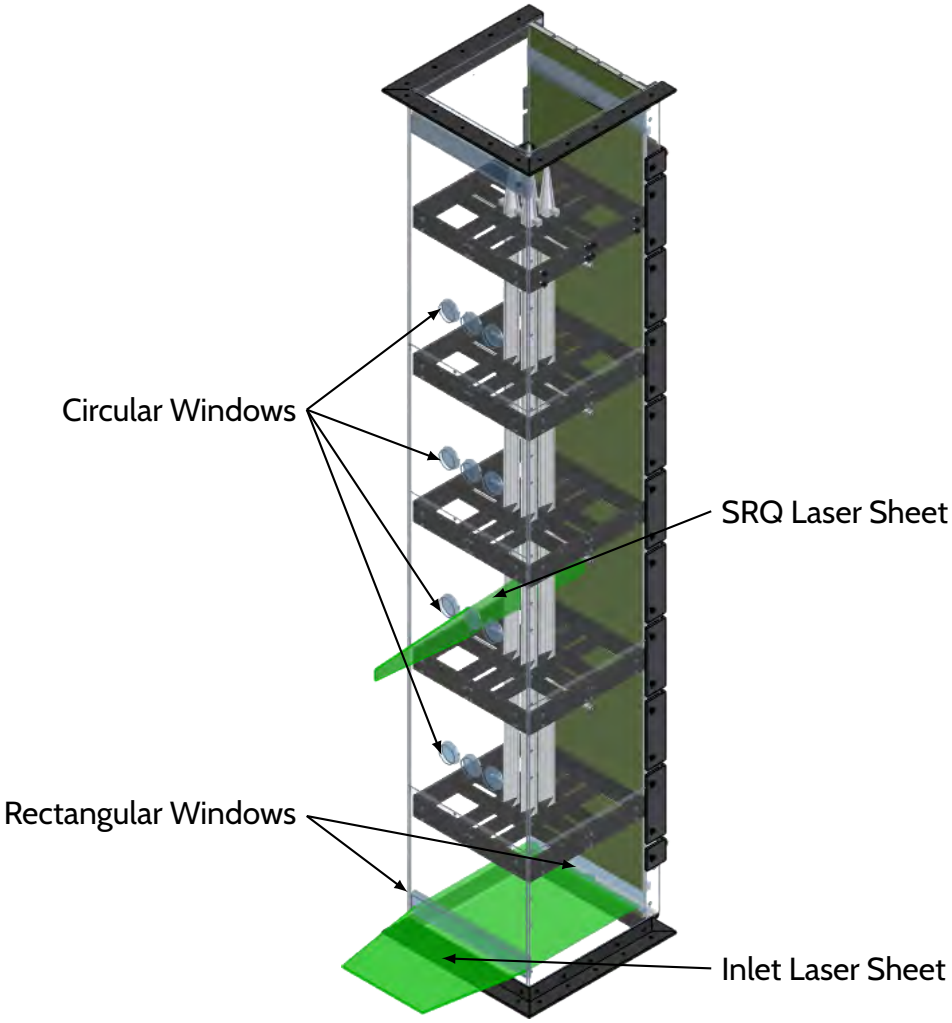

Fig. 3.2: Placement of optical windows for PIV data acquisition. Laser sheets for the inflow velocity acquisition and SRQ velocity acquisition are also shown.

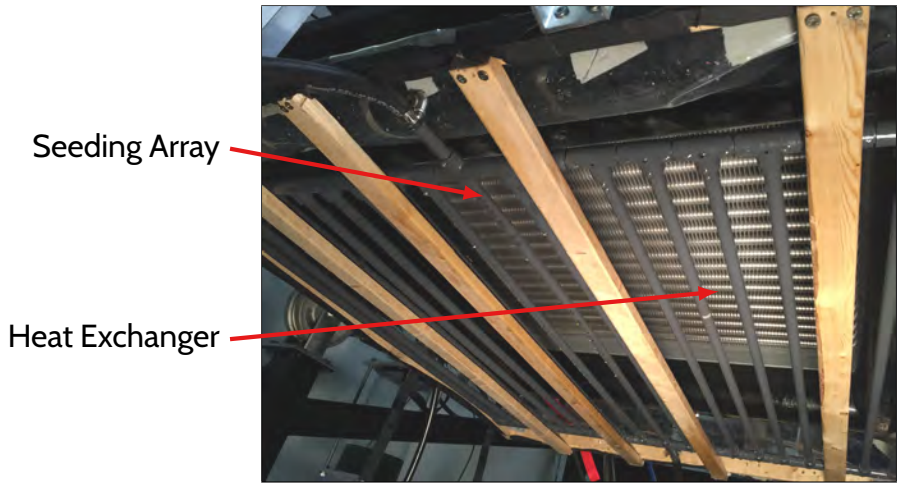

Fig. 3.3: Inlet flow conditioning including PVC seeding array attached upstream of the heat exchanger and inlet contraction.

was instrumented both axially and circumferentially to measure temperature variations in the rods. A smooth exterior surface is required for CFD meshing purposes, thus the thermocouples were embedded inside the rod sections. To achieve this, the internals of the fuel rods were machined from two aluminum 6061-T6 bars as shown in Fig. 3.4. The two halves were then bolted together and machined externally into a cylindrical shape of slightly larger diameter than the final rod size. Thermocouples were embedded internally with "high" thermal conductivity (5 W/m^2/K) epoxy. Thermocouple and heater electrical wires were routed outside the rods and the two halves were then bolted together permanently to a specified torque appropriate for the screw size and substrate (2.3 N-m). The holes containing the bolt heads were then plugged with rods of the same series aluminum and fixed in place with Duralco 4540 machinable aluminum epoxy. The rod sections were then machined to their final diameter. Finally, the rod surfaces that were exposed to fluid flow are electroless nickel plated to protect the aluminum from oxidation. The emissive properties of aluminum vary widely with surface condition as discussed by [53, 54]. The nickel plating also reduces the variation in emissive properties of the rods and acts to limit the amount of heat transfer due to radiation. The thermocouple wires and heater electrical wires were routed outside the test section via a $\varnothing$ 16 mm aluminum conduit with a ceramic spacer between the conduit and the rod in order to limit conductive heat transfer to the conduit.

The leading end of each full length rod was treated with a polished aluminum, hemispherical

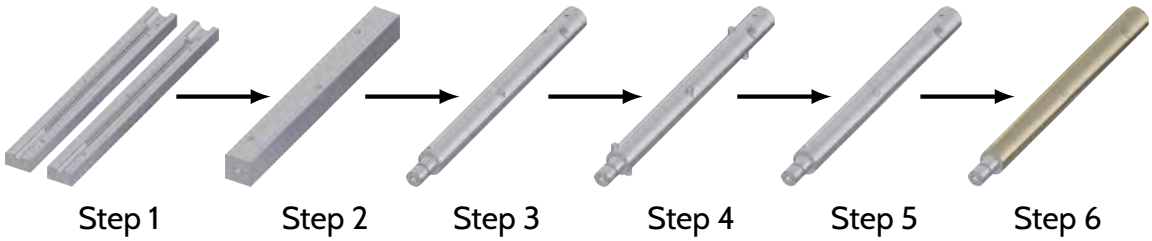

Fig. 3.4: Step-by-step progression of building the fuel rod sections. Steps are as follows: 1) Machine internal portion of rod halves from aluminum barstock, 2) Bolt two rectangular halves together, 3) Machine block into cylinder roughly larger than final diameter then separate the halves and glue thermocouples in place, 4) Bolt rod halves together and insert plugs into bolt head counterbore locations and fix in place with machineable aluminum epoxy, 5) Machine cylinder to final diameter, and 6) Use chemical deposit nickel plating to treat surface that will be in contact with fluid.

cap in order to limit the amount of flow separation which induces long time-scale turbulent fluctuations. The trailing end of each full length rod is fitted with a 128 mm long, polished aluminum cone in order to limit the low frequency turbulent fluctuations caused by a blunt rod termination and is thermally isolated using fiberglass tape.

The grid spacers used to maintain rod spacing are constructed of 4130 steel alloy and spray-painted flat black. The first four of the grid spacers in the stream-wise direction have swirl elements in order to improve mixing. The fifth grid spacer does not have swirl elements in order to allow for structural support of the rod bundle, which is suspended by two aluminum bars that have been thermally isolated with fiberglass tape. The swirl elements are right triangles that have been bent at 45° into the flow domain resulting in a blockage ratio of approximately 18%. Swirl elements are placed on two of the four corners surrounding a single rod as shown in Fig. 3.5. The shape of the swirl elements greatly affects the heat transfer in a fuel bundle [2, 14, 34]. This particular shape was chosen to simplify the geometry during boundary measurement and allow for ease in 3D model reconstruction. While considerably less effective at mixing, this shape still generates the same physics that are present in the actual fuel bundle. Four #4-40 set screws are threaded through the grid spacers to support the rods and keep them centered. Fiberglass tape has been placed on the tip of each screw to reduce conductive heat transfer to the grid spacers. The borders of each grid spacer are recessed in the polycarbonate walls to eliminate a step in the flow domain. The pitch-to-diameter ratio of the assembly is 1.52. The rod diameter and pitch-to-diameter ratio are larger than

a prototypical PWR assembly [55]. This was necessary to allow for instrumentation and assembly purposes but still allows the model to capture the physics associated with dry fuel storage.

3.3 Instrumentation

Data acquisition (DAQ) hardware from National Instruments (NI) were selected to interface with the control software LabView. A 32-channel NI-9205 analog input module was used to monitor the DAQ system as well as record differential pressure measurements made with the Baratron pressure sensor discussed below. Control of the variable frequency inverter powering the blower was performed using a 16-channel NI-9264 $\pm$ 10 V analog output module. Both the analog input and analog output modules were connected to the DAQ system using an NI cDAQ-9174 4-slot USB Chassis.

Atmospheric conditions for determining air properties were measured continuously over the entirety of the experiment. The ambient temperature and relative humidity were measured using an Omega HX93A relative humidity and temperature sensor with measurement uncertainties of $\pm$2.5% for humidity and $\pm 0.6°C$ for temperature. Ambient pressure was recorded using an SB-100 barometric pressure sensor from Apogee Instruments with a measurement uncertainty of $\pm$1.5% of reading. Each of these instruments are read by the DAQ system via an NI USB-9215A portable USB DAQ module.

A total of 316 thermocouples were used to measure the boundary temperatures. The total number of thermocouples used in the model was limited by the number of data acquisition modules (21 modules with 16 channels each) available. A total of 84 thermocouples were embedded in the test section walls, 192 in the fuel rods, 16 for the outlet fluid temperature measurement, 15 for inflow temperature characterization and the remainder were used to monitor ambient temperatures and facility conditions. The inlet thermocouples and ambient thermocouples were made from 30-gauge Type K Special Limits of Error (SLE) thermocouple wire with Neoflon™ insulation from Omega Engineering using an Argon-shielded welder. The remaining thermocouples were made from glass-insulated 30-gauge Type K SLE thermocouple wire in the same manner. The glass insulated thermocouples were calibrated using an Isotech FASTCAL-M calibration system with a

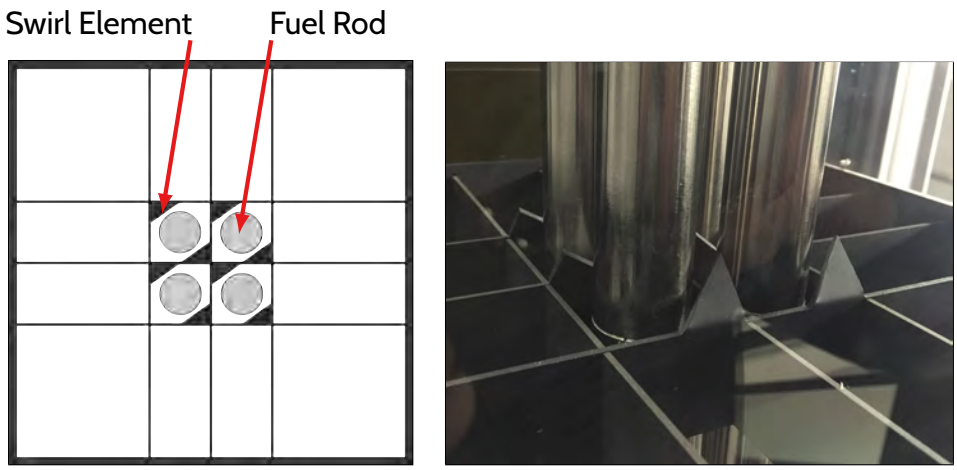

(a) (b)

Fig. 3.5: (a) Drawing of the grid spacer placement with respect to the rod bundle. (b) A photograph of the actual grid spacers in the fuel rod bundle.

0.3°C accurate reference over the range of $30 - 180$°C in 10°C increments. The calibration for these thermocouples were similar and because they were all made from the same spool, a single averaged calibration curve was applied. An overall calibration uncertainty of 0.302°C was determined. The Neoflon™ insulated thermocouples were uncalibrated and the manufacturer's uncertainty of 1.1° was used.

Various thermocouples are placed in the facility for controlling and monitoring room conditions. Thermocouples are used to monitor the heating and air conditioning system to maintain a room temperature at 20°C $\pm$ 0.5°C. A proportional-integral-derivative controller (PID controller) was used to maintain steady ambient conditions by preheating incoming air through the air conditioning system. A separate PID controller was used to control the steam heating system for the facility. Twenty one NI-9213 16-channel thermocouple input modules were used to read the thermocouple temperatures. The narrow voltage range of $\pm$ 78 mV, 24-bit ADC, and built-in Cold Junction Compensation (CJC) made them well-suited for these measurements. The modules' built-in CJC had a measurement uncertainty of 0.8°C. These modules were connected to the data acquisition computer using five NI cDAQ-9188 8-slot Ethernet Chassis. Thermocouples were routed to the reverse side of the opaque, aluminum wall as shown in Fig. 3.7.

All thermocouples used in the test section walls were embedded at 2.54 mm of the inner surface. The rod thermocouples were embedded at 3.18 mm of the rod surface. Thermocouple placement in the test section and fuel rod model was determined based on preliminary CFD simulations provided by a partnering research group at USU and is discussed at length below.

3.3.1 Wind Tunnel Inlet

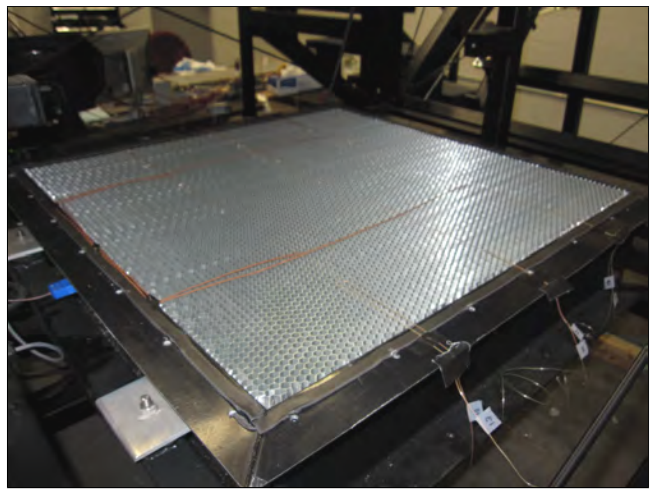

Fig. 3.6: Thermocopules (brown wires shown) placed on the honeycomb flow straightener to measure the inlet air temperature profile.

The inlet flow conditioning section of the wind tunnel contains a 3×5 array of thermocouples (3 in y and 5 in x) for inflow temperature measurement downstream of the honeycomb as shown in Fig. 3.6. These thermocouples measure the air temperature of the fluid after passing through the flow conditioning portion of the facility before entering the inlet contraction.

Due to the highly pressure and density dependent nature of free convection flows, conditioning the flow as it enters the wind tunnel causes significant impacts on the overall experiment and thus impacts the results of the CFD simulations. With such high sensitivity to inflow conditions, the heat exchanger in the flow conditioning region of the facility was not turned on during this study. In order to account for the effect of the flow conditioning on the overall experiment, the pressure drop across the flow conditioning portion of the wind tunnel was measured using a 1 Torr Baratron differential pressure sensor connected to a MKS270D Signal Conditioner. Using the measured pressure drop,

the inlet loss coefficient was calculated according to

$$K = \frac{\Delta P}{\frac{1}{2}\rho V^2} = \frac{2\rho A^2 \Delta P}{\dot{m}^2} \tag{3.1}$$

where $\dot{m}$ is the mass flow rate through the flow conditioner and is equal to the mass flow rate at the inlet of the test section according to conservation of mass, A is the cross sectional area of the flow conditioner and ΔP is the measured pressure drop. A table of the measured pressure drop and loss coefficient and their associated uncertainties for each test case are shown in Table 3.1.

Table 3.1: Volume flow rate, pressure drop and loss coefficient across the inlet flow conditioning for each test case in order of increasing volume flow rate.

Case Name	Q, [m^3/s]	ΔP, [Pa]	K
Natural400	0.0185±0.0016	0.1227±0.0220	233±56
Natural700	0.0245±0.0021	0.1531±0.0210	166±35
Forced	0.1248±0.0109	0.9218±0.0443	39±7
Mixed700	0.1252±0.0109	0.8037±0.0437	34±6
Mixed400	0.1253±0.0109	0.8000±0.0357	33±6

3.3.2 Test Section

The walls of the test section are instrumented with 21 thermocouples per wall. Three thermocouples at each z-position are evenly spaced along the span-wise direction of the wall and at 7 length-wise positions along each wall. The thermocouples are placed within 2.5 mm of the inner surface of the wall.

An array of 16 thermocouples are suspended in the outlet of the test section for air temperature measurement of the exiting fluid. These thermocouples are arranged in a 4×4 grid evenly spaced across the outlet cross section.

3.3.3 Fuel Model

Each rod section is embedded with 12 internal thermocouples at four circumferential and three axial positions. The thermocouples are placed 3 mm from the surface of the rod for measuring the

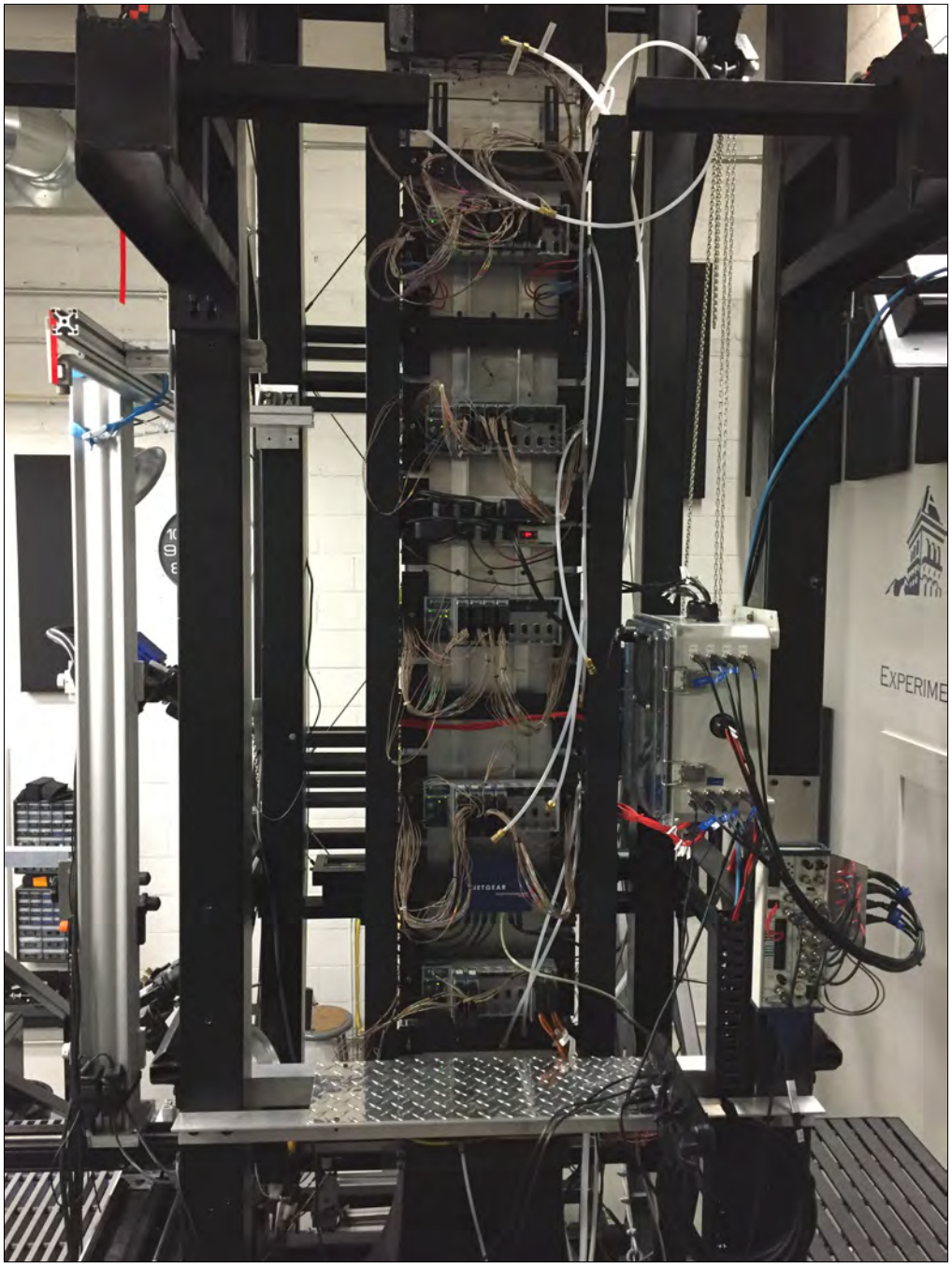

Fig. 3.7: Instrumentation used to acquire rod and wall temperatures during data acquisition. Each brown wire corresponds to a single thermocouple. The thermocouples are connected to National Instruments NI-9123 thermocouple modules and cDAQ-9188 chassis on the rear side of the aluminum test section wall.

rod surface temperature. The thermocouples were embedded with Dow-Corning 3-6751 Thermally Conductive epoxy. The wires were then embedded into machined channels inside the rods and routed outside the test section via the aluminum thermocouple conduit. Initial CFD simulations of the experiment indicated the possibility of circumferential variation of the surface temperature of the rods due to the mixing induced by the swirl elements and also due to geometric asymmetry.

Two 2-channel BK Precision Model 9174 programmable power supplies were used to electrically power the rod cartridge heaters. The power supplies were connected to the DAQ system via USB for controlling their output. Four rod sections at a given stream-wise position are wired in parallel and powered from a single power supply output. The heaters had a mean unheated resistance of 178.1 Ω and a standard deviation of 0.98 Ω. This was determined using a 4-wire resistance measurement on a calibrated Agilent 34401A multimeter.

A set of voltage dividers were used to step down the voltage by a factor of 11 to a safe level for measurement by the data acquisition system. High performance film resistors of 10MΩ and 1MΩ (Part No. USF240-10.0M-0.1%-2PPM and USF240-1.00M-0.1%-2PPM, respectively) from Caddock were used for this circuit and are 0.1% accurate with less that 2 $\mu\Omega/^{\circ}$C drift. All four cartridge heaters at a given flow-wise position are wired in parallel and controlled by a single output on the power supply. The divided voltage is measured by the DAQ system using a BNC-2120 shielded connector block connected to an M-series 16-bit analog input PCI-DAQ card (NI PCI-6221). Non-referenced single-ended (NRSE) wiring configuration was used to measure the divided voltage in order to prevent ground loop between the voltage supply and DAQ system.

No accurate, affordable current sensors were available in the range needed for this study. Therefore, the electrical current through the heaters was determined via USB from the output of the desktop programmable power supplies accurate to $\pm$0.1% with a bias error of 1 mA. The current from each power supply output was assumed to be evenly distributed to all four heaters.

3.3.4 Particle Image Velocimetry

A stereoscopic PIV system from LaVision, Inc. was used for all velocity measurements [56]. Two 16-bit Imager sCMOS cameras were used in conjunction with a 100 mJ Nd:YAG dual cavity

Fig. 3.8: Close-up of the conduit used to route thermocouple wires from the rod centers to the data acqusition system outside the test section.

Quantel Evergreen laser and a programmable timing unit. The laser contains a frequency doubling device that converts the beam from wavelength of 1064 nm infrared to 532 nm visible producing a green beam. Each laser cavity is capable of firing a single pulse at 25 Hz. Focusing optics and a cylindrical lens are placed on the front of the laser to convert the laser beam to a sheet with adjustable thickness. The Imager sCMOS cameras have a 16-bit CMOS sensor that is 2560 $\times$ 2160 pixels with a pixel size of 6.5 µm and is capable of acquisition speeds of up to 50 frames per second.

The cameras are fitted with 28 mm fixed focal length lenses and Scheimpflug mounts from LaVision for inlet velocity measurements. The Scheimpflug mounts are used to align the focal plane of camera and lens such that the entire field of view is in focus and adds approximately 12 mm to the lens focal length. The lenses are changed to 180 mm fixed focal length lenses, while still using the Scheimpflug mounts, for all SRQ data locations. Linos optical rails from Excelitas Technologies were used for camera adjustment in the flow-wise direction. Three linear traverses from Velmex, Inc. are used for positioning the cameras in the xy-plane and for adjusting the laser position in the x-direction. The repeatability of the traverses was 0.005 mm. After positioning the cameras and laser, DaVis version 8.3.0 software provided by LaVision controls image acquisition, processing and vector calculation including uncertainty [57]. All PIV measurements made for this study are stereoscopic resulting in 3-components of velocity in the laser plane with uncertainty.

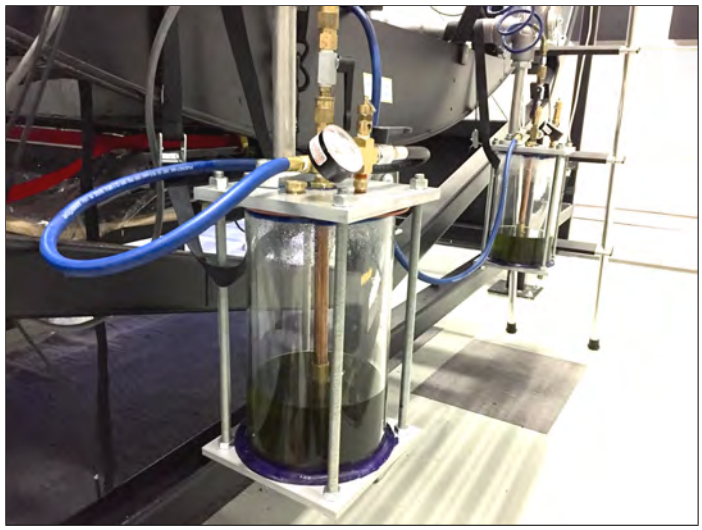

Fig. 3.9: Two Laskin nozzle seeders use compressed air to turn olive oil into a fine mist which is injected into the flow domain for PIV measurements.

Olive oil is used to seed the fluid flow using two Laskin nozzle seeders as shown in Fig. 3.9 and is injected into the flow upstream of the flow conditioning portion of the wind tunnel as mentioned previously. The physical diameter of the particles is varied using the hole diameter of the Laskin nozzle and the air pressure supplied to the seeder. Using an Aerodynamic Particle Sizer Spectrometer Model 3321 from TSI, Inc., the particles were found to have a mean diameter of 1.72 μm.

A 2-component vector field is calculated by dividing an image pair into interrogation windows of size $N \times N$ where $N = 2^n$ where n is a positive non-zero integer. Figure 3.10 shows a raw 2-component PIV image. A cross-correlation is applied to each interrogation window and the peak of the correlation corresponds to the most likely displacement of the particles within the window. This results in a vector field as that shown in Fig. 3.11. For stereoscopic PIV, two image pairs are processed separately resulting in two 2-component vector fields and then, using the field of view information from calibration, two 2-component vectors are combined to form a single 3-component vector with velocity components both in the laser plane as well as the through-plane velocity component. In Fig. 3.12 is shown a 3-component vector field from stereo-PIV where the vectors show the in-plane velocity components and the background is colored according to the through-plane velocity component.

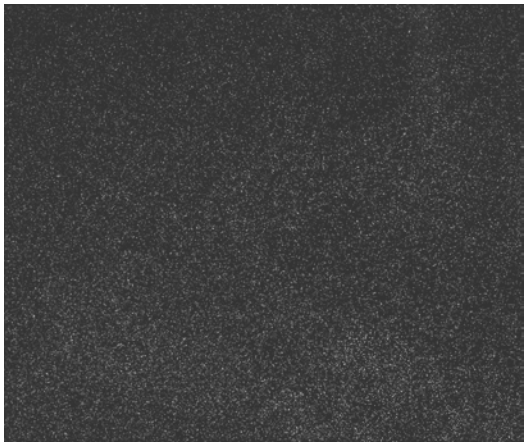

Fig. 3.10: An example of a raw 2 component PIV image.

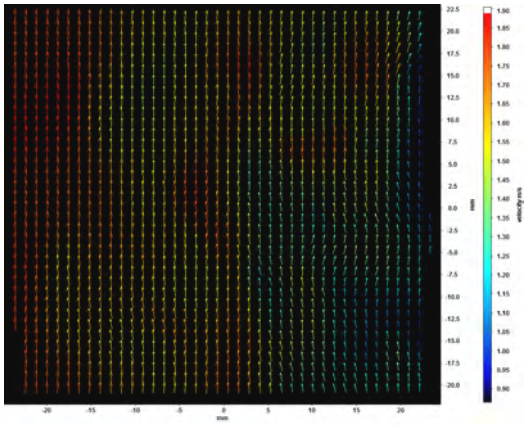

Fig. 3.11: An example of a processed 2-component vector field image.

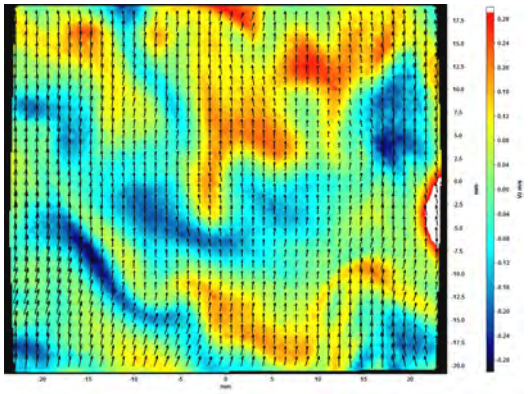

Fig. 3.12: An example of a 3-component vector field resulting from two 2-component vector fields.

Conversion of the images acquired via the PIV system from image coordinates to physical coordinates is performed using system calibration [58]. For the test section inflow measurements, a two-plane calibration plate was placed inside the test section and aligned with the laser sheet as shown in Fig. 3.14. The 11.875 in. square, two-plane calibration plate consists of holes of 0.125 in. diameter are evenly spaced every 0.625 in. and the distance between planes is 0.125 in. (see Fig. 3.13a). The calibration plate was bolted to the test section to ensure that it was aligned with the inlet plane. The DaVis software uses the definition of the plate and the images from each camera to dewarp the acquired images using a 2-D third-order polynomial fit. The largest displacements of velocity occur through the laser sheet requiring a large sheet thickness of 4 mm at the inlet. Figure 3.13 shows images of the calibration plates used for velocity measurements.

A much smaller calibration plate was used for acquiring SRQ velocity fields. It was not feasible to place the calibration plate inside the test section at each SRQ locations. Therefore, a plate of polycarbonate was bolted to the exterior of the test section aligned with the test section wall. This was required to account for index of refraction error that is present due to the wide angle placement of the cameras for stereo-PIV. The laser was first aligned with the $x = 0$ m plane of the test section. The cameras were then aligned with the outer edge of the test section wall opposite the aluminum wall using a machinist parallel. A two-dimensional dot array Max Levy Autograph calibration plate was traversed through the laser sheet thickness for multiple plane calibration. The calibration plate consisted of $\varnothing 0.25$ mm dots spaced 0.5 mm apart and was 50 mm $\times$ 50 mm in size with a replication error of less than 0.001 mm (see Fig. 3.13b). Images of the plate were acquired at -1 mm, 0 mm and 1 mm through the 2 mm laser sheet thickness for calibration. Every other dot on the plate was selected for calibration in order to limit the computation time required for dot center finding and a third-order polynomial fit was used for the calibration. An image of the calibration setup used for SRQ calibration is shown in Fig. 3.15.

Before PIV data acquisition, the lens aperture was adjusted in order to achieve an optimal particle image diameter as well as adjusting for particle brightness for maximum dynamic range of the camera sensor. An average particle image diameter between 1.7 and 1.9 pixels was used which is near the optimal diameter of 2 pixels [59]. Although the diameter is slightly below optimal, the

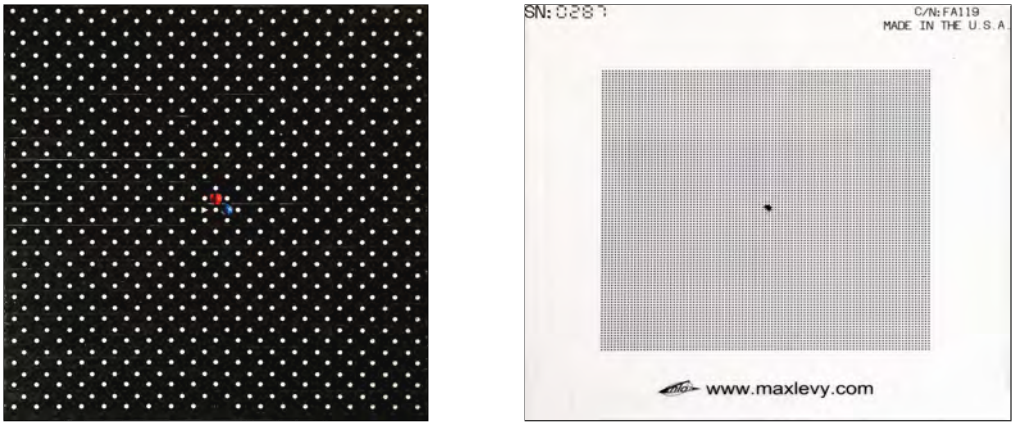

(a) (b)

Fig. 3.13: (a) The two-plane calibration plate (not to scale) used for the inflow velocity measurements. (b) The Max Levy calibration plate (not to scale) used for acquiring SRQ data. The plate is a single plane which was mounted to a traverse and moved through the laser sheet for calibration.

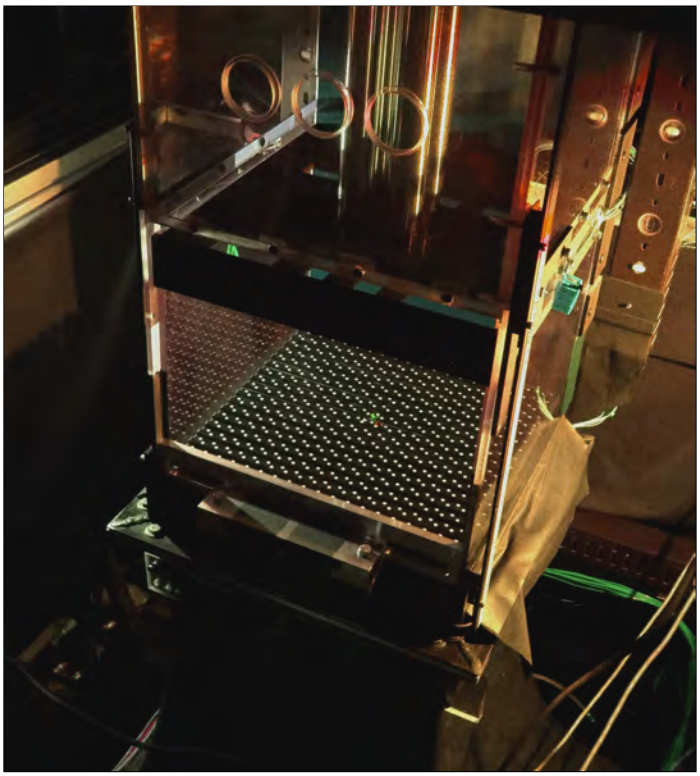

Fig. 3.14: Calibration setup used for acquiring the test section inlet velocity profile.

Fig. 3.15: Calibration setup used for acquiring the SRQ velocity data.

uncertainty calculation method used accounts for below optimal particle image diameters. The time between image pairs was also adjusted such that the flow-wise component of velocity resulted in approximately 12 pixels of displacement. For each PIV dataset, 1000 image sets (one image pair per camera) were acquired in order to ensure converged vector statistics.

After acquiring PIV data, the images were processed using the DaVis software. The following steps were used for processing the images:

1. The average of all the images was calculated and subtracted from each individual image to remove any objects that were visible in the background of the images.

2. The images were masked such that only the flow domain was used for vector calculation.

3. Multi-pass stereoscopic PIV processing was performed on the masked images. The first pass using 64 $\times$ 64 pixel square interrogation windows with 75% overlap followed by 4 passes at 32 $\times$ 32 pixel circular interrogation windows with 75% overlap and symmetric flow-based window displacement and deformation for improved accuracy. The standard FFT-based cross

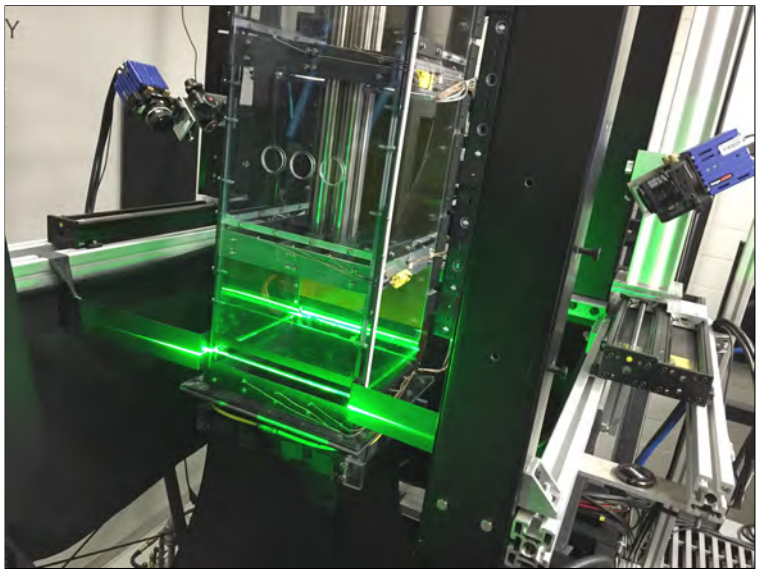

Fig. 3.16: The setup used to acquire the inlet velocity profile using stereo-PIV. Note that the laser sheet is aligned horizontally such that the stream-wise velocity component passes through the thickness of the laser sheet.

correlation algorithm was used for each two-component image separately and then, using calibration information, are reconstructed into three-components of velocity. The default acceptable stereo-reconstruction error of 3 pixels was used.

4. Vector fields were post-processed using an allowable vector range of 0 m/s $\pm$ 0.25 m/s for the two in-plane velocity components and 1.5 m/s $\pm$ 2 m/s for the through-plane velocity component for the test section inflow datasets. No vector field limits were used for the SRQ datasets due to higher quality images from being far from walls and reflective surfaces. Vectors were also removed for peak ratios less than 2 and if the standard deviation of a vector compared to its neighbors was larger than 1.

5. Vector statistics (mean and standard deviation including uncertainty) were computed.

6. Turbulence quantities (Reynolds stresses, turbulence kinetic energy and turbulent shear stress) were calculated including uncertainty for the dataset.

7. A Matlab script (ReadIMX) provided by LaVision were used to import the images and compile the data into a useable format.

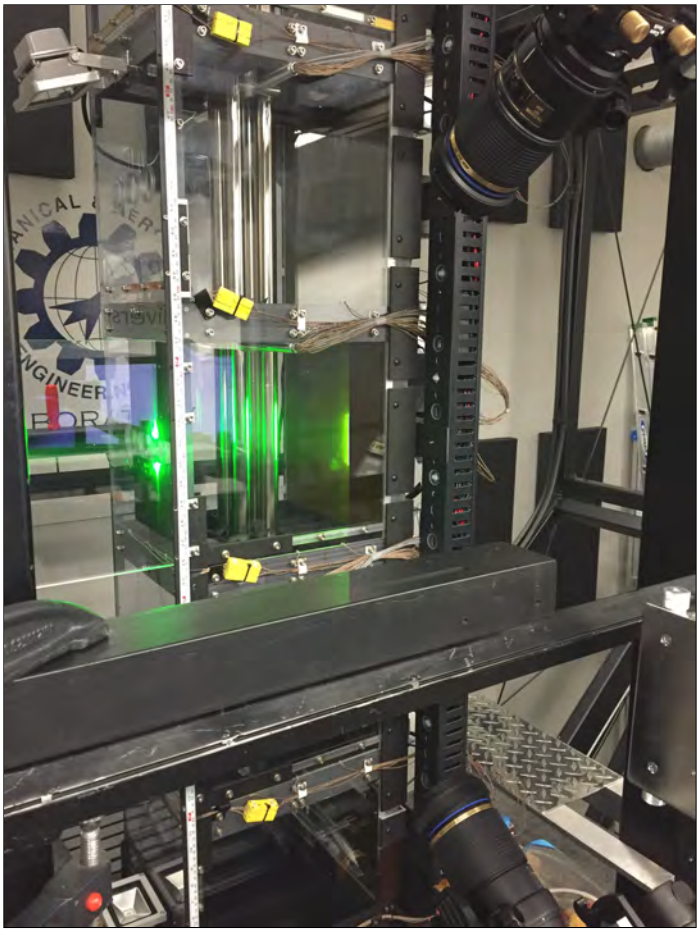

Fig. 3.17: The setup used to acquire the SRQ velocity profile using stereo-PIV. Note that the laser sheet is aligned vertically such that the stream-wise velocity component is aligned with the laser sheet.

Table 3.2: PIV acquisition parameters for the test section inlet velocity and SRQ velocity measurements. The Forced, Mixed400 and Mixed700 parameters were combined due to similarity while the Natural400 and Natural700 cases are listed separately. Ranges listed for the Forced/Mixed cases at the inlet indicate the range for the different flow heating cases, while the ranges for the SRQ velocity measurements indicate variation due to different stream-wise SRQ locations. Particle diameter listed here is approximately twice the diameter described above after [1]. Density is listed as particles per pixel or ppp.

	Inlet			SRQ Locations		
Parameter	Forced/Mixed	Natural400	Natural700	Forced/Mixed	Natural400	Natural700
No. Image Pairs per Camera	1000	1000	1000	1000	1000	1000
Sample Freq. [Hz]	2	2	2	5	0.1	0.1
dt [μs]	750	7000	6000	100-250	300-800	300-600
Laser Sheet Thickness	4 mm	4 mm	4 mm	2 mm	2 mm	2 mm
Laser Sheet Focal Length	-10 mm	-10 mm	-10 mm	-20 mm	-20 mm	-20 mm
Camera Lens	28 mm	28 mm	28 mm	180 mm	180 mm	180 mm
$f\#$	2.8	2.8	2.8	16	16	16
Calibration Plate	Two-Plane	Two-Plane	Two-Plane	Max Levy	Max Levy	Max Levy
Particle Diameter [pixel]	3.42-3.51	3.51	3.53	3.25	3.21	2.73
Density [ppp]	0.042-0.044	0.041	0.040	0.020	0.028	0.014
Average Displacement [pixel]	7.5	10.0	11.5	4.5-10.5	10.1-11.5	6.0-11.6

CHAPTER 4

APPROACH

In order for these experiments to be used for CFD validation, high fidelity measurements must be made and their associated uncertainties quantified as well as a careful accounting of all boundary conditions. All measured quantities are reported with their associated uncertainty. Reported uncertainties for derived quantities are determined through the Taylor Series Method (TSM) for uncertainty propagation as presented in Coleman and Steele [60].

No formal CFD analysis will be performed in this work although simplified simulations were made initially to assist in the test section design process. Full CFD analysis will, however, be provided later in a separate work. Two separate groups will be conducting CFD validation studies, one through a research group at Utah State University and the other through a partnering national laboratory research group.

4.1 Parameter Space

A series of five steady-state test cases were performed in the wind tunnel: forced unheated, mixed convection at two heat flux conditions, and natural convection at two heat flux conditions. Table 2.1 shows the parameter space considered. The two rod surface heat fluxes considered were approximately 400 W/m^2 and 700 W/m^2. The room was maintained at $T_{\text{amb}} = 20 \pm 0.5$°C for all test cases.

4.2 Coordinate System and Data Acquisition Locations

All data and measurements for this study are translated into a global coordinate system as shown in Fig. 4.1. The origin of the coordinate system is located at the leading edge of the opaque aluminum wall with the positive z-coordinate aligned with the flow-wise direction. The coordinate system was placed here in order to physically measure its position rather than being aligned with the center of the test section cross-section or with the center of the rod bundle. The inflow velocity

data were acquired at the $z = 0.067$ m position aligned at the center of a 4-mm-thick laser sheet.

The locations of the SRQ velocity profiles are shown in Fig. 4.2. Figure 4.2a shows the xy-plane view (with the positive y-axis corresponding to the vertical direction) of a single z-position for PIV acquisition. Figure 4.2a shows the z-position of each of the PIV acquisition locations.

4.3 Boundary Conditions

Careful measurement of the boundary conditions is necessary to ensure a successful validation assessment. All physical boundaries of the wind tunnel are measured using a micrometer accurate to 0.13 mm. The procedure was performed as shown in Fig. 4.3. Measurements were used to reconstruct an "as-built" 3D model of the assembly. Close collaboration with CFD modelers allowed for correction of meshing issues during the measurement/reconstruction process.

Thermal boundary conditions during operation of the experiments are recorded using Type K thermocouples connected to NI-9213 modules from National Instruments. The thermocouples are calibrated for temperatures between 30°C and 180°C to a 0.3°C source using a medium FastCal calibration unit from Isotech. The calibration is applied to the temperature measurements in the LabView control Virtual Instrument (VI) for controlling the entire experiment. Temperatures of each thermocouple are recorded simultaneously with the PIV data acquisition system.

4.4 System Response Quantities

SRQ velocity data were acquired at the midpoint between each grid spacer in the z-direction. Three components of velocity were acquired in the laser plane using the stereoscopic PIV system described previously. In order for stereoscopic PIV to be acquired in the flow domain, wide angles between the cameras was desirable for through-plane sensitivity, limiting the number of positions possible for data acquisition. Two 180 mm lenses (with an approximate focal distance of 600 mm) are positioned at approximately 60° apart. A viewing window of $45\ \mathrm{mm} \times 42\ \mathrm{mm}$ at each location were acquired. Camera view windows for data acquisition were positioned at $x = 0.0$ m, $y = 0.152$ m and $x = -0.60$ m, $y = 0.152$ m and $x = -0.60$ m, $y = 0.197$ m for each z-position of the optical windows $z = 0.476$ m, 0.825 m, 1.174 m, 1.524 m.

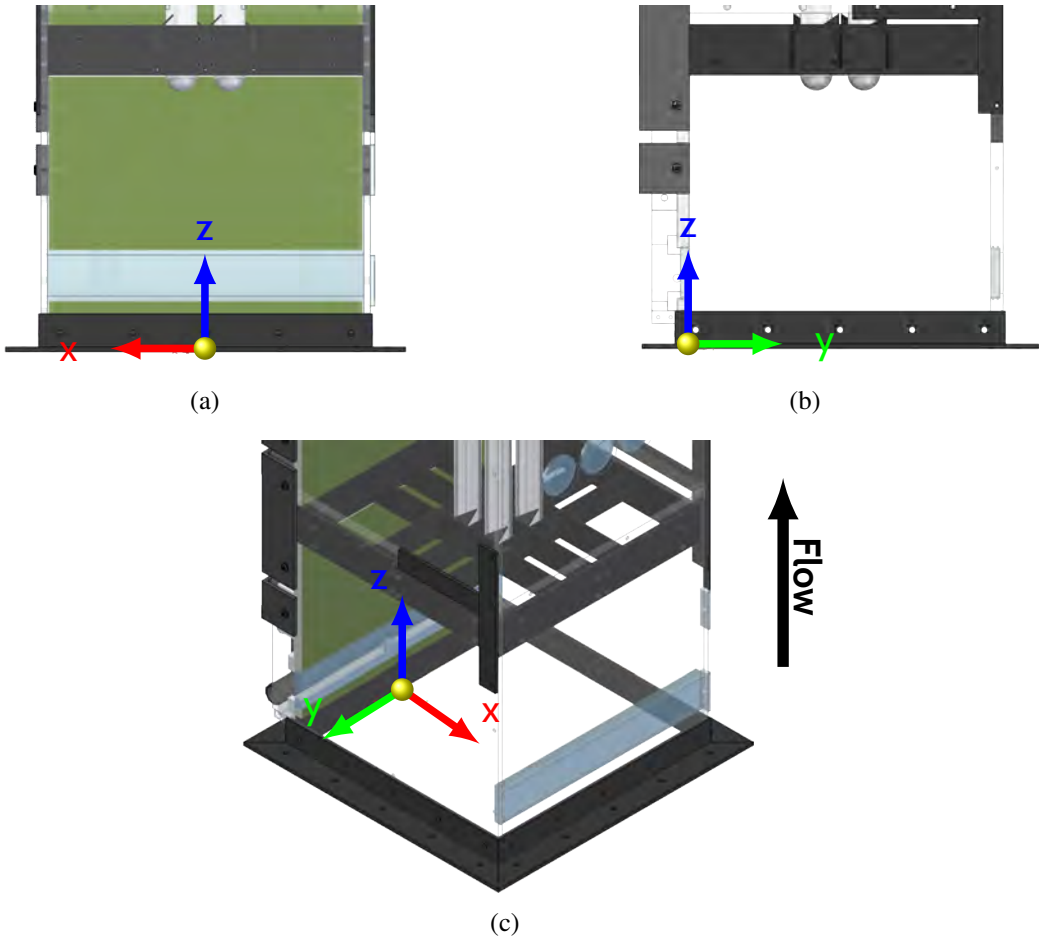

Fig. 4.1: Test section inlet views of coordinate system. (a) xz-plane with y-axis leaving the page. (b) yz-plane with x-axis leaving the page. (c) Isometric view of coordinate system.

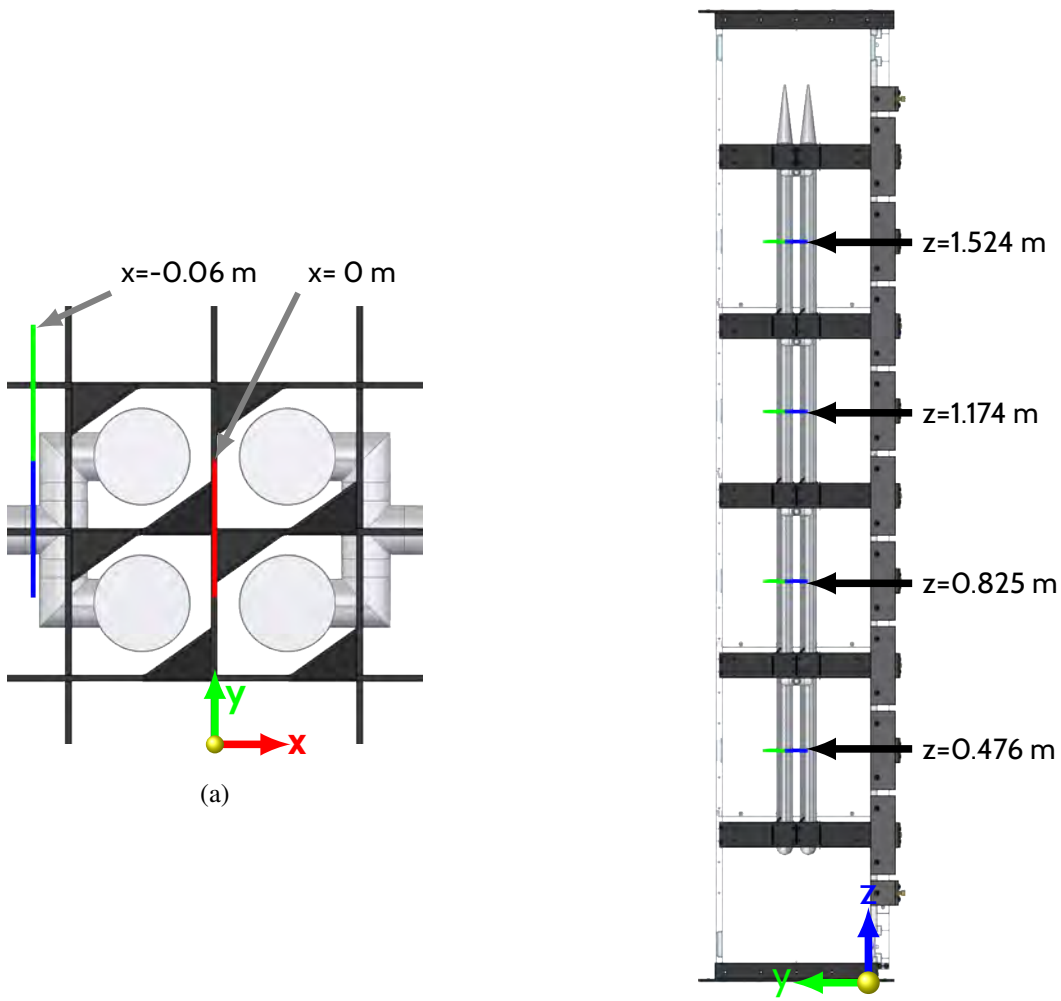

Fig. 4.2: Locations of the PIV viewing windows for SRQ data acquisition. (a) The cameras for these fields of view (FOVs) were positioned on the left of the figure looking towards the rod bundle. The red line represents the top edge of the camera FOV for the $x = 0$ m dataset for a given z-position. The blue and green lines represent the top edge of the two FOVs taken on the $x = -0.06$ m plane for a given z-position. The dataset for the blue and green FOVs were stitched together after processing to form a single time-averaged velocity field. Each FOV is 45 mm wide. The coordinate system shown is for directional reference only and does not correspond to the actual origin location. (b)The location of the velocity profiles for each z-position. The blue line represents the length of the velocity profile for the $x = 0$ m plane. Combining the blue and green profiles together forms the complete time-averaged velocity profile for the $x = -0.06$ m plane.

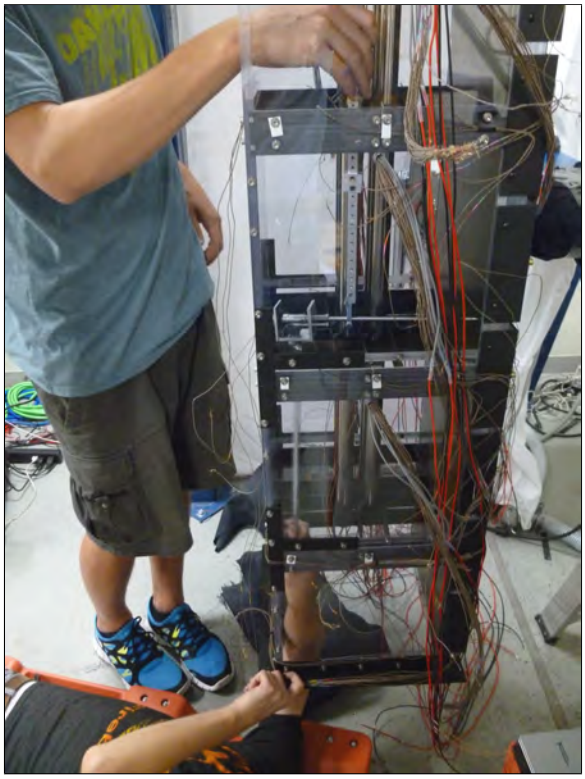

Fig. 4.3: Measurement of the test section after construction. From the “as-built” measurements a 3D model is constructed for use in CFD simulations.

After preliminary tests, it was determined that the pressure drop across the test section could not be used as an SRQ because the pressure drop for natural convection cases is on the order of hydrostatic pressure and below the measurable range of available equipment. Using a 1-Torr Baratron differential pressure sensor across the test section resulted in a measurement on the order of hydrostatic pressure.

4.5 Measurement Uncertainty Quantification

Assessment of a CFD model using validation data requires quantification of uncertainty for the modelers determine the model's credibility for a particular application. From the ASME V&V-20 Standard [21], the validation comparison error E is defined as the difference between the simulation solution S and the experimental data D as

$$E = S - D. \tag{4.1}$$

Assuming that the error sources are independent, the validation uncertainty is the estimate of the numerical uncertainty and experimental uncertainty and, for measured variables, is calculated by

$$U_{\text{val}} = \sqrt{U_{\text{num}}^2 + U_{\text{input}}^2 + U_D^2} \tag{4.2}$$

where U_{num} is the numerical uncertainty of the model, U_{input} is the simulation uncertainty due to errors in the simulation inputs and U_D is the experimental data uncertainty. The validation comparison error is satisfactory if the validation comparison error E is sufficiently smaller than the validation uncertainty U_{val} for the intended application of the model. This work will provide U_D for the SRQs used to validate the CFD models as well as uncertainties of the BCs applied to the CFD models in order to determine U_{input}.

Uncertainties for individual PIV velocity vectors are calculated using the DIC uncertainty estimation method described by Wieneke and Prevost [61]. This uncertainty estimation method is built into the DaVis software used for vector calculation. According to Wieneke and Sciacchitano [62],

uncertainty of the mean velocity in DaVis is calculated as

$$U_x = \frac{\sigma_x}{\sqrt{N}} \tag{4.3}$$

where σ_x is the standard deviation of the velocity component x and N is the number of statistically independent and normally distributed samples.

Uncertainties for BCs are determined from the instrumentation used to measure it, for example uncertainty from physical dimensions of the test section is determined by the uncertainty of the micrometer used for the measurements. Uncertainty for a particular measurement U_r can be broken into systematic or bias error B_r and random error S_r as

$$U_r^2 = B_r^2 + S_r^2. \tag{4.4}$$

Uncertainties for calculated variables are propagated using TSM for uncertainty propagation as described previously and is expanded in Appendix D.

Uncertainties for length measurements are presented in Appendix C. The method for determining all other uncertainties is presented. Uncertainties for derived quantities are calculated using the Taylor Series Method (TSM) for uncertainty propagation. All uncertainties are presented at 95% confidence.

4.5.1 Stereoscopic PIV Uncertainty

Uncertainties for all PIV measurements were calculated using the built-in uncertainty quantification in the DaVis software. Neal, *et al.* and Sciacchitano, *et al.* have discussed several of the current PIV uncertainty estimate methods in order to determine the most accurate for uncertainty estimation [63, 64]. The correlation statistics method used by DaVis software was found to accurately estimate the uncertainty and is described by Wieneke and Prevost [61].

4.5.2 Thermocouple Uncertainty

As previously mentioned, the thermocouples used in the test section and fuel rods of the wind

tunnel were calibrated to a 0.3°C source for temperatures between 30°C and 180°C. Temperature measurements below 30°C and uncalibrated thermocouples (such as those previously placed in the facility before the construction of this experiment) were given an uncertainty of 1.1°C as per the thermocouple manufacturer.

4.5.3 Pressure Measurement Uncertainty

Without characterizing the seeding array and flow conditioner of the wind tunnel, it would not be possible to obtain an accurate CFD solution. The pressure drop present across these parts was measured using the 1-Torr Baratron pressure sensor mentioned previously. Three sources of uncertainty are present in the differential pressure measurements performed in this study: the bias uncertainty from zeroing the pressure sensor, the readout uncertainty of the signal conditioner and the uncertainty of the data acquisition system. The total uncertainty for pressure measurements was determined to be less than 20%. The pressure drop for each test case is shown in Table 3.1.

4.5.4 Taylor Series Method for Uncertainty Propagation

Uncertainties for derived quantities are determined using the TSM as described in Coleman and Steele [60] where the total uncertainty of a quantity $r = f(x, y, ...)$, assuming correlated errors are negligible, is

$$U_r = \sqrt{U_x^2 \left(\frac{\partial r}{\partial x}\right)^2 + U_y^2 \left(\frac{\partial r}{\partial y}\right)^2 + ...} \tag{4.5}$$

where U_x is the uncertainty of the independent variable x and U_y is the uncertainty of the independent variable y and is repeated for N variables. Using this method, the uncertainty of derived quantities such as Reynolds number, for example, are determined. Using the Reynolds number definition of

$$\mathrm{Re} = \frac{\rho V L}{\mu} \tag{4.6}$$

as the data reduction equation (DRE), the uncertainty of Reynolds number is expanded as

$$U_{\mathrm{Re}} = \sqrt{U_\rho^2 \left(\frac{\partial \mathrm{Re}}{\partial \rho}\right)^2 + U_V^2 \left(\frac{\partial \mathrm{Re}}{\partial V}\right)^2 + U_L^2 \left(\frac{\partial \mathrm{Re}}{\partial L}\right)^2 + U_\mu^2 \left(\frac{\partial \mathrm{Re}}{\partial \mu}\right)^2} \tag{4.7}$$

where the subscript of each u term indicates the uncertainty of that variable. Expanding this method to each quantity of interest, the uncertainties for all outputs may be determined. The expanded TSM equations for each quantity presented are shown in Appendix D.

Inlet mass flow rate is defined as the product of the fluid density and volume flow rate. The volume flow rate through the test section is determined by integrating the velocity flow field using the trapezoid rule, defined as

$$Q = \sum_{i=1}^{N-1} (x_{i+1} - x_i) \left(\frac{V_i + V_{i+1}}{2} \right). \tag{4.8}$$

Using the trapezoid rule as the DRE, uncertainties were propagated through the integral of the velocity field, including correlated uncertainties, and then used to determine the uncertainty of the mass flow rate. The uncertainty for air properties was determined using TSM and standard psychrometrics for moist air as described in Appendix D.

4.5.5 Effect of Seed

During data acquisition it was determined that the introduction of seed into the test section caused a drop in overall rod temperature (<0.5°C). In order to determine the impact associated with the introduction of olive oil seed, the density of oil particles in the flow domain was calculated using the method described by Warner and Smith [1]. The average particle density from the inflow velocity measurements was found to be 0.035 ppp (particles per pixel) in the images. The total number of particles in a 32 pixel $\times$ 32 pixel interrogation window is then $\sim$36 particles. Using the calculated volume of an interrogation window (32 pixel $\times$ 32 pixel $\times$ 4 mm laser sheet thickness) and with a measured particle diameter of $d_p = 1.694$ µm it follows that the volume fraction of olive oil is 1.06×10^{-9}. The ratio of heating required to heat the mass of oil to air is then

$$\frac{(mc_p)_{\text{oil}}}{(mc_p)_{\text{air}}} \cong 1.84 \times 10^{-6} \tag{4.9}$$

indicating that due to the extremely low volume fraction of oil particles, essentially no heat is lost to the oil. This, however, does not agree with the noticeable drop in temperature upon introducing

the seeding particles.

A hot film probe (TSI Model No. 1210-20) and an IFA100 anemometry system from TSI, Inc. [65] was used to determine if the fluid velocity changed upon introducing seed. The probe was first calibrated using a 14 mm orifice on a TSI Model 1129 calibrator and then placed at the center of the test section inlet. Air pressure supplied to the calibrator was controlled by an inline needle valve and a ControlAir Inc. Electropneumatic Pressure Regulator (Type 500X E/P, Part No. 500-EH). The mean inflow velocity for the Natural700 case was approximately 0.3 m/s which is below the calibratable range for the probe. The inlet velocity was unchanged when seed was introduced in the flow indicating that any change in the mass flow rate of the system is smaller than the uncertainty of the measurements made.

These results indicate that using olive oil seed does not impact the fluid flow while the temperature drop when seed is introduced indicated the contrary. There is currently no way to account for the introduction of seed and will therefore be neglected with the recommendation that further investigation is needed to determine the impact of olive oil.

4.6 Sampling Parameters

While PIV data acquisition is a relatively "slow" (usually around 10 Hz) measurement technique, natural convection flow is much slower requiring that a method for determining statistical independence of samples be applied. During the preliminary acquisition process, a Matlab [66] script was run after acquiring PIV data to determine the required acquisition frequency of the data to ensure independent samples. Wieneke and Sciacchitano [62] determined that the number of samples needed can be determined using the integral of the normalized autocorrelation of the signal using the method described by Tennekes and Lumley [67] for determining the integral time scale of a fluctuating function. An autocorrelation represents the cross-correlation of a signal with itself that is calculated by integrating the product of a function $f(t)$ with a time-lagged version of itself $f(t+\tau)$ over all time delays [68]. This is written mathematically as

$$\rho(\tau) = \frac{1}{\sigma^2}\int_{-\infty}^{\infty} f(t)f(t+\tau)dt. \tag{4.10}$$

where σ^2 is the signal variance and is used to normalize the correlation. Therefore, by definition, a random signal will be perfectly correlated with no lag and will not be correlated for any non-zero lag if sample independence was achieved during acquisition. If the samples are not independent, the integral of the autocorrelation result from $\tau = 0$ to the location of the first zero-crossing relates to the number of independent samples present in the data [69]. Using the acquisition rate and number of independent samples, the new maximum sampling rate may be determined. An example of the positive half of an autocorrelation for a dataset with statistically dependent samples and statistically independent samples are shown in Fig. 4.4a and Fig. 4.4b. Only the positive half of the autocorrelation is shown because the function is symmetric about $\tau = 0$.

4.7 Turbulence Quantities

The data acquired in this study may be used for validation of several different turbulence models. These models require different turbulence inflow quantities, all of which will need to be provided to the modelers. The velocity data acquired from PIV can be broken into a mean term $\overline{u}$ and a fluctuating term u' through Reynolds decomposition

$$u(t) \equiv \overline{u} + u'. \tag{4.11}$$

Reynolds stresses are defined as the time average of the products of the fluctuating velocity terms and using index notation are written as

$$\tau_{ij} \equiv -\overline{u_i' \, u_j'} \tag{4.12}$$

where the overbar represents a time average. Reynolds-Averaged Navier-Stokes (RANS) CFD models have been developed as a method for solving the Navier-Stokes equations for turbulent flow with relatively low computational expense. In order to use the RANS turbulence models, two commonly used turbulence length scales in terms of the normal Reynolds stresses are required, namely turbulence intensity and turbulence kinetic energy, and are applied as turbulence boundary conditions [70]. Turbulence intensity is defined as the square-root of normal Reynolds stresses normalized

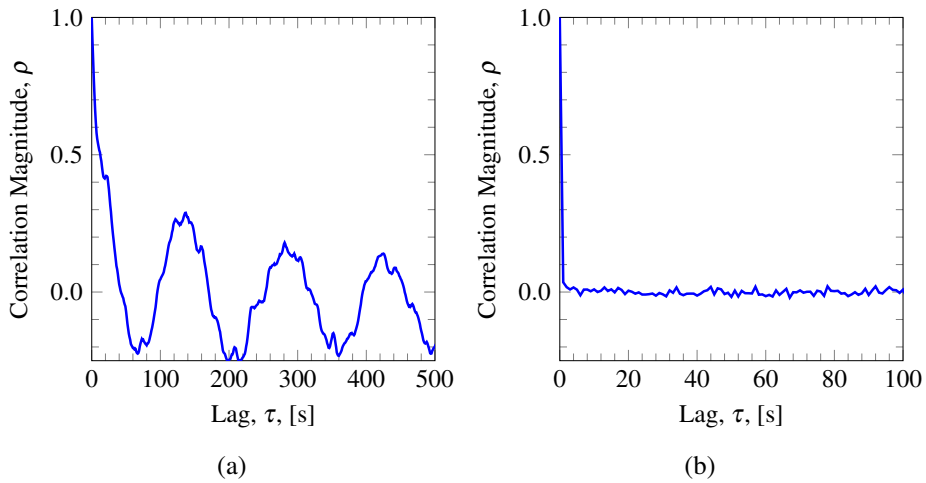

Fig. 4.4: Autocorrelations for preliminary dataset to test for sample independence and determine PIV sampling rate. Figure (a) shows the autocorrelation for a sample natural convection dataset acquired at 1 Hz indicating sample dependence. Integrating $\rho(\tau)$ from 0 to the zero-crossing indicated that the sampling rate should be reduced to 0.1 Hz. Figure (b) shows the autocorrelation of the same natural convection case acquired at 0.1 Hz and indicates statistical sample independence.

by the free stream velocity, U_∞, and each velocity component is written as

$$\hat{u} \equiv \frac{\sqrt{\overline{u'u'}}}{U_\infty}, \quad \hat{v} \equiv \frac{\sqrt{\overline{v'v'}}}{U_\infty}, \quad \hat{w} \equiv \frac{\sqrt{\overline{w'w'}}}{U_\infty} \tag{4.13}$$

where $\overline{u'u'}$, $\overline{v'v'}$, $\overline{w'w'}$ are the normal Reynolds stress components from the Reynolds stress tensor. The overall turbulence level is defined as the root-mean-square of the turbulent fluctuations normalized by the free stream velocity as

$$I \equiv \frac{\sqrt{\frac{1}{3}(\overline{u'u'} + \overline{v'v'} + \overline{w'w'})}}{U_\infty} = \frac{\sqrt{\frac{2}{3}k}}{U_\infty} \tag{4.14}$$

where k is the turbulence kinetic energy and is defined as

$$k \equiv \frac{1}{2}\left(\overline{u'u'} + \overline{v'v'} + \overline{w'w'}\right). \tag{4.15}$$

The use of turbulence kinetic energy as an input to a turbulence model assumes more-or-less isotropic turbulence because it does not differentiate between the individual normal stress components. The standard $k-\epsilon$ and $k-\omega$ RANS models are known as linear eddy viscosity models

and transport turbulence kinetic energy and turbulence dissipation ϵ or turbulence dissipation rate ω, respectively, as a turbulence closure method. Turbulence dissipation is the rate at which turbulence kinetic energy is dissipated into thermal energy and is defined as

$$\epsilon \equiv 2\,\nu\,\overline{s_{ij}\,s_{ij}} \tag{4.16}$$

where s_{ij} is the fluctuating rate of strain

$$s_{ij} \equiv \frac{1}{2}\left(\frac{\partial u_i'}{\partial x_j} + \frac{\partial u_j'}{\partial x_i}\right) \tag{4.17}$$

and $\partial u_i'/\partial x_j$ are elements of the fluctuating velocity gradient tensor. Using stereo PIV in a plane allows for the calculation of 5 of the 12 terms of the fluctuating velocity gradient tensor. It is possible to use DNS to calculate the remaining terms as shown by Xu, *et al.* [71] but is a numerically expensive process and will not be considered here. Others have used a combination of PIV, LDV, and CFD in determining the remaining terms of s_{ij} for small scale, anisotropic turbulent flows [72–77]. Due to the lack of spatial resolution in the third velocity direction, the turbulence dissipation rate will be estimated using the empirical formula

$$\epsilon \cong C_\mu^{3/4}\frac{k^{3/2}}{\ell} \tag{4.18}$$

where ℓ is the mixing length and is approximated as $\ell = 0.07D_h$ where D_h is the hydraulic diameter [78, 79].

Specific turbulence dissipation rate ω is the rate at which turbulence kinetic energy is converted to thermal energy per unit time and volume. There is no strict mathematical definition for ω as there is for ϵ. It was simply formulated as a closure model with experimentally determined model constants and is defined as

$$\omega \equiv \frac{\epsilon}{\beta^*\,k} \tag{4.19}$$

where β^* is a model constant and is usually set to $\beta^* = C_\mu = 0.09$ for the standard $k-\omega$ model [70]. Each of these parameters can serve as turbulence boundary conditions in RANS, large eddy

simulation (LES) and Reynolds stress tensor (RST) CFD models.

4.8 Heat Transfer Coefficient

The heat transfer coefficient for the rod bundle can be calculated using Eq. 1.4 and rearranging

$$h = \frac{q''}{(T_s - T_m)} \tag{4.20}$$

where q'' is the surface heat flux of the rods and T_m is the mixed mean fluid temperature for internal flow. The mixed mean fluid temperature was calculated using an energy balance for a control volume spanning from the contraction inlet, where fluid temperature and mass flow rate are known, to the axial position of each thermocouple as shown in Fig. 5.4. The energy balance is written as

$$\Delta E_{\text{st}} = E_{\text{in}} - E_{\text{out}} + E_{\text{g}} \tag{4.21}$$

where E_{st} is the energy stored in the control volume, E_{in} is the energy entering the control volume, E_{out} is the energy leaving the control volume and E_g is the energy generated inside the control volume. Assuming ideal gas, steady-state and incompressible fluid flow, the energy balance reduces to

$$q = q''\, A_s = \dot{m}\, c_p\, (T_m - T_i) \tag{4.22}$$

where $\dot{m}$ is the mass flow rate through the control volume, c_p is the specific heat of the air and T_i is the inlet fluid temperature [6]. Solving for T_m and inserting Eq. (4.22) into Eq. (4.20), the calculation of the heat transfer becomes

$$h = \frac{q''}{T_s - \left(\frac{q''\, A_s}{\dot{m}\, c_p} + T_i\right)} \tag{4.23}$$

Using the calculated mixed mean fluid temperature, rod surface temperature, and power input to the heaters, the heat transfer coefficient was calculated. The Nusselt number for these cases were determined by using the calculated heat transfer coefficient input into Eq. 1.5.

CHAPTER 5
RESULTS

5.1 Boundary Conditions

Boundary conditions in CFD simulations are used as inputs to the system and are what determine the outcome of the governing equations. A simulation solution is only as accurate as its boundary conditions. Large uncertainties on boundary conditions may result in a completely unusable solution. Aside from physically measuring and digitally reconstructing the geometry, the boundary conditions necessary for CFD simulations are presented here.

The test section walls are designated as follows: The opaque, aluminum wall of the test section (on the $y = 0$ mm plane) is referred to as the "Plate", the wall opposite the Plate (on the $y = 304.8$ mm plane) is the "Top Wall", the wall that lies on the $x = +152.4$ mm plane is referred to as the "Left Wall" and the wall at the $x = -152.4$ mm plane is referred to as the "Right Wall". The rods are designated by numbers 1-4 starting at the top right corner going counter-clockwise when looking from the test section inlet in the positive z-direction.

5.1.1 Inflow

The test section inlet velocity field was acquired in the xy-plane at $z = 0.067$ m for each of the test cases. The inlet velocity field and profile for the Natural700 case are shown in Fig. 5.1.

The average turbulence quantities and their individual uncertainty discussed in Section 4.7 are presented in Table 5.1. The turbulent shear stress $\overline{\tau}$ is calculated by

$$\overline{\tau} = \sqrt{\frac{1}{4}(\overline{v'v'} - \overline{u'u'})^2 + (\overline{u'v'})^2}. \tag{5.1}$$

The turbulence dissipation rate for the Natural400 and Natural700 cases are nearly zero and as a result have very large relative uncertainty. However, given their small magnitude will not have an impact on the simulation result.

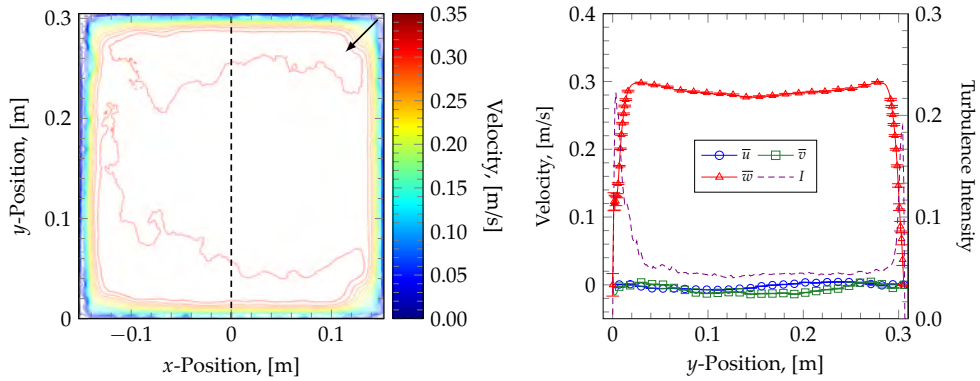

(a) (b)

Fig. 5.1: Test section inflow velocity measurements for the Natural700 case. (a) Contour plot of the through plane velocity component. The first contour level begins at 0 m/s and the increment is 0.0175 m/s. The arrow indicates increasing contour levels and the dashed line represents the location of the line profile. (a) Velocity profiles of the centerline ($x = 0$ m). The velocity used for calculating turbulence intensity was 0.2584 m/s.

Table 5.1: Test section inflow average turbulence quantities for each flow case.

Case	U_∞, [m/s]	k, [m^2/s^2]	$\overline{\tau}$, [m^2/s^2]
Forced	1.341 ± 0.005	0.01217 ± 0.00117	0.00484 ± 0.00031
Mixed400	1.346 ± 0.005	0.01196 ± 0.00117	0.00477 ± 0.00030
Mixed700	1.371 ± 0.004	0.01085 ± 0.00106	0.00432 ± 0.00027
Natural400	0.199 ± 0.002	0.00040 ± 0.00004	0.00007 ± 0.00001
Natural700	0.263 ± 0.002	0.00052 ± 0.00005	0.00013 ± 0.00001

Case	I	ϵ, [m^2/s^3]	ω, [1/s]
Forced	0.0672 ± 0.0032	0.01034 ± 0.00217	9.44 ± 2.18
Mixed400	0.0663 ± 0.0033	0.01007 ± 0.00217	9.36 ± 2.22
Mixed700	0.0620 ± 0.0030	0.00871 ± 0.00197	8.91 ± 2.19
Natural400	0.0820 ± 0.0039	0.00006 ± 0.00007	1.71 ± 2.01
Natural700	0.0708 ± 0.0036	0.00009 ± 0.00010	1.95 ± 2.11

Integrating the inlet velocity profile results in the volume flow rate of the air through the wind tunnel and the mass flow rate through the test section is

$$\dot{m} = \rho Q \tag{5.2}$$

where Q is the volume flow rate. The mass flow rate for each test case is presented in Table 5.2. The Reynolds number for each case is then calculated by

$$\mathrm{Re} = \frac{\rho V D_h}{\mu} = \frac{(\dot{m}/A)\, D_h}{\mu} \tag{5.3}$$

where the hydraulic diameter is $D_h = 4A/P$, A is the cross sectional area and P is the inlet perimeter. The Reynolds number at the test section inlet and mass flow rate for each case is also shown in Table 5.2. The mass flow rate will be used as the inflow boundary condition in the Forced, Mixed400, and Mixed700 cases and as an SRQ for the Natural400 and Natural700 cases. The Richardson number is also presented in Table 5.2 for considering the relative impact of heating on the flow.

The inflow data (mass flow rate/inlet velocity profile) should be used as a BC for the *forced/mixed cases only*. Applying a mass flow boundary condition to the natural convection cases would result in a mixed convection solution. The inlet velocity profile and mass flow rate may be used as an SRQ for the natural convection cases.

Table 5.2: Break down of mass flow rate, $\dot{m}$, Reynolds number, Re, and Richardson number, Ri, for each test case based on the integrated velocity profile at the test section inlet with Re calculated according to Eq. 5.3. The Richardson number was calculated using the Grashof number based on the average rod temperature for each case.

Case	$\dot{m}$, [kg/s]	Re	Ri
Forced	0.13±0.011	23,294±2,302	N/A±N/A
Mixed400	0.13±0.011	23,373±2,310	10.9±2.2
Mixed700	0.13±0.011	23,159±2,285	15.6±3.1
Natural400	0.02±0.002	3,452±341	550.0±108.7
Natural700	0.03±0.002	4,596±454	383.1±75.7

The loss coefficient of the contraction inlet was discussed previously and is presented in Table 3.1. Introduction of this loss coefficient has been found to greatly impact the accuracy of the simulation.

5.1.2 Power Input

Four cartridge heaters of ∅ 9.5 mm with a heated length of 314.3 mm. The gap between the heated sections of each cartridge heater is 33.4 mm. All four heaters in the rod sections at a particular z-position in the rod bundle are powered in parallel from a single power supply output. Power input to the rods was determined using the formula for electric power

$$P_{\text{rod}} = E\,I \tag{5.4}$$

where E is the supplied voltage and I is the supplied current and the uncertainty is determined using Eq. 5.4 as the DRE for the TSM for uncertainty propagation. Figure 5.2 shows the z-dimensions of the rod bundle that are heated and unheated for input into the CFD simulation. Table 5.3 shows the break-down of power input for each heater section for the flow cases considered. The dimensions over which cartridge heaters are in contact with the inner surface of the fuel rods are shown in Fig. 5.2.

Table 5.3: Power input to the rod bundles at each rod section level for heated each flow case.

Case	Rod Section 1, [W]	Rod Section 2, [W]	Rod Section 3, [W]	Rod Section 4, [W]
Mixed400	57.34±0.13	57.05±0.13	56.87±0.13	57.02±0.13
Mixed700	99.30±0.21	98.80±0.21	98.48±0.21	98.75±0.21
Natural400	56.23±0.13	56.92±0.13	56.77±0.13	56.95±0.13
Natural700	98.99±0.21	98.61±0.21	98.32±0.21	98.61±0.21

5.1.3 Surface Treatment

Reduction and stabilizing of radiation heat transfer is critical to the ability to simulate strongly

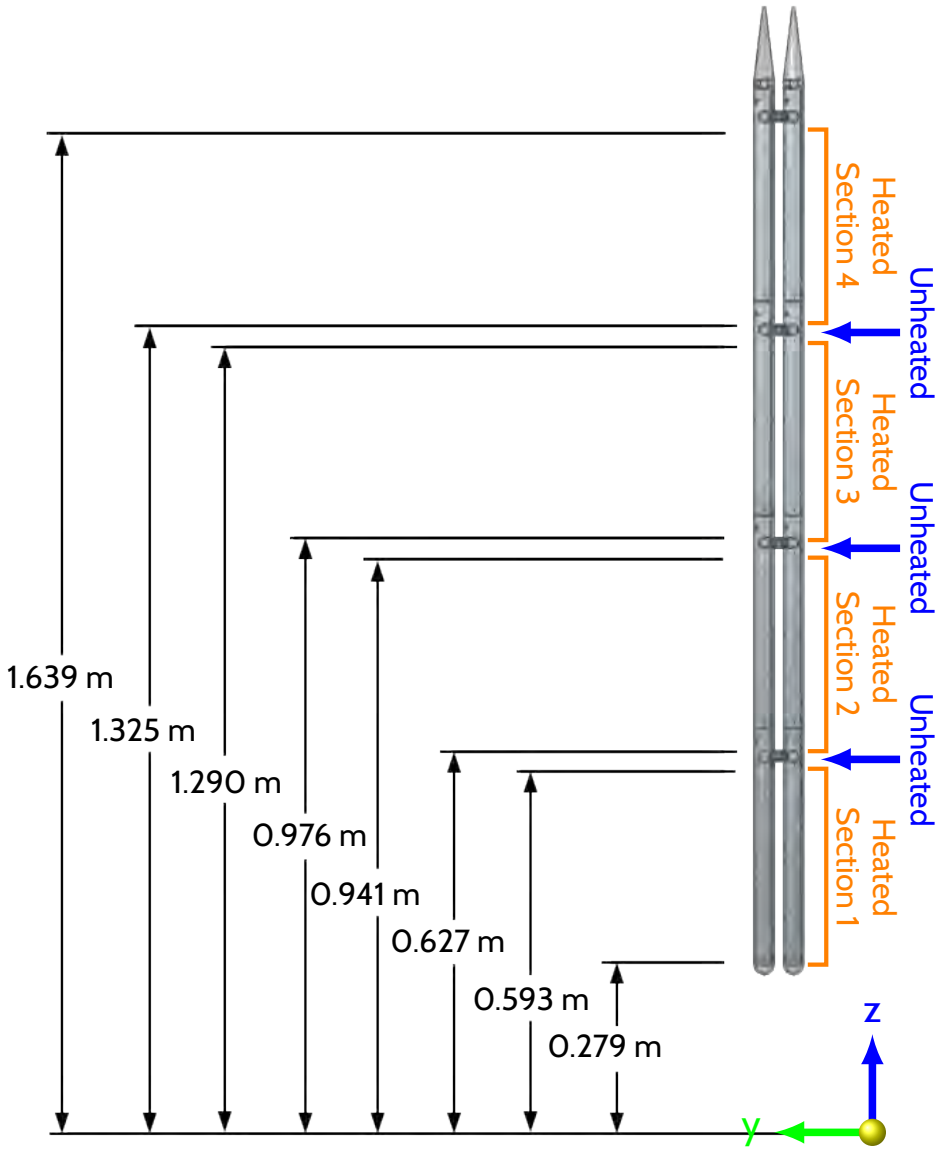

Fig. 5.2: Dimensions of the heated and unheated sections of the rod bundle. Uncertainty for lengths are ± 0.001 m.

heated flows while ignoring radiation. The emissive properties of aluminum have been shown to vary widely with surface finish and oxidation [53, 54]. Treatment of the rod surface with electroless nickel plating not only lowers the emissivity of the aluminum but also prevents the wide variation of emissivity as the aluminum oxidizes. As mentioned previously, the nickel plating used to treat the fuel rods has a total hemispherical emissivity of $\epsilon_s = 0.10 \pm 0.01$. Figure 5.3 shows the rod surfaces that were treated with nickel plating and the untreated aluminum surfaces which were polished so as to have a stable emissivity.

5.2 System Response Quantities

The outputs of the CFD simulations must be compared to the system response quantities (SRQs) of the benchmark experiments in order to assess the accuracy of the simulation. System response quantities are measurements that vary according to boundary conditions that are input to the system. Each section below will discuss the SRQs that may be used to assess the simulation accuracy.

5.2.1 Heat Transfer Coefficient

Newton's law of cooling describes the heat loss from a surface due to convection and is defined as

$$q = hA_s \left(T_{s,o} - T_{m,o}\right) \tag{5.5}$$

where h is the heat transfer coefficient, A_s is the surface area, $T_{s,o}$ is the surface temperature and $T_{m,o}$ is the mean fluid temperature. The mean fluid temperature for flow in a heated circular tube is defined as

$$T_m = \frac{\int_A \rho u c_p T dA}{\dot{m} c_p} \tag{5.6}$$

where the integral is applied over the cross-sectional area. For this study surface temperature, heat lost from the surface and surface area are known. To determine h, the mean fluid temperature at each flow-wise rod thermocouple location must be calculated. Drawing a control volume from the inlet of the contraction and extending along the walls of the wind tunnel to each z-location of the rod thermocouples, the mean fluid temperature is determined using an energy balance on the control

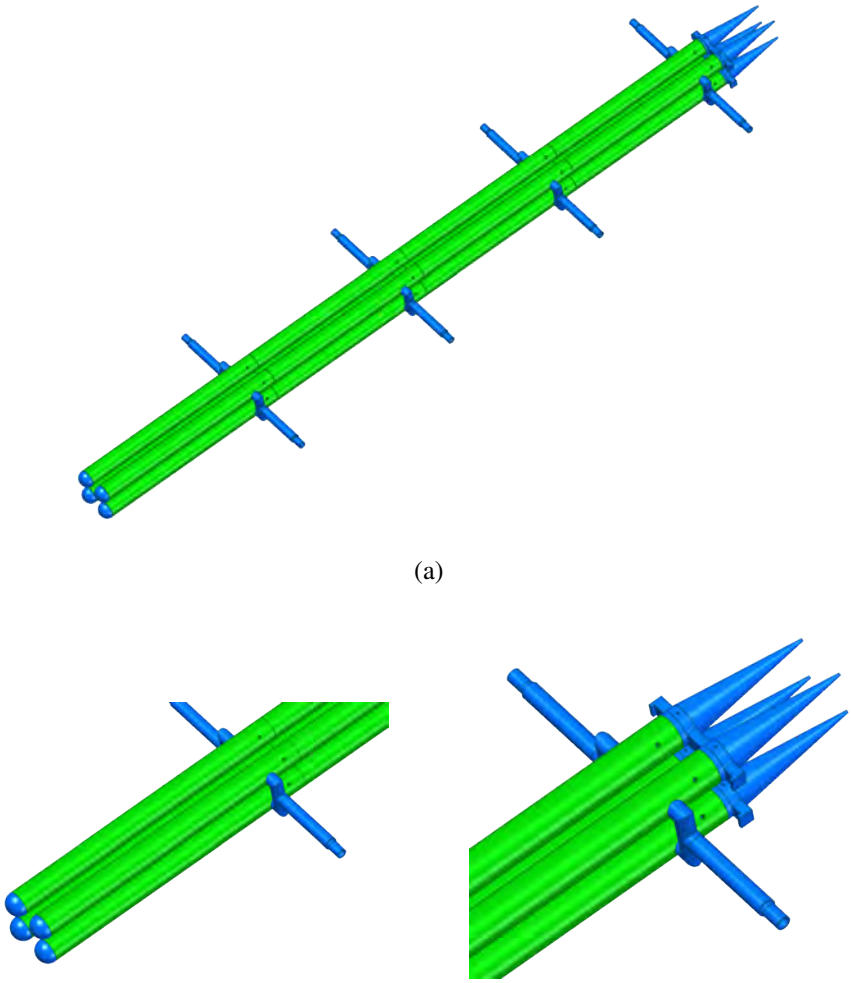

(a)

(b) (c)

Fig. 5.3: Surface treatment of the fuel rod assembly. Blue surfaces represent polished aluminum and green surfaces represent nickel plating. (b) Close up of leading edge of fuel rods. (c) Close up of trailing edge of fuel rods. (a) Overview of full fuel rod assembly.

volume (shown in Fig. 5.4)

$$\Delta q = \dot{m} c_p \left(T_{m,o} - T_{m,i} \right) \tag{5.7}$$

where dq is the power input into the control volume from the fuel rods, $\dot{m}$ is the mass flow rate, c_p is the specific heat of the fluid, $T_{m,i}$ is the mean fluid temperature entering the volume and $T_{m,o}$ is mean fluid temperature exiting the volume. Using Eqs. 5.5 and 5.7, a system of equations may be used to calculate the local heat transfer coefficient over the length of the rod bundle. The local heat transfer coefficient is plotted for each z-location of the rod thermocouples and is shown in Fig. 5.5 for the heated cases. The heat transfer coefficient drops between points 3 and 4, 6 and 7, and 9 and 10 due to the presence of the grid spacers.

Literature has provided Nusselt number correlations for heat transfer in fuel rod bundles [9,10]. The Rayleigh number (based on the hydraulic diameter) for their results, however, are far below the Rayleigh number used in this study and therefore does not provide a useful comparison.

5.2.2 Grashof and Rayleigh Number

The Grashof number is a dimensionless parameter that represents the ratio of buoyancy to viscous forces acting on a fluid. The local Grashof number of a vertical plate is defined as

$$\mathrm{Gr}_x = \frac{g\beta \left(T_{s,o} - T_{m,o} \right) x^3}{\nu^2}. \tag{5.8}$$

where the mean fluid temperature $T_{m,o}$ is determined using the methodology described above. The surface of the fuel rods behaves much like a vertical plate and, therefore, this definition is used.

The Rayleigh number is a dimensionless number used to determine the transition from laminar to turbulent for buoyancy-driven flows. It is defined as the product of the Grashof number and Prandtl number. Thus the local Rayleigh number is

$$\mathrm{Ra}_x = \mathrm{Gr}_x \, \mathrm{Pr} = \frac{g\beta \left(T_s - T_m \right) x^3}{\nu\alpha}. \tag{5.9}$$

The variation of Rayleigh number over the length of the rods for each heated flow case is shown in Fig. 5.6 and indicates that turbulence occurs ($\mathrm{Ra} \gtrsim 10^9$) approximately at the midpoint of the rod

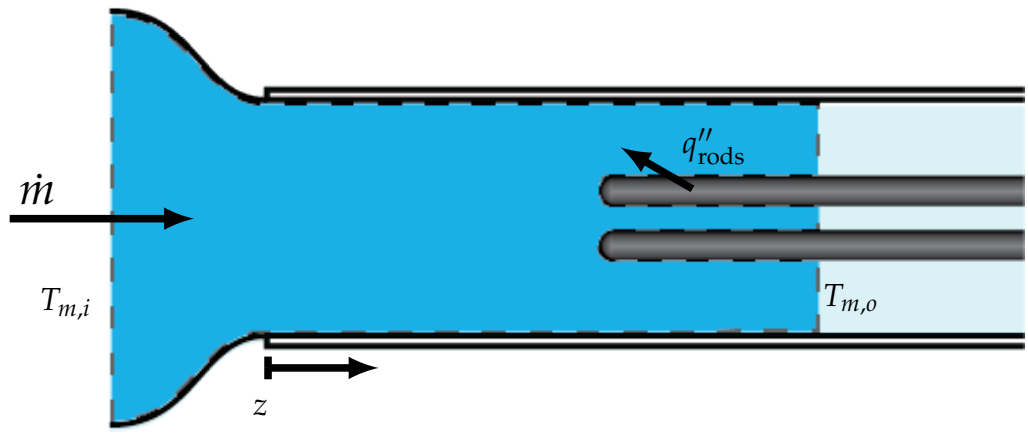

Fig. 5.4: Sketch of the control volume used to determine mean fluid temperature along rods in the z-direction. The dashed line represents the boundaries of the control volume. The control volume extends to the z-position of each axial rod thermocouple position.

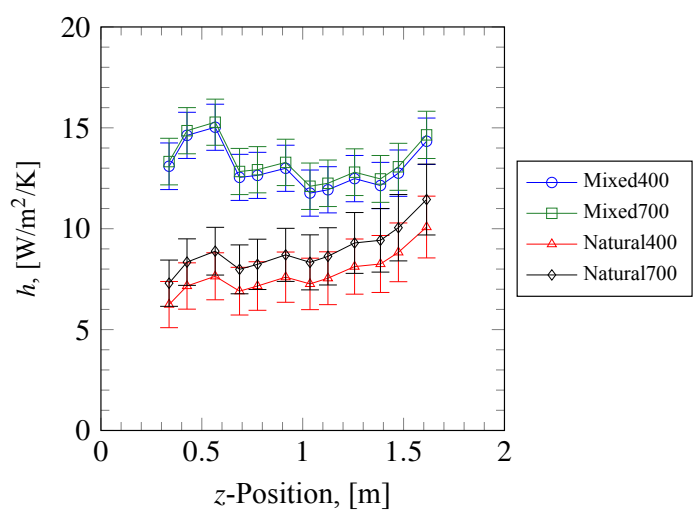

Fig. 5.5: Local heat transfer coefficient, h, versus z-location for each rod thermocouple position.

bundles for all heated cases.

5.2.3 Rod and Wall Temperature Distribution

The Biot number is a dimensionless parameter that represents the ratio of convection to material conductivity

$$\mathrm{Bi} = \frac{hL_c}{k} \tag{5.10}$$

where L_c is the characteristic length and is defined as the ratio of volume to surface area $L_c \equiv V/A_s$ and k is the conductivity of the solid. For Biot numbers less than 0.1, it can be assumed that the transient temperature gradient through the fuel rods is negligible. The Biot number for this experiment was found to be smaller than 4×10^{-4}. Due to such a low Biot number, it is assumed that there is no gradient across the radial direction of the rods and, at steady-state, any variation in the circumferential temperature is lower than the uncertainty of the thermocouple measurements.

In order for the temperature distributions to be easily compared to the CFD simulations, the temperatures have been converted to degrees Kelvin and then non-dimensionalized as follows

$$\theta = \frac{T - T_{\mathrm{amb}}}{T_{\mathrm{amb}}} \tag{5.11}$$

where T is the measured temperature and T_{amb} is the ambient temperature, both in degrees Kelvin. Figure 5.7 shows the temperature distribution of the rods for the heated cases considered. The slight jump present between points 3 and 4, 6 and 7, and 9 and 10 is due to combination of contact resistance between the rod sections and the unheated length between cartridge heaters. All uncertainties have been calculated using Eq. 5.11 as the DRE for the TSM according to Appendix D of this document. The temperature distribution for the mixed convection cases (Figs. 5.7a and 5.7b) is significantly different than the natural convection cases (Figs. 5.7c and 5.7d). The peak temperature for the natural convection cases occurs near the leading edge of the rod bundle due to the presence of laminar flow as the boundary layer develops and flow is accelerated while the peak temperature for the mixed convection cases occurs towards the trailing edge of the rod bundle due to the overall heating of the passing fluid. A similar trend is seen in the heat transfer coefficient in Fig. 5.5 in

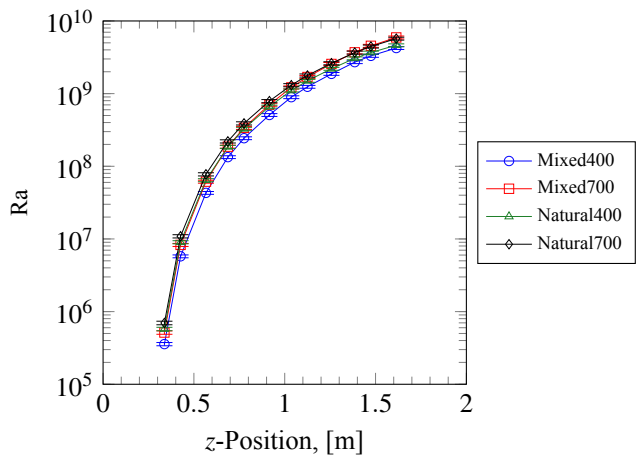

Fig. 5.6: Local Rayleigh number for heated flow cases.

which the natural convection cases have a trend of increasing heat transfer as the flow accelerates while the mixed cases have a much more steady heat transfer rate due to the flow being forced through the rod bundle.

The non-dimensionalized centerline wall temperature for all four walls in the flow-wise direction are shown in Fig. 5.8. The high thermal conductivity of the aluminum wall results in a slight warming of the wall further upstream when compared to the polycarbonate walls. An estimate of the heat loss from the walls due to heating is found in Section 5.2.6.

5.2.4 Outlet Fluid Temperature

The outlet fluid temperatures were recorded by a 4×4 square grid of thermocouples evenly spaced across the test section outlet at $z = 2$ m. Contour plots of the non-dimensionalized temperature are shown in Fig. 5.9. Higher temperature fluid is concentrated near the center of the test section exit due to the presence of the rods.

For a given heat flux level, the mean fluid temperature at the outlet is higher for natural convection compared to natural convection due to the lower mass flow rate. Equation 5.6 shows that the mean fluid temperature is inversely proportional to the mass flow rate, consistent with the contour plots shown in Fig. 5.9.

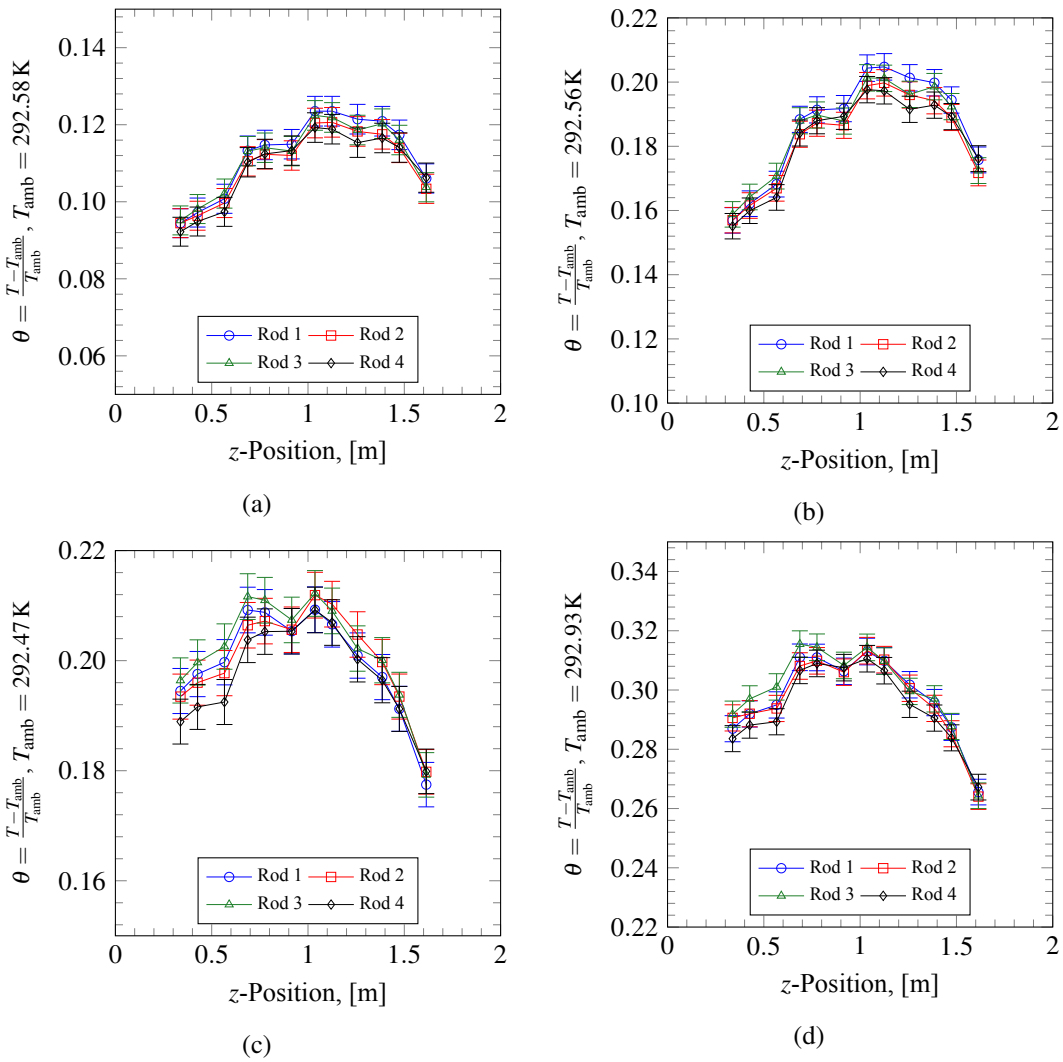

Fig. 5.7: Rod surface temperature distribution in flow-wise direction for (a) the Mixed400 case, (b) the Mixed700 case, (c) the Natural400 case, and (d) the Natural700 case.

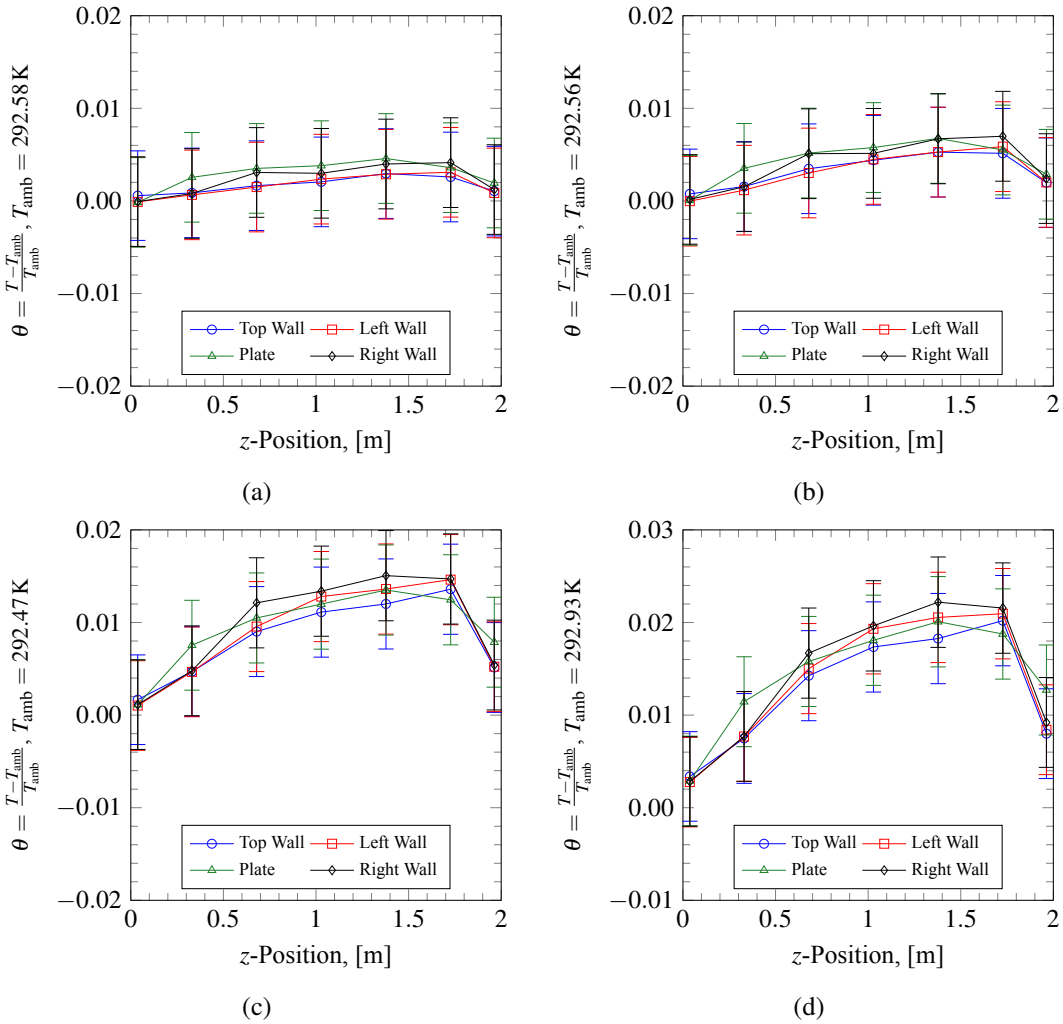

Fig. 5.8: Test section wall temperature distribution in flow-wise direction for (a) the Mixed400 case, (b) the Mixed700 case, (c) the Natural400 case, and (d) the Natural700 case.

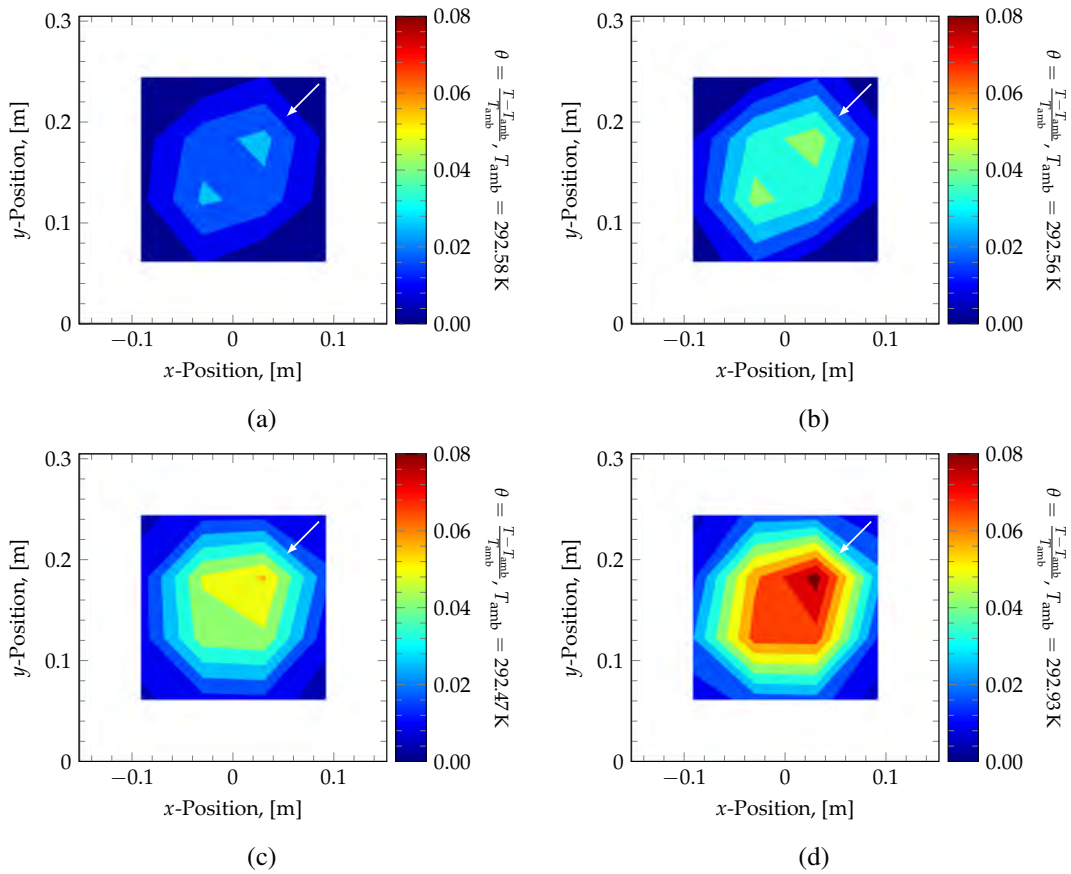

Fig. 5.9: Outlet fluid temperature contour (at $z = 2$ m) for (a) the Mixed400 case, (b) the Mixed700 case, (c) the Natural400 case, and (d) the Natural700 case. The contour scale begins at $\theta = 0$ and has an increment of 0.008. The arrow indicates the direction of increasing temperature. The thermocouples were arranged in a 4×4 square grid and were evenly spaced across the test section outlet (61 mm apart in the x and y directions).

5.2.5 Radiation Heat Transfer

The estimation of radiation heat loss is complex due to the complexity of the geometry. In order to estimate the heat loss from the rods, it was assumed that a single rod was suspended in the test section and the radiation loss to the surroundings was calculated. This results in an over-estimation of the heat transfer that occurs in the full model because the other rods block part of the heat transfer that occurs between a single rod and the surrounding walls. The loss for a single rod is tabulated in Table 5.4 as well as the percentage of the total heat input to the system that is due to radiation.

Table 5.4: Estimated heat loss from rods due to radiation heat transfer.

Case	q_{rad}, [W]	$q_{\text{rad}}/q_{\text{total}}$
Mixed400	8.5±0.86	3.73%
Mixed700	15.8±1.58	3.99%
Natural400	17.2±1.72	7.58%
Natural700	29.7±2.97	7.52%

The polycarbonate walls have the potential of heat loss through radiation transmission. There is currently no information available for the transmissivity of polycarbonate in the infrared radiation range emitted from the fuel rods. However, when placed in front of an infrared camera, the polycarbonate visibly blocks the radiation from the rods providing confidence that there is little infrared transmission through the test section walls. Further investigation of the transmissivity and absorption of the polycarbonate walls in the radiation spectrum considered for this system is needed. Radiation transmitted through the walls of the test section with therefore be neglected and all losses will be attributed to convection as discussed below.

5.2.6 Wall Heat Loss

Proper modelling of the system requires that the amount of heat lost from the test section walls be quantified. The heat lost per unit area from the test section walls is estimated using a surface

energy balance of the outer surface of the wall where

$$q''_{\text{cond}} - q''_{\text{conv}} = k_s \frac{dT}{dx} - \overline{h}(T_s - T_\infty) = 0 \tag{5.12}$$

where k is the thermal conductivity of the wall, dT/dx is the temperature gradient through the wall, $\overline{h}$ is the heat transfer coefficient of natural convection on the outside of the wall and $T_s - T_\infty$ is the temperature difference between the surface and ambient air. The heat transfer coefficient on the walls may be determined using a Nusselt number correlation for a vertical flat plate in quiescent fluid and is represented as

$$\overline{\text{Nu}}_L = \left\{ 0.825 + \frac{0.387\text{Ra}_L^{1/6}}{\left[1 + (0.492/\text{Pr})^{9/16}\right]^{8/27}} \right\}^2 \tag{5.13}$$

which is applicable over the entire range of Ra_L [80]. Error on the Nusselt number correlation discussed by Churchill and Chu [80] was determined by extracting numerical values from correlation figure presented and calculating the standard deviation of the fit error. The fit uncertainty was found to be 28.2%. Table 5.5 provides a breakdown of the estimated wall heat loss for each of the cases considered as well as their percent heat loss relative to the power input to the fuel rods.

The heat loss through the polycarbonate walls in all cases is essentially negligible due to their low thermal conductivity. The loss through the aluminum wall, however, is larger due to its higher mean temperature and larger thermal conductivity. Wall losses are not significant for the forced and mixed convection cases. The wall loss for the natural convection cases is negligible on the polycarbonate walls and only reaches a maximum of 1.2% of the rod power input. Cases where q_{loss} is negative should be considered zero due to large uncertainty contributed by the temperature difference $T_s - T_\infty$.

5.2.7 Velocity Profiles

Velocity SRQ measurements were performed on two planes in the x-direction and at four z-positions for a total of 12 velocity fields for each flow case. A velocity profile (in the y-direction)

Table 5.5: Estimated wall heat loss due to test section wall heating for each of the heated cases.

Case	Wall	q_{loss}, [W]	% Loss
Mixed400	Top	0.11 ± 0.031	0.03
	Left	0.09 ± 0.024	0.02
	Plate	0.46 ± 0.131	0.12
	Right	0.17 ± 0.049	0.04
Mixed700	Top	0.37 ± 0.107	0.09
	Left	0.34 ± 0.098	0.09
	Plate	1.07 ± 0.304	0.27
	Right	0.46 ± 0.131	0.12
Natural400	Top	0.47 ± 0.228	0.12
	Left	0.48 ± 0.240	0.12
	Plate	2.85 ± 0.810	0.72
	Right	0.49 ± 0.270	0.12
Natural700	Top	0.00 ± 0.113	0.00
	Left	-0.02 ± 0.281	-0.01
	Plate	4.81 ± 1.367	1.22
	Right	-0.08 ± 0.417	-0.02

was extracted from the vector fields for direct comparison with CFD line plots of velocity. The velocity profiles for the Natural700 case are presented in Fig. 5.11 for the $x = 0$ m plane and the $x = -0.06$ m planes with the figures showing the velocity profiles in the upward direction representing the progression of the flow in the positive z-direction. The background of each figure shows the relative y-position of the swirl elements for visual reference but are not positioned vertically with respect to the actual location of the profiles. The Reynolds stresses were also calculated from the velocity fields and are included with the velocity profiles using the right hand axis for scaling. The mean streamwise velocity component (w_{bulk}) has been subtracted from the streamwise velocity in order to visually compare all three components of velocity on the same plot. The value of w_{bulk} is shown in the y-axis label of each plot.

For the $x = 0$ m plane (lying between the fuel rods) in Fig. 5.11a, the effect of the swirl elements strongly present in the $\overline{u}$ velocity component where $y = 0.154$ m corresponds to the centerline of the fuel rod bundle. The increasing magnitude of w_{bulk} in the flow wise direction is present due to the acceleration of the flow due to buoyancy. The Reynolds stresses in the $z = 0.476$ m and $z = 0.825$ m positions are negligible, however, after entering the transition flow regime

the Reynolds stresses increase rapidly as shown in the $z = 1.174$ m and $z = 1.524$ m positions of Fig. 5.11a. This phenomenon is in good agreement with the local Rayleigh number presented in Fig. 5.6 which occurs at approximately half the length of the rod bundle (in between $z = 0.825$ m and $z = 1.174$ m).

The strong through-plane swirl effect of the swirl elements is visible at all z-locations of the $x = 0$ m plane (Fig. 5.11a) while the in plane horizontal velocity component, $\overline{v}$, is nearly zero at all z-positions. The normal Reynolds stresses at this x-position are also the only significant contributors to the Reynolds stress tensor with the Reynolds shear stresses being nearly zero at all z-positions.

The fluid flow on the $x = -0.060$ m plane (just outside the rod bundle) differs greatly from that of the $x = 0$ m plane shown in Fig. 5.11b. The fluid acceleration due to the growth of the boundary layer increases less quickly due to the mass of bulk fluid accelerating outside the fuel rod bundle. This results in lower velocity magnitudes as well as decreased Reynolds stresses outside the rod bundle. At the lowest z-location, a slight decrease in streamwise velocity immediately downstream of the swirl elements is present. The Reynolds stresses in the $z = 0.476$ m and $z = 0.825$ m are nearly zero lying in the laminar flow regime. At $z = 1.174$ m the Reynolds stresses become non-zero near the center of the rod bundle (the left side of the plot) as the bulk fluid velocity also increases in this region. Upon reaching the $z = 1.524$ m, turbulence diffuses outward into the flow (toward the right of the x-axis) causing non-zero Reynolds stresses and increased bulk velocity.

5.2.8 Autocorrelation

An autocorrelation provides information about the frequency of the fluid structures, as discussed in Section 4.6. PIV data were acquired at 25 Hz for the Natural400 and Natural700 cases and processed using the procedure explained in Section 3.3.4. The fluctuating time series of the streamwise velocity vectors at each location were extracted from the post-processed vector fields. An autocorrelation was performed and the results are shown in Fig. 5.10. The sinusoidal form of each curve is indicative of repeating turbulent structures flowing through the vector location. The autocorrelation of Natural400 at Location 1 indicates that the turbulent structures have a period of approximately 15 seconds, Natural400 at Location 2 a period of 7 seconds, Natural700 at Location

1 a period of 10 seconds and Natural700 at Location 2 a period of about 7 seconds. This long period of turbulent fluctuations is characteristic of slow-moving natural convection flows and requires extremely slow acquisition rates in order to have statistical independence.

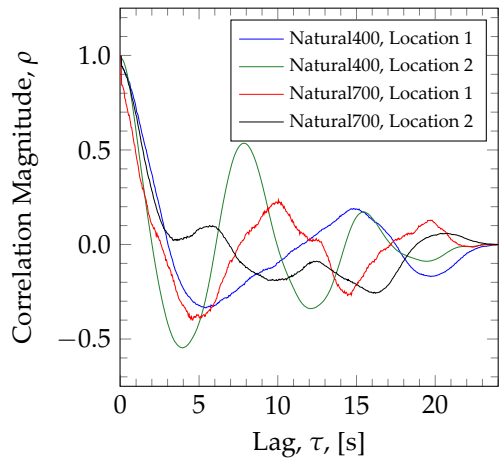

Fig. 5.10: Autocorrelation of time-series velocity fluctuations in the stream-wise direction. Location 1 corresponds to $(x = -0.06\ \text{m},\ y = 0.152\ \text{m},\ z = 0.476\ \text{m})$ and Location 2 corresponds to $(x = -0.06\ \text{m},\ y = 0.197\ \text{m},\ z = 0.476\ \text{m})$.

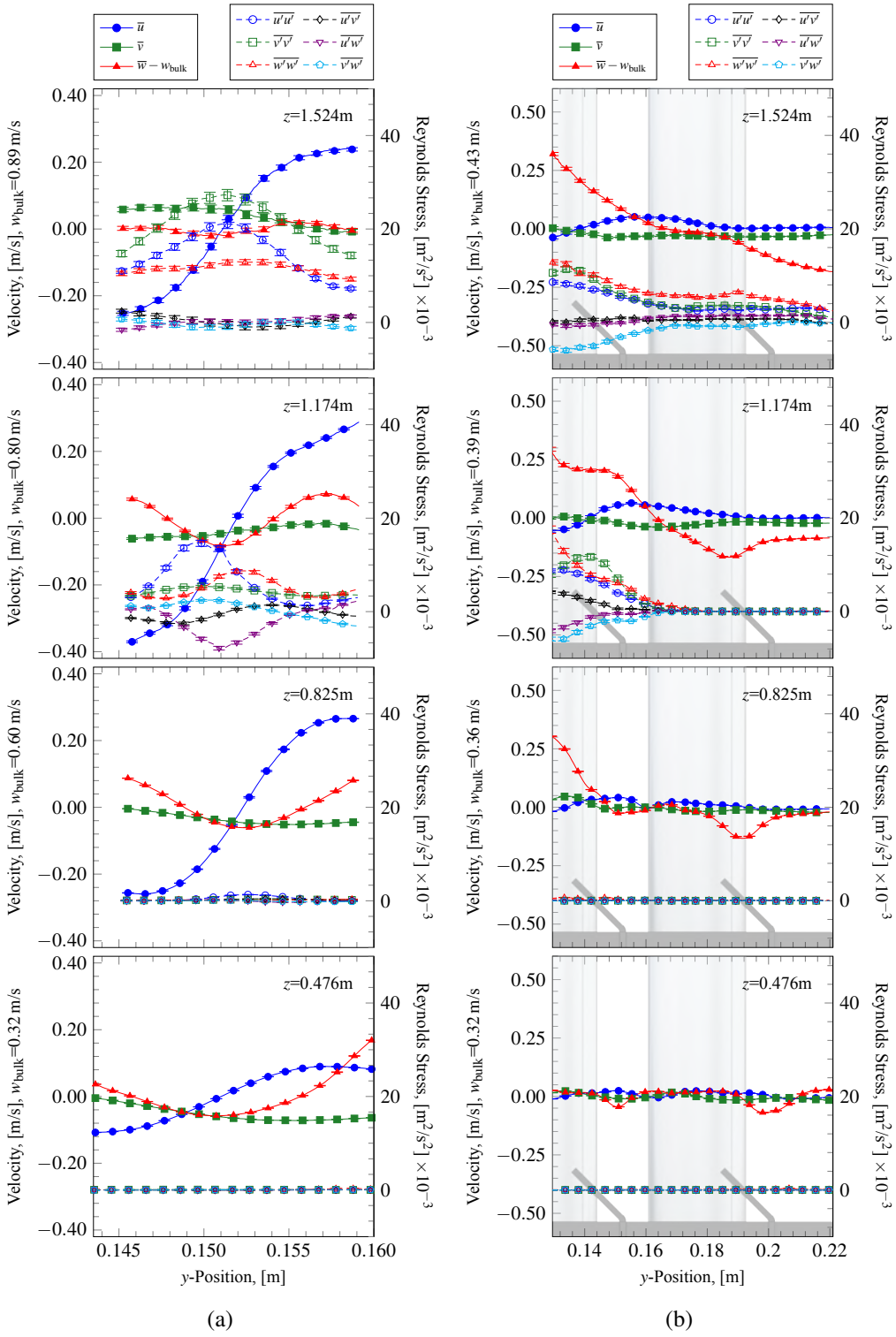

Fig. 5.11: Velocity profile along y-direction for (a) $x = 0$ m and (b) $x = -0.06$ m at four z-positions indicated on each plot for the Natural700 case. The inner edges of the fuel rods are aligned with the y-axes on the $x = 0$ m. The relative locations of the swirl elements in the y-position (not to scale in z) are shown in the background of the $x = -0.06$ m figure.

CHAPTER 6

CONCLUSION

Spent nuclear fuel is removed from spent fuel pools and placed in dry storage following years of decay heat removal. Fuel remaining in wet storage for such an extended period of time leaves them vulnerable to a variety of disasters both natural and human-caused. Current models of spent fuel dry storage are based on conduction only and do not account for recirculation through the storage casks which would greatly enhance heat removal. Simulations including convection through spent fuel rod bundles must be validated in order to assess its accuracy. The benchmark experiments presented in this study provide validation data for spent fuel rod bundles under forced and mixed convection. The benchmark experiments include a forced unheated case, two mixed convection cases at different heat flux levels and two natural convection cases at different heat flux levels.

The Rotatable Buoyancy Tunnel (RoBuT) facility at Utah State University was ideal for the execution of these benchmark experiments due to its design and instrumentation for performance of CFD validation exercises. The facility is rotatable to change the acting direction of gravity on the experiment although the buoyancy-aided orientation was the only orientation considered in this study. Ambient conditions are measured and recorded through the duration of the study and the room was maintained at $20°\mathrm{C} \pm 0.5°\mathrm{C}$ and the ambient relative humidity and atmospheric pressure were recorded for calculation of fluid properties for air entering the experimental apparatus. The fluid entering the wind tunnel is conditioned using a seeding array (for PIV measurements), a honeycomb mesh flow straightener and fine wire mesh for generating small uniform turbulence before being uniformly accelerated to the test section inlet. For the forced convection cases, a blower is placed on the outlet of the wind tunnel for drawing the fluid through the test section. For the natural convection cases the connecting baffle between the test section outlet and blower was removed and the blower was not turned on.

The RoBuT facility was designed with a 12 in. $\times$ 12 in. (0.3048 m $\times$ 0.3048 m) cross-sectional test section that is 2 m in length. A test section was designed and constructed to match this

constraint. A fuel rod bundle model was designed to mimic the physics present in a prototypical fuel rod bundle while still allowing for instrumentation necessary to measure all relevant boundary conditions for CFD validation. Four fuel rods were constructed of 6061-T6 aluminum in two halves to allow for internal placement of thermocouples and to maintain a smooth outer surface. The two halves were then bolted together and the surface was nickel plated in order to reduce emitted radiation and prevent the oxidation of the aluminum surfaces. Cartridge heaters were placed inside four rod sections which were bolted together to form a full length rod. The thermocouple and electrical were routed outside the test section to the data acquisition system via aluminum conduit. Grid spacers with triangular swirl elements were constructed of 4130 carbon steel and placed inside the test section to maintain spacing between the rods as well as mimic the swirl elements present in commercially produced rod bundles. Hemispherical caps were placed on the leading edge of the fuel rods and extended cones on the trailing edge of the rods in order to limit flow separation and the long time scale turbulent fluctuations that result from a blunt termination. The test section walls were also instrumented with thermocouples.

Stereoscopic PIV measurements were used to measure both the test section inlet velocity profile as well as all velocity SRQs measured in the fuel rod bundle at steady-state. Stereoscopic PIV uses two cameras that acquire images simultaneously to measure all three components of velocity in a single laser plane. All PIV images were acquired and processed using the DaVis PIV suite [57]. Uncertainties for all measured and derived quantities are reported for comparison to CFD simulations.

All boundary conditions and system response quantities are available for use by any research group wishing to assess the accuracy of their CFD models and are available for download at the USU Digital Commons. While specifically designed for validation of the nuclear fuel life cycle, these benchmark experiments are also useful for general modeling of free convection which to the present time has been unavailable. A description of the files and their contents is found in Appendix A.

REFERENCES

[1] Warner, S. O. and Smith, B. L., "Autocorrelation-Based Estimate of Particle Image Density for Diffraction Limited Particle Images," *Measurement Science and Technology*, Vol. 25, No. 6, Apr 2014, pp. 065201. doi:10.1088/0957-0233/25/6/065201.

[2] Karoutas, Z., Gu, C.-Y., and Shölin, B., "3-D Flow Analyses for Design of Nuclear Fuel Spacer," *7th International Meeting on Nuclear Reactor Thermal-Hydraulics NURETH-7*, 1995, pp. 3153–3174.

[3] Navarro, M. A. and Santos, A. A. C., "Numerical Evaluation of Flow Through a 5×5 PWR Rod Bundle: Effect of the Vane Arrangement in a Spacer Grid," *International Nuclear Atlantic Conference - INAC 2009*, Rio de Janeiro, Brazil, Sep 2009.

[4] AIAA, *Guide for the Verification and Validation of Computational Fluid Dynamics Simulations*, Vol. G-077-1998, AIAA, 1998. doi:10.1016/S0306-4379(01)00039-4.

[5] Oberkampf, W. L. and Roy, C. J., *Verification and Validation in Scientific Computing*, Cambridge University Press, 2010.

[6] Incropera, F. P., Dewitt, D. P., Bergman, T. L., and Lavine, A. S., *Fundamentals of Heat and Mass Transfer*, John Wiley & Sons, Inc., 6th ed., 2006.

[7] Kays, W., Crawford, M., and Weigand, B., *Convective Heat and Mass Transfer*, McGraw-Hill Higher Education, Boston, Massachusetts, 4th ed., 2005.

[8] Davis, L. P. and Perona, J. J., "Development of Free Convection Axial Flow Through a Tube Bundle," *International Journal of Heat and Mass Transfer*, Vol. 16, No. 7, July 1973, pp. 1425–1438. doi:10.1016/0017-9310(73)90149-X.

[9] Keyhani, M., Kulacki, F. A., and Christensen, R. N., "Experimental Investigation of Free Convection in a Vertical Rod Bundle–A General Correlation for Nusselt Numbers," *Journal of Heat Transfer*, Vol. 107, No. 3, 1985, pp. 611–623. doi:10.1115/1.3247468.

[10] Arya, M. S. and Keyhani, M., "Convection Heat Transfer in a Sealed Vertical Storage Cask Containing Spent-Fuel Canisters," *Nuclear Science and Engineering*, Vol. 105, No. 4, 1989, pp. 391–403.

[11] Canaan, R. E., *Natural Convection Heat Transfer within Horizontal Spent Nuclear Fuel Assemblies*, PhD Dissertation, The University of Texas at Austin, 1995.

[12] Haldar, S. C., Mohanty, A. K., and Dubey, M. R., "Laminar Free Convection in Open-Ended Vertical 7-Rod Bundles: Experiments and Porous Model," *Nuclear Engineering and Design*, Vol. 198, No. 3, 2000, pp. 295–305. doi:10.1016/S0029-5493(00)00225-9.

[13] Krishna, D. J., Thansekhar, M. R., Venkateshan, S. P., Basak, T., and Das, S. K., "Natural Convection in a Partially Heat Generating Rod Bundle Inside an Enclosure," *Journal of Heat Transfer*, Vol. 132, No. 10, 2010, pp. 1–11. doi:10.1115/1.4001610.

[14] Yao, S. C., Hochreiter, L. E., and Leech, W. J., "Heat-Transfer Augmentation in Rod Bundles Near Grid Spacers," *Journal of Heat Transfer*, Vol. 104, No. 1, 1982, pp. 76–81. doi:10.1115/1.3245071.

[15] Durbin, S., Lindgren, E., and Zighb, A., "Measurements of Laminar Velocity Profiles in a Prototypic PWR Fuel Assembly," *Computational Fluid Dynamics (CFD) for Nuclear Reactor Safety Applications CFD4NRS-3*, Bethesda, Maryland, USA, 2010.

[16] Hille, D., Schrödel, B., Ganzmann, I., and Schmidt, H., "PIV (Particle Image Velocimetry) Measurements for Detection of the Cross Flow Distrbution Downstream of 5×5 Test Spacer Grids," *The 15th International Topical Meeting on Nuclear Reactor Thermal-Hydraulics, NURETH-15*, 2013.

[17] Ylönen, A. and Prasser, H. M., "Flow Mixing Experiments with Spacer Grids in a 4×4 Rod Bundle," *The 15th International Topical Meeting on Nuclear Reactor Thermal-Hydraulics, NURETH-15*, 2013.

[18] Hutli, E., Gottlasz, V., Tar, D., Ezsol, G., and Baranyai, G., "Experimental Approach to Investigate the Dynamics of Mixing Coolant Flow in Complex Geometry Using PIV and PLIF Techniques," *Thermal Science*, Vol. 19, No. 3, 2015, pp. 989–1004. doi:10.2298/TSCI130603051H.

[19] Song, K.-N., Lee, S.-B., and Lee, S.-H., "Performance Evaluation of New Spacer Grid Shapes for PWRs," *Nuclear Engineering and Technology*, Vol. 39, No. 6, Dec 2007, pp. 737–746.

[20] U.S. Department of Defense, *Verification, Validation and Accreditation (VV&A) Recommended Practices Guide*, Defense Modeling and Simulation Office, Office of the Director of Defense Research and Engineering, Nov 1996.

[21] ASME, *Standard for Verification and Validation in Computational Fluid Dynamics and Heat Transfer*, American Society of Mechanical Engineers, 2009.

[22] Oberkampf, W. L. and Smith, B., "Assessment Criteria for Computational Fluid Dynamics Validation Benchmark Experiments," *52nd Aerospace Sciences Meeting*, Vol. 205, American Institute of Aeronautics and Astronautics, Reston, Virginia, Jan 2014, pp. 1–27. doi:10.2514/6.2014-0205.

[23] Roache, P. J., *Fundamentals of Verification and Validation*, Hermosa Publishing, 2009.

[24] Oberkampf, W. L. and Trucano, T. G., "Validation Methodology in Computational Fluid Dynamics," *Fluids 2000*, AIAA, 2000.

[25] Oberkampf, W. L. and Trucano, T. G., *Verification and Validation in Computational Fluid Dynamics*, Cambridge University Press, 2002. doi:10.1016/S0376-0421(02)00005-2.

[26] Oberkampf, W. L. and Barone, M. F., "Measures of Agreement Between Computation and Experiment: Validation Metrics," *Journal of Computational Physics*, Vol. 217, No. 1, 2006, pp. 5–36. doi:10.1016/j.jcp.2006.03.037.

[27] De Vahl Davis, G., "Natural Convection of Air in a Square Cavity: A Benchmark Numerical Solution," *International Journal for Numerical Methods in Fluids*, Vol. 3, No. 3, May 1983, pp. 249–264. doi:10.1002/fld.1650030305.

[28] Leong, W., Hollands, K., and Brunger, A., "On a Physically-Realizable Benchmark Problem in Internal Natural Convection," *International Journal of Heat and Mass Transfer*, Vol. 41, No. 23, Dec 1998, pp. 3817–3828. doi:10.1016/s0017-9310(98)00095-7.

[29] Leong, W. H., Hollands, K. G. T., and Brunger, A. P., "Experimental Nusselt Numbers for a Cubical-Cavity Benchmark Problem in Natural Convection," *International Journal of Heat and Mass Transfer*, Vol. 42, No. 11, Jun 1999, pp. 1979–1989. doi:10.1016/s0017-9310(98)00299-3.

[30] Mamun, M. A. H., Leong, W. H., Hollands, K. G. T., and Johnson, D. A., "Cubical-Cavity Natural-Convection Benchmark Experiments: An Extension," *International Journal of Heat and Mass Transfer*, Vol. 46, No. 19, Sep 2003, pp. 3655–3660. doi:10.1016/s0017-9310(03)00155-8.

[31] Ampofo, F. and Karayiannis, T., "ExperimentalBenchmark Data for Turbulent Natural Convection in an Air Filled Square Cavity," *International Journal of Heat and Mass Transfer*, Vol. 46, No. 19, Sep 2003, pp. 3551–3572. doi:10.1016/s0017-9310(03)00147-9.

[32] Betts, P. L. and Bokhari, I. H., "Experiments on Turbulent Natural Convection in an Enclosed Tall Cavity," *International Journal of Heat and Fluid Flow*, Vol. 21, No. 6, Dec 2000, pp. 675–683. doi:10.1016/s0142-727x(00)00033-3.

[33] Tian, Y. and Karayiannis, T., "Low Turbulence Natural Convection in an Air Filled Square Cavity," *International Journal of Heat and Mass Transfer*, Vol. 43, No. 6, Mar 2000, pp. 849–866. doi:10.1016/s0017-9310(99)00199-4.

[34] In, W. K., Oh, D. S., and Chun, T. H., "Flow Analysis for Optimum Design of Mixing Vane in a PWR Fuel Assembly," *Journal of the Korean Nuclear Society*, Vol. 33, No. 3, 2001, pp. 327–338.

[35] Cui, X.-Z. and Kim, K.-Y., "Three-Dimensional Analysis of Turbulent Heat Transfer and Flow Through Mixing Vane in a Subchannel of Nuclear Reactor," *Journal of Nuclear Science and Technology*, Vol. 40, No. 10, 2003, pp. 719–724. doi:10.1080/18811248.2003.9715412.

[36] Liu, B., Knott, R., Young, M., Paramonov, D., Smith III, D. L., Conner, M., and Karoutas, Z., "CFD Approach for Investigating Flow and Heat Transfer in PWR Fuel Assembly," *The 13th International Conference on Nuclear Engineering*, Vol. 38, American Society of Mechanical Engineers, 2005, p. 409.

[37] Tiftikçi, A., Ayhan, H., Kocar, C., and Sökmen, C. N., "Simulation of Spacer Grid with Mixing Vane on a Typical PWR Fuel Rod Bundle System Using Lattice-Boltzmann Method," *The 15th International Topical Meeting on Nuclear Reactor Thermal-Hydraulics, NURETH-15*, No. NURETH15-324, Pisa, Italy, May 2013.

[38] Keyhani, M. and Luo, L., "A Numerical Study of Convection Heat Transfer within Enclosed Horizontal Rod Bundles," *Nuclear Science and Engineering*, Vol. 119, No. 2, 1995, pp. 116–127.

[39] Keyhani, M. and Dalton, T., "Natural Convection Heat Transfer in Horizontal Rod-Bundle Enclosures," *Journal of Heat Transfer*, Vol. 118, No. 3, 1996, pp. 598–605. doi:10.1115/1.2822674.

[40] Ustinenko, V., Samigulin, M., Ioilev, A., Lo, S., Tentner, A., Lychagin, A., Razin, A., Girin, V., and Vanyukov, Y., "Validation of CFD-BWR, A New Two-Phase Computational Fluid Dynamics Model for Boiling Water Reactor Analysis," *OECD/NEA International Workshop on the Benchmarking of CFD Codes for Application to Nuclear Reactor Safety (CFD4NRS)*, 2006.

[41] Tentner, A., Pointer, W. D., Sofu, T., Weber, D., Lo, S., Splawski, A., and Approach, I., "Development and Validation of an Extended Two-Phase Boiling Flow in Reactor Fuel Assemblies," *International Congress on Advances in Nuclear Power Plants*, 2007, pp. 2682–2691.

[42] Smith III, L. D., Conner, M. E., Liu, B., Dzodzo, B., Paramonov, D. V., Beasley, D. E., Langford, H. M., and Holloway, M. V., "Benchmarking Computational Fluid Dynamics for Application to PWR Fuel," *10th International Conference on Nuclear Engineering*, Vol. 3, ASME, Arlington, Virginia, USA, Apr 2002. doi:10.1115/ICONE10-2247.

[43] Holloway, M. V., McClusky, H. L., Beasley, D. E., and Conner, M. E., "The Effect of Support Grid Features on Local, Single-Phase Heat Transfer Measurements in Rod Bundles," *Journal of Heat Transfer*, Vol. 126, No. 1, 2004, pp. 43–53. doi:10.1115/1.1643091.

[44] Conner, M. E., Smith III, L. D., Holloway, M. V., and Beasley, D. E., "Heat Transfer Coefficient Testing in Nuclear Fuel Rod Bundles with Mixing Vane Grids," *2005 Water Reactor Fuel Performance Meeting*, Oct 2005.

[45] Holloway, M. V., Conover, T. a., McClusky, H. L., Beasley, D. E., and Conner, M. E., "The Effect of Support Grid Design on Azimuthal Variation in Heat Transfer Coefficient for Rod Bundles," *Journal of Heat Transfer*, Vol. 127, No. 6, 2005, pp. 598–605. doi:10.1115/1.1863274.

[46] Conner, M. E. and Holloway, M. V., "Heat Transfer Coefficient Variations in Nuclear Fuel Rod Bundles," *2007 LWR Fuel Performance Meeting*, San Francisco, CA, Oct 2007.

[47] Holloway, M. V., Beasley, D. E., and Conner, M. E., "Single-Phase Convective Heat Transfer in Rod Bundles," *Nuclear Engineering and Design*, Vol. 238, No. 4, 2008, pp. 848–858. doi:10.1016/j.nucengdes.2007.08.003.

[48] Conner, M. E., Baglietto, E., and Elmahdi, A. M., "CFD Methodology and Validation for Single-Phase Flow in PWR Fuel Assemblies," *Nuclear Engineering and Design*, Vol. 240, No. 9, 2010, pp. 2088–2095. doi:10.1016/j.nucengdes.2009.11.031.

[49] Conner, M. E., Hassan, Y. A., and Dominguez-Ontiveros, E. E., "Hydraulic Benchmark Data for PWR Mixing Vane Grid," *Nuclear Engineering and Design*, Vol. 264, 2013, pp. 97–102. doi:10.1016/j.nucengdes.2012.12.001.

[50] National Instruments, *LabView Software ver. 14.0*, National Instruments, Austin, Texas, 2014.

[51] Harris, J. R., *A Computational Fluid Dynamics Validation Experiment for Forced and Mixed Convection on a Vertical Heated Plate*, PhD Dissertation, Utah State University, 2014.

[52] Lance, B. W., *Experimental Validation Data for CFD of Steady and Transient Mixed Convection on a Vertical Flat Plate*, PhD Dissertation, Utah State University, 2015.

[53] Wen, C.-D. and Mudawar, I., "Experimental Investigation of Emissivity of Aluminum Alloys and Temperature Determination Using Multispectral Radiation Thermometry (MRT) Algorithms," *Journal of Materials Engineering and Performance*, Vol. 11, No. October, 2002, pp. 551–562. doi:10.1361/105994902770343818.

[54] Gustavsen, A. and Berdahl, P., "Spectral Emissivity of Anodized Aluminum and the Thermal Transmittance of Aluminum Window Frames," *Nordic Journal of Building Physics*, Vol. 3, No. 1970, 2003, pp. 1–12.

[55] Westinghouse Electric Corporation, *The Westinghouse Pressurized Water Reactor Nuclear Power Plant*, Westinghouse Electric Corporation, Nuclear Operations Division, P.O. Box 355 Pittsburgh, Pennsylvania 15230, 1984.

[56] LaVision GmbH, *FlowMaster Product Manual, Item Number: 1105011-4*, LaVision GmbH, Anna-Vandenhoeck-Ring 19, D-37081 Göttingen, Germany, Mar 2015.

[57] LaVision GmbH, *DaVis Software ver. 8.2.3*, LaVision GmbH, Anna-Vandenhoeck-Ring 19, D-37081 Göttingen, Germany, Mar 2015.

[58] Smith, B. L. and Neal, D. R., *Handbook of Fluid Dynamics, Second Edition*, chap. 48, CRC PR Inc., 2nd ed., 2016.

[59] Raffel, M., Willert, C. E., and Kompenhans, J., *Particle Image Velocimetry: A Practical Guide*, Springer, Berlin, Germany, 3rd ed., 1998.

[60] Coleman, H. W. and Steele, W. G., *Experimentation, Validation, and Uncertainty Analysis for Engineers*, John Wiley and Sons, Hoboken, NJ, 3rd ed., 2009.

[61] Wieneke, B. and Prevost, R., *DIC Uncertainty Estimation from Statistical Analysis of Correlation Values*, Springer, 2014, pp. 125–136. doi:10.1007/978-3-319-00768-7_15.

[62] Wieneke, B. and Sciacchitano, A., "PIV Uncertainty Propagation," *The 11th International Symposium on Particle Image Velocimetry–PIV15*, Santa Barbara, CA, Sep 2015, p. 38.

[63] Neal, D. R. and Sciacchitano, A., "Collaborative Framework for PIV Uncertainty Quantification: The Experimental Database," *17th International Symposium on Applications of Laser Techniques to Fluid Mechanics*, Lisbon, Portugal, 2014. doi:10.1088/0957-0233/26/7/074003.

[64] Sciacchitano, A., Neal, D. R., Smith, B. L., Warner, S. O., Vlachos, P. P., Wieneke, B., and Scarano, F., "Collaborative Framework for PIV Uncertainty Quantification: Comparative Assessment of Methods," *Measurement Science and Technology*, Vol. 26, No. 7, 2015, pp. 1–15. doi:10.1088/0957-0233/26/7/074004.

[65] TSI Inc., *TSI IFA100 User's Manual*, St. Paul, MN.

[66] The MathWorks, Inc., *MATLAB Software ver. 8.5*, The MathWorks, Inc., Natick, Massachusetts, © 2015, The MathWorks, Inc. MATLAB and Simulink are registered trademarks of The MathWorks, Inc. See www.mathworks.com/trademarks for a list of additional trademarks.

Other product or brand names may be trademarks or registered trademarks of their respective holders.

[67] Tennekes, H. and Lumley, J. L., *A First Course in Turbulence*, MIT Press, 1972.

[68] James, J. F., *A Student's Guide to Fourier Transforms*, Cambridge University Press, Cambridge, UK, 3rd ed., 2011.

[69] Smith, B. L. and Neal, D. R., "How to Efficiently Sample Data for Computation of Statistics," *68th Annual Meeting of the APS Division of Fluid Dynamics*, Vol. 60, American Physical Society, Boston, MA, Nov 2015.

[70] Wilcox, D. C., *Turbulence Modeling for CFD*, Turbulence Modeling for CFD, DCW Industries, 3rd ed., 2006.

[71] Xu, D. and Chen, J., "Accurate Estimate of Turbulent Dissipation Rate using PIV Data," *Experimental Thermal and Fluid Science*, Vol. 44, No. 2013, September 2012, pp. 662âĂŞ672. doi:10.1016/j.expthermflusci.2012.09.006.

[72] Sharp, K. V., Kim, K. C., and Adrian, R., "Dissipation Estimation Around a Rushton Turbine using Particle Image Velocimetry," *Laser Techniques Applied to Fluid Mechanics: Selected Papers from the 9th International Symposium*, Jul 1998, pp. 337–354. doi:10.1007/978-3-642-56963-0_22.

[73] Sharp, K. V., Kim, K. C., and Adrian, R. J., "A Comparison of Dissipation Estimation Methods in a Stirred Tank Using Particle Image Velocimetry," *ASME/JSME Fluids Engineering Meeting*, Jul 1999.

[74] Sharp, K. V. and Adrian, R. J., "PIV Study of Small-Scale Flow Structure Around a Rushton Turbine," *AIChE Journal*, Vol. 47, No. 4, Apr 2001, pp. 766–778. doi:10.1002/aic.690470403.

[75] Micheletti, M., Baldi, S., Yeoh, S., Ducci, A., Papadakis, G., Lee, K., and Yianneskis, M., "On Spatial and Temporal Variations and Estimates of Energy Dissipation in Stirred Reactors," *Chemical Engineering Research and Design*, Vol. 82, No. 9, Sep 2004, pp. 1188–1198. doi:10.1205/cerd.82.9.1188.44172.

[76] Baldi, S. and Yianneskis, M., "On the Quantification of Energy Dissipation in the Impeller Stream of a Stirred Vessel from Fluctuating Velocity Gradient Measurements," *Chemical Engineering Science*, Vol. 59, No. 13, Jul 2004, pp. 2659–2671. doi:10.1016/j.ces.2004.03.021.

[77] Tanaka, T. and Eaton, J. K., "A Correction Method for Measuring Turbulence Kinetic Energy Dissipation Rate by PIV," *Exp Fluids*, Vol. 42, No. 6, apr 2007, pp. 893–902. doi:10.1007/s00348-007-0298-y.

[78] Versteeg, H. K. and Malalasekera, W., *An Introduction to Computational Fluid Dynamics: The Finite Volume Method*, Pearson Education Ltd., Harlow, England, 2nd ed., 2007.

[79] Pope, S. B., *Turbulent Flows*, Cambridge University Press, 2007.

[80] Churchill, S. W. and Chu, H. H., "Correlating Equations for Laminar and Turbulent Free Convection from a Vertical Plate," *International Journal of Heat and Mass Transfer*, Vol. 18, No. 11, Nov 1975, pp. 1323–1329. doi:10.1016/0017-9310(75)90243-4.

[81] Çengel, Y. and Boles, M., *Thermodynamics: An Engineering Approach*, McGraw-Hill Higher Education, 2008.

[82] Touloukian, Y. S., *Thermophysical Properties of Matter*, Purdue University. Thermophysical Properties Research Center., 1970.

APPENDICES

Appendix A

Data Download Information

Data files associated with these experiments have been uploaded to the Digital Commons at Utah State University for public download and use. The files can be found at the USU Digital Commons.

The geometry, boundary conditions and system response quantities are available in tabulated format. A solid model of the 'as-built' geometry is available as a Binary Stereolothography (`.STL`), Parasolid (`.x_t`), and as a STEP-File (`.stp`) under the name '`FuelRods_AsBuilt`' and also in the '`Geometry.zip`' file.

The boundary conditions and system response quantities for the 5 test cases considered are available individually as well as in `.zip` files beginning with the name of each case shown in Table 2.1. Each file is available as a Comma Separated Values (`.csv`) file with the heading of each column containing the variable name and units in square brackets. For example, a column labeled as '`W[m/s]`' contains values for the w-velocity component with units of m/s. Uncertainties for each value are presented with a preceding, lowercase 'u'. Thus the column '`uW[m/s]`' is the uncertainty of the w-velocity component with units of m/s. Similarly, the standard deviation is preceded by a lowercase 's', for example, '`sW[m/s]`' is the standard deviation of the w-velocity component with units of m/s.

The AmbientConditions.csv files contain tabulated data for the ambient air temperature, relative humidity and barometric pressure measurements. The fluid properties were calculated using psychrometric relationships presented in Appendix D. These files are presented in a different format than the other files with columns of 'Name', 'Symbol', 'Value', 'Uncertainty', and 'Units'. The uncertainty for each variable was calculated using the Taylor Series Method for uncertainty propagation and is presented at 95% confidence.

The column names contained in each of the boundary condition and system response quantity files correspond to the following variables in this study:

`X`	Location in the x-direction
`Y`	Location in the y-direction
`Z`	Location in the z-direction
`U`	Velocity component in the x-direction
`V`	Velocity component in the y-direction
`W`	Velocity component in the z-direction
`RSXX`	Normal Reynolds stress in the x-direction, $\overline{u'u'}$
`RSXY`	Reynolds shear stress in the xy-direction, $\overline{u'v'}$
`RSXZ`	Reynolds shear stress in the xz-direction, $\overline{u'w'}$
`RSYY`	Normal Reynolds stress in the y-direction, $\overline{v'v'}$
`RSYZ`	Reynolds shear stress in the yz-direction, $\overline{v'w'}$
`RSZZ`	Normal Reynolds stress in the z-direction, $\overline{w'w'}$
`dP`	Differential pressure, dP
`T`	Temperature, T
`TKE`	Turbulence kinetic energy, k
`mdot`	Mass flow rate, $\dot{m}$

The location of each of the system response velocity profiles is contained in the filename in units of mm. For example, the file '`Mixed700_ReynoldsStress_x-60,z825.csv`' contains the Reynolds stress profiles for the Mixed700 case in the y-direction at the $x = -0.06$ m and $z = 0.825$ m location. Likewise, the file '`Mixed700_Velocity_x-60,z825.csv`' contains

the velocity profiles for the Mixed700 case in the y-direction at the $x = -0.06$ m and $z = 0.825$ m location.

Appendix B

Velocity Results

B.1 Inlet Velocity Fields and Profiles

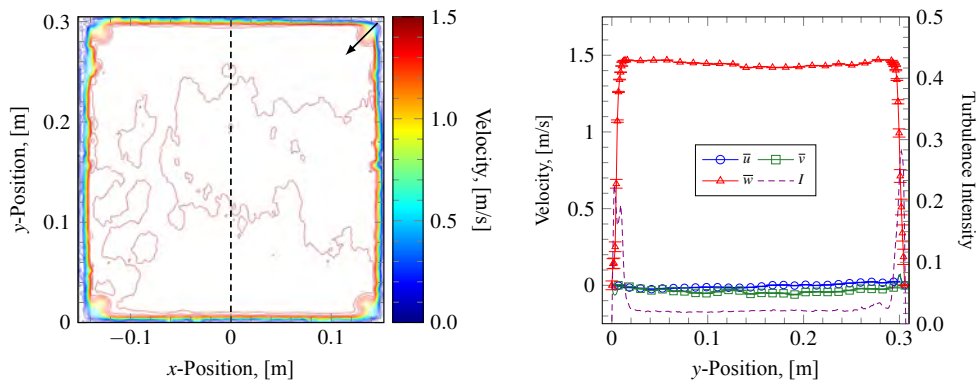

(a) (b)

Fig. B.1: Test section inflow velocity measurements for the Forced case. (a) Contour plot of the through plane velocity component. The first contour level begins at 0 m/s and the increment is 0.075 m/s. The arrow indicates increasing contour levels and the dashed line represents the location of the line profile. (a) Velocity profiles of the centerline ($x = 0$ m). The velocity used for calculating turbulence intensity was 1.3188 m/s.

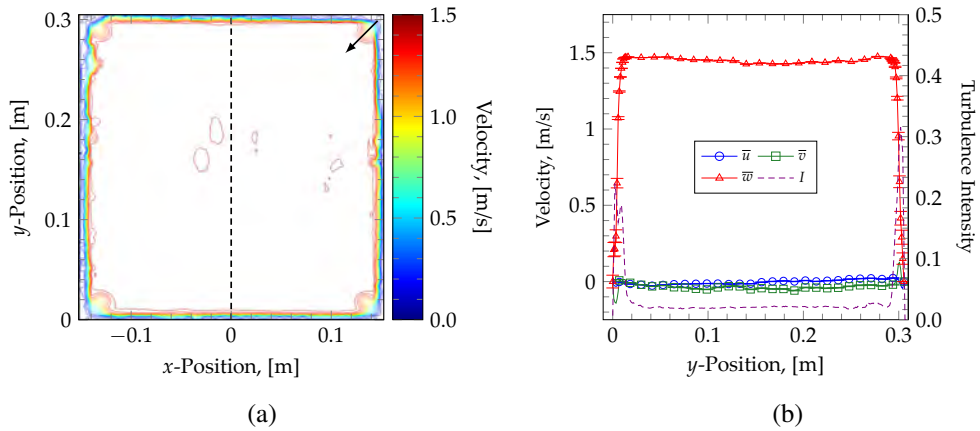

(a) (b)

Fig. B.2: Test section inflow velocity measurements for the Mixed400 case. (a) Contour plot of the through plane velocity component. The first contour level begins at 0 m/s and the increment is 0.075 m/s. The arrow indicates increasing contour levels and the dashed line represents the location of the line profile. (a) Velocity profiles of the centerline ($x = 0$ m). The velocity used for calculating turbulence intensity was 1.3239 m/s.

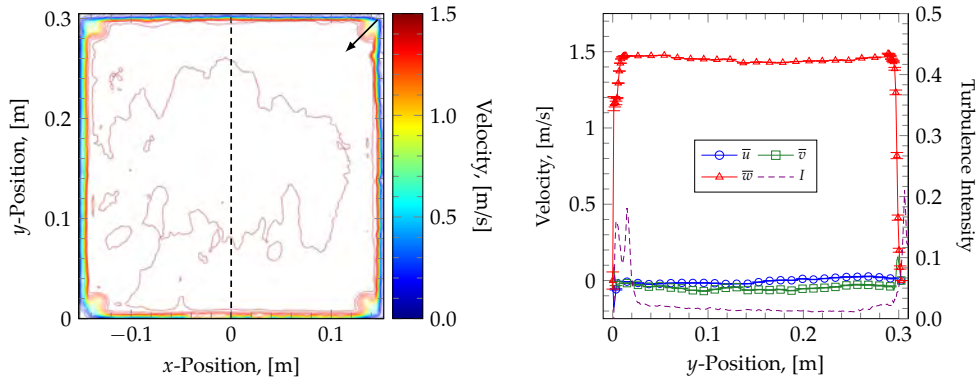

(a) (b)

Fig. B.3: Test section inflow velocity measurements for the Mixed700 case. (a) Contour plot of the through plane velocity component. The first contour level begins at 0 m/s and the increment is 0.075 m/s. The arrow indicates increasing contour levels and the dashed line represents the location of the line profile. (a) Velocity profiles of the centerline ($x = 0$ m). The velocity used for calculating turbulence intensity was 1.3564 m/s.

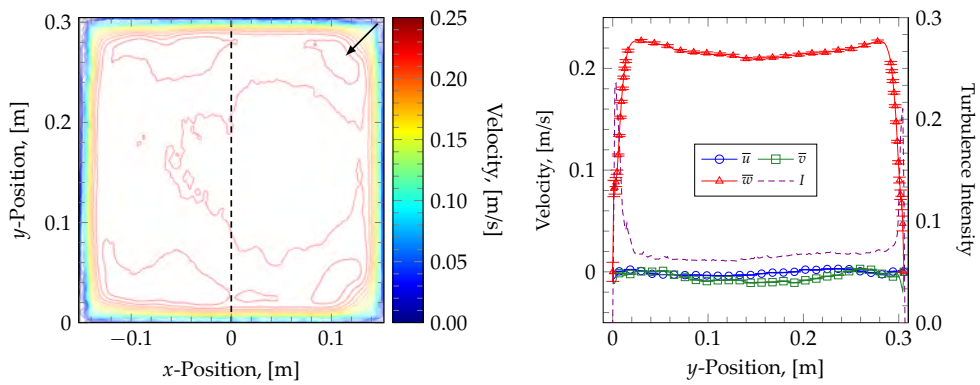

(a) (b)

Fig. B.4: Test section inflow velocity measurements for the Natural400 case. (a) Contour plot of the through plane velocity component. The first contour level begins at 0 m/s and the increment is 0.0125 m/s. The arrow indicates increasing contour levels and the dashed line represents the location of the line profile. (a) Velocity profiles of the centerline ($x = 0$ m). The velocity used for calculating turbulence intensity was 0.1956 m/s.

B.2 SRQ Velocity Profiles

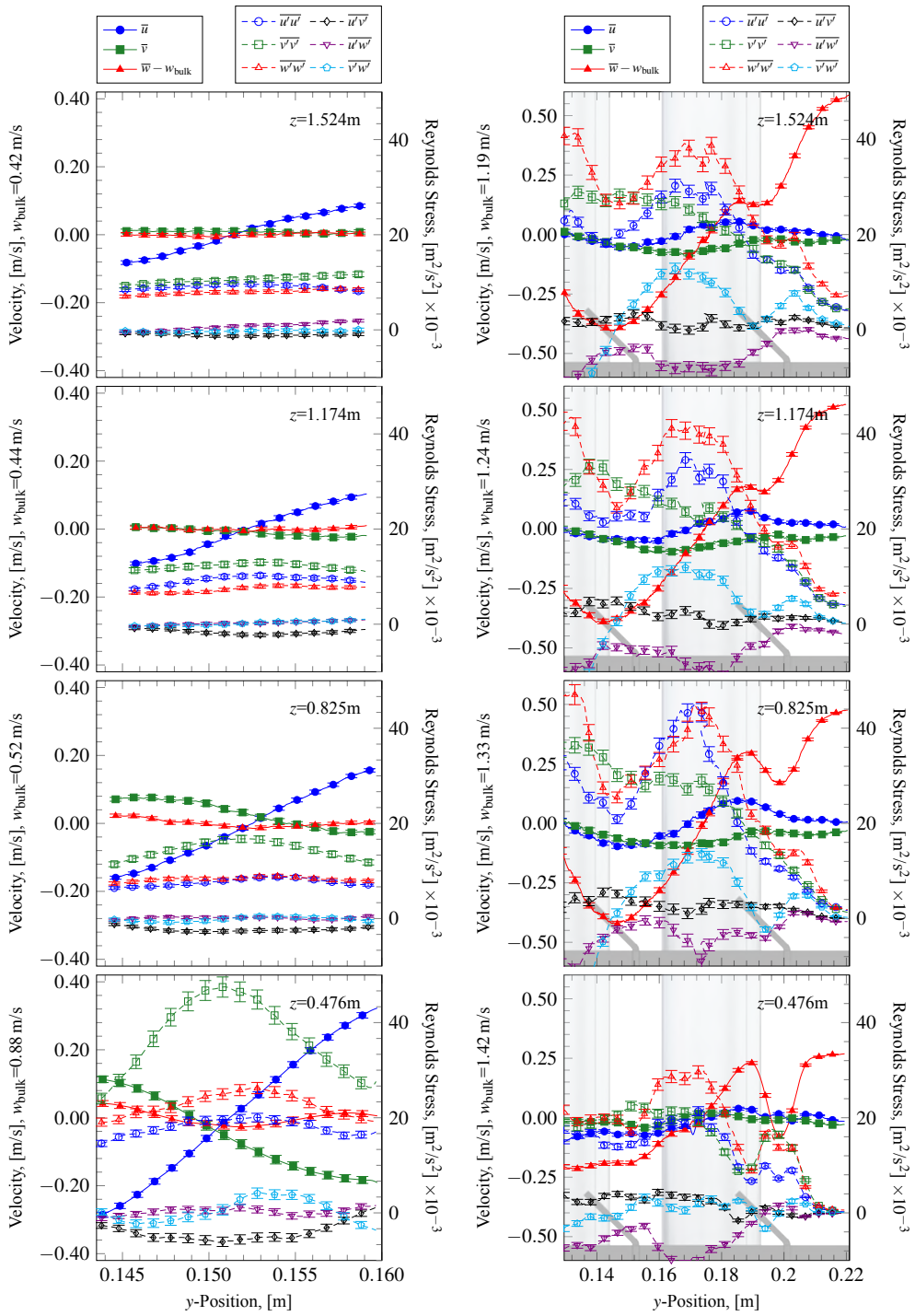

(a) (b)

Fig. B.5: Velocity profile along y-direction for (a) $x = 0$ m and (b) $x = -0.06$ m at four z-positions indicated on each plot for the forced case. The inner edges of the fuel rods are aligned with the y-axes on the $x = 0$ m. The relative locations of the swirl elements in the y-position (not to scale in z) are shown in the background of the $x = -0.06$ m figure.

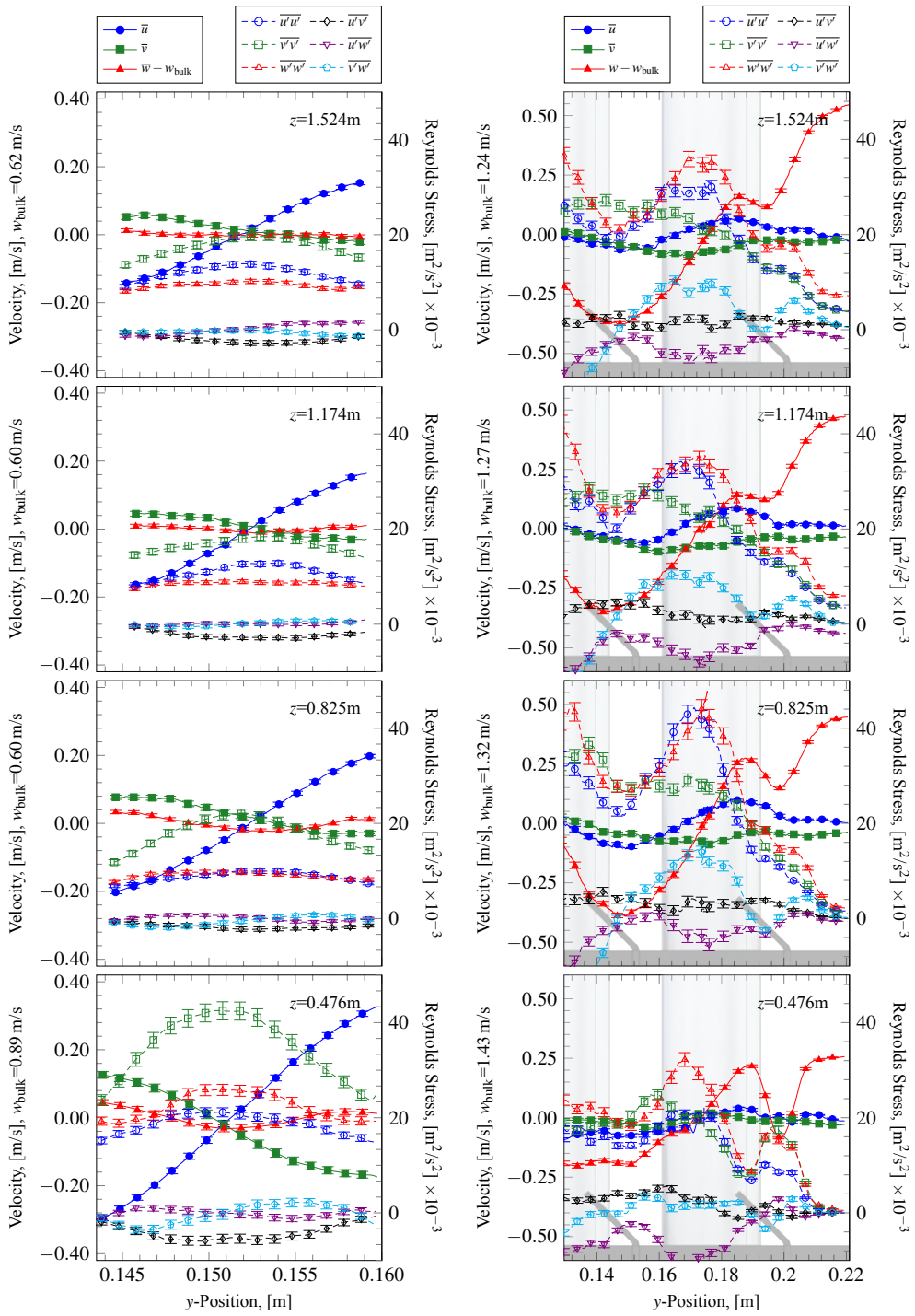

(a) (b)

Fig. B.6: Velocity profile along y-direction for (a) $x = 0$ m and (b) $x = -0.06$ m at four z-positions indicated on each plot for the Mixed400 case. The inner edges of the fuel rods are aligned with the y-axes on the $x = 0$ m. The relative locations of the swirl elements in the y-position (not to scale in z) are shown in the background of the $x = -0.06$ m figure.

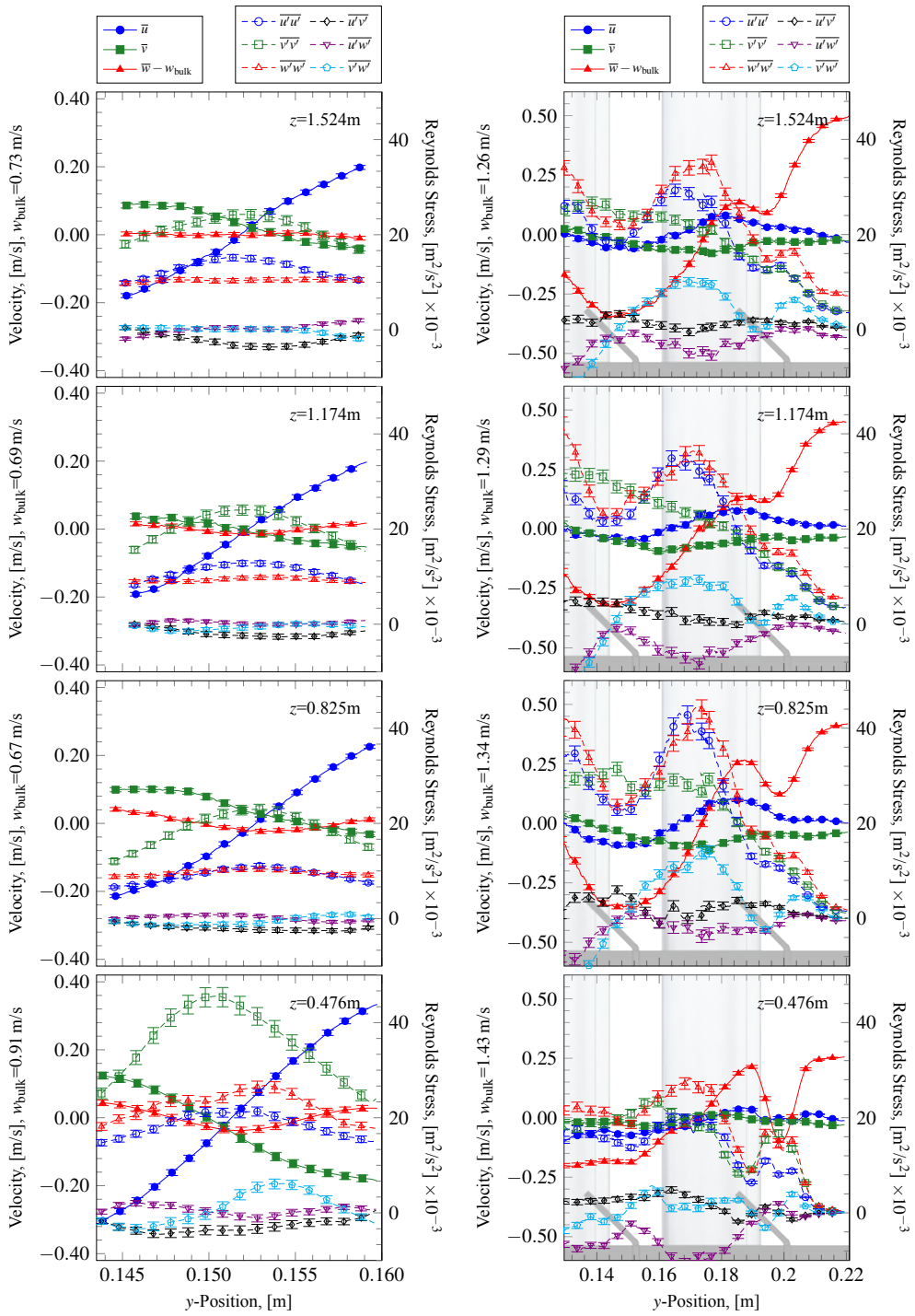

(a) (b)

Fig. B.7: Velocity profile along y-direction for (a) $x = 0$ m and (b) $x = -0.06$ m at four z-positions indicated on each plot for the Mixed700 case. The inner edges of the fuel rods are aligned with the y-axes on the $x = 0$ m. The relative locations of the swirl elements in the y-position (not to scale in z) are shown in the background of the $x = -0.06$ m figure.

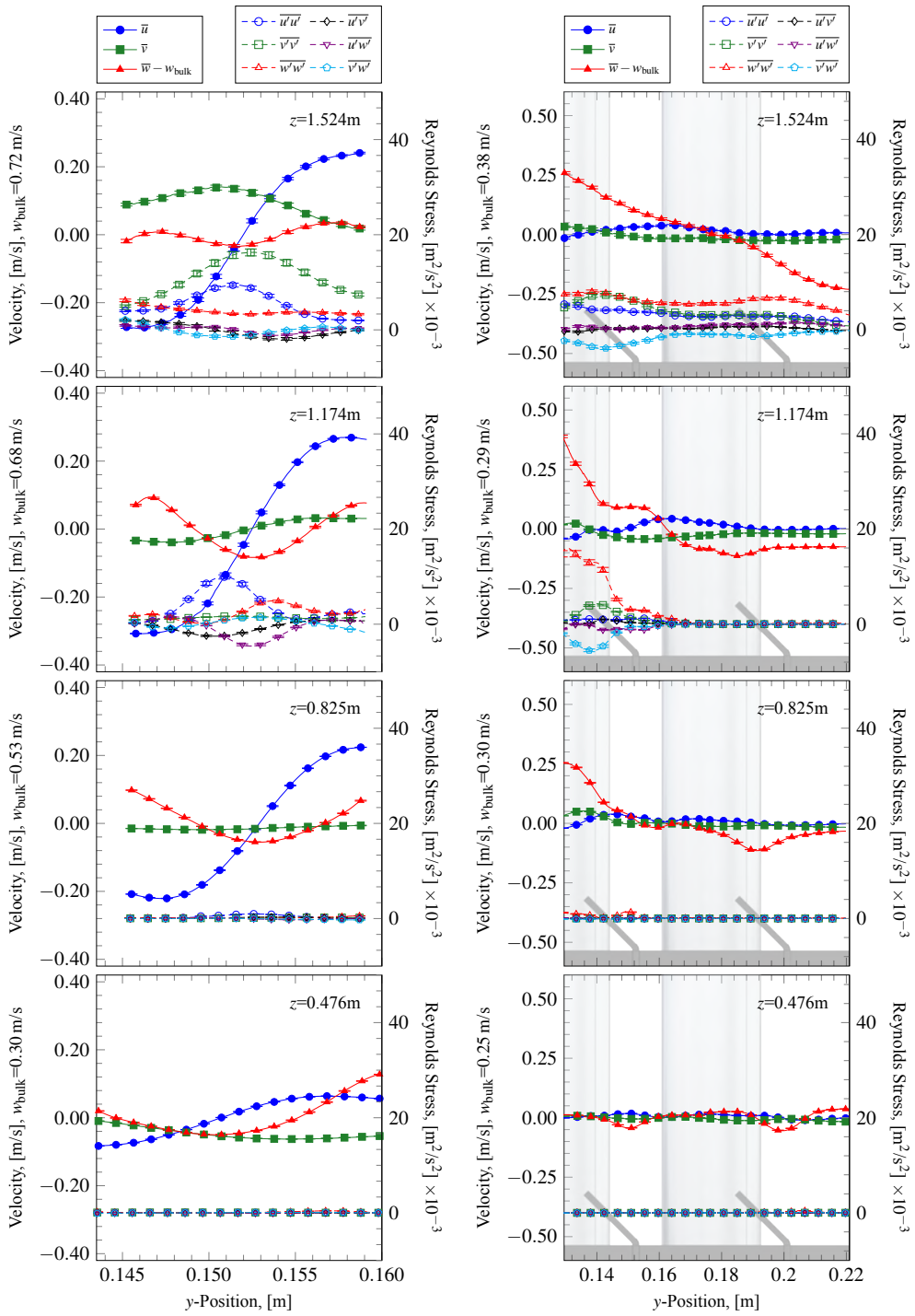

(a) (b)

Fig. B.8: Velocity profile along y-direction for (a) $x = 0$ m and (b) $x = -0.06$ m at four z-positions indicated on each plot for the Natural400 case. The inner edges of the fuel rods are aligned with the y-axes on the $x = 0$ m. The relative locations of the swirl elements in the y-position (not to scale in z) are shown in the background of the $x = -0.06$ m figure.

Appendix C

Uncertainties

The use of different instruments for measuring length resulted in two uncertainties for all length measurements. Lengths and diameter measurements under 32mm have a measurement uncertainty of 0.03mm and lengths larger than 32mm have a measurement unceertainty of 2mm.

Uncertainties for individual velocity measurements, differential pressure and temperature measurements are reported with the measurement. Uncertainties for ambient temperature measurement is 0.6°C. Uncertainty for relative humidity is 2.5%. Uncertainty for atmospheric pressure is 1.5% of measurement. The facility control system maintained the ambient temperature at 20°C $\pm$ 0.5°C. Uncertainties of derived quantities are propagated using the Taylor Series method described by Coleman and Steele [60] and as presented in Appendix D.

Appendix D

Uncertainty Analysis

The following equations were used for determining the air properties of the fluid entering the test section during this study. From psychrometrics [81], the saturation pressure of water, P_{sat}, is defined as

$$P_{\text{sat}}(T) = \exp\left(\frac{77.3450 + 0.0057T - 7235/T}{T^{8.2}}\right) \tag{D.1}$$

where T is the fluid temperature. The vapor pressure of humid air is then defined as

$$P_v = \phi \cdot P_{\text{sat}} \tag{D.2}$$

where ϕ is the relative humidity. It then follows that the partial pressure of dry air, P_d, is

$$P_d = P_{\text{atm}} - P_v \tag{D.3}$$

where P_{atm} is the measured air pressure. Finally, the density of moist air is

$$\rho = \frac{P_d}{R_d T} + \frac{P_v}{R_v T} \tag{D.4}$$

where R_d is the gas constant for dry air and R_v is the gas constant for water vapor. The Taylor series propagation then follows as

$$U_\rho^2 = U_{P_d}^2\left(\frac{\partial\rho}{\partial P_d}\right)^2 + U_{R_d}^2\left(\frac{\partial\rho}{\partial R_d}\right)^2 + U_{P_v}^2\left(\frac{\partial\rho}{\partial P_v}\right)^2 + U_{R_v}^2\left(\frac{\partial\rho}{\partial R_v}\right)^2 + U_T^2\left(\frac{\partial\rho}{\partial T}\right)^2, \tag{D.5}$$

$$U_{P_d}^2 = U_{P_{\text{atm}}}^2\left(\frac{\partial P_d}{\partial P_{\text{atm}}}\right)^2 + U_{P_v}^2\left(\frac{\partial P_d}{\partial P_v}\right)^2, \tag{D.6}$$

$$U_{P_v}^2 = U_\phi^2\left(\frac{\partial P_v}{\partial \phi}\right)^2 + U_{P_{\text{sat}}}^2\left(\frac{\partial P_v}{\partial P_{\text{sat}}}\right)^2, \tag{D.7}$$

$$U_{P_{\text{sat}}}^2 = U_T^2 \left(\frac{\partial P_{\text{sat}}}{\partial T} \right)^2 . \tag{D.8}$$

The absolute viscosity for air is determined using Sutherland's law

$$\mu = \frac{b\, T^{(3/2)}}{T + S_T} \tag{D.9}$$

where b is the Sutherland's law coefficient and S_T is Sutherland's temperature. And the uncertainty becomes

$$U_\mu^2 = U_T^2 \left(\frac{\partial \mu}{\partial T} \right)^2 . \tag{D.10}$$

The kinematic viscosity is define as

$$\nu = \frac{\mu}{\rho} \tag{D.11}$$

with the uncertainty written as

$$U_\nu^2 = U_\mu^2 \left(\frac{\partial \nu}{\partial \mu} \right)^2 + U_\rho^2 \left(\frac{\partial \nu}{\partial \rho} \right)^2 + 2 \left(\frac{\partial \nu}{\partial \mu} \right) \left(\frac{\partial \nu}{\partial \rho} \right) U_\mu U_\rho . \tag{D.12}$$

According to Volume 6 of Thermophysical Properties of Matter [82], the specific heat of air between 260 K and 610 K is calculated with a polynomial fit

$$c_p = 0.249679 - 7.55179 \times 10^{-5} \cdot T + 1.69194 \times 10^{-7} \cdot T^2 - 6.46128 \times 10^{-11} \cdot T^3 \tag{D.13}$$

in units of cal/g/K with temperature in K and is accurate to 0.01%. The thermal conductivity of air is determined through a linear interpolation of tabular data from Volume 3 of Thermophysical Properties of Matter [82] and is accurate to 4%. Thermal diffusivity is defined as

$$\alpha = \frac{k_f}{\rho\, c_p} \tag{D.14}$$

while the uncertainty is

$$U_\alpha^2 = U_{k_f}^2 \left(\frac{\partial \alpha}{\partial k_f} \right)^2 + U_\rho^2 \left(\frac{\partial \alpha}{\partial \rho} \right)^2 + U_{c_p}^2 \left(\frac{\partial \alpha}{\partial c_p} \right)^2 + . \tag{D.15}$$

The coefficient of thermal expansion is then approximated as

$$\beta = \frac{1}{T} \tag{D.16}$$

assuming air acts as an ideal gas and the uncertainty is

$$U_\beta^2 = U_T^2 \left(\frac{\partial \beta}{\partial T}\right)^2 \tag{D.17}$$

The Reynolds number, Re, is defined as

$$\mathrm{Re} = \frac{V D_h}{\nu} \tag{D.18}$$

where D_h is the hydraulic diameter and is defined as $D_h = 4A/P$ with A as the cross section area and P as the perimeter. The uncertainty is determined by

$$U_{\mathrm{Re}}^2 = U_V^2 \left(\frac{\partial \mathrm{Re}}{\partial V}\right)^2 + U_{D_h}^2 \left(\frac{\partial \mathrm{Re}}{\partial D_h}\right)^2 + U_\nu^2 \left(\frac{\partial \mathrm{Re}}{\partial \nu}\right)^2. \tag{D.19}$$

The local Grashof number, Gr_z, is defined as

$$\mathrm{Gr}_z = \frac{g\beta(T_s - T_m)z^3}{\nu^2} \tag{D.20}$$

where g is the acceleration due to gravity, T_s is the surface temperature, T_m is the mean fluid temperature, and z is the position in the flow-wise direction of the rods. The mead fluid temperature T_m is determined using an energy balance on a control volume extending from the wind tunnel inlet (downstream of the flow conditioner) and extending to the z-location where T_s is measured as described in Section 5.2.1. The uncertainty is then calculated as

$$\begin{aligned} U_{\mathrm{Gr}}^2 &= U_g^2 \left(\frac{\partial \mathrm{Gr}}{\partial g}\right)^2 + U_\beta^2 \left(\frac{\partial \mathrm{Gr}}{\partial \beta}\right)^2 + U_{T_s}^2 \left(\frac{\partial \mathrm{Gr}}{\partial T_s}\right)^2 + \ldots \\ & U_{T_m}^2 \left(\frac{\partial \mathrm{Gr}}{\partial T_m}\right)^2 + U_z^2 \left(\frac{\partial \mathrm{Gr}}{\partial z}\right)^2 + U_\nu^2 \left(\frac{\partial \mathrm{Gr}}{\partial \nu}\right)^2. \end{aligned} \tag{D.21}$$

The remaining derived variables used in this experiment can easily be determined by inspection and therefore will not be included here in the interest of brevity. The Matlab codes used to calculate the uncertainties are found in Appendix E and may be used as a guide should any questions arise.

Appendix E

Codes

E.1 Air Properties and Uncertainty Code

```
function [rho,mu,nu,cp,k,alpha,beta] = AirUncertainty(T,P,RH)
% Air Uncertainty is a function that will calculate the properties of air
% based on Temperature, Pressure and Relative Humidity along with the
% associated uncertainty of each.
% Input parameters:
%   NOTE: All input variables are two component vectors with the first component
%   being the variable istelf and the second term being the uncertainty of
%   that variable in the same units.
%   T  = Air temperature, [K]
%   P  = Air pressure, [Pa]
%   RH = Relative humidity of room, [%]

% Output parameters:
%   NOTE: All output variables are two component vectors with the first ...
    component
%   being the variable istelf and the second term being the uncertainty of
%   that variable in the same units.
%   rho   = Air Density, [kg/m^3]
%   mu    = Absolute (dynamic) Viscosity, [Pa-s]
%   nu    = Kinematic Viscosity, [m^2/s]
%   cp    = Specific Heat, [J/kg/K]
%   k     = Thermal Conductivity, [W/m/K]
%   alpha = Thermal Diffusivity, [m^2/s]
%   beta  = Thermal Expansion Coefficient, [1/K]

%Constants
Rair  = 8314.47/28.97;  %Gas Constant of Air, [J/K/kg]
uRair = 0;              %Assume negligible uncertainty of Rair
Rv    = 8314.47/18.02;  %Gas Constant of Water Vapor, [J/K/kg]
uRv   = 0;              %Assume negligible uncertainty of Rv
b     = 1.458*10^(-6);  %Sutherland's Law Coefficient, [kg/m/s/K^(1/2)]
S     = 110.4;          %Sutherland's Temperature, [K]

%Convert relative humidity from percentage
RH(1) = RH(1)/100;  RH(2) = RH(2)/100;

%Density for Humid Air
Psat       = exp( 77.3450+0.0057*(T(1))-7235/(T(1)) ) / ( (T(1))^8.2 ); ...
    %Saturation pressure, [Pa]
dPsat_dT   = (7235/T(1)^2+0.0057)*exp( 77.3450+0.0057*(T(1))-7235/(T(1)) ) / ...
    ( (T(1))^8.2 ) - ...
             8.2*exp( 77.3450+0.0057*(T(1))-7235/(T(1)) ) / ( (T(1))^9.2 );
```

```
uPsat      = T(2)*dPsat_dT;
Pv         = RH(1)*Psat;
dPv_dRH    = Psat;
dPv_dPsat  = RH(1);
uPv        = sqrt( (RH(2))^2*dPv_dRH^2 + uPsat^2*dPv_dPsat^2 );
Pd         = P(1)-Pv;
uPd        = sqrt( P(2)^2 + uPv^2 );
rho        = Pd/Rair/T(1) + Pv/Rv/T(1);
drho_dPd   = 1/Rair/T(1);
drho_dPv   = 1/Rv/T(1);
drho_dT    = -Pd/Rair/T(1)^2-Pv/Rv/T(1)^2;
drho_dRair = -Pd/Rair^2/T(1);
drho_dRv   = -Pv/Rv^2/T(1);
urho       = sqrt( uPd^2*drho_dPd^2 + uPv^2*drho_dPv^2 + T(2)^2*drho_dT^2 +...
                   uRair^2*drho_dRair^2 + uRv^2*drho_dRv^2 );

%Dynamic Viscosity Uncertainty
dmu_dT = ( (T(1)+S)*(3/2*b*T(1)^(1/2)) - b*T(1)^(3/2) )/( T(1)+S )^2;
mu     = b*T(1)^(3/2)/(T(1)+S); %Sutherlands Law
umu    = sqrt( T(2)^2*dmu_dT^2 );

%Kinematic Viscosity Uncertainty
dnu_dmu  = 1/rho;
dnu_drho = -mu/rho^2;
drho_dT  = -P(1)/Rair/T(1)^2;
dmu_dT   = 3/2*b*T(1)^0.5/(T(1)+S) - b*T(1)^1.5/(T(1)+S)^2;
umurho   = T(2)^2*dmu_dT*drho_dT;
nu       = mu/rho;
unu      = sqrt( umu^2*dnu_dmu^2 + urho^2*dnu_drho^2 + ...
    2*dnu_dmu*dnu_drho*umurho );

%Specific Heat
cp  = (0.249679 - 7.55179e-5.*T(1)+1.69194e-7.*T(1).^2-6.46128e-11.*T(1).^3);
cp  = cp*4183.99722; %cal/g/K to J/kg/K
ucp = 0.0001.*cp;

%Thermal Conductivity (Table Lookup) from Thermophysical Properties of Matter
%T [K], k [mW/cm/K]
ktable = [250,0.2226;
    260,0.2305;
    270,0.2384;
    280,0.2461;
    290,0.2538;
    300,0.2614;
    310,0.2687;
    320,0.2759;
    330,0.2830;
    340,0.2900;
    350,0.2970;
    360,0.3039;
    370,0.3107;
    380,0.3173;
    390,0.3239;
    400,0.3305;
    410,0.3371;
    420,0.3437;
```

```
    430,0.3503;
    440,0.3568;
    450,0.3633;
    460,0.3697;
    470,0.3761;
    480,0.3825;
    490,0.3888;
    500,0.3951];
ktable = [ktable(:,1),ktable(:,2)*0.1]; %Convert k units to [W/m/K]
k = interp1(ktable(:,1),ktable(:,2),T(1));
uk = 0.04*k;

%Thermal Diffusivity
alpha       = k/rho/cp;
dalpha_dk   = 1/rho/cp;
dalpha_drho = -k/rho^2/cp;
dalpha_dcp  = -k/rho/cp^2;
ualpha      = sqrt( uk^2*dalpha_dk^2 + urho^2*dalpha_drho^2 + ...
    ucp^2*dalpha_dcp^2 );

%Coefficient of Thermal Expansion
beta     = 1/T(1);
dbeta_dT =-1/T(1)^2;
ubeta    = sqrt( T(2)^2*dbeta_dT^2 );

%Combine terms for output
rho(2)   = urho;
mu(2)    = umu;
nu(2)    = unu;
cp(2)    = ucp;
k(2)     = uk;
alpha(2) = ualpha;
beta(2)  = ubeta;
```

E.2 Mass Flow Rate and Reynolds Number Code

```
clear all; close all;
if ispc; sl = '\'; else sl = '/'; end

%Get folder strings
codedir  = [pwd,sl];
cd ../..;
projdir  = [pwd,sl];
cd(codedir);
codesdir = [projdir,'Codes',sl];
addpath(codesdir);

propdir  = [projdir,'Room Measurements',sl];
flowcase = {'Forced';'Mixed400';'Mixed700';'Natural400';'Natural700'};
avename  = 'B00001_AvgV.vc7';
stdname  = 'B00002_StdevV.vc7';
tkename  = 'B00002_TurbKineticE.im7';
rmname   = 'RoomMeasurements.txt';
```

```
date     = {'15-10-08';'15-10-08';'15-10-20';'15-10-09';'15-10-09'};
time     = {'11:06 AM';'4:03 PM';'11:58 AM';'2:23 PM';'11:00 AM'};

for c=1:length(flowcase)
    clear Tarray uTarray T1 uT1 im_mean im_stdv x0_prof x0_tke;

    %Get temperature, pressure and humidity data
    fid = fopen([propdir,'Meas_',date{c},'_0000.lvm']);
    temp = textscan(fid,'%f %f %f %f %f %s %s','Headerlines',23);
    for i=1:size(temp{1,1},1)
        temp{1,6}(i) = strcat(temp{1,6}(i),{' '},temp{1,7}(i));
    end
    ind = find(strcmpi(temp{1,6},time{c})==1,1);

    %Inflow properties
    Tamb  = temp{1,2}(ind)+273;     %K
    Patm  = temp{1,4}(ind)*1000;    %Pa
    RH    = temp{1,3}(ind);         %Percent
    DP    = temp{1,5}(ind)+273;     %K
    uRH   = 0.025*Tamb;             %Percent
    uPatm = 0.015*Patm;             %Pa
    uTamb = 0.6;                    %degC
    clear temp;

    %Calculate Air Properties
    [temp1,temp2,temp3,temp4,temp5,temp6,temp7] = ...
        AirUncertainty([Tamb,uTamb],[Patm,uPatm],[RH,uRH]);
    rho   = temp1(1); urho   = temp1(2);
    mu    = temp2(1); umu    = temp2(2);
    nu    = temp3(1); unu    = temp3(2);
    cp    = temp4(1); ucp    = temp4(2);
    k     = temp5(1); uk     = temp5(2);
    alpha = temp6(1); ualpha = temp6(2);
    beta  = temp7(1); ubeta  = temp7(2);

    %Read in vector fields
    im_mean   = readimx([flowcase{c},sl,avename]);
    im_stdv   = readimx([flowcase{c},sl,stdname]);
    im_tke    = readimx([flowcase{c},sl,tkename]);
    NX        = size(im_mean.Frames{1}.Components{1}.Planes{1},1);
    NY        = size(im_mean.Frames{1}.Components{1}.Planes{1},2);
    CompNames = im_mean.Frames{1,1}.ComponentNames;
    ScaleX    = [im_mean.Frames{1}.Scales.X.Slope, ...
        im_mean.Frames{1}.Scales.X.Offset, im_mean.Frames{1}.Grids.X];
    ScaleY    = [im_mean.Frames{1}.Scales.Y.Slope, ...
        im_mean.Frames{1}.Scales.Y.Offset, im_mean.Frames{1}.Grids.Y];
    ScaleZ    = [im_mean.Frames{1}.Scales.Z.Slope, ...
        im_mean.Frames{1}.Scales.Z.Offset, im_mean.Frames{1}.Grids.Z];
    X   = (ScaleX(1)*(0:NX-1)*ScaleX(3)+ScaleX(2))/1000;
    Y   = (ScaleY(1)*(0:NY-1)*ScaleY(3)+ScaleY(2))/1000;
    Vx  = im_mean.Frames{1}.Components{ 1}.Planes{1}' * ...
        im_mean.Frames{1}.Components{ 1}.Scale.Slope + ...
        im_mean.Frames{1}.Components{ 1}.Scale.Offset;
    Vy  =-im_mean.Frames{1}.Components{ 2}.Planes{1}' * ...
        im_mean.Frames{1}.Components{ 2}.Scale.Slope + ...
        im_mean.Frames{1}.Components{ 2}.Scale.Offset;
```

```
Vz  = im_mean.Frames{1}.Components{ 5}.Planes{1}' * ...
    im_mean.Frames{1}.Components{ 5}.Scale.Slope + ...
    im_mean.Frames{1}.Components{ 5}.Scale.Offset;
Uvx = im_mean.Frames{1}.Components{ 8}.Planes{1}' * ...
    im_mean.Frames{1}.Components{ 8}.Scale.Slope + ...
    im_mean.Frames{1}.Components{ 8}.Scale.Offset;
Uvy = im_mean.Frames{1}.Components{ 9}.Planes{1}' * ...
    im_mean.Frames{1}.Components{ 9}.Scale.Slope + ...
    im_mean.Frames{1}.Components{ 9}.Scale.Offset;
Uvz = im_mean.Frames{1}.Components{10}.Planes{1}' * ...
    im_mean.Frames{1}.Components{10}.Scale.Slope + ...
    im_mean.Frames{1}.Components{10}.Scale.Offset;
Sx  = im_stdv.Frames{1}.Components{ 1}.Planes{1}' * ...
    im_stdv.Frames{1}.Components{ 1}.Scale.Slope + ...
    im_stdv.Frames{1}.Components{ 1}.Scale.Offset;
Sy  =-im_stdv.Frames{1}.Components{ 2}.Planes{1}' * ...
    im_stdv.Frames{1}.Components{ 2}.Scale.Slope + ...
    im_stdv.Frames{1}.Components{ 2}.Scale.Offset;
Sz  = im_stdv.Frames{1}.Components{ 5}.Planes{1}' * ...
    im_stdv.Frames{1}.Components{ 5}.Scale.Slope + ...
    im_stdv.Frames{1}.Components{ 5}.Scale.Offset;

NXTKE = size(im_tke.Frames{1}.Components{1}.Planes{1},1);
NYTKE = size(im_tke.Frames{1}.Components{1}.Planes{1},2);
XTKE  = (im_tke.Frames{1}.Scales.X.Slope * (0:NXTKE-1) * ...
    im_tke.Frames{1}.Grids.X + im_tke.Frames{1}.Scales.X.Offset)/1000;
YTKE  = (im_tke.Frames{1}.Scales.Y.Slope * (0:NXTKE-1) * ...
    im_tke.Frames{1}.Grids.Y + im_tke.Frames{1}.Scales.Y.Offset)/1000;
TKE   = im_tke.Frames{1}.Components{1}.Planes{1}' * ...
    im_tke.Frames{1}.Components{1}.Scale.Slope + ...
    im_tke.Frames{1}.Components{1}.Scale.Offset;
uTKE  = im_tke.Frames{1}.Components{3}.Planes{1}' * ...
    im_tke.Frames{1}.Components{3}.Scale.Slope + ...
    im_tke.Frames{1}.Components{3}.Scale.Offset;

%Crop out zeroes on edges of image
crop   = 0;
left   = find(sum(Vz,1)~=0,1)-1+crop;
right  = size(Vz,2)-find(fliplr(sum(Vz,1))~=0,1)+1-crop;
top    = find(sum(Vz,2)~=0,1)-1+crop;
bottom = size(Vz,1)-find(flipud(sum(Vz,2))~=0,1)+1-crop;
ybnd   = left:right;
xbnd   = top:bottom;
X      = X(ybnd);
Y      = Y(xbnd);
Vx     = Vx(xbnd,ybnd); Vx(1,:)=0; Vx(:,1)=0; Vx(end,:)=0; Vx(:,end)=0;
Vy     = Vy(xbnd,ybnd); Vy(1,:)=0; Vy(:,1)=0; Vy(end,:)=0; Vy(:,end)=0;
Vz     = Vz(xbnd,ybnd); Vz(1,:)=0; Vz(:,1)=0; Vz(end,:)=0; Vz(:,end)=0;
Uvx    = Uvx(xbnd,ybnd);
Uvy    = Uvy(xbnd,ybnd);
Uvz    = Uvz(xbnd,ybnd);
Sx     = Sx(xbnd,ybnd);
Sy     = Sy(xbnd,ybnd);
Sz     = Sz(xbnd,ybnd);
dx     = X(2)-X(1);
udx    = 0.0001;
```

```
    left   = find(sum(TKE,1)~=0,1)-1+crop;
    right  = size(TKE,2)-find(fliplr(sum(TKE,1))~=0,1)+1-crop;
    top    = find(sum(TKE,2)~=0,1)-1+crop;
    bottom = size(TKE,1)-find(flipud(sum(TKE,2))~=0,1)+1-crop;
    ybnd   = left:right;
    xbnd   = top:bottom;
    XTKE   = XTKE(ybnd);
    YTKE   = YTKE(xbnd);
    TKE    = TKE(xbnd,ybnd)'; TKE(1,:)=0; TKE(:,1)=0; TKE(end,:)=0; ...
        TKE(:,end)=0;
    uTKE   = uTKE(xbnd,ybnd)';
    XTKEg  = XTKE;
    YTKEg  = -(-YTKE+YTKE(end));

    %Extract out X=0 velocity profile
    yi = find(abs(Y)==min(abs(Y)));
    Yglobal =-X+X(end);
    Xglobal = Y;
    x0_prof(:,1) = Vx(yi,:)';
    x0_prof(:,2) = Vy(yi,:)';
    x0_prof(:,3) = Vz(yi,:)';
    x0_prof(:,4) = Uvx(yi,:)';
    x0_prof(:,5) = Uvy(yi,:)';
    x0_prof(:,6) = Uvz(yi,:)';
    x0_prof(:,7) = Sx(yi,:)';
    x0_prof(:,8) = Sy(yi,:)';
    x0_prof(:,9) = Sz(yi,:)';
    xi = find(abs(XTKE)==min(abs(XTKE)));
    x0_tke(:,1) = TKE(xi,:);
    x0_tke(:,2) = uTKE(xi,:);
    ubar = mean2(Vz); uubar = mean2(Uvz);
    x0_tke(:,3) = sqrt( 2/3*x0_tke(:,1) )/ubar;
    x0_tke(:,4) = sqrt( x0_tke(:,2).^2.*( ...
        sqrt(2/3).*x0_tke(:,1).^(-0.5)./ubar ).^2 + ...
         uubar.^2.*(-sqrt( 2/3.*x0_tke(:,1) )./ubar.^2 ).^2 );

    %Make surface plot of velocity
    figure,surf(Xglobal,Yglobal,Vz','EdgeColor','none')
    colormap jet; caxis([0,max(max(Vz))]); colorbar;
    zlim([0,ceil(max(max(Vz)))]);
    xlabel('y Position, [mm]');
    ylabel('x Position, [mm]');
    zlabel('Velocity, [m/s]');
    saveas(gcf,[flowcase{c},sl,'InletSurfacePlot.png']);

    figure,plot(Yglobal,x0_prof(:,1)); hold on;
    plot(Yglobal,x0_prof(:,2));
    plot(Yglobal,x0_prof(:,3));
    plot(Yglobal,x0_prof(:,4));
    plot(Yglobal,x0_prof(:,5));
    plot(Yglobal,x0_prof(:,6));
    plot(Yglobal,x0_prof(:,7));
    plot(Yglobal,x0_prof(:,8));
    plot(Yglobal,x0_prof(:,9));
    ylabel('Velocity, [m/s]');
```

```
    xlabel('y-Position, [mm]');
    legend('Vx','Vy','Vz','Uvx','Uvy','Uvz','Sx','Sy','Sz');
    saveas(gcf,[flowcase{c},sl,'InletProfile_x=0.png']);

    figure,errorbar(YTKEg,x0_tke(:,1),x0_tke(:,2));
    ylabel('TKE, [m^2/s^2]');
    xlabel('y-Position, [mm]');
    saveas(gcf,[flowcase{c},sl,'TKEProfile_x=0.png']);

    fid = fopen([flowcase{c},sl,'InletProfile_x0.txt'],'w');
    fprintf(fid,'Y,U,V,W,uU,uV,uW,sU,sV,sW\n');
    for it = 1:length(Yglobal)
        fprintf(fid,'%e,%e,%e,%e,%e,%e,%e,%e,%e,%e\n',...
            Yglobal(it),x0_prof(it,:));
    end
    fclose(fid); clear fid it;

    bl   = 12;
    step = 12;
    fid  = fopen([flowcase{c},sl,'InletProfileUncert_x0.txt'],'w');
    fprintf(fid,'Y,U,V,W,uU,uV,uW,sU,sV,sW\n');
    for it=1:bl
        fprintf(fid,'%e,%e,%e,%e,%e,%e,%e,%e,%e,%e\n',...
            Yglobal(it),x0_prof(it,:));
    end
    for it=bl+1:step:length(Yglobal)-bl-1
        fprintf(fid,'%e,%e,%e,%e,%e,%e,%e,%e,%e,%e\n',...
            Yglobal(it),x0_prof(it,:));
    end
    for it=length(Yglobal)-bl:length(Yglobal)
        fprintf(fid,'%e,%e,%e,%e,%e,%e,%e,%e,%e,%e\n',...
            Yglobal(it),x0_prof(it,:));
    end
    fclose(fid); clear fid it;

    fid = fopen([flowcase{c},sl,'InletProfileTurbInt_x0.txt'],'w');
    fprintf(fid,'Y,TKE,uTKE,TurbInt,uTurbInt\n');
    for it=1:length(YTKEg)
        fprintf(fid,'%e,%e,%e,%e,%e\n',YTKEg(it),x0_tke(it,:));
    end
    fclose(fid); clear fid it;

    fid = fopen([flowcase{c},sl,'Inlet_w_bulk.txt'],'w');
    fprintf(fid,'%6.4f\n',ubar);
    fclose(fid);

    figure,contour(Xglobal,Yglobal,Vz',20,'LineWidth',0.25); colormap('jet');
    axis square;
    set(gca,'XTick',[]);
    set(gca,'YTick',[]);
    if c<=3
        set(gca,'CLim',[0,1.5]);
    elseif c==4
        set(gca,'CLim',[0,0.25]);
    else
        set(gca,'CLim',[0,0.35]);
```

```
    end
    saveas(gcf,[flowcase{c},sl,'InletContour.png']);
    cont   = imread([flowcase{c},sl,'InletContour.png']);
    iminv  = 255-cont;
    imgray = mean(iminv,3);
    row    = find(imgray(round(size(imgray,1)/2),:)>0,1,'first'):...
        find(imgray(round(size(imgray,1)/2),:)>0,1,'last');
    col    = find(imgray(:,round(size(imgray,2)/2))>0,1,'first'):...
        find(imgray(:,round(size(imgray,2)/2))>0,1,'last');
    imwrite(cont(col,row,:),[flowcase{c},sl,'InletContour.png']);

    %Trapezoid Rule Integration for Vz and Uvz
    Tarray  = zeros(size(Vz,2),1);
    uTarray = zeros(size(Vz,2),1);
    dT_dVz1 = 0.5*dx;
    dT_dVz2 =-0.5*dx;
    for j=1:size(Vz,2)
        dT_ddx     = 0.5*(Vz(1:end-1,j)+Vz(2:end,j));
        Tarray(j)  = sum(Vz(1:end-1,j)+Vz(2:end,j))*dx/2;
        uTarray(j) = sum(sqrt( Uvz(1:end-1,j).^2.*dT_dVz1.^2 + ...
            Uvz(2:end,j).^2.*dT_dVz2.^2 +...
            udx.^2.*dT_ddx.^2 + ...
                2*dT_dVz1*dT_dVz2.*Uvz(1:end-1,j).*Uvz(2:end,j)));
    end
    dT_ddx = 0.5*(Tarray(1:end-1)+Tarray(2:end));
    vdot   = sum(Tarray(1:end-1)+Tarray(2:end))*dx/2;
    uvdot  = sum(sqrt( uTarray(1:end-1).^2.*dT_dVz1.^2 + ...
        uTarray(2:end).^2.*dT_dVz2.^2 +...
        udx.^2.*dT_ddx(1:end).^2 + ...
            2*dT_dVz1*dT_dVz2.*uTarray(1:end-1).*uTarray(2:end)));

    %Calculate mass flow rate
    mdot   = rho*vdot;
    umdot  = sqrt( urho^2*vdot^2 + uvdot^2*rho^2 );

    fid = fopen([codedir,flowcase{c},'_MassFlowRate.txt'],'w');
    fprintf(fid,'mdot = %12.8f +/- %12.8f kg/s\n',mdot,umdot);
    fclose(fid);
    fid = fopen([codedir,flowcase{c},'_VolumeFlowRate.txt'],'w');
    fprintf(fid,'Vdot = %12.8f +/- %12.8f m^3/s\n',vdot,uvdot);
    fclose(fid);
    width  = (X(end)-X(1))/.0254;
    height = (Y(1)-Y(end))/.0254;
    fprintf('%11s: mdot = %9.6f +- %9.6f kg/s, vdot = %9.6f +- %9.6f m^3/s, ...
        Area = %f x %f [in]\n',flowcase{c},mdot,umdot,vdot,uvdot,width,height);

    %Inlet Reynolds Number
    P  = 12*0.0254*4;
    uP = 0.020*0.0254;
    Re = 4*mdot/rho/P/nu;
    dRe_dmdot = 4/rho/nu/P;
    dRe_drho  = -8*mdot/rho^2/nu/P;
    dRe_dnu   = -8*mdot/rho/nu^2/P;
    dRe_dP    = -8*mdot/rho/nu/P^2;
    uRe       = sqrt( umdot^2*dRe_dmdot^2 + urho^2*dRe_drho^2 + ...
        uP^2*dRe_dP^2 + unu^2*dRe_dnu^2 );
```

```
    fid = fopen([codedir,flowcase{c},'_ReynoldsNumber.txt'],'w');
    fprintf(fid,'Re = %12.8f +/- %12.8f kg/s\n',Re,uRe);
    fclose(fid);
end
rmpath(codesdir);
close all;
```

Appendix F

Drawings and Schematics

F.1 Fuel Rod Drawings

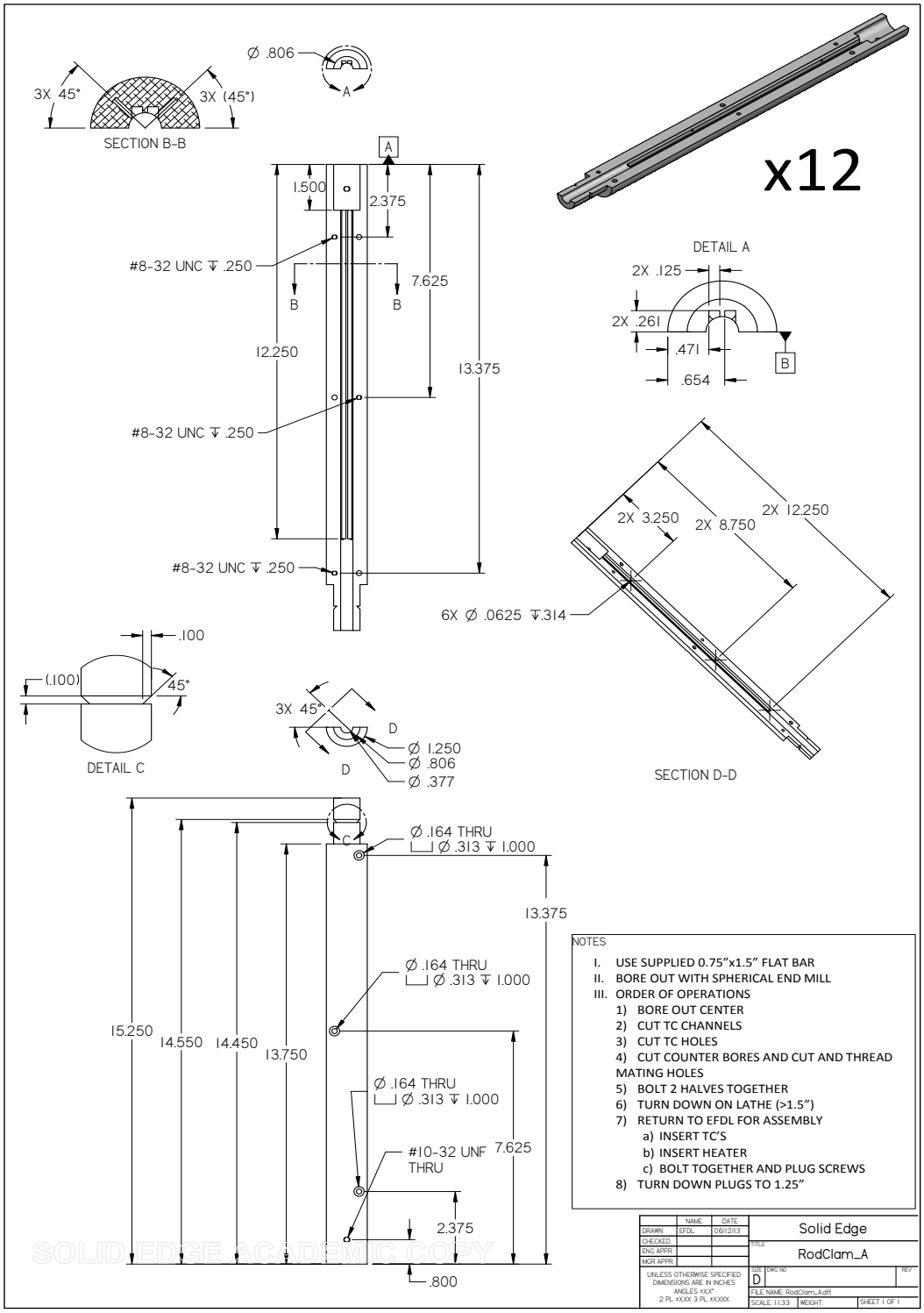

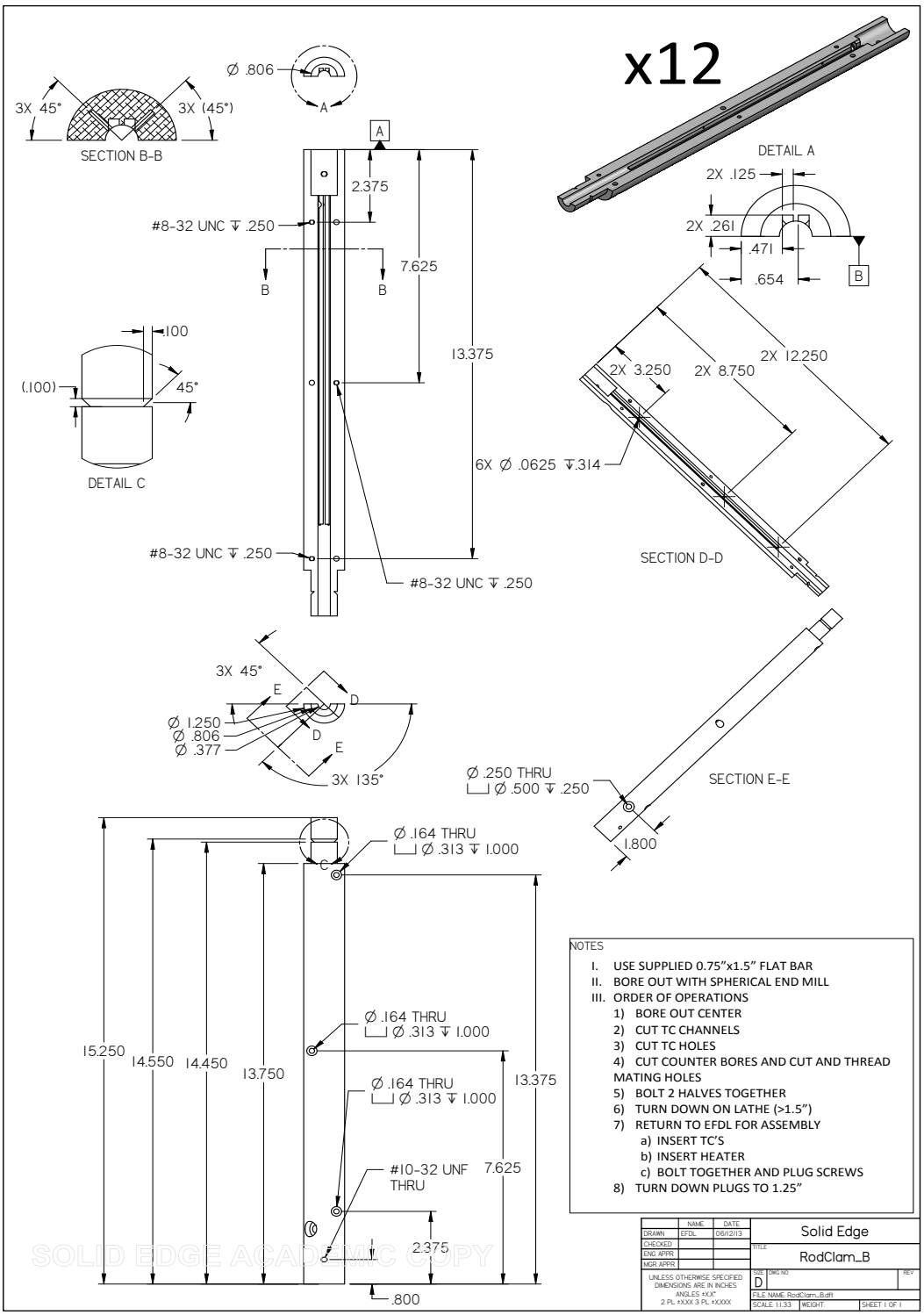
x12
Ø .806
A
3X 45°
3X (45°)
SECTION B-B
A
2.375
#8-32 UNC ↧ .250
7.625
B
B
13.375
.100
(.100)
45°
DETAIL C
#8-32 UNC ↧ .250
#8-32 UNC ↧ .250
DETAIL A
2X .125
2X .261
.471
.654
B
2X 3.250
2X 8.750
2X 12.250
6X Ø .0625 ↧.314
SECTION D-D
3X 45°
E
D
Ø 1.250
Ø .806
Ø .377
D
E
3X 135°
Ø .250 THRU
⌴ Ø .500 ↧ .250
SECTION E-E
1.800
Ø .164 THRU
⌴ Ø .313 ↧ 1.000
C
Ø .164 THRU
⌴ Ø .313 ↧ 1.000
15.250
14.550
14.450
13.750
13.375
Ø .164 THRU
⌴ Ø .313 ↧ 1.000
#10-32 UNF
THRU
7.625
2.375
.800
NOTES
I. USE SUPPLIED 0.75"x1.5" FLAT BAR
II. BORE OUT WITH SPHERICAL END MILL
III. ORDER OF OPERATIONS
1) BORE OUT CENTER
2) CUT TC CHANNELS
3) CUT TC HOLES
4) CUT COUNTER BORES AND CUT AND THREAD MATING HOLES
5) BOLT 2 HALVES TOGETHER
6) TURN DOWN ON LATHE (>1.5")
7) RETURN TO EFDL FOR ASSEMBLY
a) INSERT TC'S
b) INSERT HEATER
c) BOLT TOGETHER AND PLUG SCREWS
8) TURN DOWN PLUGS TO 1.25"
NAME DATE
DRAWN EFDL 06/12/13
CHECKED
ENG APPR.
MGR APPR.
UNLESS OTHERWISE SPECIFIED DIMENSIONS ARE IN INCHES
ANGLES ±X.X°
2 PL ±XXX 3 PL ±XXXX
Solid Edge
TITLE
RodClam_B
SIZE D
DWG NO
REV
FILE NAME: RodClam_B.dft
SCALE: 1:1.33
WEIGHT:
SHEET 1 OF 1
SOLID EDGE ACADEMIC COPY

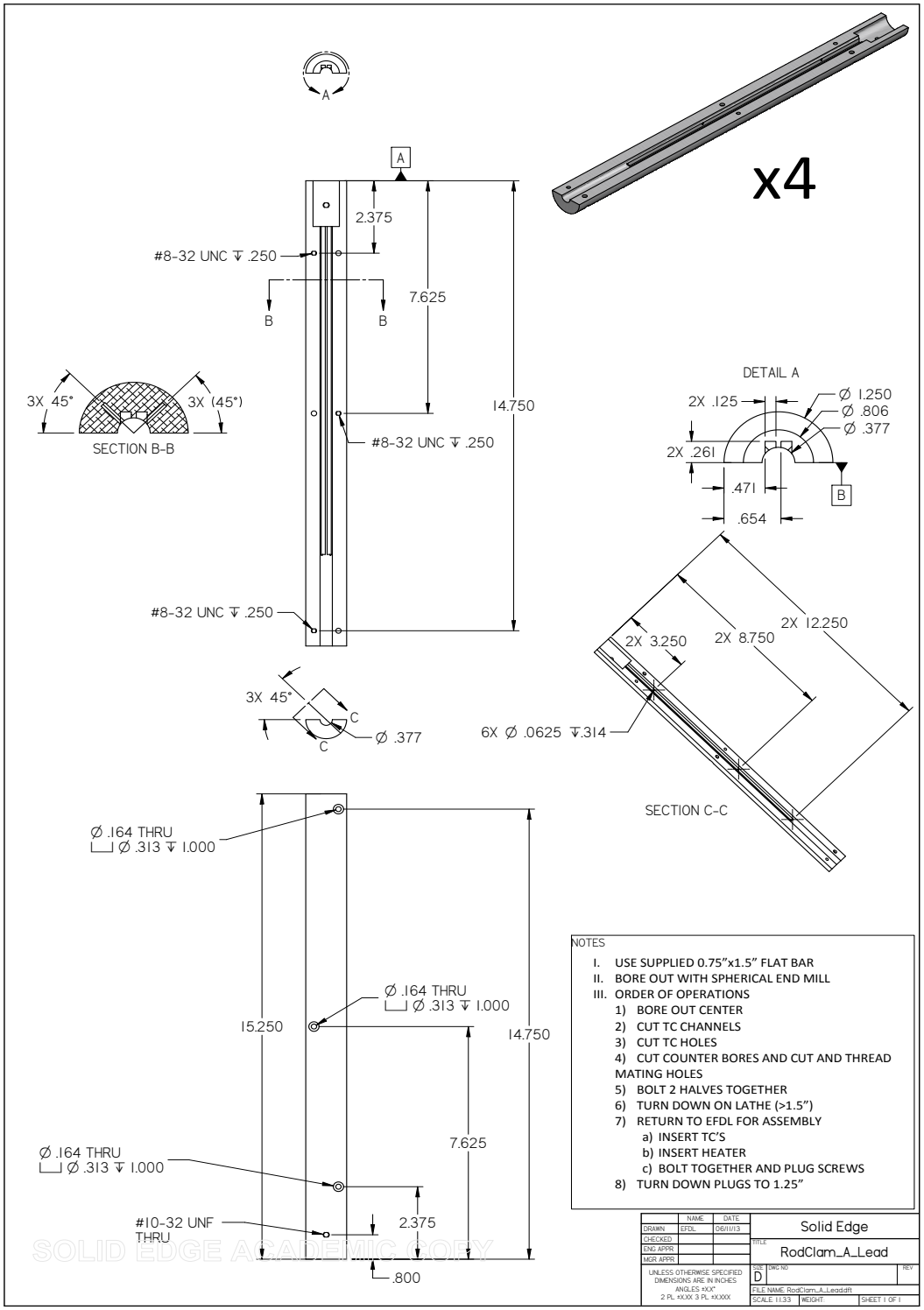
x4
A
2.375
#8-32 UNC ↧ .250
7.625
B
B
14.750
#8-32 UNC ↧ .250
#8-32 UNC ↧ .250
3X 45°
3X (45°)
SECTION B-B
DETAIL A
2X .125
Ø 1.250
Ø .806
Ø .377
2X .261
.471
.654
B
2X 12.250
2X 8.750
2X 3.250
6X Ø .0625 ↧.314
SECTION C-C
3X 45°
C
C
Ø .377
Ø .164 THRU
Ø .313 ↧ 1.000
Ø .164 THRU
Ø .313 ↧ 1.000
15.250
14.750
7.625
Ø .164 THRU
Ø .313 ↧ 1.000
#10-32 UNF
THRU
2.375
.800
NOTES
I. USE SUPPLIED 0.75"x1.5" FLAT BAR
II. BORE OUT WITH SPHERICAL END MILL
III. ORDER OF OPERATIONS
1) BORE OUT CENTER
2) CUT TC CHANNELS
3) CUT TC HOLES
4) CUT COUNTER BORES AND CUT AND THREAD MATING HOLES
5) BOLT 2 HALVES TOGETHER
6) TURN DOWN ON LATHE (>1.5")
7) RETURN TO EFDL FOR ASSEMBLY
a) INSERT TC'S
b) INSERT HEATER
c) BOLT TOGETHER AND PLUG SCREWS
8) TURN DOWN PLUGS TO 1.25"
NAME
DATE
DRAWN
EFDL
06/11/13
CHECKED
ENG APPR
MGR APPR
UNLESS OTHERWISE SPECIFIED
DIMENSIONS ARE IN INCHES
ANGLES ±XX°
2 PL ±XXX 3 PL ±XXXX
Solid Edge
TITLE
RodClam_A_Lead
SIZE
D
DWG NO
REV
FILE NAME: RodClam_A_Lead.dft
SCALE: 1:1.33
WEIGHT:
SHEET 1 OF 1
SOLID EDGE ACADEMIC COPY

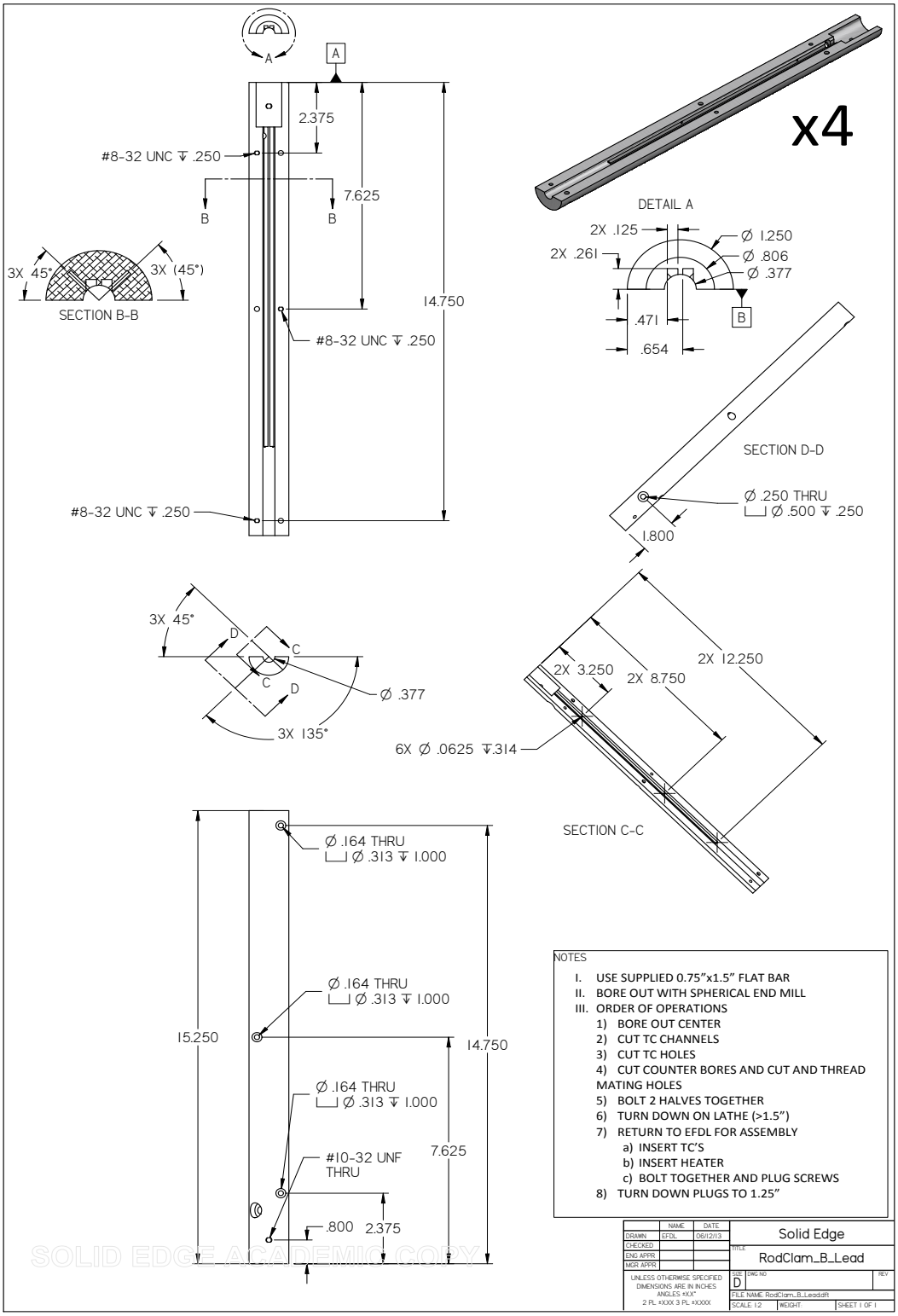
A
A
2.375
#8-32 UNC ↧ .250
7.625
B
B
14.750
#8-32 UNC ↧ .250
#8-32 UNC ↧ .250
3X 45°
3X (45°)
SECTION B-B
x4
DETAIL A
2X .125
2X .261
Ø 1.250
Ø .806
Ø .377
.471
.654
B
SECTION D-D
Ø .250 THRU
⌴ Ø .500 ↧ .250
1.800
3X 45°
D
C
C
D
Ø .377
3X 135°
2X 3.250
2X 8.750
2X 12.250
6X Ø .0625 ↧.314
SECTION C-C
Ø .164 THRU
⌴ Ø .313 ↧ 1.000
Ø .164 THRU
⌴ Ø .313 ↧ 1.000
15.250
14.750
Ø .164 THRU
⌴ Ø .313 ↧ 1.000
7.625
#10-32 UNF
THRU
.800
2.375
NOTES
I. USE SUPPLIED 0.75"x1.5" FLAT BAR
II. BORE OUT WITH SPHERICAL END MILL
III. ORDER OF OPERATIONS
1) BORE OUT CENTER
2) CUT TC CHANNELS
3) CUT TC HOLES
4) CUT COUNTER BORES AND CUT AND THREAD MATING HOLES
5) BOLT 2 HALVES TOGETHER
6) TURN DOWN ON LATHE (>1.5")
7) RETURN TO EFDL FOR ASSEMBLY
a) INSERT TC'S
b) INSERT HEATER
c) BOLT TOGETHER AND PLUG SCREWS
8) TURN DOWN PLUGS TO 1.25"
NAME
DATE
DRAWN
EFDL
06/12/13
CHECKED
ENG APPR.
MGR. APPR.
UNLESS OTHERWISE SPECIFIED:
DIMENSIONS ARE IN INCHES
ANGLES ±X.X°
2 PL. ±XXX 3 PL. ±XXXX
Solid Edge
TITLE
RodClam_B_Lead
SIZE
D
DWG NO
REV
FILE NAME: RodClam_B_Lead.dft
SCALE: 1:2
WEIGHT:
SHEET 1 OF 1
SOLID EDGE ACADEMIC COPY

F.2 Grid Spacer Drawings

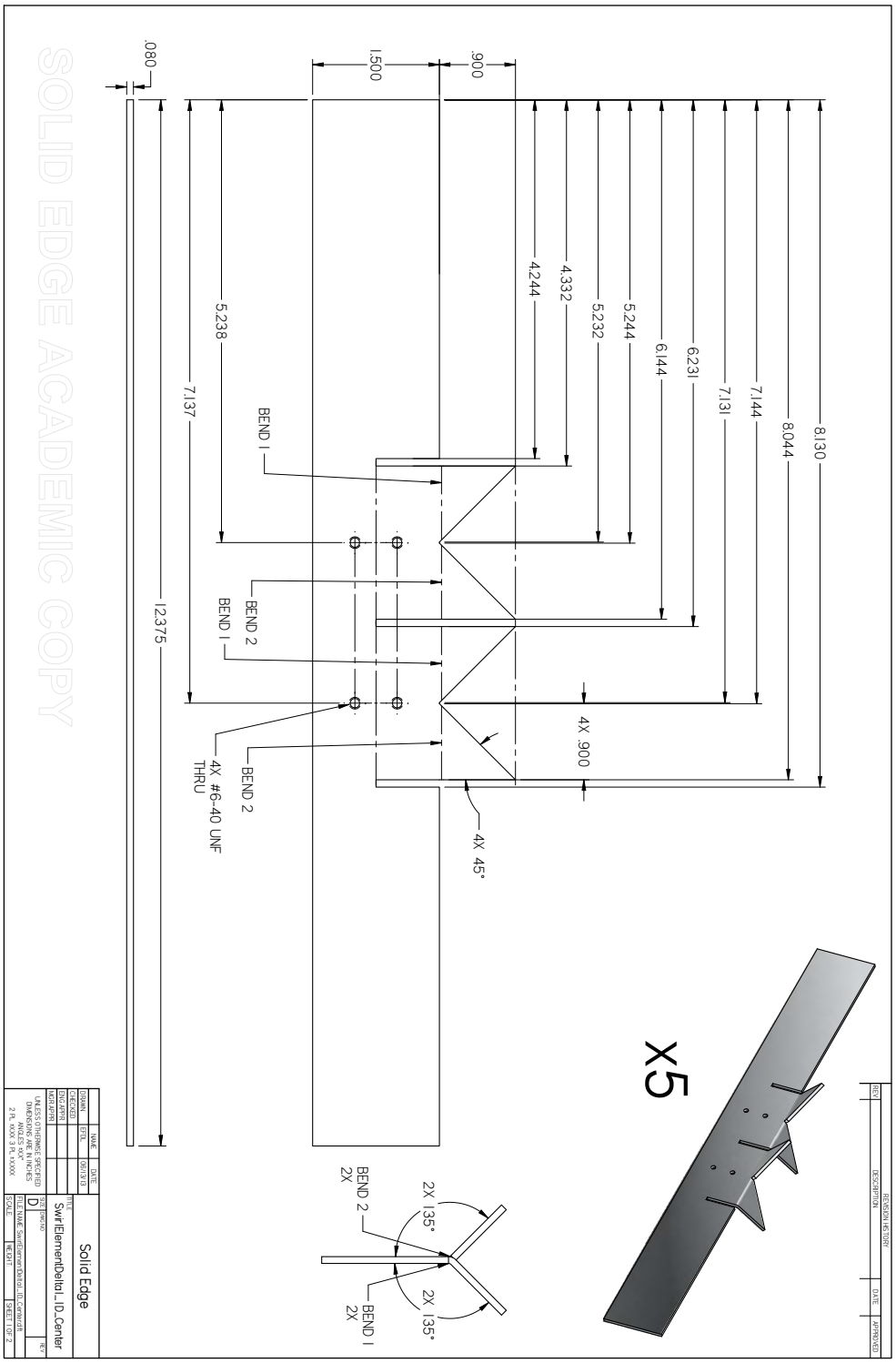

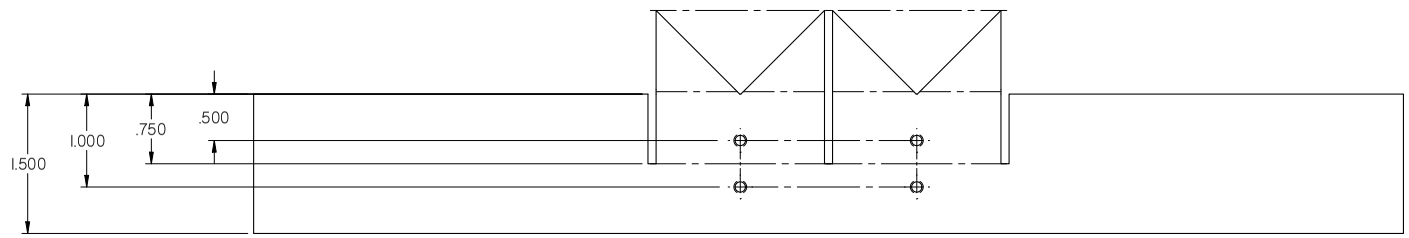

REVISION HISTORY

REV	DESCRIPTION	DATE	APPROVED

	NAME	DATE
DRAWN	EFDL	06/13/13
CHECKED		
ENG APPR.		
MGR APPR.		

UNLESS OTHERWISE SPECIFIED
DIMENSIONS ARE IN INCHES
ANGLES: ±0X°
2 PL: ±XXX 3 PL: ±XXXX

Solid Edge

TITLE: SwirlElementDelta1_ID_Center

SIZE: D | DWG NO | REV

FILE NAME: SwirlElementDelta1_ID_Center.dft

SCALE | WEIGHT | SHEET 2 OF 2

SOLID EDGE ACADEMIC COPY

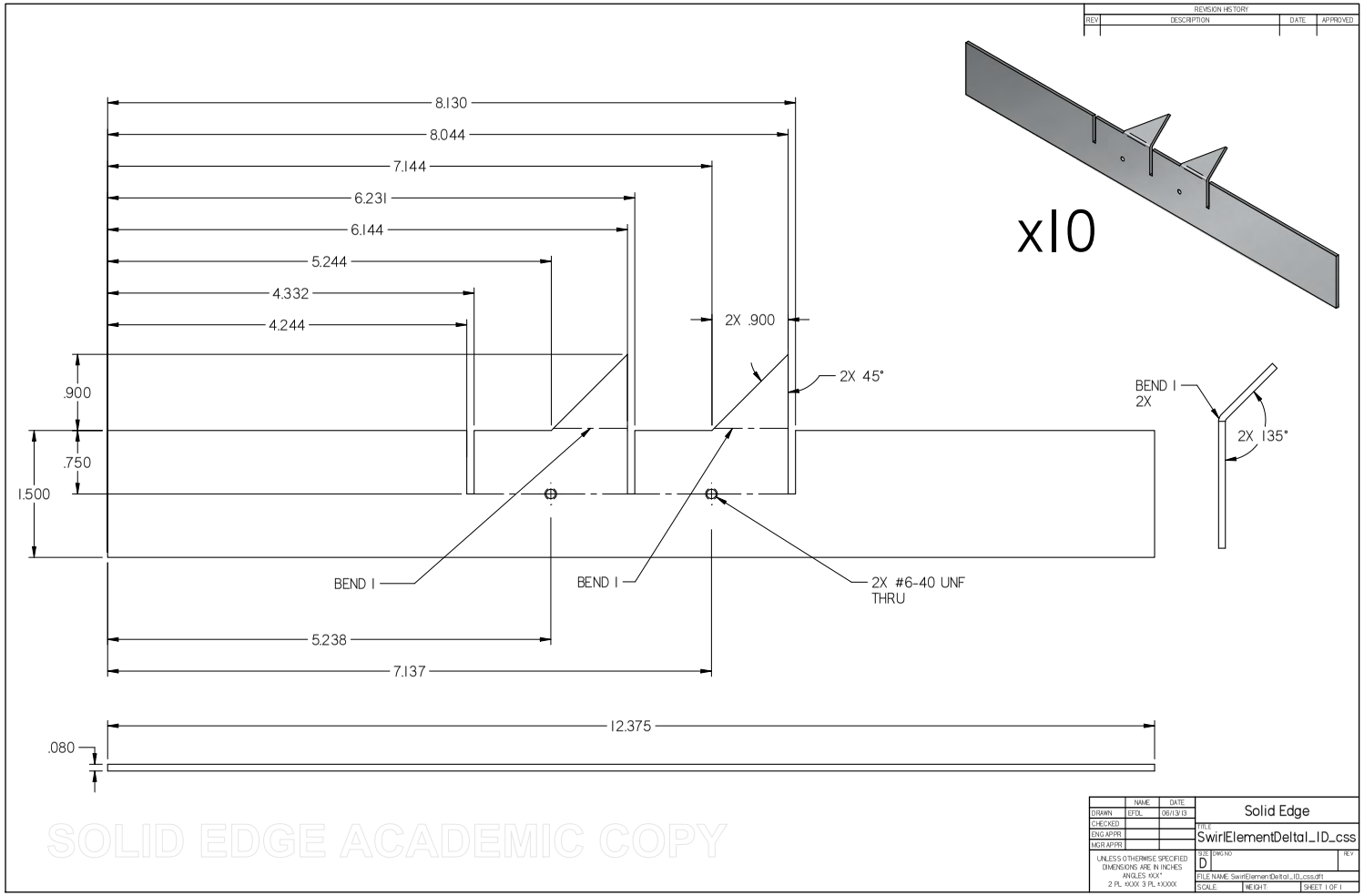
REVISION HISTORY
REV
DESCRIPTION
DATE
APPROVED
8.130
8.044
7.144
6.231
6.144
5.244
4.332
4.244
2X .900
2X 45°
.900
.750
1.500
BEND 1
BEND 1
2X #6-40 UNF
THRU
5.238
7.137
12.375
.080
x10
BEND 1
2X
2X 135°
SOLID EDGE ACADEMIC COPY
NAME
DATE
DRAWN
EFDL
06/13/13
CHECKED
ENG APPR.
MGR APPR.
UNLESS OTHERWISE SPECIFIED
DIMENSIONS ARE IN INCHES
ANGLES: ±0X°
2 PL: ±XXX 3 PL: ±XXXX
Solid Edge
TITLE
SwirlElementDeltaI_ID_css
SIZE
D
DWG NO
REV
FILE NAME: SwirlElementDeltaI_ID_css.dft
SCALE
WEIGHT
SHEET 1 OF 1

F.3 Test Section Drawings

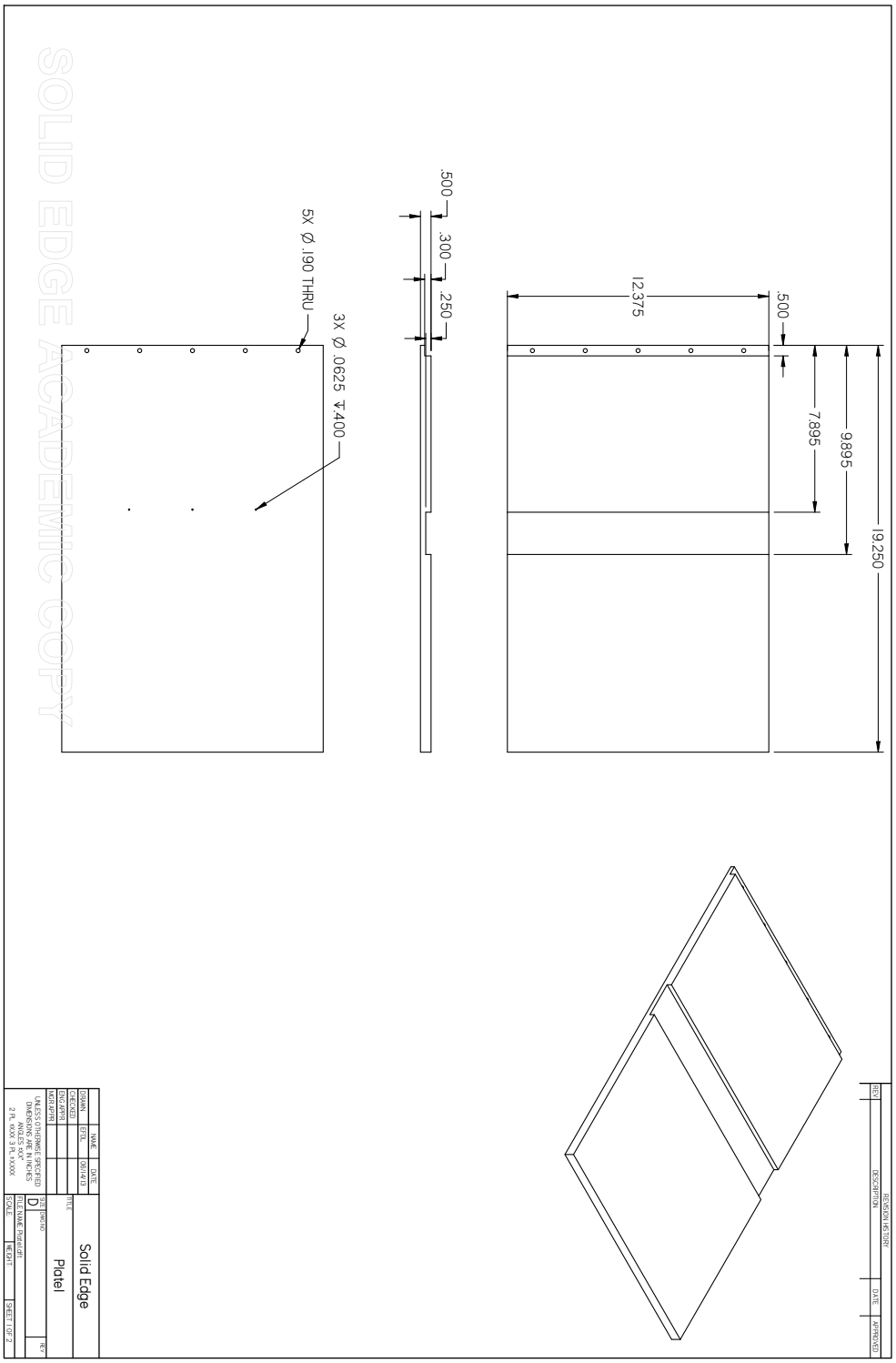

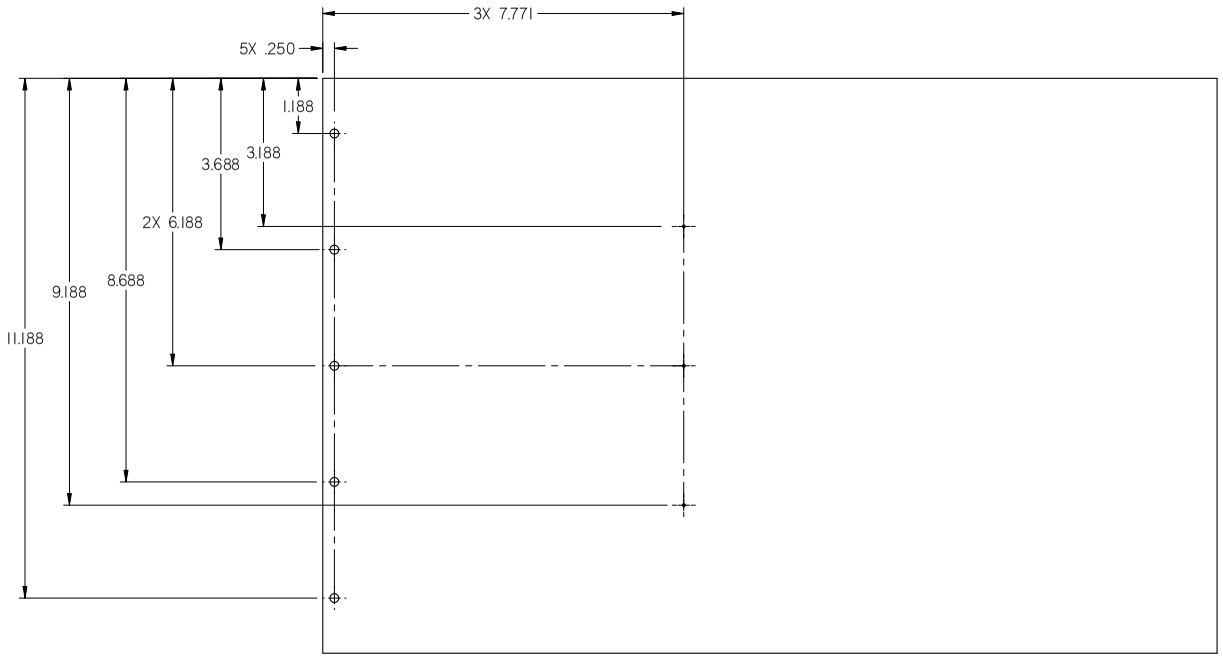

REVISION HISTORY

REV	DESCRIPTION	DATE	APPROVED

	NAME	DATE
DRAWN	EFDL	06/14/13
CHECKED		
ENG APPR.		
MGR APPR.		

UNLESS OTHERWISE SPECIFIED
DIMENSIONS ARE IN INCHES
ANGLES ±0X°
2 PL ±XXX 3 PL ±XXXX

Solid Edge

TITLE
Platel

SIZE D DWG NO REV

FILE NAME Platel.dft

SCALE WEIGHT SHEET 2 OF 2

SOLID EDGE ACADEMIC COPY

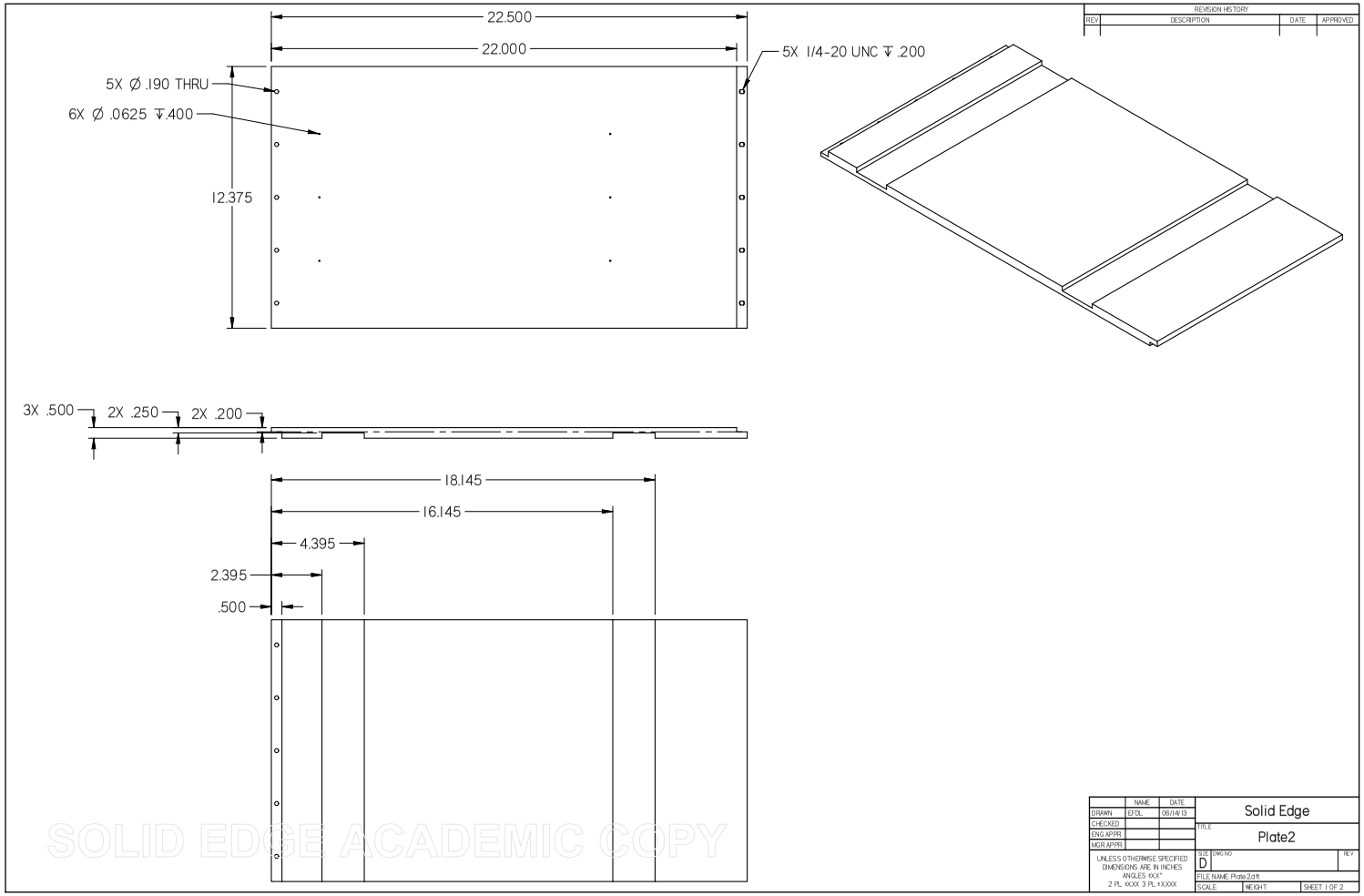
22.500
22.000
5X Ø .190 THRU
6X Ø .0625 ↧.400
5X 1/4-20 UNC ↧ .200
12.375
3X .500
2X .250
2X .200
18.145
16.145
4.395
2.395
.500
REVISION HISTORY
REV
DESCRIPTION
DATE
APPROVED
NAME
DATE
DRAWN
EFDL
06/14/13
CHECKED
ENG APPR.
MGR APPR.
UNLESS OTHERWISE SPECIFIED
DIMENSIONS ARE IN INCHES
ANGLES: ±0.5°
2 PL: ±0.XX 3 PL: ±0.XXX
Solid Edge
TITLE
Plate2
SIZE
D
DWG NO
REV
FILE NAME: Plate2.dft
SCALE:
WEIGHT:
SHEET 1 OF 2
SOLID EDGE ACADEMIC COPY

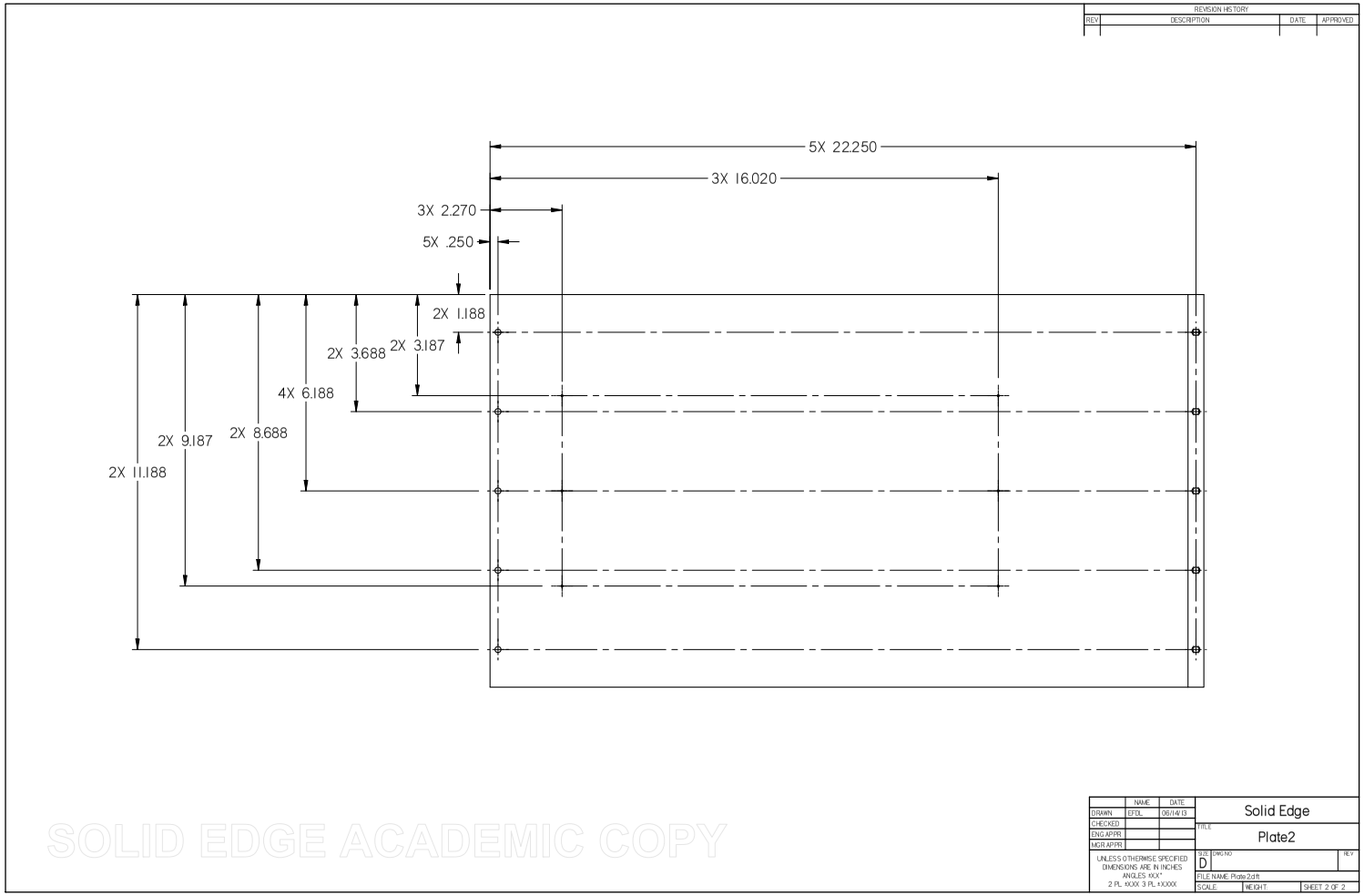
REVISION HISTORY
REV
DESCRIPTION
DATE
APPROVED
5X 22.250
3X 16.020
3X 2.270
5X .250
2X 1.188
2X 3.687
2X 3.688
4X 6.188
2X 8.688
2X 9.187
2X 11.188
SOLID EDGE ACADEMIC COPY
NAME
DATE
DRAWN
EFDL
06/14/13
CHECKED
ENG APPR.
MGR APPR.
UNLESS OTHERWISE SPECIFIED
DIMENSIONS ARE IN INCHES
ANGLES: ±0X°
2 PL: ±XXX 3 PL: ±XXXX
Solid Edge
TITLE
Plate2
SIZE
D
DWG NO
REV
FILE NAME: Plate2.dft
SCALE
WEIGHT
SHEET 2 OF 2

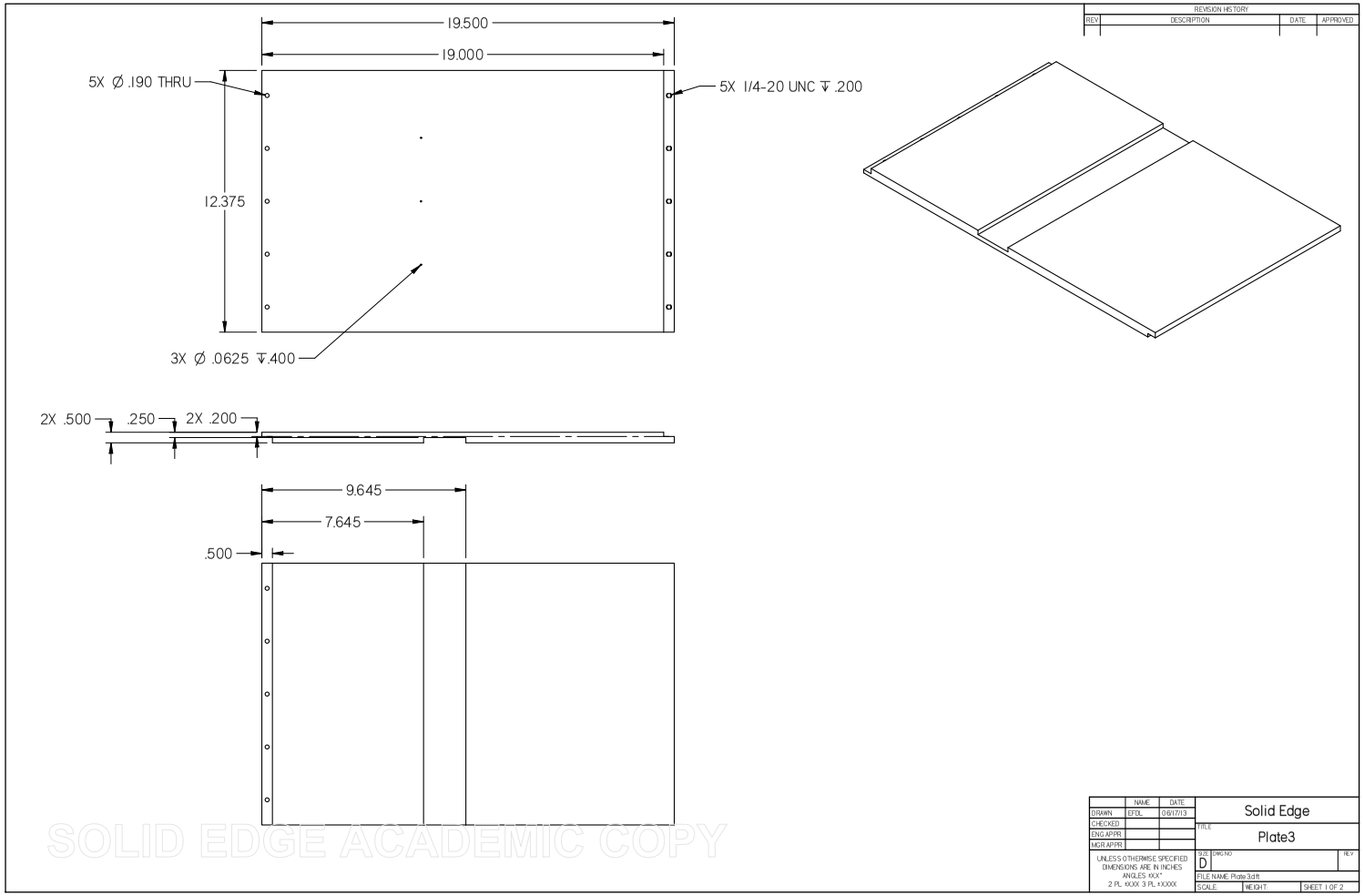
19.500
19.000
5X Ø .190 THRU
5X 1/4-20 UNC ↧ .200
12.375
3X Ø .0625 ↧.400
2X .500
.250
2X .200
9.645
7.645
.500
REVISION HISTORY
REV
DESCRIPTION
DATE
APPROVED
NAME
DATE
DRAWN
EFDL
06/17/13
CHECKED
ENG APPR.
MGR APPR.
UNLESS OTHERWISE SPECIFIED
DIMENSIONS ARE IN INCHES
ANGLES: ±0.5°
2 PL: ±0.XX 3 PL: ±0.XXX
Solid Edge
TITLE
Plate3
SIZE
D
DWG NO
REV
FILE NAME: Plate3.dft
SCALE:
WEIGHT:
SHEET 1 OF 2
SOLID EDGE ACADEMIC COPY

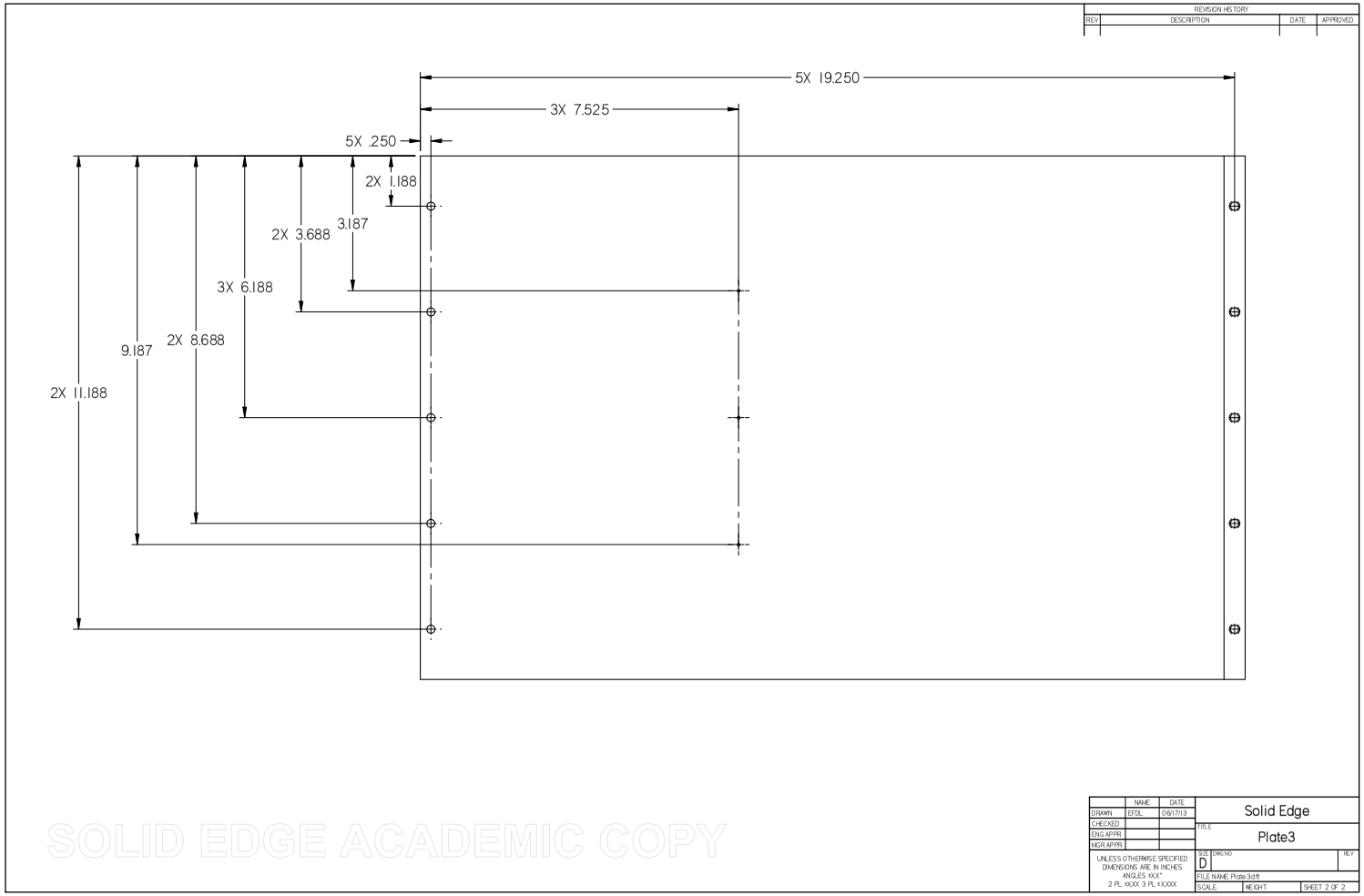
REVISION HISTORY
REV
DESCRIPTION
DATE
APPROVED
5X 19.250
3X 7.525
5X .250
2X 1.188
3.187
2X 3.688
3X 6.188
9.187
2X 8.688
2X 11.188
NAME
DATE
DRAWN
EFDL
06/17/13
CHECKED
ENG APPR.
MGR APPR.
UNLESS OTHERWISE SPECIFIED
DIMENSIONS ARE IN INCHES
ANGLES: ±0.5°
2 PL: ±0.XX 3 PL: ±0.XXX
Solid Edge
TITLE
Plate3
SIZE
D
DWG NO
REV
FILE NAME: Plate3.dft
SCALE
WEIGHT
SHEET 2 OF 2
SOLID EDGE ACADEMIC COPY

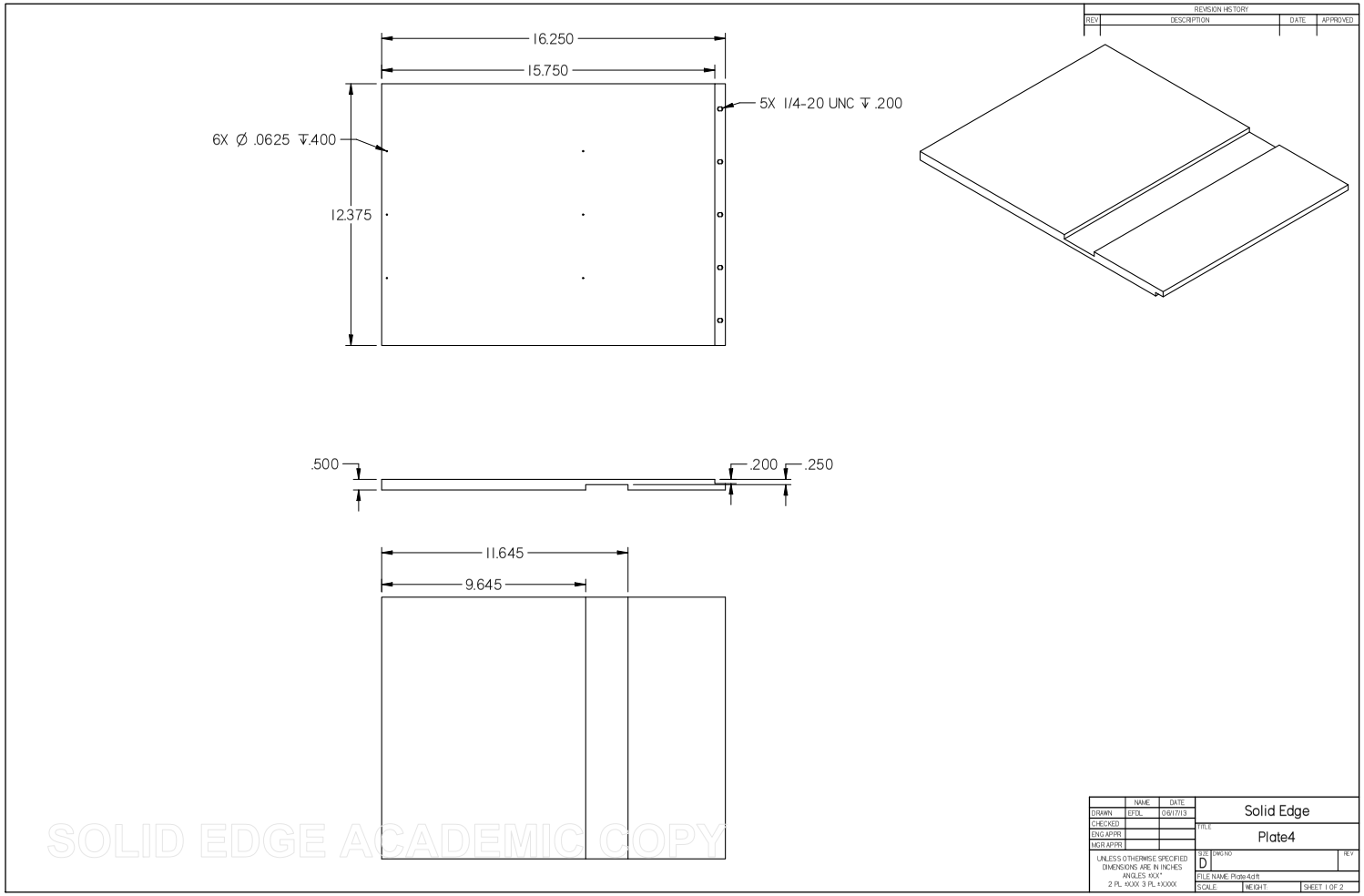
16.250
15.750
5X 1/4-20 UNC ↧ .200
6X ∅ .0625 ↧.400
12.375
.500
.200
.250
11.645
9.645
REVISION HISTORY
REV
DESCRIPTION
DATE
APPROVED
NAME
DATE
DRAWN
EFDL
06/17/13
CHECKED
ENG APPR.
MGR APPR.
UNLESS OTHERWISE SPECIFIED
DIMENSIONS ARE IN INCHES
ANGLES: ±0.5°
2 PL: ±0.XX 3 PL: ±0.XXX
Solid Edge
TITLE
Plate4
SIZE
D
DWG NO
REV
FILE NAME: Plate4.dft
SCALE
WEIGHT
SHEET 1 OF 2
SOLID EDGE ACADEMIC COPY

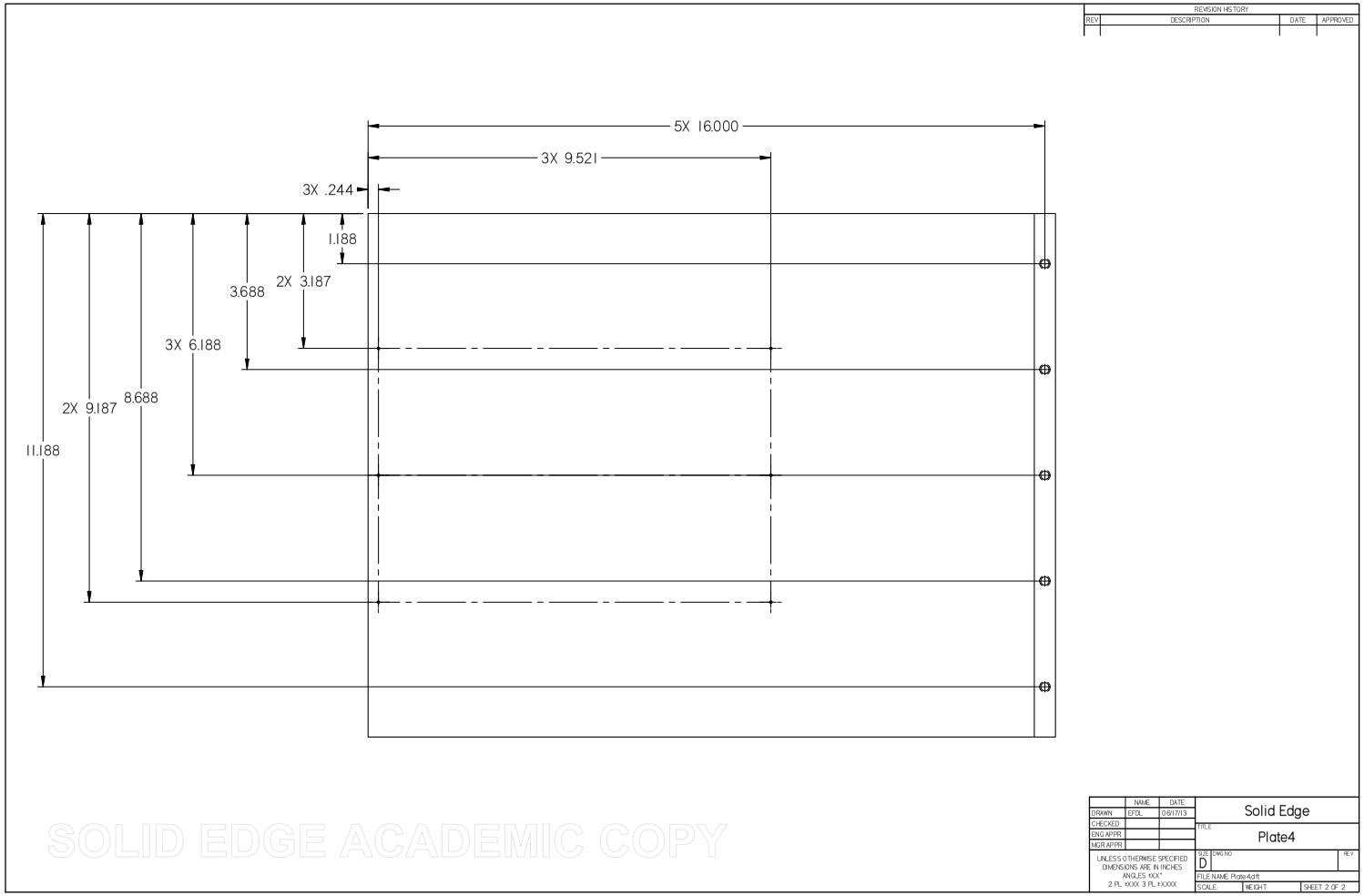
REVISION HISTORY
REV
DESCRIPTION
DATE
APPROVED
5X 16.000
3X 9.521
3X .244
1.188
2X 3.187
3.688
3X 6.188
8.688
2X 9.187
11.188
SOLID EDGE ACADEMIC COPY
NAME
DATE
DRAWN
EFDL
06/17/13
CHECKED
ENG APPR.
MGR APPR.
UNLESS OTHERWISE SPECIFIED
DIMENSIONS ARE IN INCHES
ANGLES: ±0.5°
2 PL: ±0.XX 3 PL: ±0.XXX
Solid Edge
TITLE
Plate4
SIZE
D
DWG NO
REV
FILE NAME: Plate4.dft
SCALE:
WEIGHT:
SHEET 2 OF 2

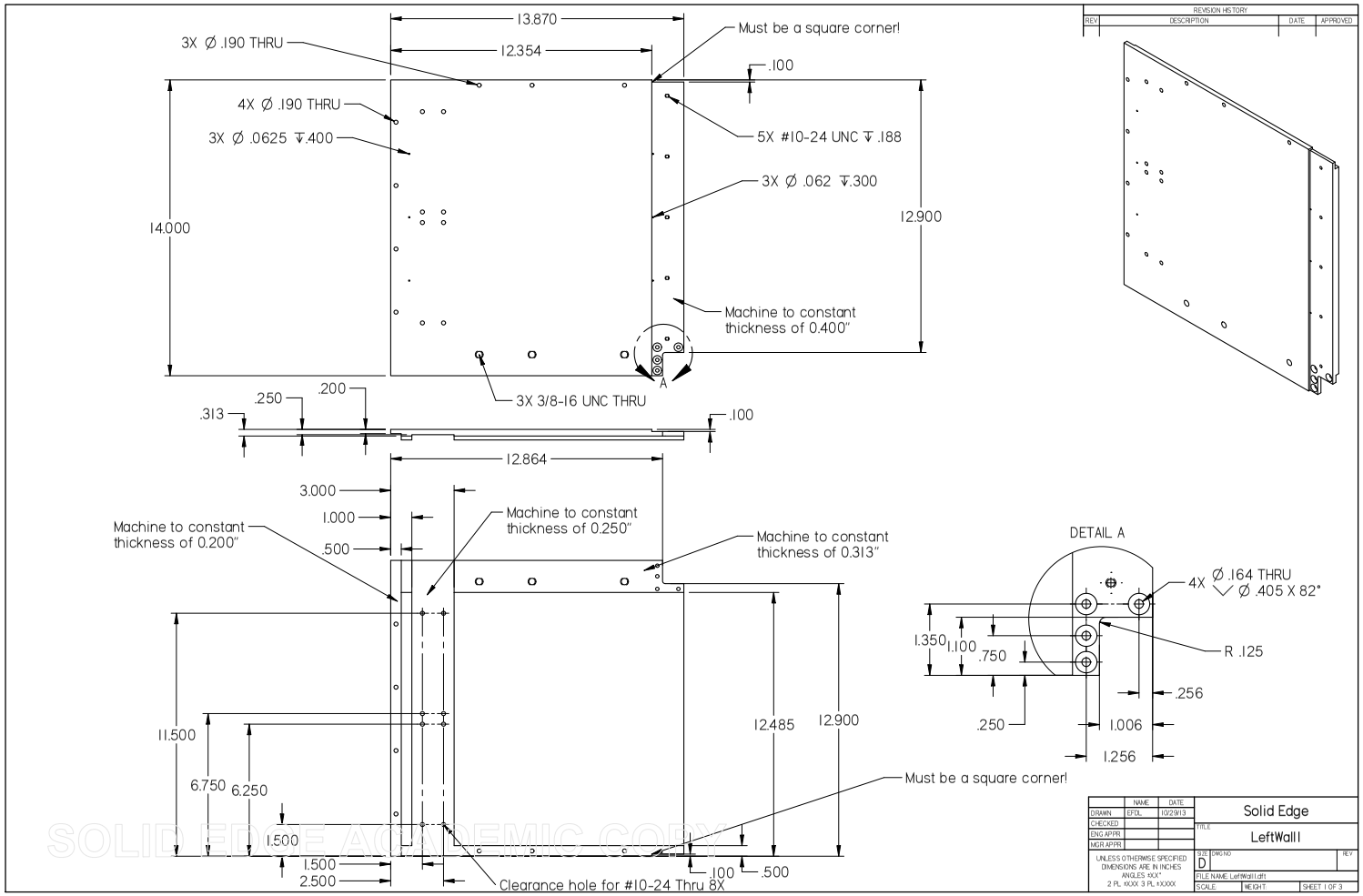

SOLID EDGE ACADEMIC COPY

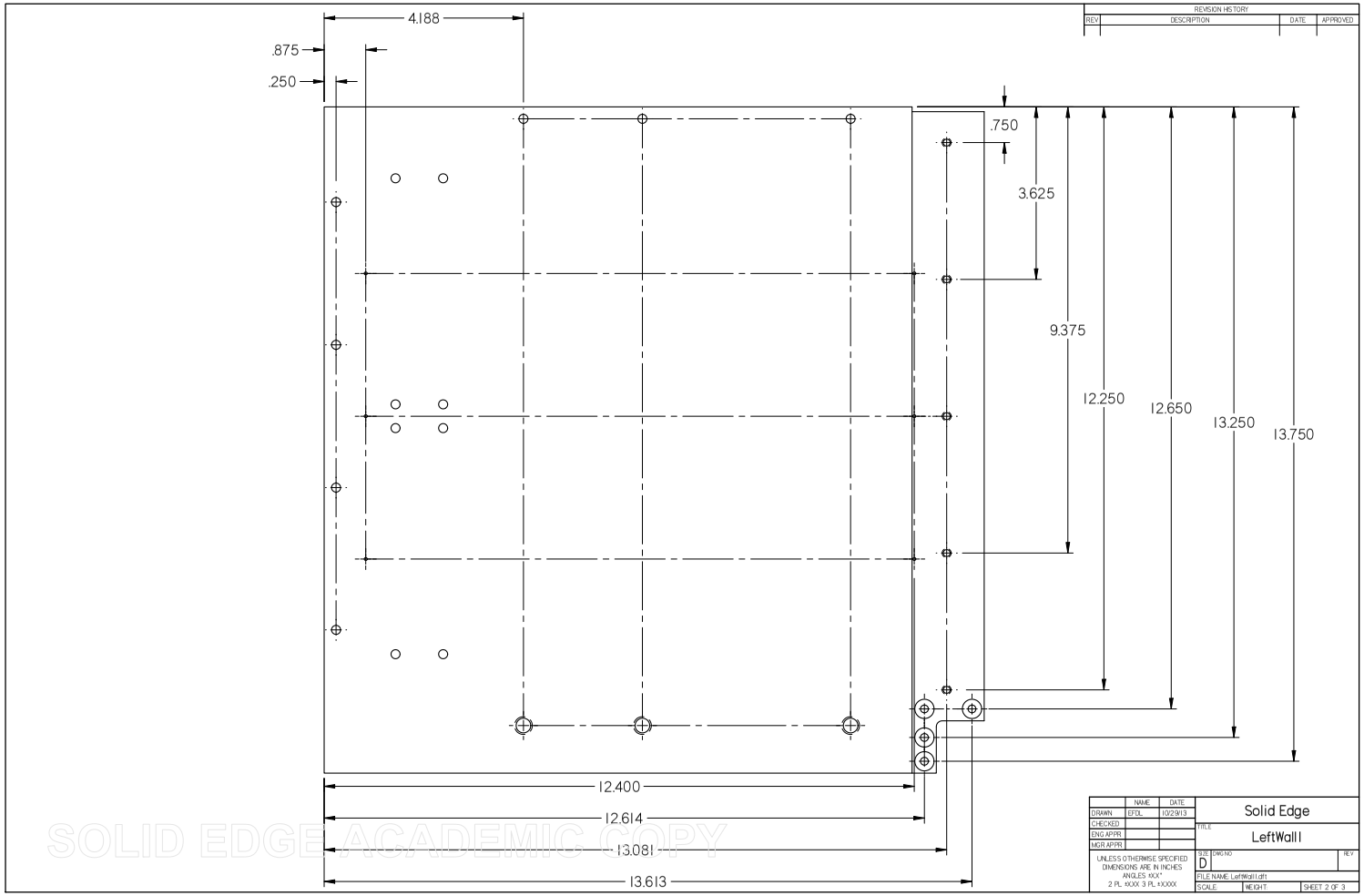
4.188
.875
.250
.750
3.625
9.375
12.250
12.650
13.250
13.750
12.400
12.614
13.081
13.613
REVISION HISTORY
REV
DESCRIPTION
DATE
APPROVED
NAME
DATE
DRAWN
EFDL
10/29/13
CHECKED
ENG APPR.
MGR APPR.
UNLESS OTHERWISE SPECIFIED
DIMENSIONS ARE IN INCHES
ANGLES: ±0X°
2 PL: ±XXX 3 PL: ±XXXX
Solid Edge
TITLE
LeftWall1
SIZE
D
DWG NO
REV
FILE NAME: LeftWall1.dft
SCALE:
WEIGHT:
SHEET 2 OF 3
SOLID EDGE ACADEMIC COPY

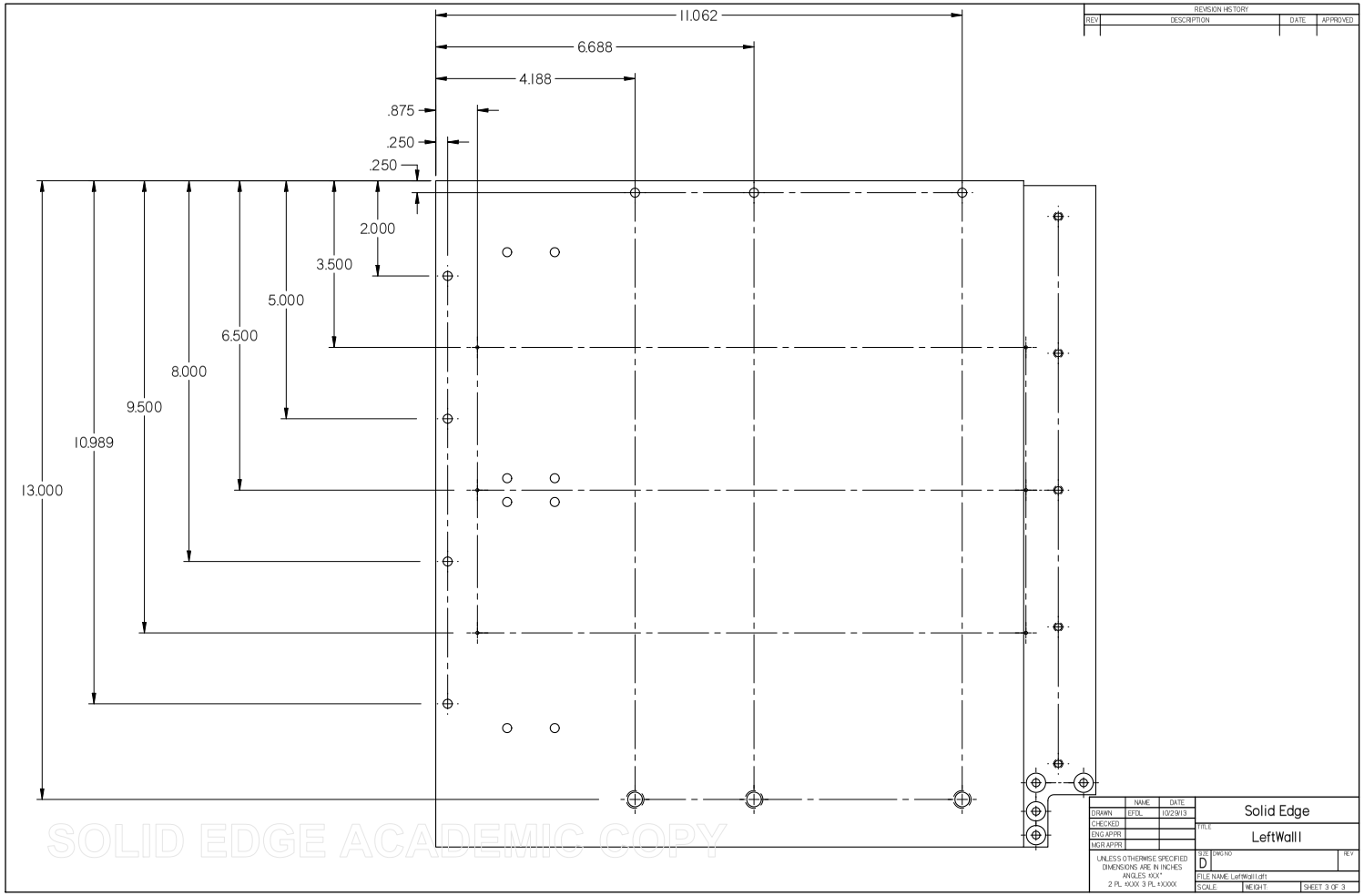
11.062
6.688
4.188
.875
.250
.250
2.000
3.500
5.000
6.500
8.000
9.500
10.989
13.000
REVISION HISTORY
REV
DESCRIPTION
DATE
APPROVED
NAME
DATE
DRAWN
EFDL
10/29/13
CHECKED
ENG APPR.
MGR APPR.
UNLESS OTHERWISE SPECIFIED
DIMENSIONS ARE IN INCHES
ANGLES: ±0.5°
2 PL: ±0.XX 3 PL: ±0.XXX
Solid Edge
TITLE
LeftWall1
SIZE
D
DWG NO
REV
FILE NAME: LeftWall1.dft
SCALE
WEIGHT
SHEET 3 OF 3
SOLID EDGE ACADEMIC COPY

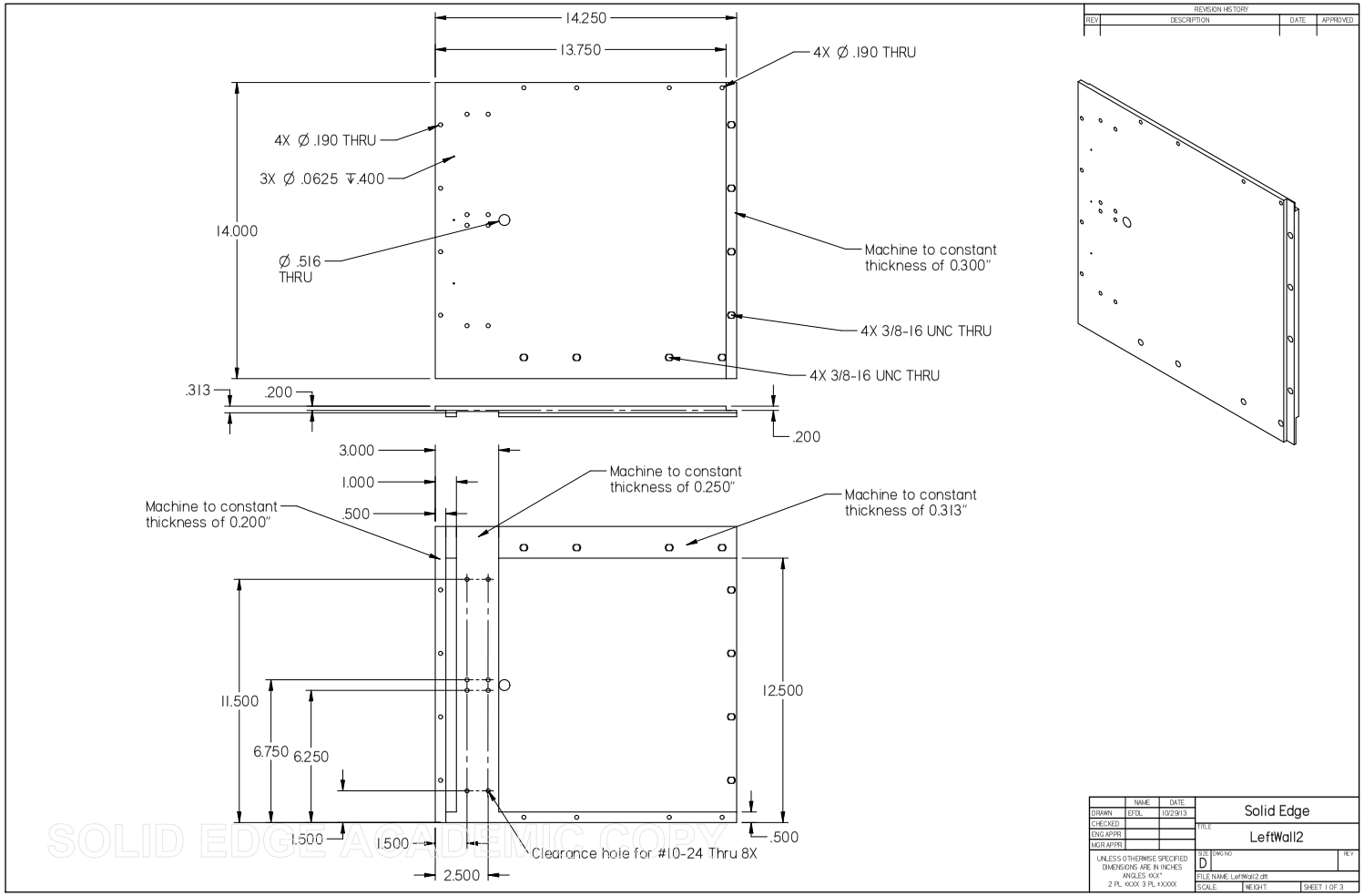

SOLID EDGE ACADEMIC COPY

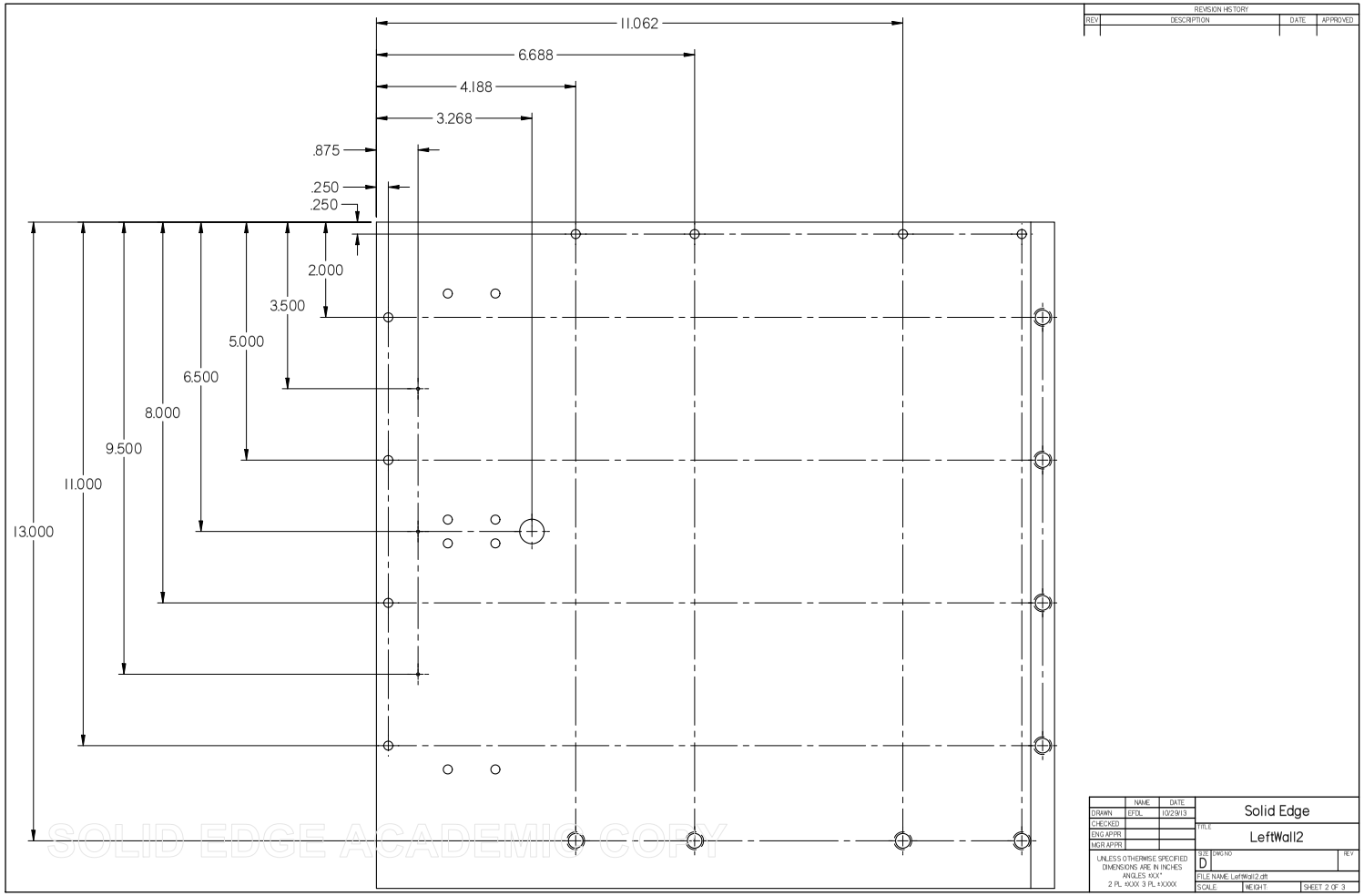
11.062
6.688
4.188
3.268
.875
.250
.250
2.000
3.500
5.000
6.500
8.000
9.500
11.000
13.000
REVISION HISTORY
REV
DESCRIPTION
DATE
APPROVED
NAME
DATE
DRAWN
EFDL
10/29/13
CHECKED
ENG APPR.
MGR APPR.
UNLESS OTHERWISE SPECIFIED
DIMENSIONS ARE IN INCHES
ANGLES: ±0.5°
2 PL: ±0.XX 3 PL: ±0.XXX
Solid Edge
TITLE
LeftWall2
SIZE
D
DWG NO
REV
FILE NAME: LeftWall2.dft
SCALE
WEIGHT
SHEET 2 OF 3
SOLID EDGE ACADEMIC COPY

REVISION HISTORY			
REV	DESCRIPTION	DATE	APPROVED

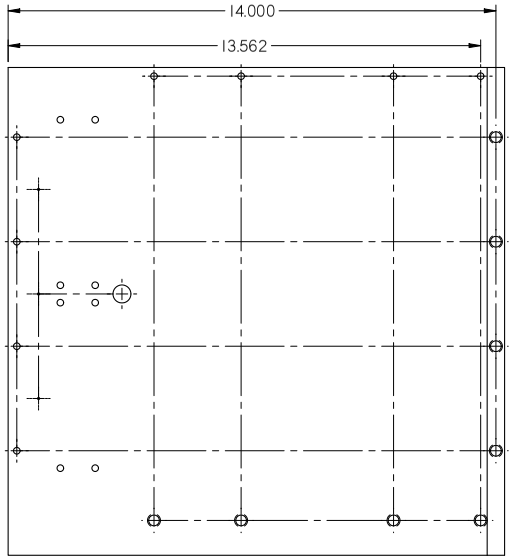

SOLID EDGE ACADEMIC COPY

	NAME	DATE
DRAWN	EFDL	10/29/13
CHECKED		
ENG APPR.		
MGR APPR.		

UNLESS OTHERWISE SPECIFIED
DIMENSIONS ARE IN INCHES
ANGLES ±0X°
2 PL ±XXX 3 PL ±XXXX

Solid Edge

TITLE
LeftWall2

SIZE D | DWG NO | REV

FILE NAME LeftWall2.dft

SCALE | WEIGHT | SHEET 3 OF 3

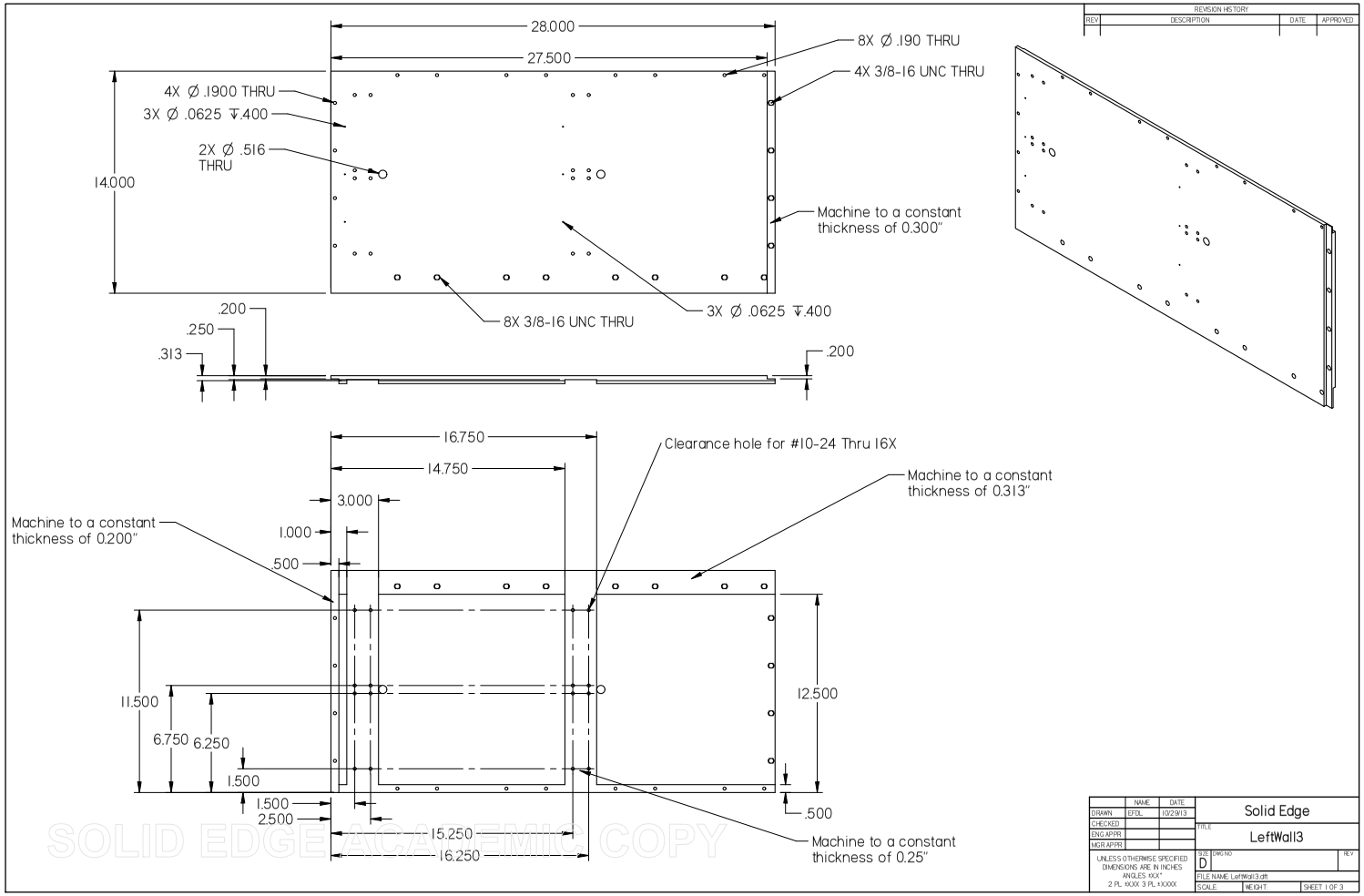

SOLID EDGE ACADEMIC COPY

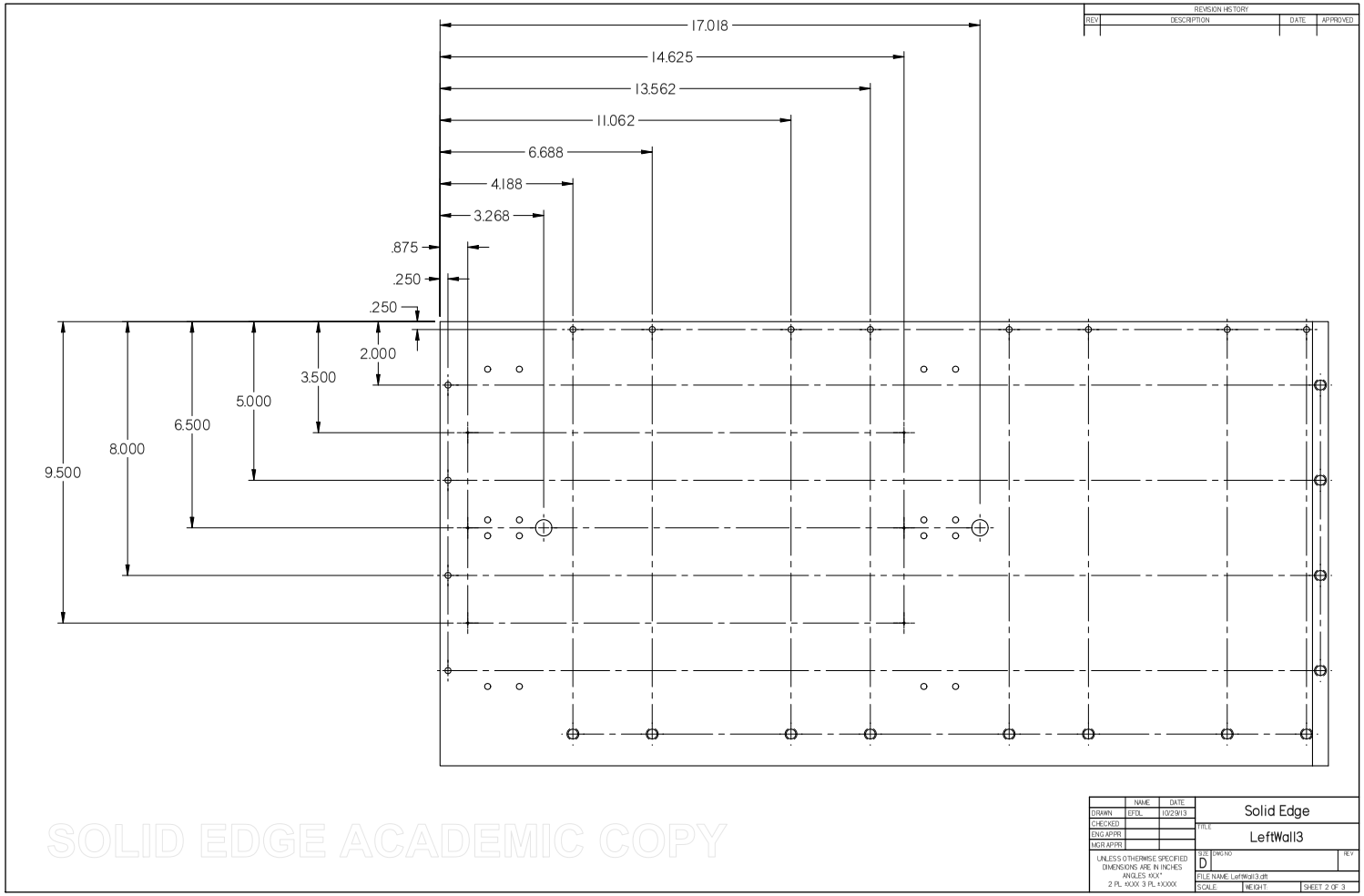
17.018
14.625
13.562
11.062
6.688
4.188
3.268
.875
.250
.250
2.000
3.500
5.000
6.500
8.000
9.500
REVISION HISTORY
REV
DESCRIPTION
DATE
APPROVED
NAME
DATE
DRAWN
EFDL
10/29/13
CHECKED
ENG APPR.
MGR APPR.
UNLESS OTHERWISE SPECIFIED
DIMENSIONS ARE IN INCHES
ANGLES: ±0X°
2 PL: ±XXX 3 PL: ±XXXX
Solid Edge
TITLE
LeftWall3
SIZE
D
DWG NO
REV
FILE NAME: LeftWall3.dft
SCALE
WEIGHT
SHEET 2 OF 3
SOLID EDGE ACADEMIC COPY

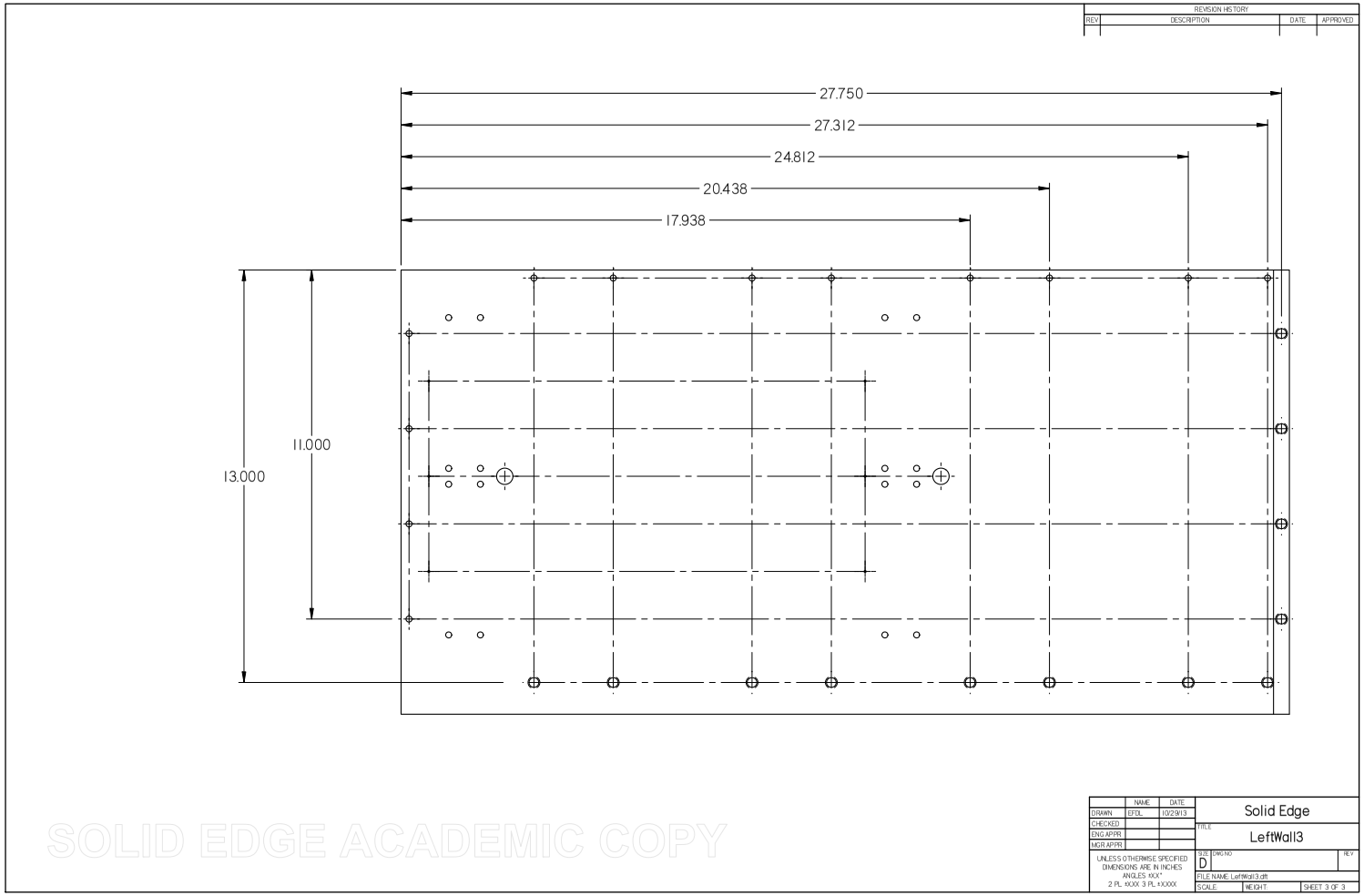
REVISION HISTORY
REV
DESCRIPTION
DATE
APPROVED
27.750
27.312
24.812
20.438
17.938
11.000
13.000
SOLID EDGE ACADEMIC COPY
NAME
DATE
DRAWN
EFDL
10/29/13
CHECKED
ENG APPR.
MGR APPR.
UNLESS OTHERWISE SPECIFIED
DIMENSIONS ARE IN INCHES
ANGLES: ±0X°
2 PL: ±XXX 3 PL: ±XXXX
Solid Edge
TITLE
LeftWall3
SIZE
D
DWG NO
REV
FILE NAME: LeftWall3.dft
SCALE
WEIGHT
SHEET 3 OF 3

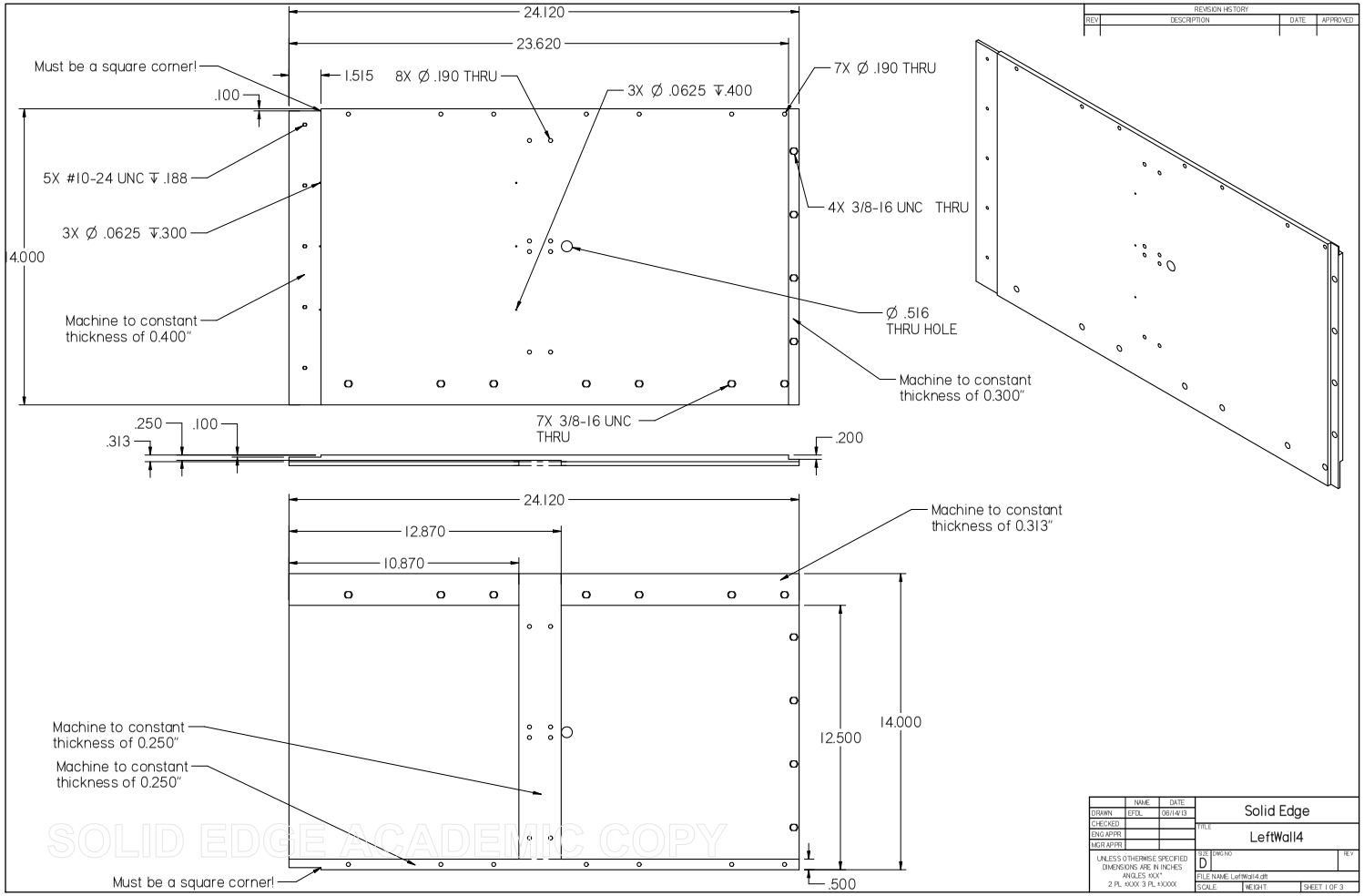

SOLID EDGE ACADEMIC COPY

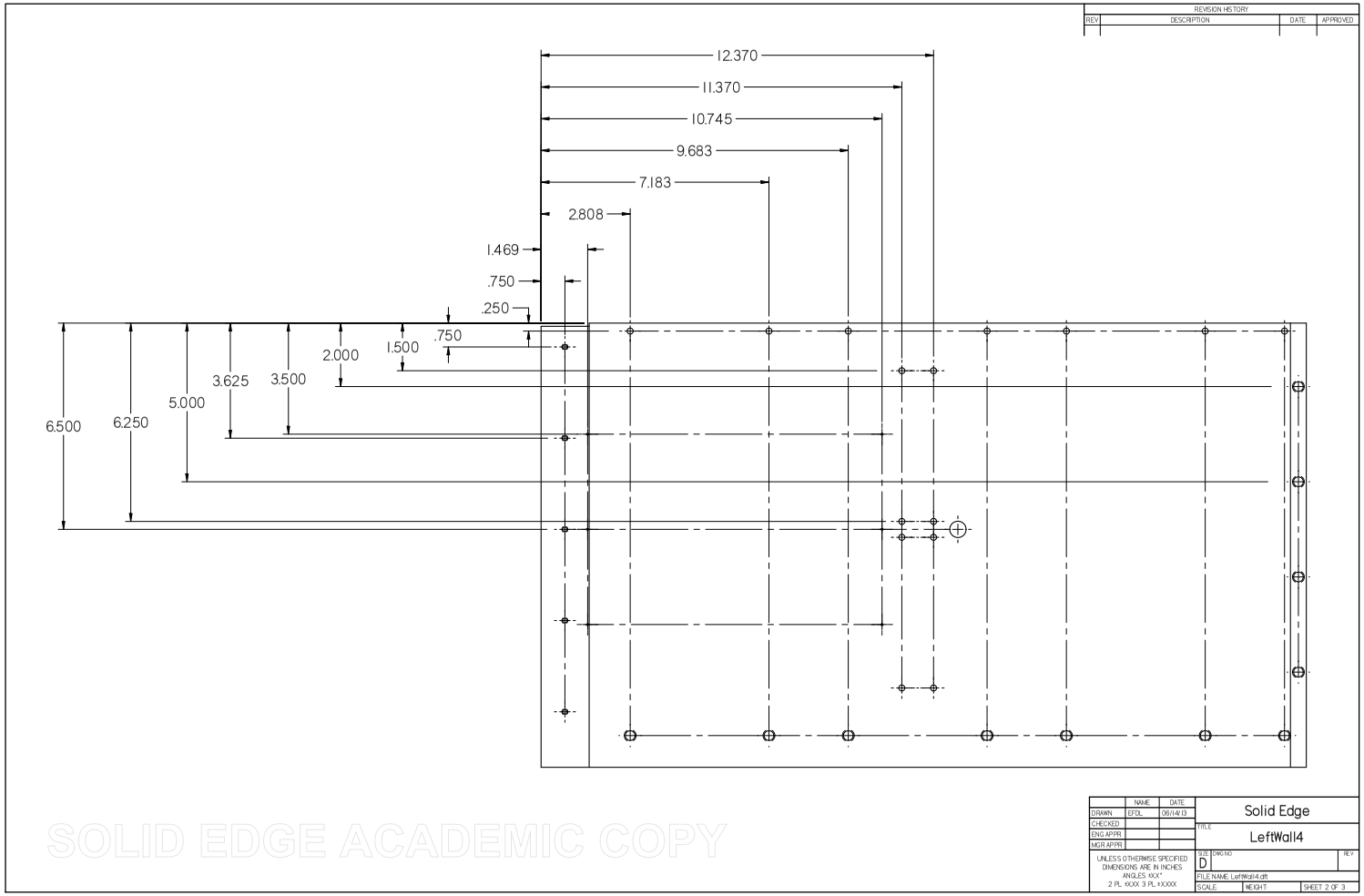
REVISION HISTORY
REV
DESCRIPTION
DATE
APPROVED
12.370
11.370
10.745
9.683
7.183
2.808
1.469
.750
.250
.750
1.500
2.000
3.500
3.625
5.000
6.250
6.500
SOLID EDGE ACADEMIC COPY
NAME
DATE
DRAWN
EFDL
06/14/13
CHECKED
ENG APPR.
MGR APPR.
UNLESS OTHERWISE SPECIFIED
DIMENSIONS ARE IN INCHES
ANGLES: ±0X°
2 PL: ±XXX 3 PL: ±XXXX
Solid Edge
TITLE
LeftWall4
SIZE
D
DWG NO
REV
FILE NAME: LeftWall4.dft
SCALE:
WEIGHT:
SHEET 2 OF 3

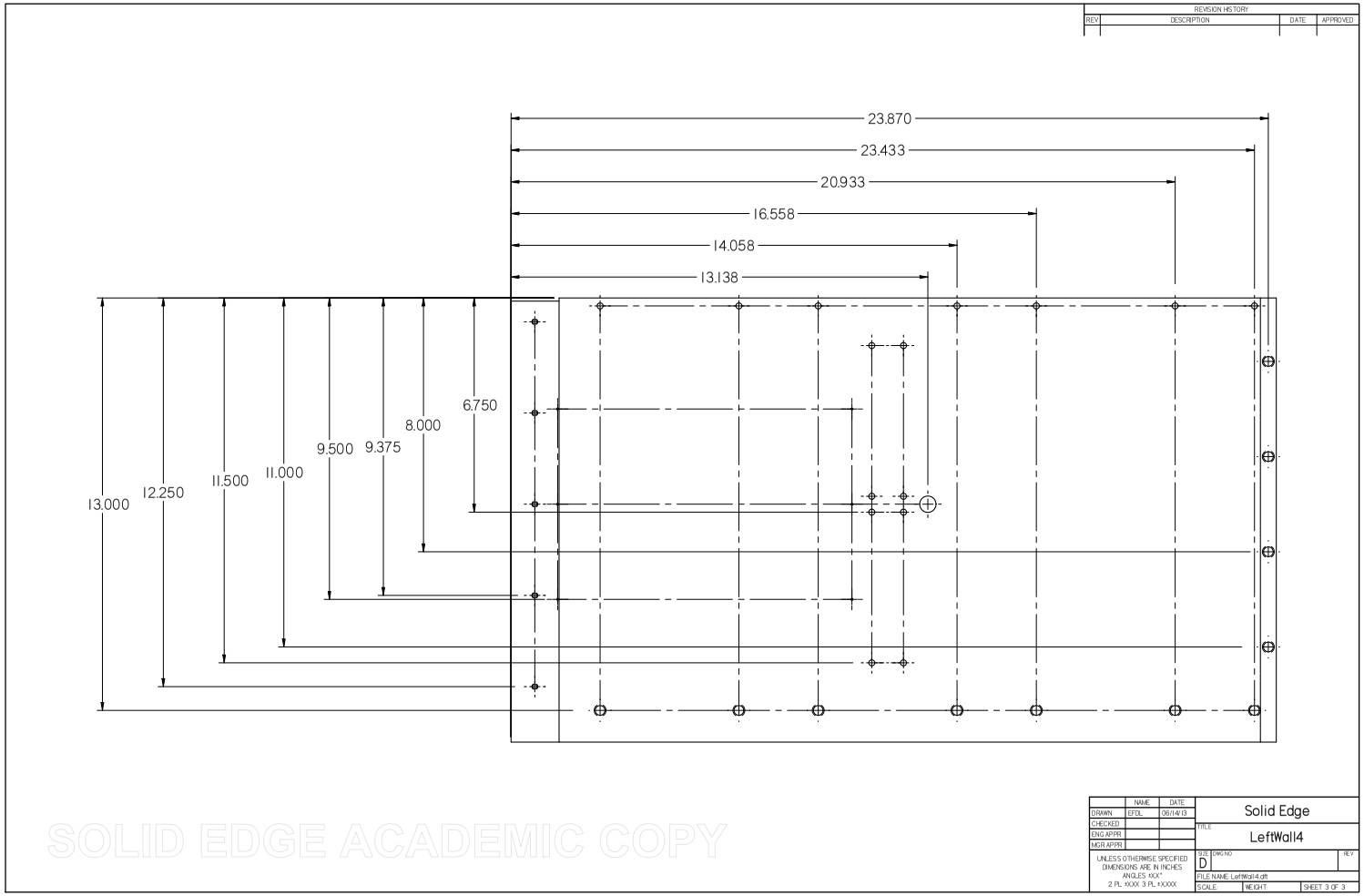
REVISION HISTORY
REV
DESCRIPTION
DATE
APPROVED
23.870
23.433
20.933
16.558
14.058
13.138
6.750
8.000
9.375
9.500
11.000
11.500
12.250
13.000
SOLID EDGE ACADEMIC COPY
NAME
DATE
DRAWN
EFDL
06/14/13
CHECKED
ENG APPR.
MGR APPR.
UNLESS OTHERWISE SPECIFIED
DIMENSIONS ARE IN INCHES
ANGLES: ±0X°
2 PL: ±XXX 3 PL: ±XXXX
Solid Edge
TITLE
LeftWall4
SIZE
D
DWG NO
REV
FILE NAME: LeftWall4.dft
SCALE
WEIGHT
SHEET 3 OF 3

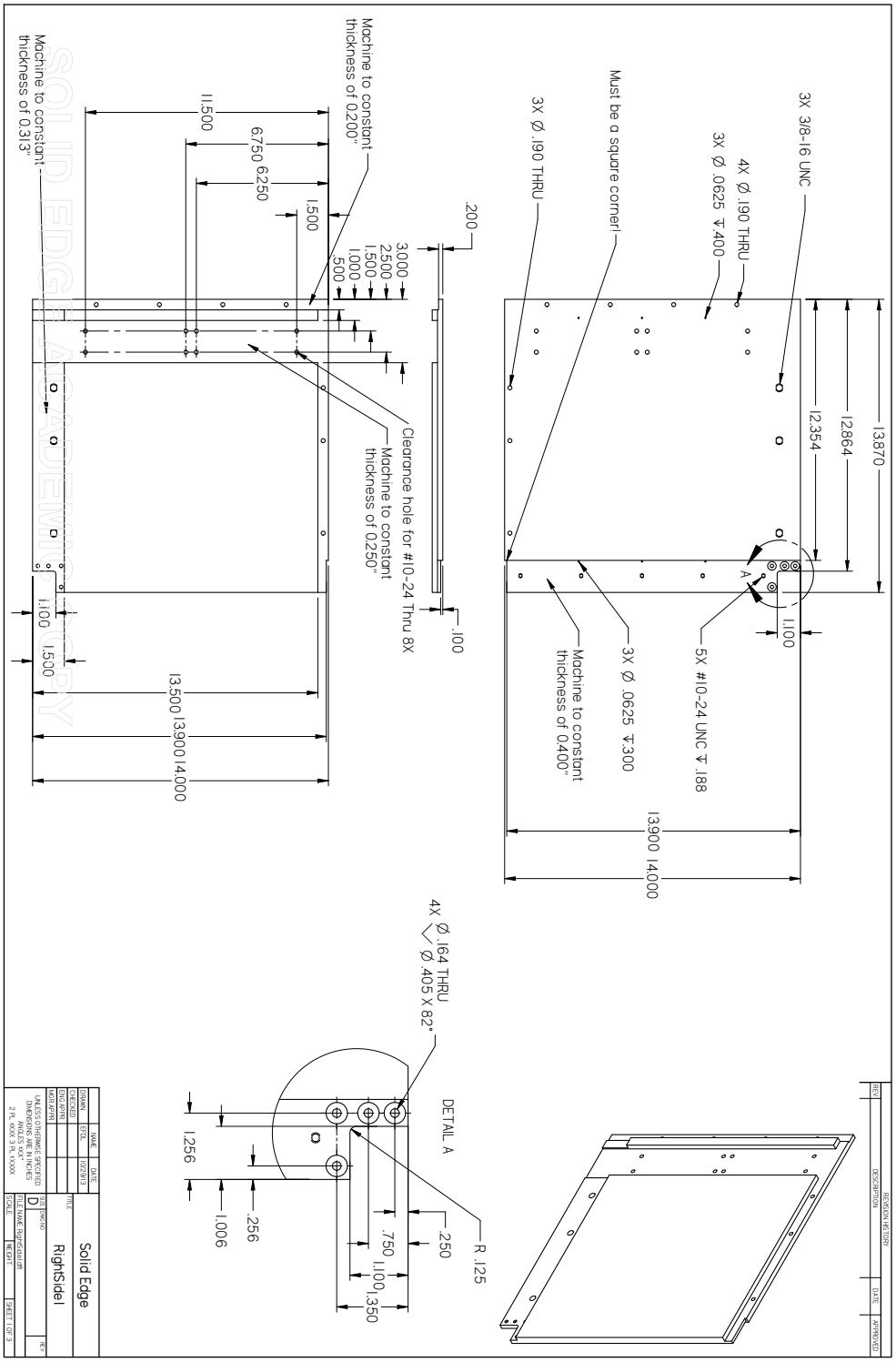
3X 3/8-16 UNC
4X Ø .190 THRU
3X Ø .0625 ↧.400
Must be a square corner!
3X Ø .190 THRU
13.870
12.864
12.354
1.100
A
5X #10-24 UNC ↧ .188
3X Ø .0625 ↧.300
Machine to constant thickness of 0.400"
13.900 14.000
.200
.100
3.000
2.500
1.500
1.000
.500
Machine to constant thickness of 0.200"
Clearance hole for #10-24 Thru 8X
Machine to constant thickness of 0.250"
1.500
6.750 6.250
11.500
Machine to constant thickness of 0.313"
1.100
1.500
13.500 13.900 14.000
4X Ø .164 THRU
Ø .405 X 82°
DETAIL A
R .125
.250
.750
1.100
1.350
.256
1.006
1.256
REVISION HISTORY
REV
DESCRIPTION
DATE
APPROVED
DRAWN
NAME
DATE
EFTL
10/29/13
CHECKED
ENGINEERING
MFG APPR
UNLESS OTHERWISE SPECIFIED
DIMENSIONS ARE IN INCHES
ANGLES ±X°
2 PL ±XX ± 3 PL ±XXX
Solid Edge
TITLE
RightSide1
SIZE
D
DWG NO
REV
FILE NAME RightSide1.dft
SCALE
WEIGHT
SHEET 1 OF 3

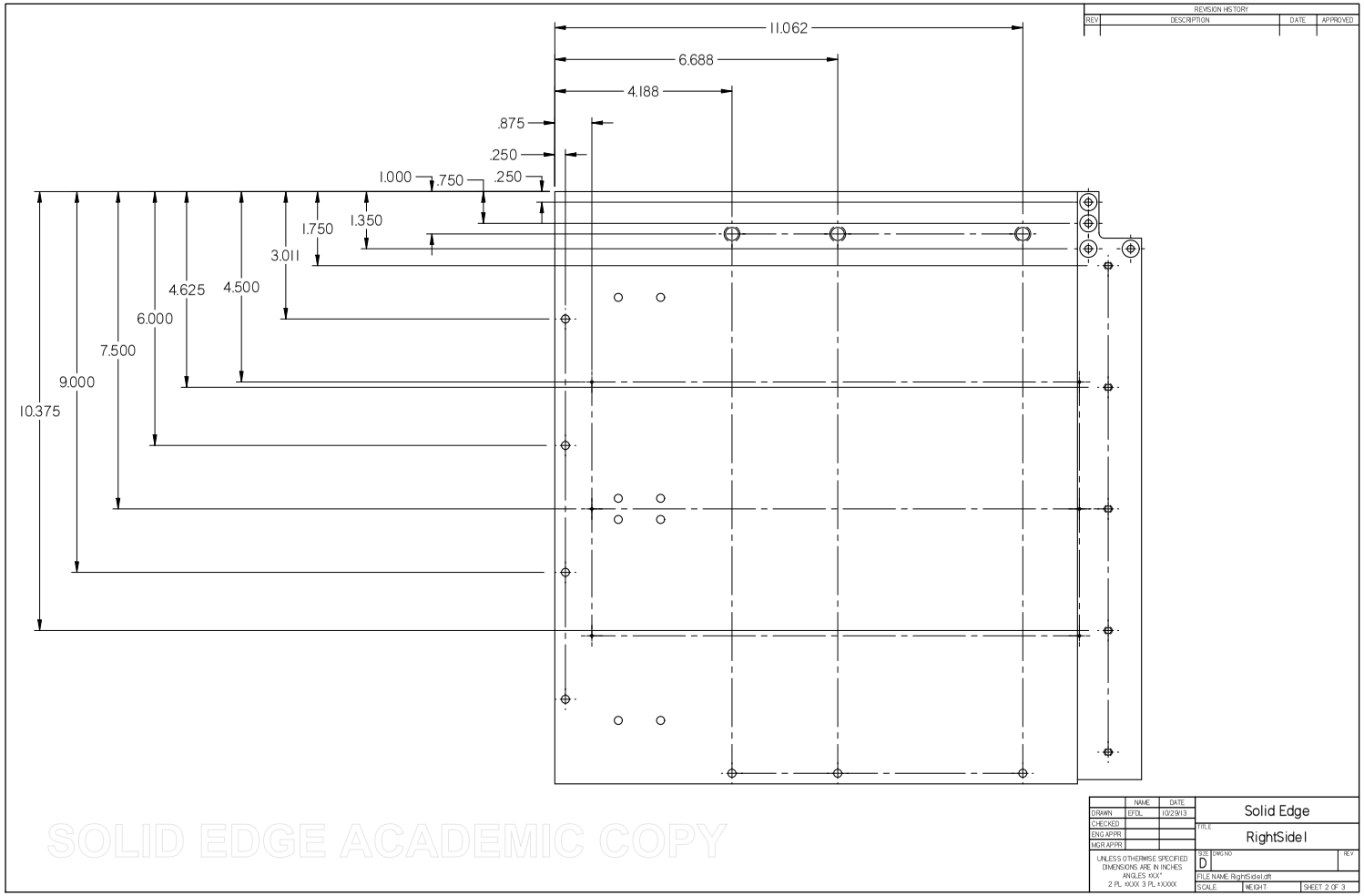
11.062
6.688
4.188
.875
.250
1.000
.750
.250
1.750
1.350
3.011
4.625
4.500
6.000
7.500
9.000
10.375
REVISION HISTORY
REV
DESCRIPTION
DATE
APPROVED
NAME
DATE
DRAWN
EFDL
10/29/13
CHECKED
ENG APPR.
MGR APPR.
UNLESS OTHERWISE SPECIFIED
DIMENSIONS ARE IN INCHES
ANGLES: ±0.5°
2 PL: ±0.XX 3 PL: ±0.XXX
Solid Edge
TITLE
RightSide1
SIZE
D
DWG NO
REV
FILE NAME: RightSide1.dft
SCALE
WEIGHT
SHEET 2 OF 3
SOLID EDGE ACADEMIC COPY

REVISION HISTORY			
REV	DESCRIPTION	DATE	APPROVED

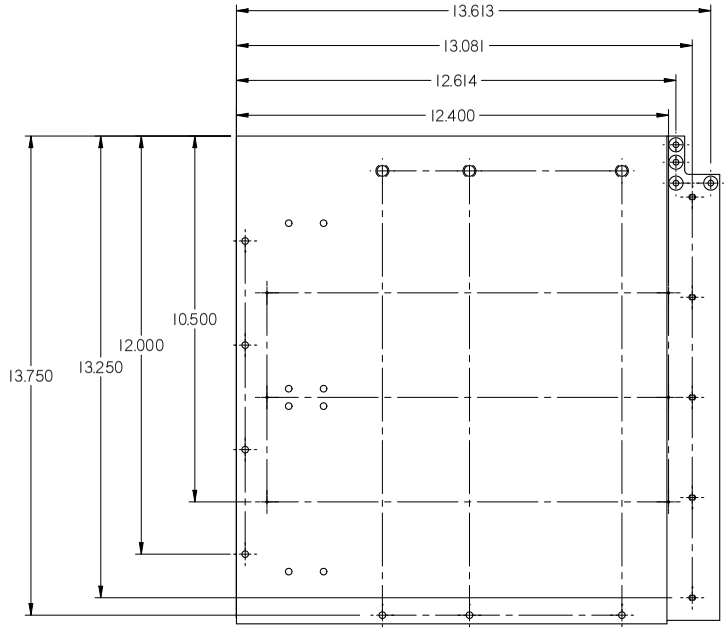

SOLID EDGE ACADEMIC COPY

	NAME	DATE
DRAWN	EFDL	10/29/13
CHECKED		
ENG APPR.		
MGR APPR.		

UNLESS OTHERWISE SPECIFIED
DIMENSIONS ARE IN INCHES
ANGLES ±0.5°
2 PL ±0.XX 3 PL ±0.XXX

Solid Edge

TITLE
RightSide1

SIZE D | DWG NO | REV

FILE NAME RightSide1.dft

SCALE | WEIGHT | SHEET 3 OF 3

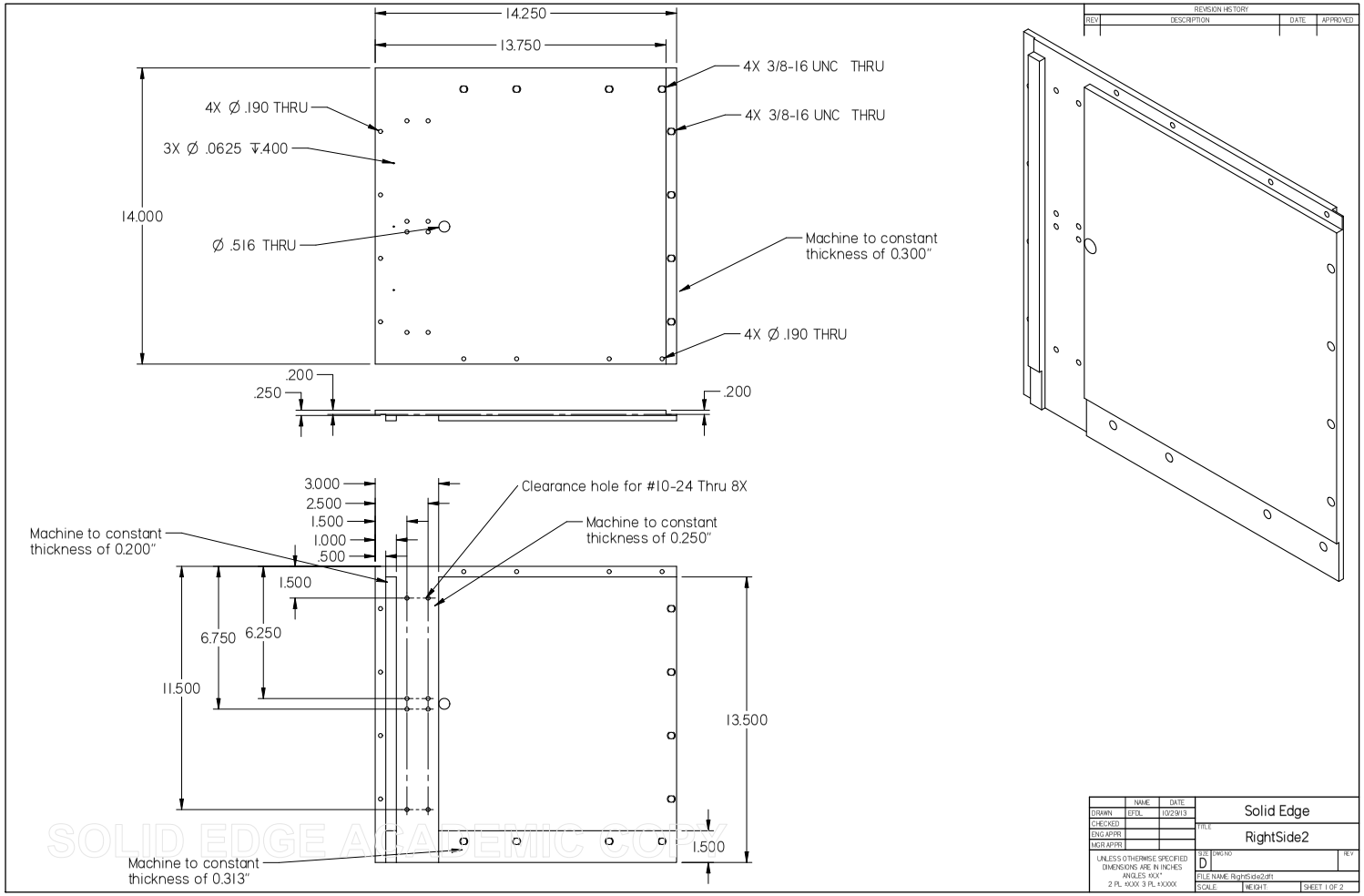
14.250
13.750
4X 3/8-16 UNC THRU
4X 3/8-16 UNC THRU
4X Ø .190 THRU
3X Ø .0625 ↧.400
14.000
Ø .516 THRU
Machine to constant thickness of 0.300"
4X Ø .190 THRU
.200
.250
.200
3.000
2.500
1.500
1.000
.500
Clearance hole for #10-24 Thru 8X
Machine to constant thickness of 0.250"
Machine to constant thickness of 0.200"
1.500
6.750
6.250
11.500
13.500
1.500
Machine to constant thickness of 0.313"
REVISION HISTORY
REV
DESCRIPTION
DATE
APPROVED
NAME
DATE
DRAWN
EFDL
10/29/13
CHECKED
ENG APPR.
MGR APPR.
UNLESS OTHERWISE SPECIFIED DIMENSIONS ARE IN INCHES ANGLES: ±0X° 2 PL ±XXX 3 PL ±XXXX
Solid Edge
TITLE
RightSide2
SIZE
D
DWG NO
REV
FILE NAME: RightSide2.dft
SCALE
WEIGHT
SHEET 1 OF 2

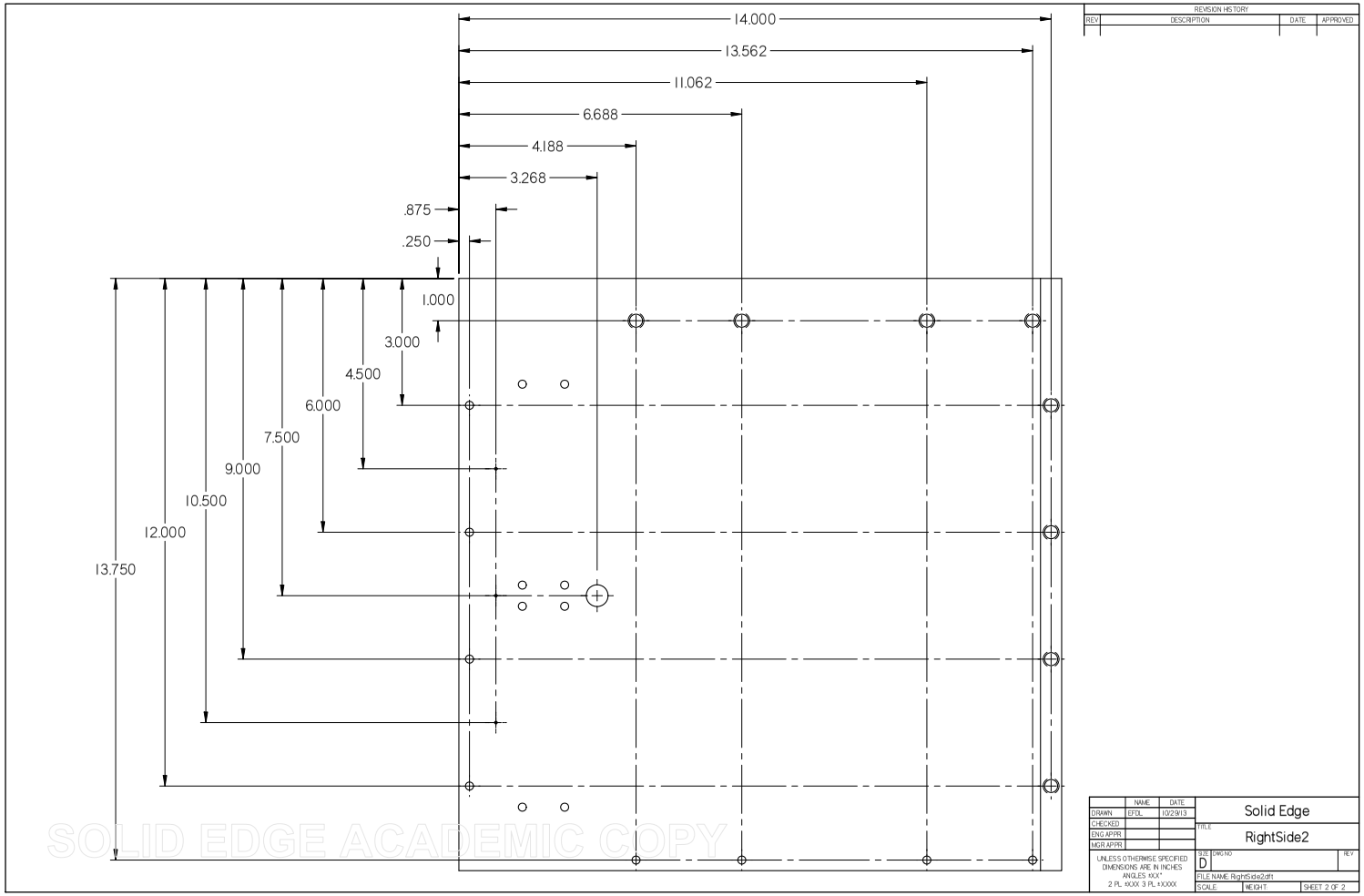
14.000
13.562
11.062
6.688
4.188
3.268
.875
.250
1.000
3.000
4.500
6.000
7.500
9.000
10.500
12.000
13.750
REVISION HISTORY
REV
DESCRIPTION
DATE
APPROVED
NAME
DATE
DRAWN
EFDL
10/29/13
CHECKED
ENG APPR.
MGR APPR.
UNLESS OTHERWISE SPECIFIED
DIMENSIONS ARE IN INCHES
ANGLES: ±0X°
2 PL: ±XXX 3 PL: ±XXXX
Solid Edge
TITLE
RightSide2
SIZE
D
DWG NO
REV
FILE NAME: RightSide2.dft
SCALE
WEIGHT
SHEET 2 OF 2
SOLID EDGE ACADEMIC COPY

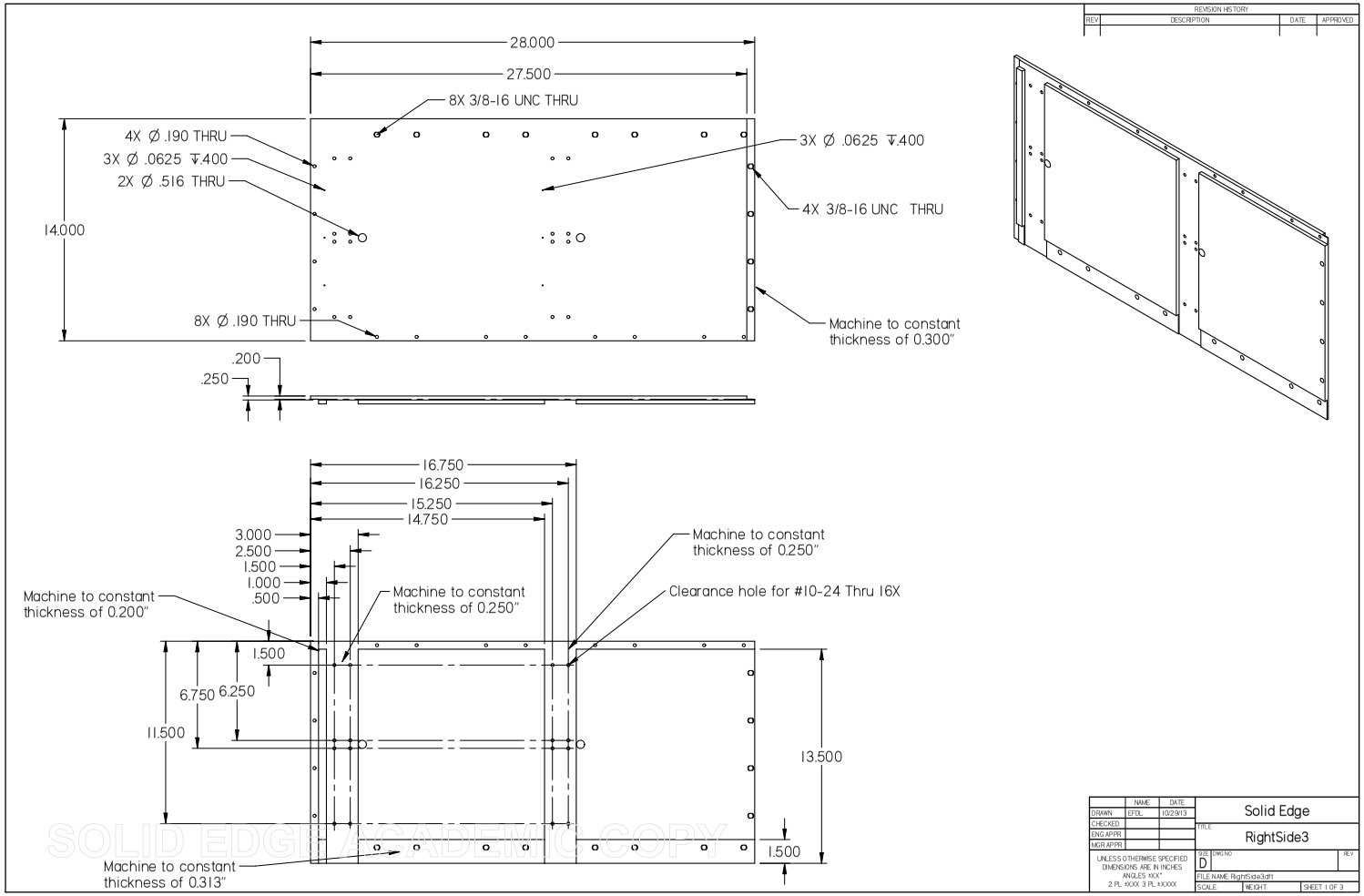
REVISION HISTORY
REV
DESCRIPTION
DATE
APPROVED
28.000
27.500
8X 3/8-16 UNC THRU
4X Ø .190 THRU
3X Ø .0625 ↧.400
2X Ø .516 THRU
3X Ø .0625 ↧.400
4X 3/8-16 UNC THRU
14.000
8X Ø .190 THRU
Machine to constant thickness of 0.300"
.200
.250
16.750
16.250
15.250
14.750
3.000
2.500
1.500
1.000
.500
Machine to constant thickness of 0.250"
Machine to constant thickness of 0.200"
Machine to constant thickness of 0.250"
Clearance hole for #10-24 Thru 16X
1.500
6.750
6.250
11.500
13.500
1.500
Machine to constant thickness of 0.313"
SOLID EDGE ACADEMIC COPY
NAME
DATE
DRAWN
EFDL
10/29/13
CHECKED
ENG APPR.
MGR APPR.
UNLESS OTHERWISE SPECIFIED DIMENSIONS ARE IN INCHES ANGLES: ±0X° 2 PL ±XXX 3 PL ±XXXX
Solid Edge
TITLE
RightSide3
SIZE
D
DWG NO
REV
FILE NAME RightSide3.dft
SCALE
WEIGHT
SHEET 1 OF 3

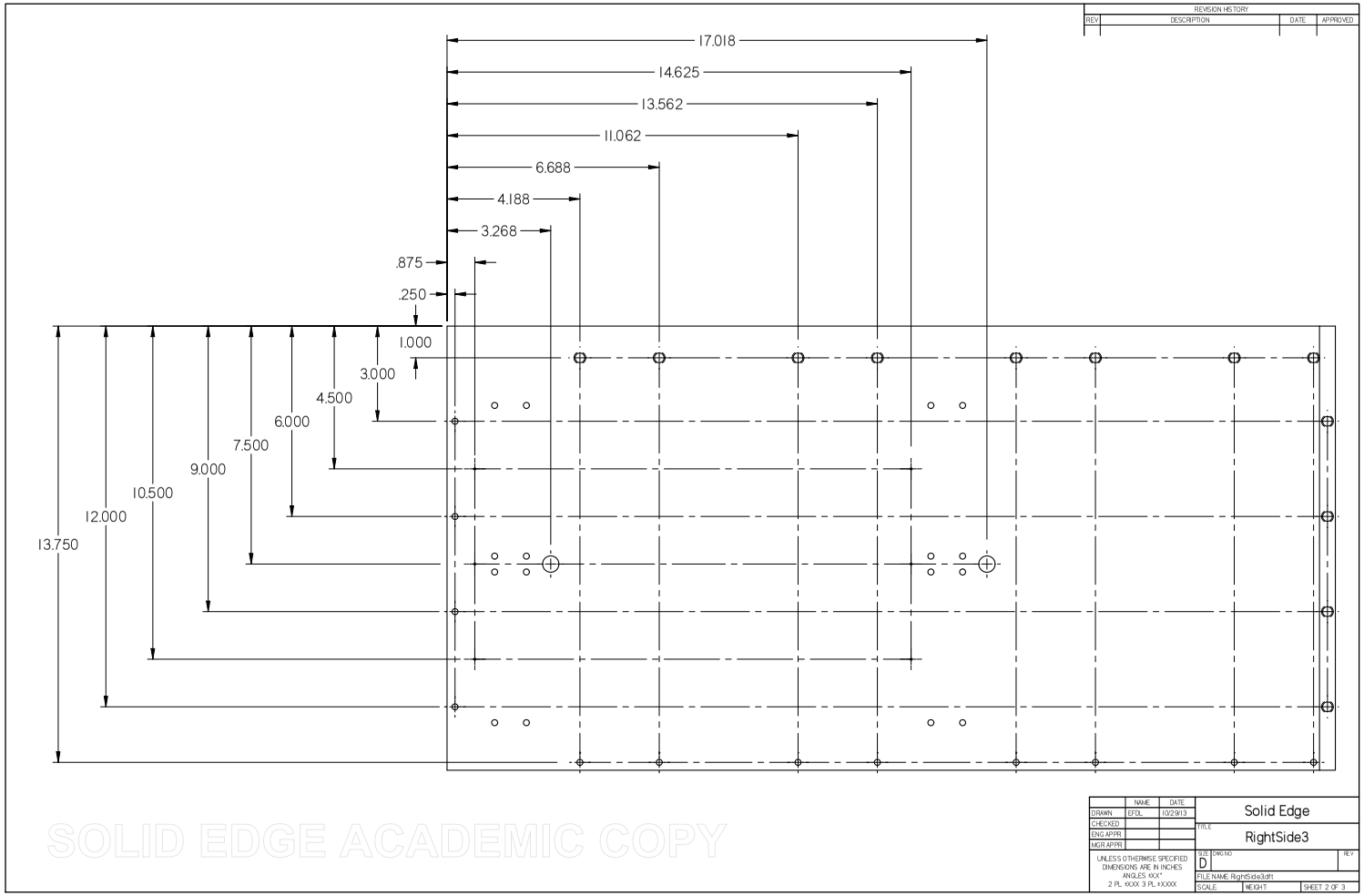
REVISION HISTORY
REV
DESCRIPTION
DATE
APPROVED
17.018
14.625
13.562
11.062
6.688
4.188
3.268
.875
.250
1.000
3.000
4.500
6.000
7.500
9.000
10.500
12.000
13.750
SOLID EDGE ACADEMIC COPY
NAME
DATE
DRAWN
EFDL
10/29/13
CHECKED
ENG APPR.
MGR APPR.
UNLESS OTHERWISE SPECIFIED
DIMENSIONS ARE IN INCHES
ANGLES: ±0X°
2 PL: ±XXX 3 PL: ±XXXX
Solid Edge
TITLE
RightSide3
SIZE
D
DWG NO
REV
FILE NAME: RightSide3.df1
SCALE
WEIGHT
SHEET 2 OF 3

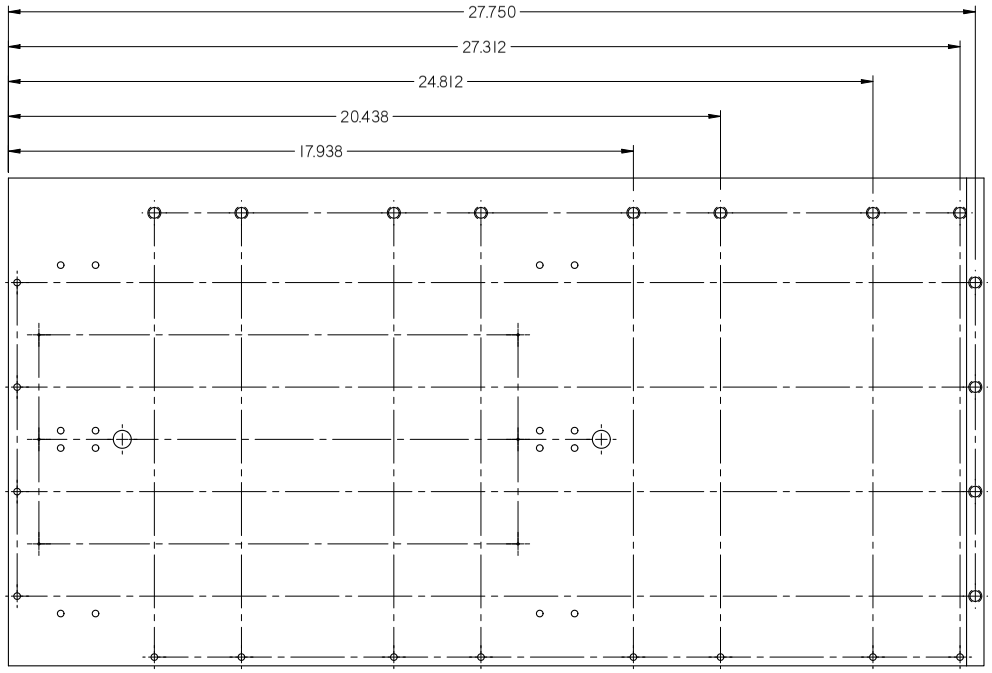

REVISION HISTORY

REV	DESCRIPTION	DATE	APPROVED

	NAME	DATE
DRAWN	EFDL	10/29/13
CHECKED		
ENG APPR.		
MGR APPR.		

UNLESS OTHERWISE SPECIFIED
DIMENSIONS ARE IN INCHES
ANGLES: ±0.5°
2 PL: ±0.XX 3 PL: ±0.XXX

Solid Edge

TITLE: RightSide3

SIZE: D | DWG NO | REV

FILE NAME: RightSide3.dft

SCALE | WEIGHT | SHEET 3 OF 3

SOLID EDGE ACADEMIC COPY

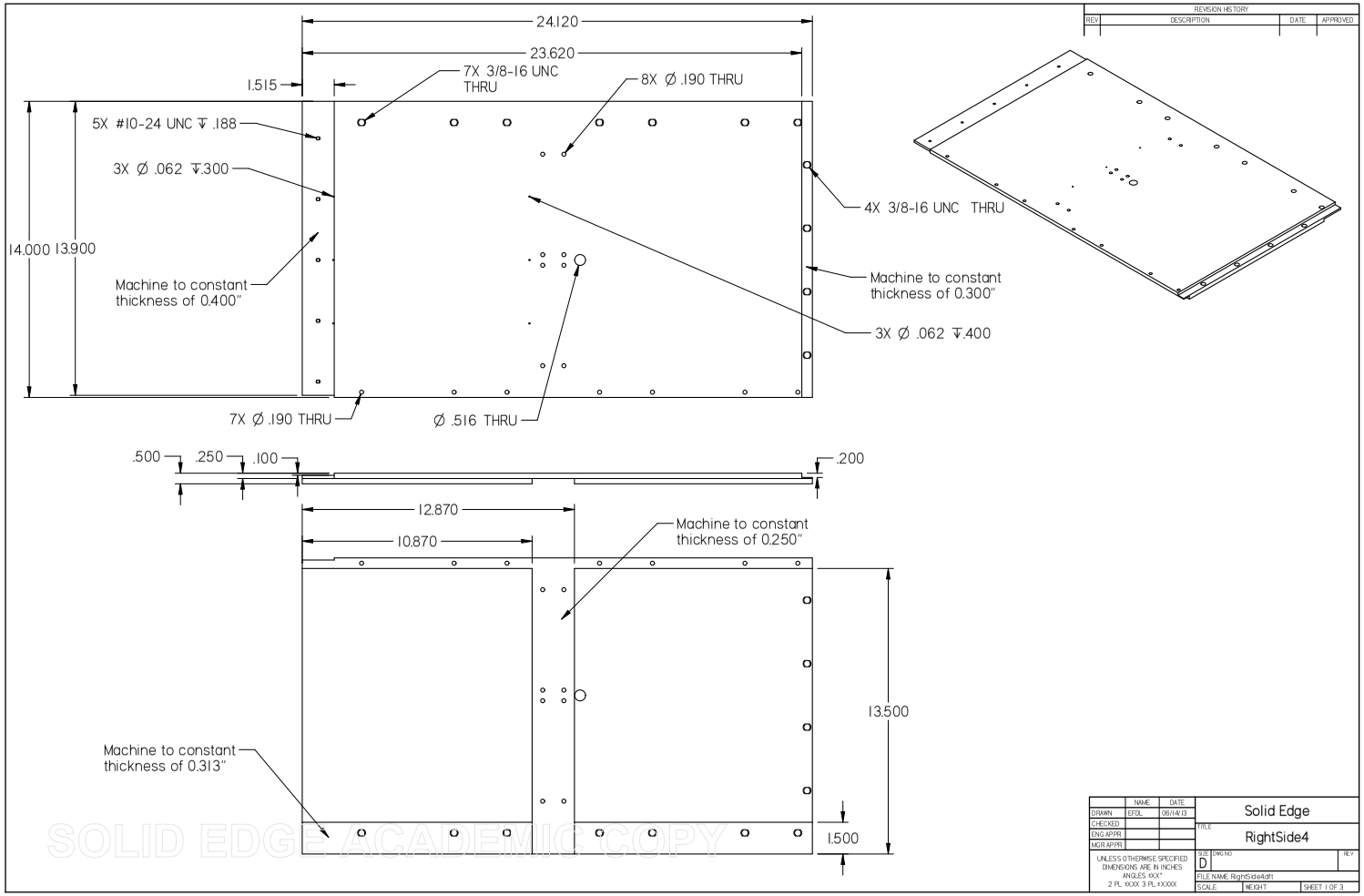
24.120
23.620
1.515
7X 3/8-16 UNC THRU
8X Ø .190 THRU
5X #10-24 UNC ↧ .188
3X Ø .062 ↧.300
14.000 13.900
Machine to constant thickness of 0.400"
4X 3/8-16 UNC THRU
Machine to constant thickness of 0.300"
3X Ø .062 ↧.400
7X Ø .190 THRU
Ø .516 THRU
.500
.250
.100
.200
12.870
10.870
Machine to constant thickness of 0.250"
13.500
Machine to constant thickness of 0.313"
1.500
REVISION HISTORY
REV
DESCRIPTION
DATE
APPROVED
NAME
DATE
DRAWN
EFDL
06/14/13
CHECKED
ENG APPR.
MGR APPR.
UNLESS OTHERWISE SPECIFIED DIMENSIONS ARE IN INCHES ANGLES: ±0.5° 2 PL: ±0.XX 3 PL: ±0.XXX
Solid Edge
TITLE
RightSide4
SIZE
D
DWG NO
REV
FILE NAME: RightSide4.dft
SCALE:
WEIGHT:
SHEET 1 OF 3
SOLID EDGE ACADEMIC COPY

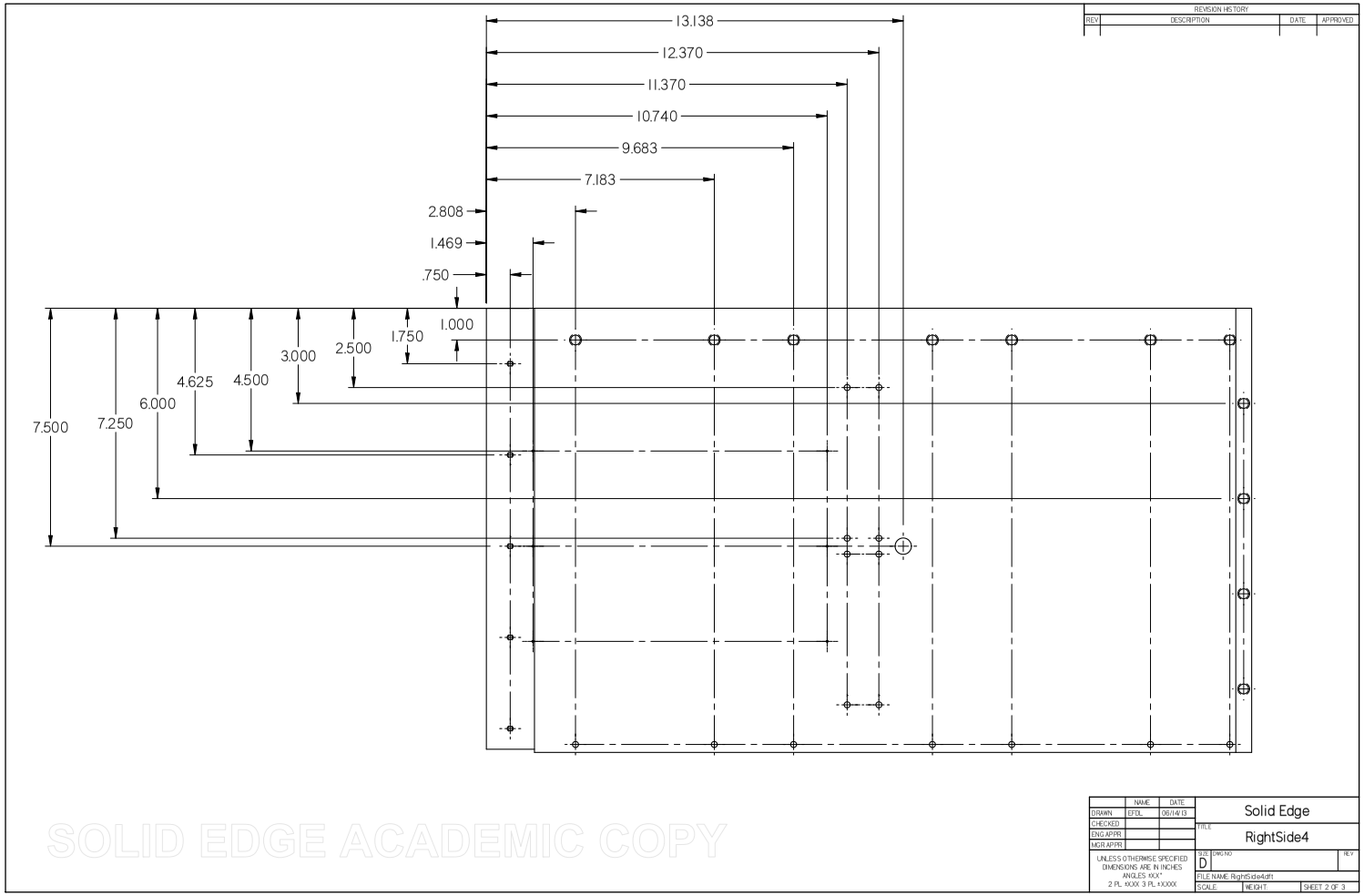
REVISION HISTORY
REV
DESCRIPTION
DATE
APPROVED
13.138
12.370
11.370
10.740
9.683
7.183
2.808
1.469
.750
1.000
1.750
2.500
3.000
4.500
4.625
6.000
7.250
7.500
SOLID EDGE ACADEMIC COPY
NAME
DATE
DRAWN
EFDL
06/14/13
CHECKED
ENG APPR
MGR APPR
UNLESS OTHERWISE SPECIFIED
DIMENSIONS ARE IN INCHES
ANGLES: ±0X°
2 PL: ±XXX 3 PL: ±XXXX
Solid Edge
TITLE
RightSide4
SIZE
D
DWG NO
REV
FILE NAME: RightSide4.dft
SCALE
WEIGHT
SHEET 2 OF 3

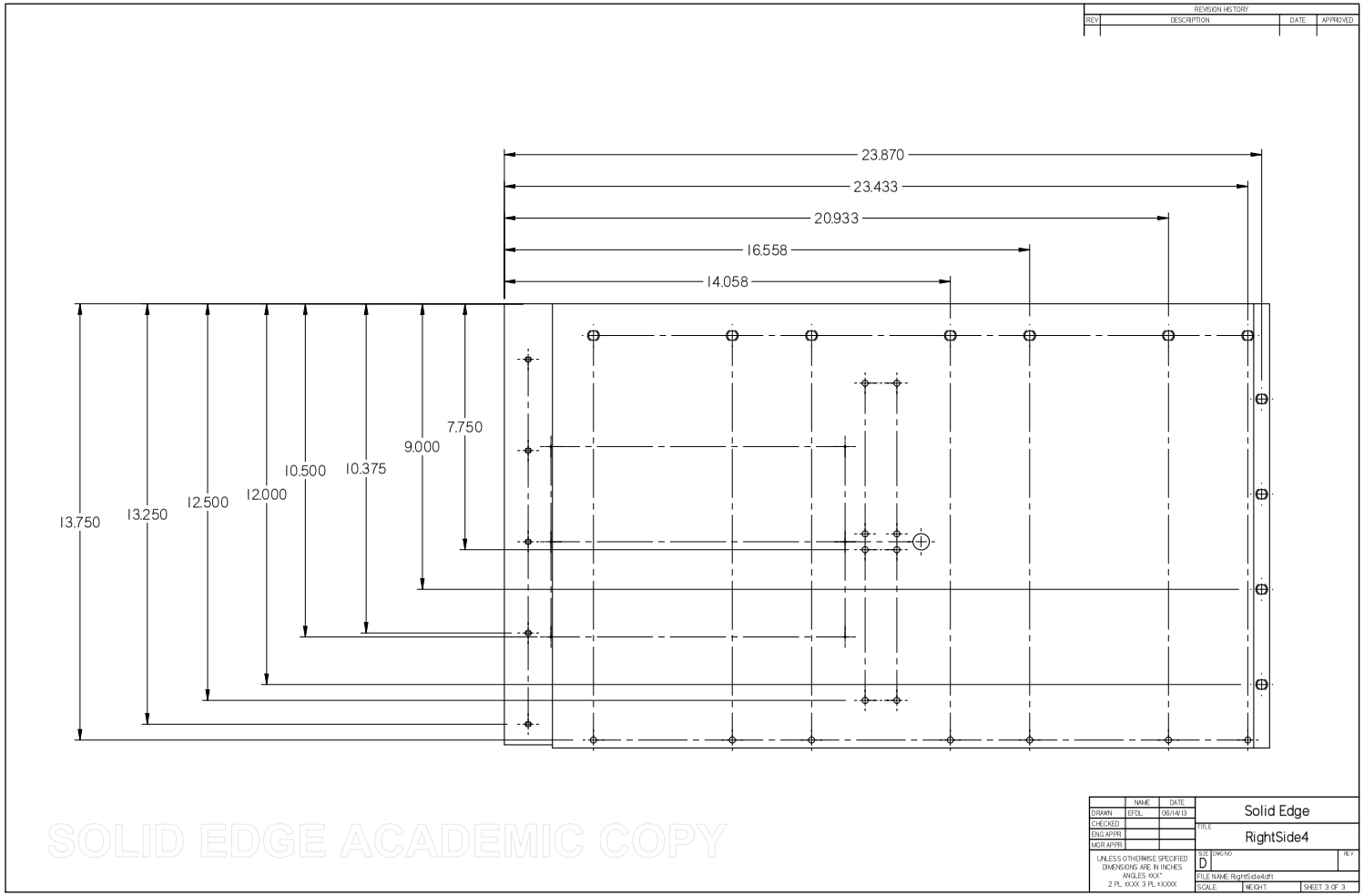
REVISION HISTORY
REV
DESCRIPTION
DATE
APPROVED
23.870
23.433
20.933
16.558
14.058
13.750
13.250
12.500
12.000
10.500
10.375
9.000
7.750
SOLID EDGE ACADEMIC COPY
NAME
DATE
DRAWN
EFDL
06/14/13
CHECKED
ENG APPR.
MGR APPR.
UNLESS OTHERWISE SPECIFIED
DIMENSIONS ARE IN INCHES
ANGLES: ±0.5°
2 PL: ±0.XX 3 PL: ±0.XXX
Solid Edge
TITLE
RightSide4
SIZE
D
DWG NO
REV
FILE NAME: RightSide4.dft
SCALE
WEIGHT
SHEET 3 OF 3

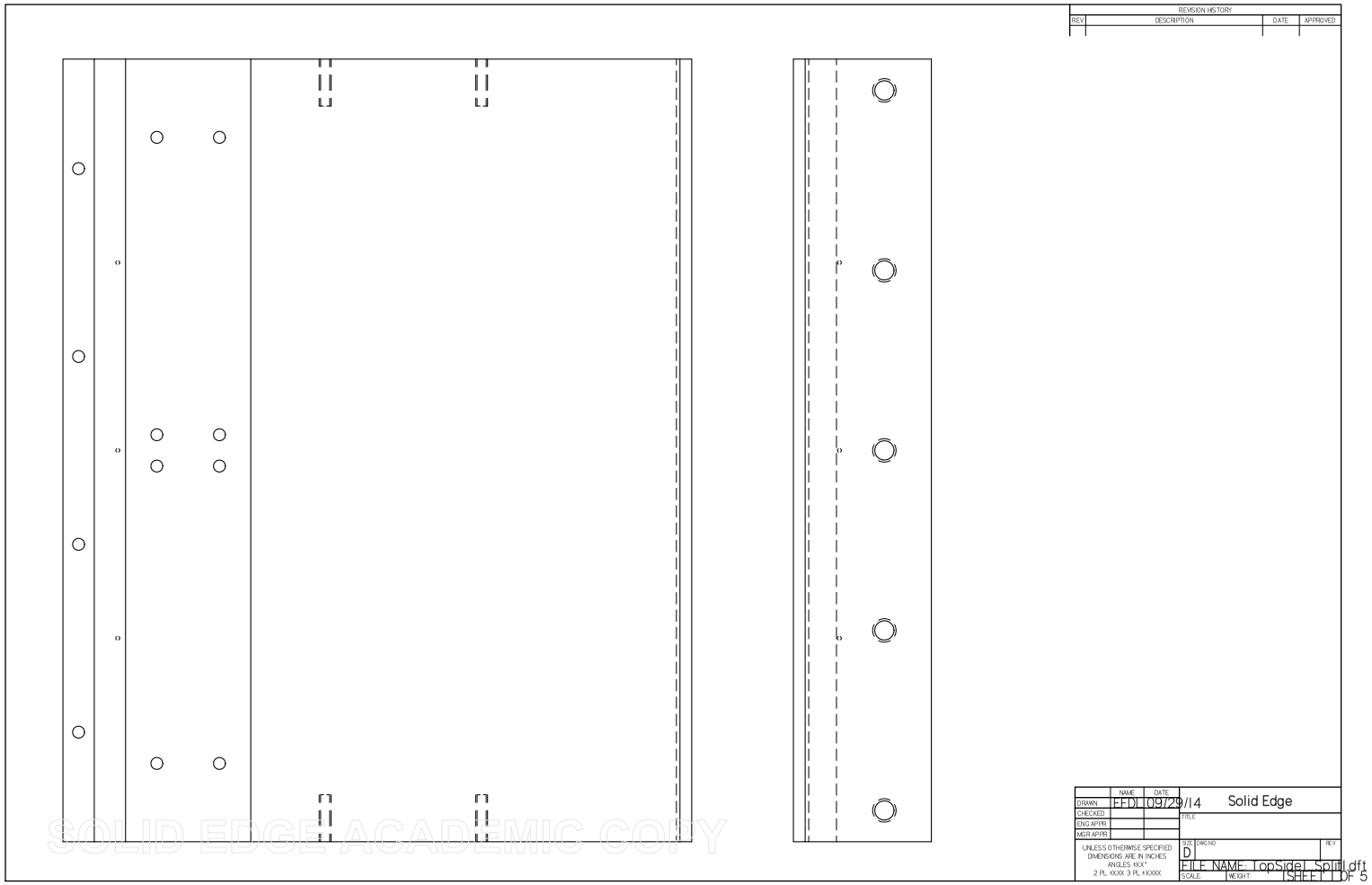
REVISION HISTORY
REV
DESCRIPTION
DATE
APPROVED
NAME
DATE
DRAWN
EFDL
09/29/14
CHECKED
ENG APPR.
MGR APPR.
UNLESS OTHERWISE SPECIFIED
DIMENSIONS ARE IN INCHES
ANGLES: XX.X°
2 PL ±XXX 3 PL ±XXXX
Solid Edge
TITLE
SIZE
D
DWG NO
REV
FILE NAME: TopSideL SplitL.dft
SCALE
WEIGHT
SHEET 1 OF 5
SOLID EDGE ACADEMIC COPY

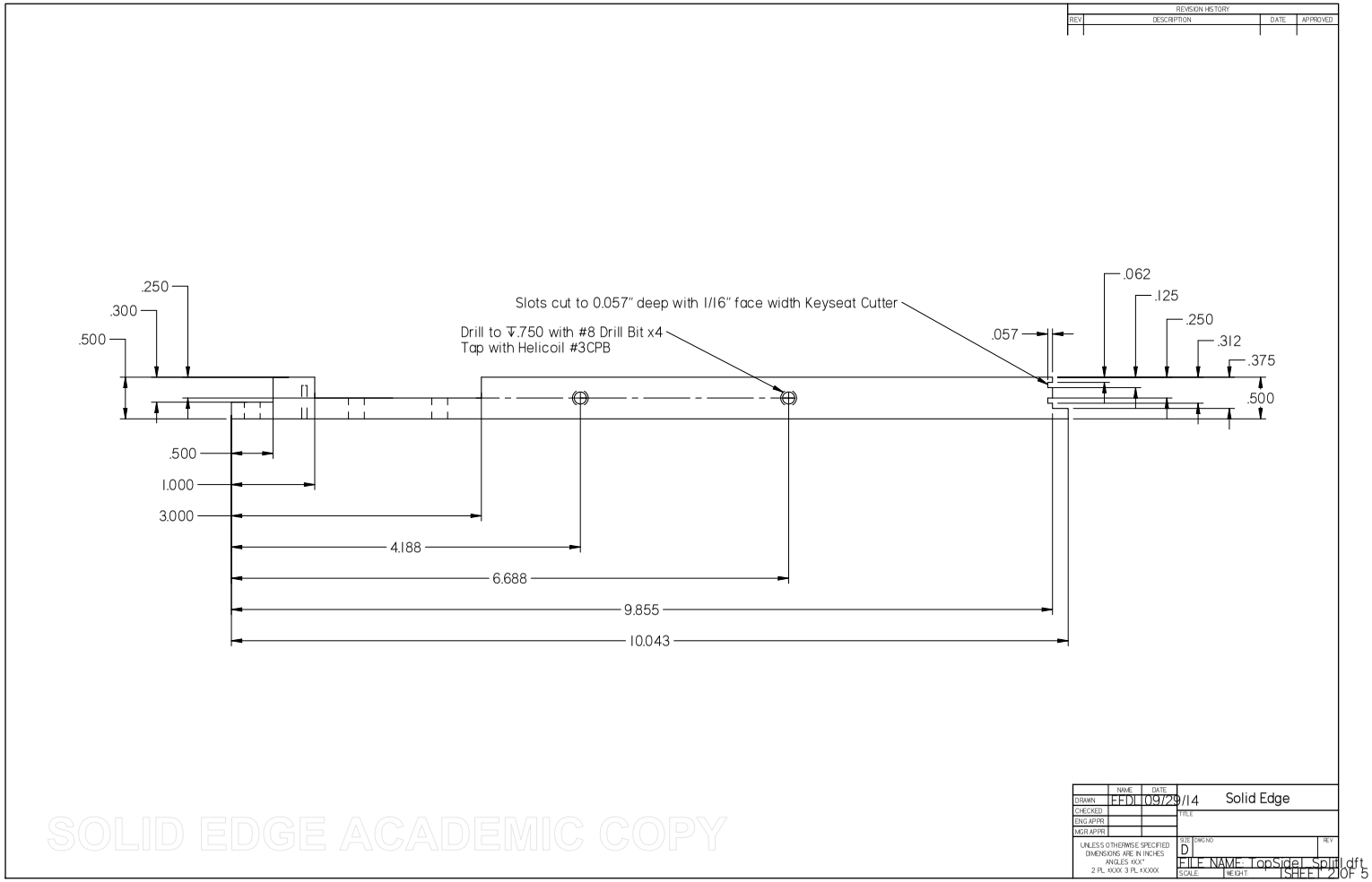
REVISION HISTORY
REV
DESCRIPTION
DATE
APPROVED
.250
.300
.500
Slots cut to 0.057" deep with 1/16" face width Keyseat Cutter
Drill to ∓.750 with #8 Drill Bit x4
Tap with Helicoil #3CPB
.057
.062
.125
.250
.312
.375
.500
.500
1.000
3.000
4.188
6.688
9.855
10.043
NAME
DATE
DRAWN
FFDL
09/29/14
CHECKED
ENG APPR.
MGR APPR.
Solid Edge
TITLE
UNLESS OTHERWISE SPECIFIED
DIMENSIONS ARE IN INCHES
ANGLES: ±0.5°
2 PL: ±0.XX 3 PL: ±0.XXX
SIZE
DWG NO
REV
D
FILE NAME: TopSideLSplit.dft
SCALE
WEIGHT
SHEET 2 OF 5
SOLID EDGE ACADEMIC COPY

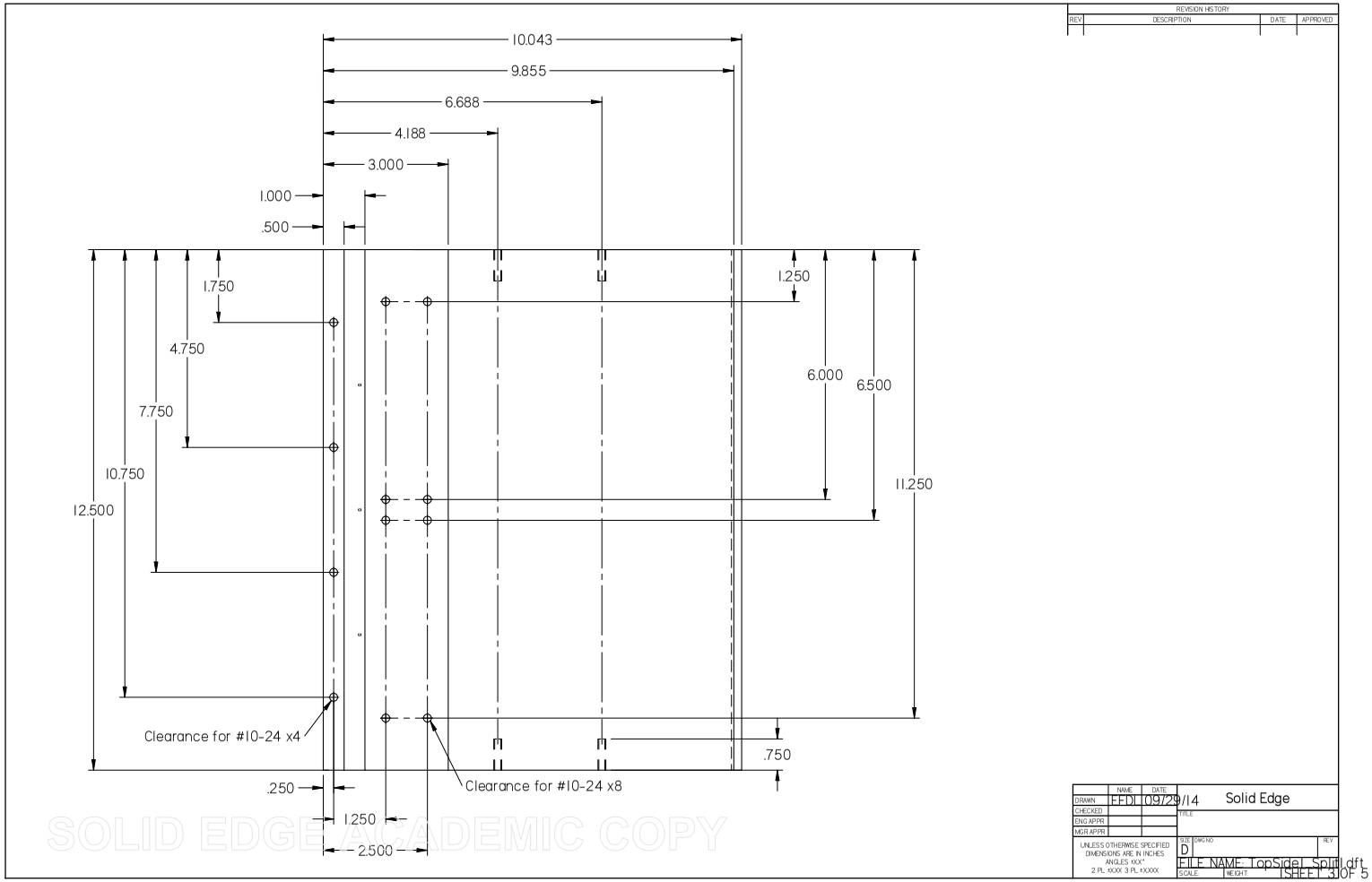

SOLID EDGE/ACADEMIC COPY

REVISION HISTORY			
REV	DESCRIPTION	DATE	APPROVED

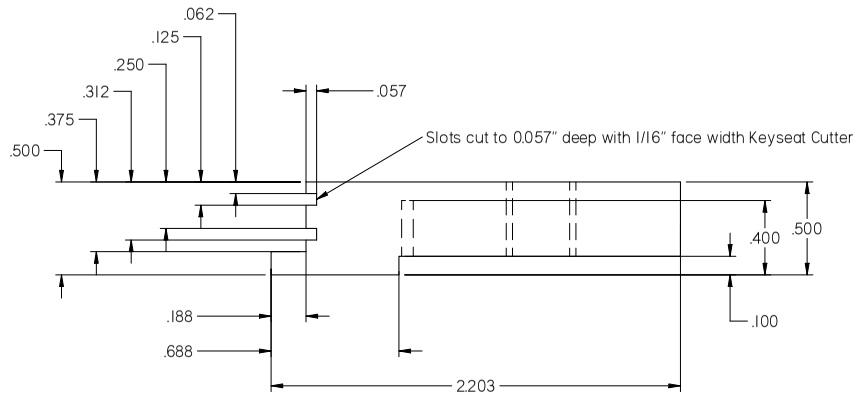

	NAME	DATE	
DRAWN	FFDL	09/29/14	Solid Edge
CHECKED			TITLE
ENG APPR.			
MGR APPR.			

UNLESS OTHERWISE SPECIFIED
DIMENSIONS ARE IN INCHES
ANGLES: ±0.5°
2 PL: ±0.XX 3 PL: ±0.XXX

SIZE D | DWG NO | REV

FILE NAME: TopSideL_Spill.dft

SCALE | WEIGHT | SHEET 4 OF 5

SOLID EDGE ACADEMIC COPY

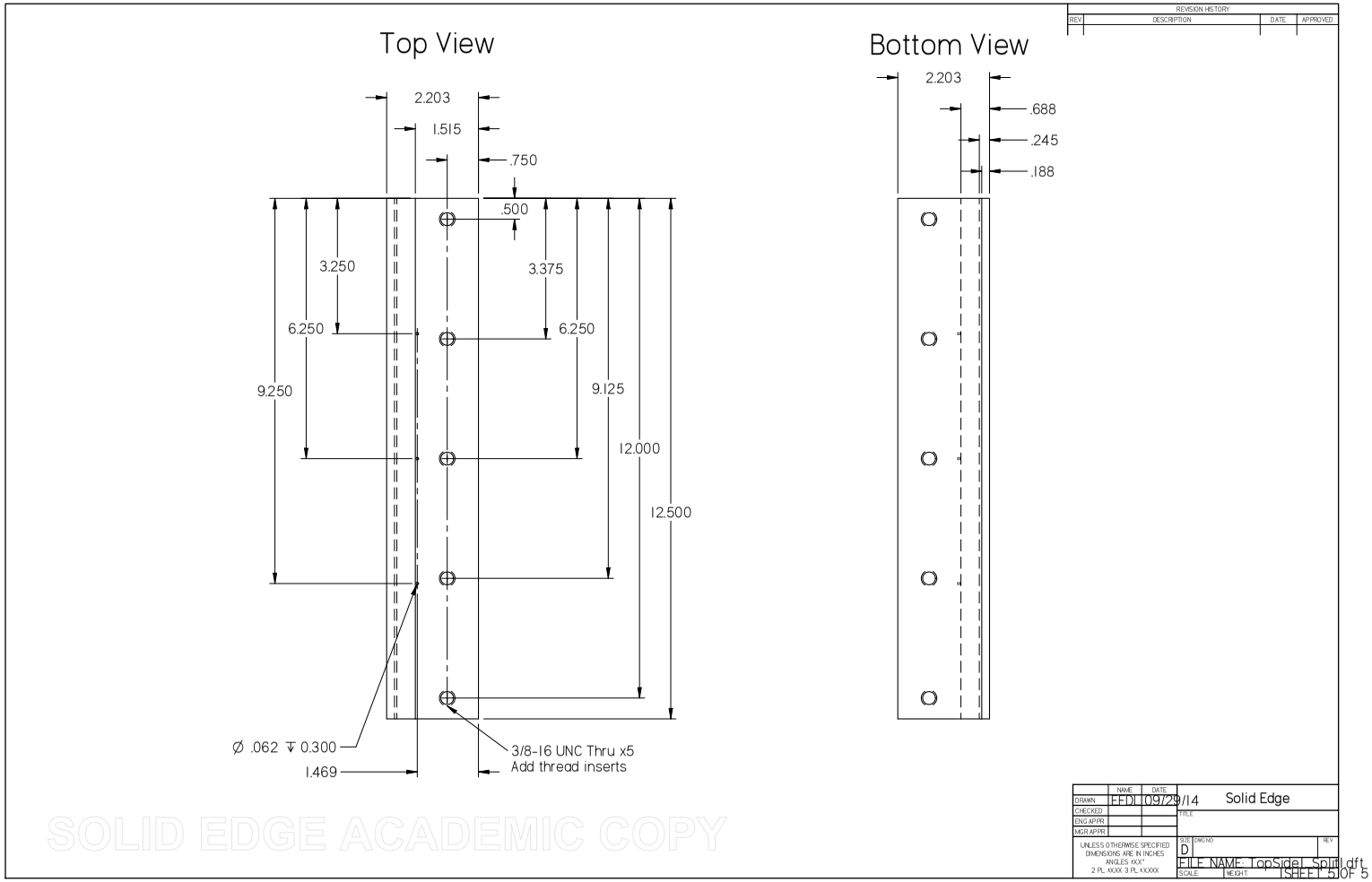
Top View
2.203
1.515
.750
.500
3.250
3.375
6.250
6.250
9.250
9.125
12.000
12.500
Ø .062 ↧ 0.300
1.469
3/8-16 UNC Thru x5
Add thread inserts
Bottom View
2.203
.688
.245
.188
REVISION HISTORY
REV
DESCRIPTION
DATE
APPROVED
DRAWN
EFDL 09/29/14
CHECKED
ENG APPR.
MGR APPR.
UNLESS OTHERWISE SPECIFIED
DIMENSIONS ARE IN INCHES
ANGLES: ±0.5°
2 PL: ±0.XX 3 PL: ±0.XXX
Solid Edge
TITLE
SIZE
D
DWG NO
REV
FILE NAME: TopSideLSplit.dft
SCALE
WEIGHT
SHEET 5 OF 5
SOLID EDGE ACADEMIC COPY

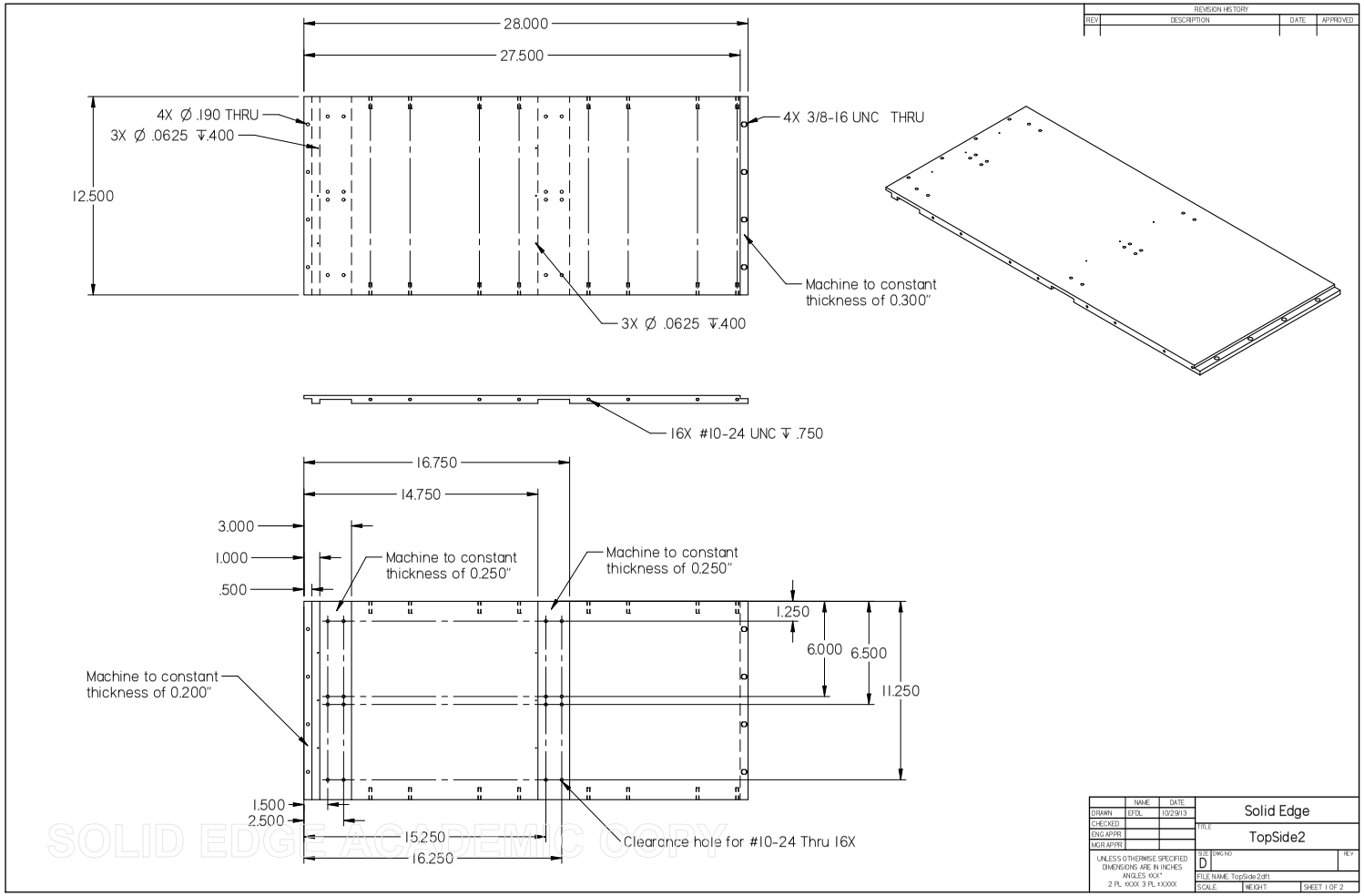

SOLID EDGE ACADEMIC COPY

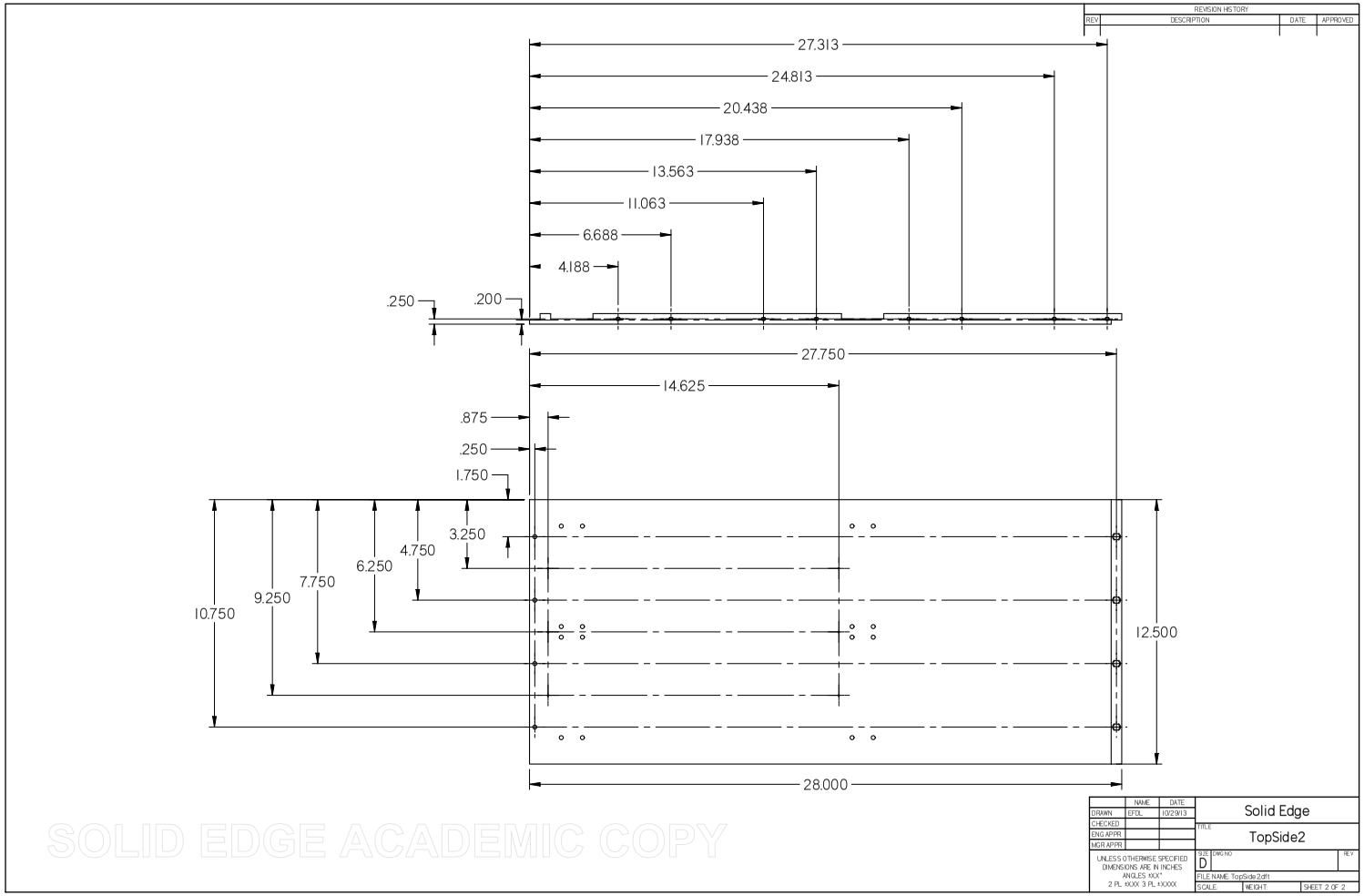
REVISION HISTORY
REV
DESCRIPTION
DATE
APPROVED
27.313
24.813
20.438
17.938
13.563
11.063
6.688
4.188
.250
.200
27.750
14.625
.875
.250
1.750
3.250
4.750
6.250
7.750
9.250
10.750
12.500
28.000
NAME
DATE
DRAWN
EFDL
10/29/13
CHECKED
ENG APPR.
MGR APPR.
UNLESS OTHERWISE SPECIFIED
DIMENSIONS ARE IN INCHES
ANGLES: ±0.5°
2 PL: ±0.XX 3 PL: ±0.XXX
Solid Edge
TITLE
TopSide2
SIZE
D
DWG NO
REV
FILE NAME: TopSide2.dft
SCALE
WEIGHT
SHEET 2 OF 2
SOLID EDGE ACADEMIC COPY

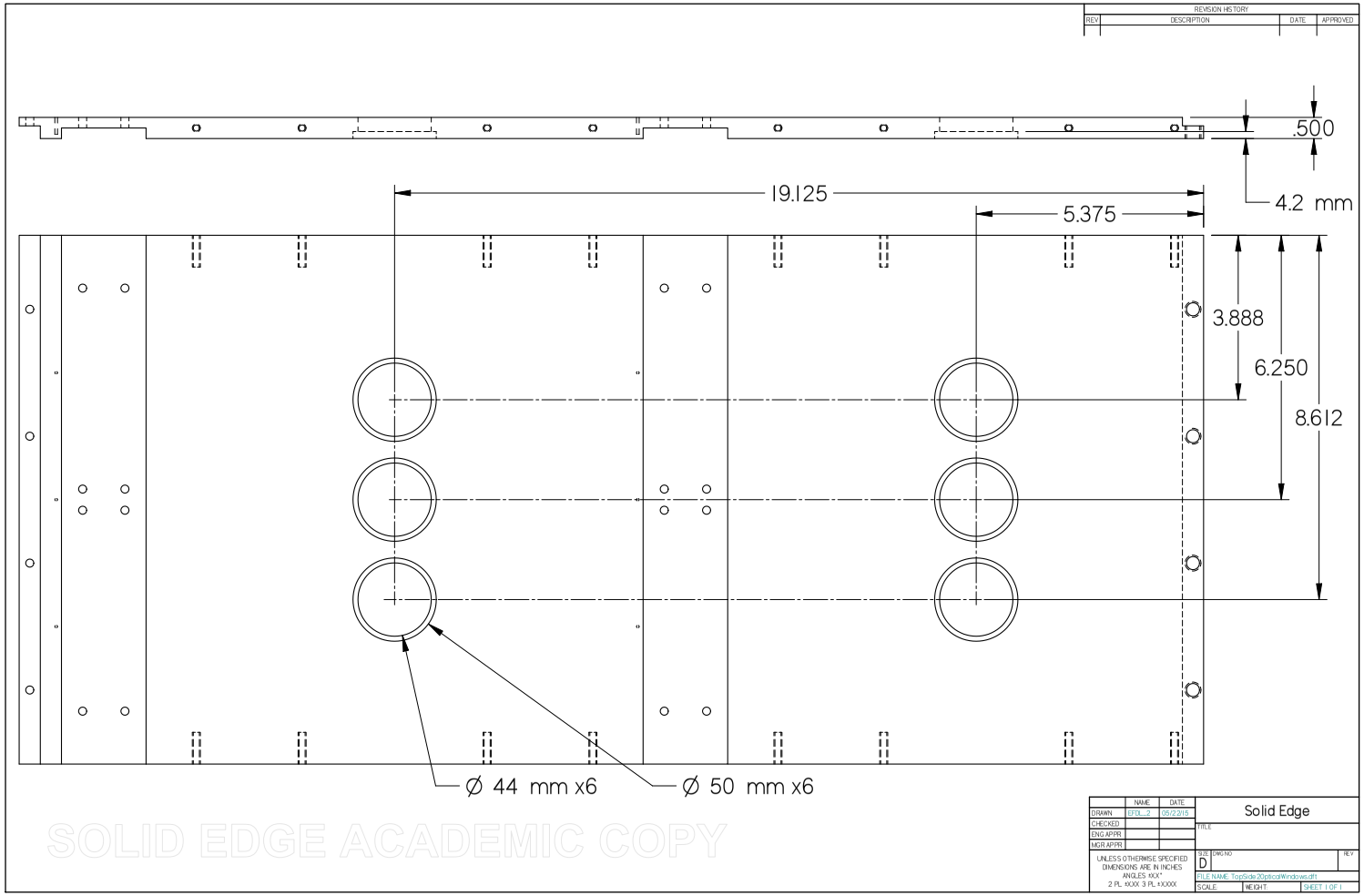
REVISION HISTORY
REV
DESCRIPTION
DATE
APPROVED
.500
4.2 mm
19.125
5.375
3.888
6.250
8.612
Ø 44 mm x6
Ø 50 mm x6
SOLID EDGE ACADEMIC COPY
NAME
DATE
DRAWN
EFTL...2
05/22/15
CHECKED
ENG APPR.
MGR APPR.
UNLESS OTHERWISE SPECIFIED
DIMENSIONS ARE IN INCHES
ANGLES: ±0.X°
2 PL: ±0.XX 3 PL: ±0.XXX
Solid Edge
TITLE
SIZE
D
DWG NO
REV
FILE NAME: TopSide 20psicadWindows.dft
SCALE:
WEIGHT:
SHEET 1 OF 1

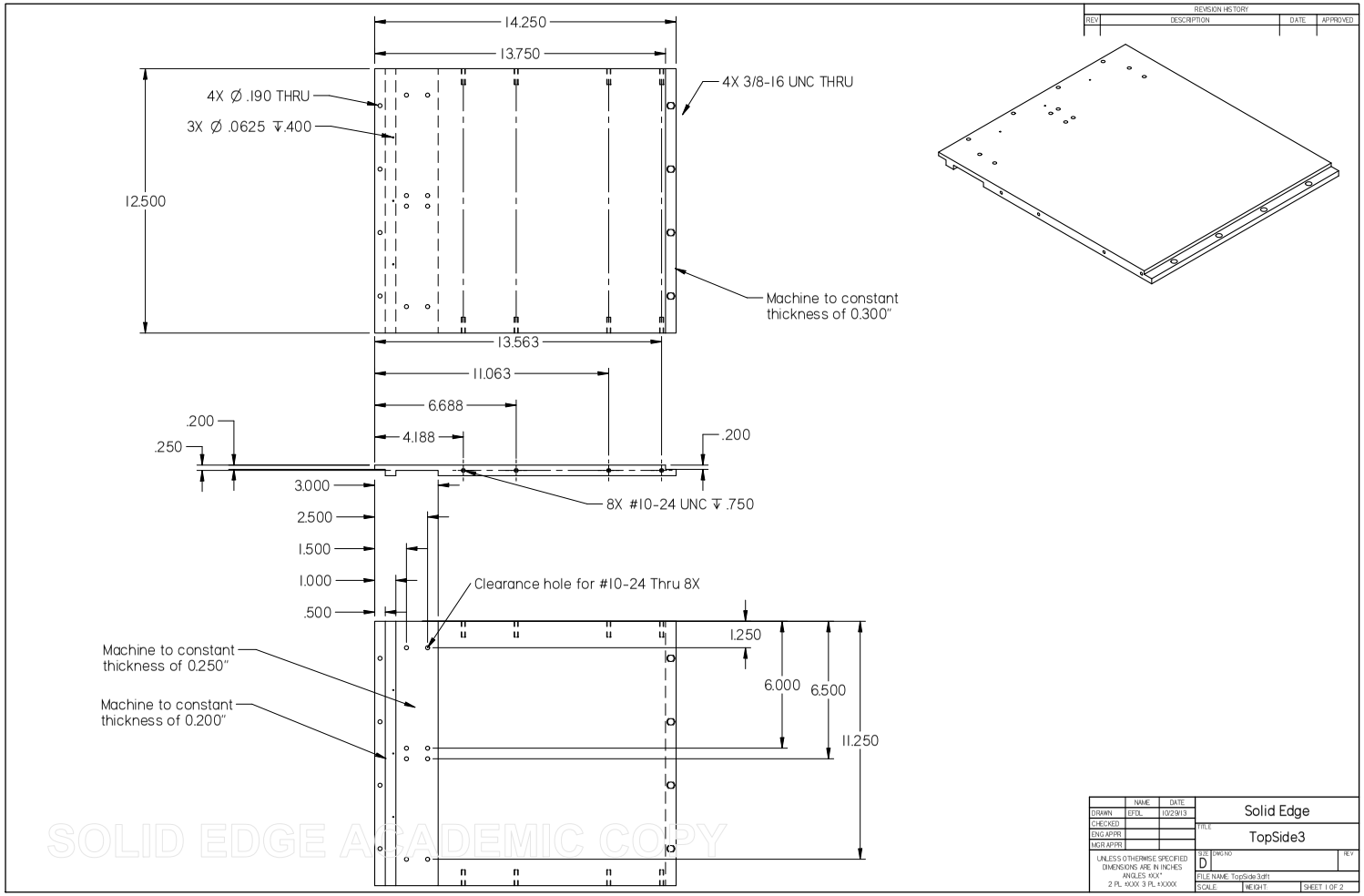
14.250
13.750
4X Ø .190 THRU
3X Ø .0625 ↧.400
4X 3/8-16 UNC THRU
12.500
Machine to constant thickness of 0.300"
13.563
11.063
6.688
4.188
.200
.250
.200
3.000
2.500
1.500
1.000
.500
8X #10-24 UNC ↧ .750
Clearance hole for #10-24 Thru 8X
1.250
6.000
6.500
11.250
Machine to constant thickness of 0.250"
Machine to constant thickness of 0.200"
REVISION HISTORY
REV
DESCRIPTION
DATE
APPROVED
NAME
DATE
DRAWN
EFDL
10/29/13
CHECKED
ENG APPR.
MGR APPR.
UNLESS OTHERWISE SPECIFIED DIMENSIONS ARE IN INCHES ANGLES ±0X° 2 PL ±XXX 3 PL ±XXXX
Solid Edge
TITLE
TopSide3
SIZE
D
DWG NO
REV
FILE NAME TopSide3.dft
SCALE
WEIGHT
SHEET 1 OF 2
SOLID EDGE ACADEMIC COPY

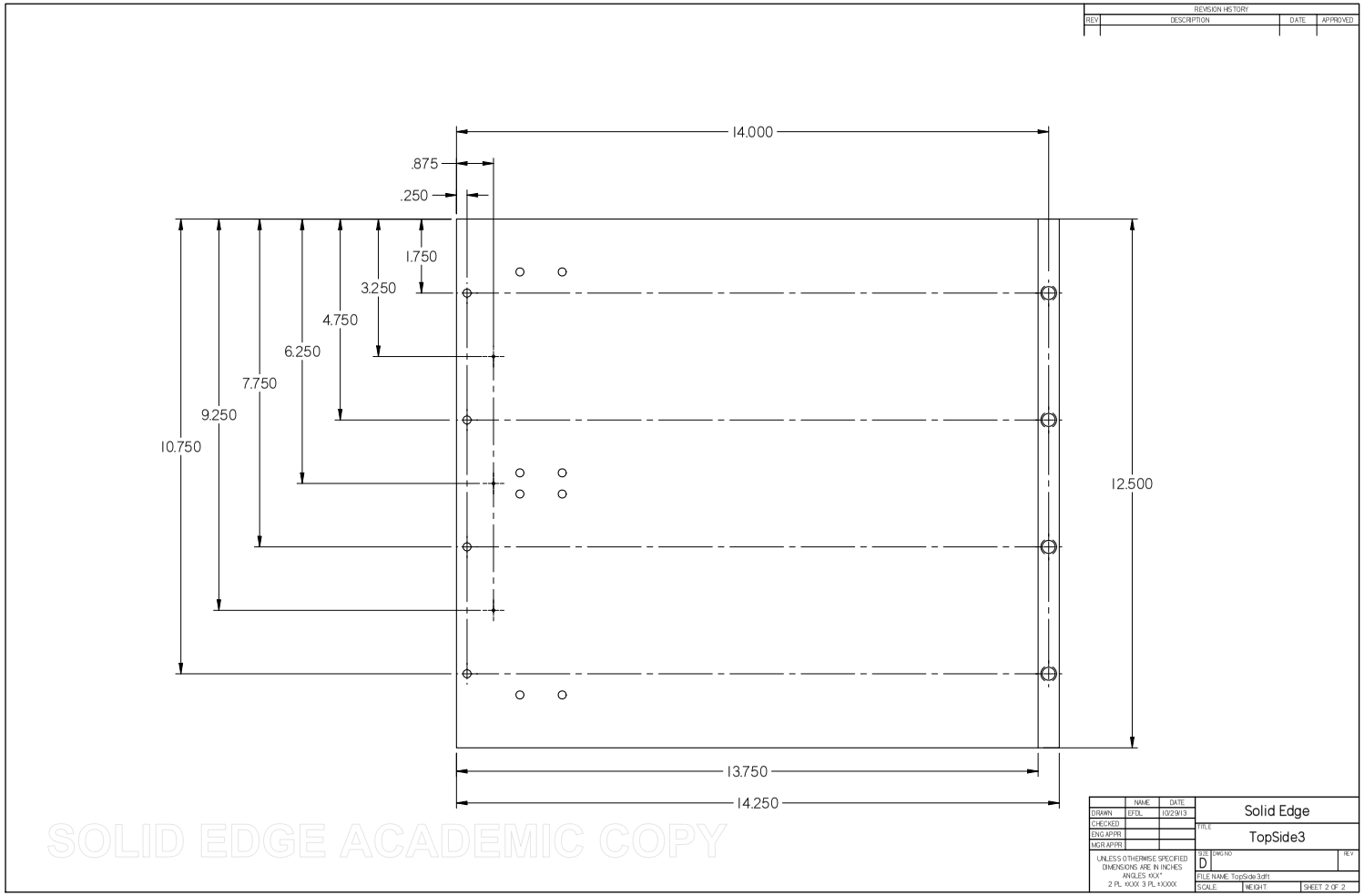
REVISION HISTORY
REV
DESCRIPTION
DATE
APPROVED
14.000
.875
.250
1.750
3.250
4.750
6.250
7.750
9.250
10.750
12.500
13.750
14.250
SOLID EDGE ACADEMIC COPY
NAME
DATE
DRAWN
EFDL
10/29/13
CHECKED
ENG APPR.
MGR APPR.
UNLESS OTHERWISE SPECIFIED
DIMENSIONS ARE IN INCHES
ANGLES: ±0X°
2 PL: ±XXX 3 PL: ±XXXX
Solid Edge
TITLE
TopSide3
SIZE
D
DWG NO
REV
FILE NAME: TopSide3.dft
SCALE
WEIGHT
SHEET 2 OF 2

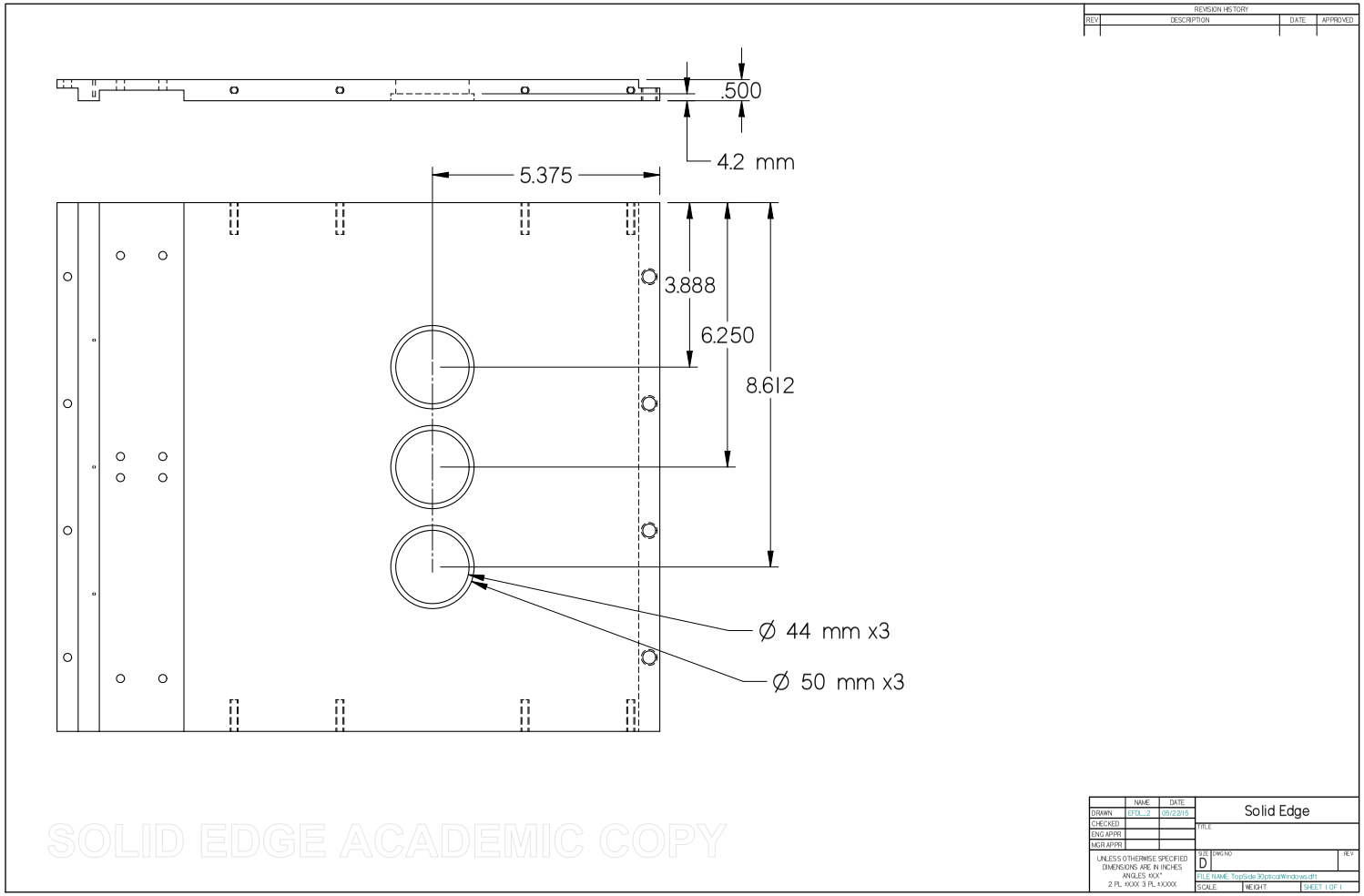
REVISION HISTORY
REV
DESCRIPTION
DATE
APPROVED
.500
4.2 mm
5.375
3.888
6.250
8.612
Ø 44 mm x3
Ø 50 mm x3
SOLID EDGE ACADEMIC COPY
NAME
DATE
DRAWN
EFTL...2
05/22/15
CHECKED
ENG APPR.
MGR APPR.
UNLESS OTHERWISE SPECIFIED
DIMENSIONS ARE IN INCHES
ANGLES: ±0X°
2 PL: ±XXX 3 PL: ±XXXX
Solid Edge
TITLE
SIZE
D
DWG NO
REV
FILE NAME: TopSide3Dpticad Windows.dft
SCALE:
WEIGHT:
SHEET 1 OF 1

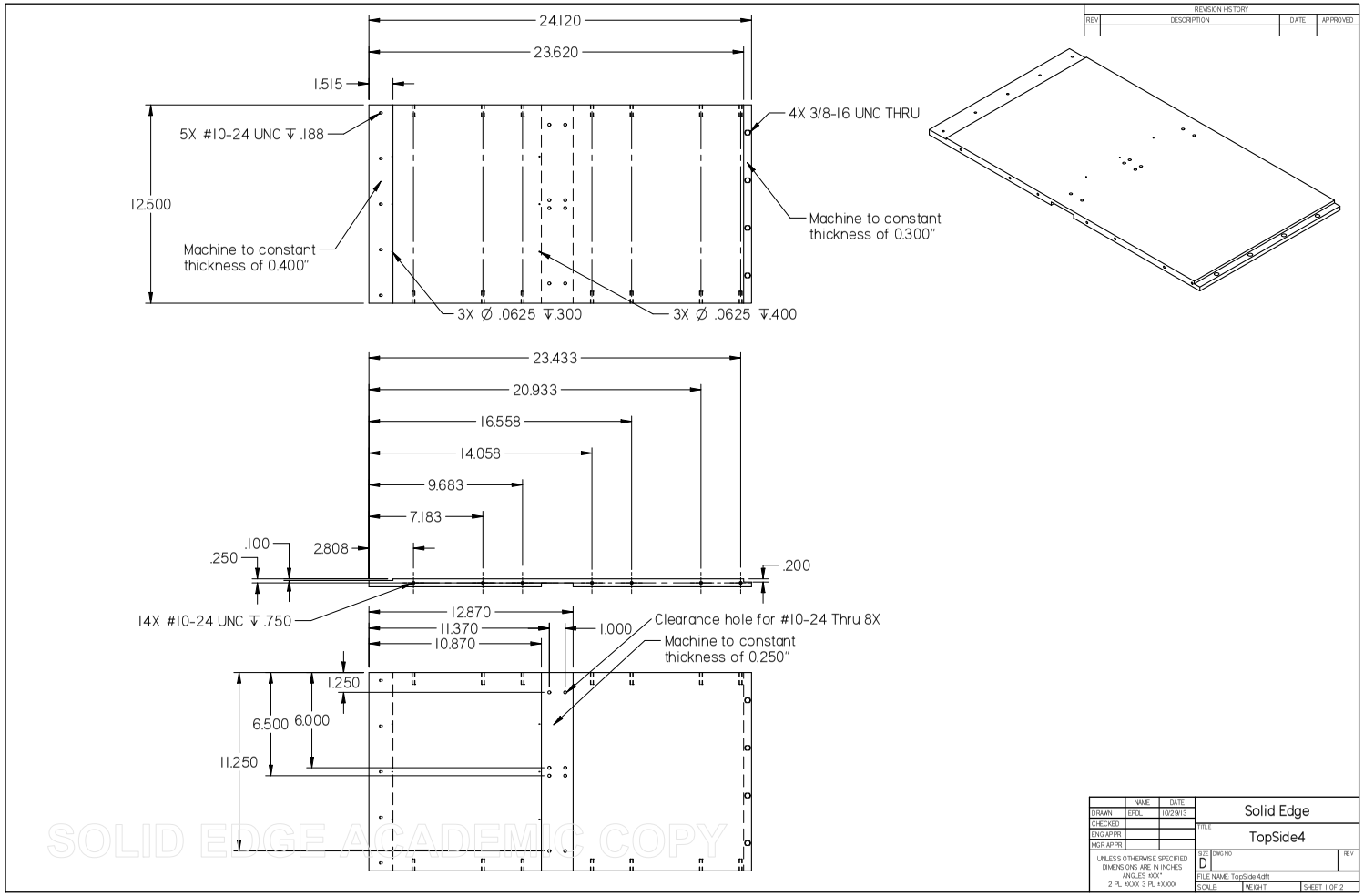
24.120
23.620
1.515
5X #10-24 UNC ↧ .188
4X 3/8-16 UNC THRU
12.500
Machine to constant thickness of 0.300"
Machine to constant thickness of 0.400"
3X Ø .0625 ↧.300
3X Ø .0625 ↧.400
23.433
20.933
16.558
14.058
9.683
7.183
.100
.250
2.808
.200
14X #10-24 UNC ↧ .750
12.870
11.370
10.870
1.000
Clearance hole for #10-24 Thru 8X
Machine to constant thickness of 0.250"
1.250
6.500
6.000
11.250
REVISION HISTORY
REV
DESCRIPTION
DATE
APPROVED
NAME
DATE
DRAWN
EFDL
10/29/13
CHECKED
ENG APPR.
MGR APPR.
UNLESS OTHERWISE SPECIFIED DIMENSIONS ARE IN INCHES ANGLES ±0X° 2 PL ±XXX 3 PL ±XXXX
Solid Edge
TITLE
TopSide4
SIZE
D
DWG NO
REV
FILE NAME TopSide4.dft
SCALE
WEIGHT
SHEET 1 OF 2
SOLID EDGE ACADEMIC COPY

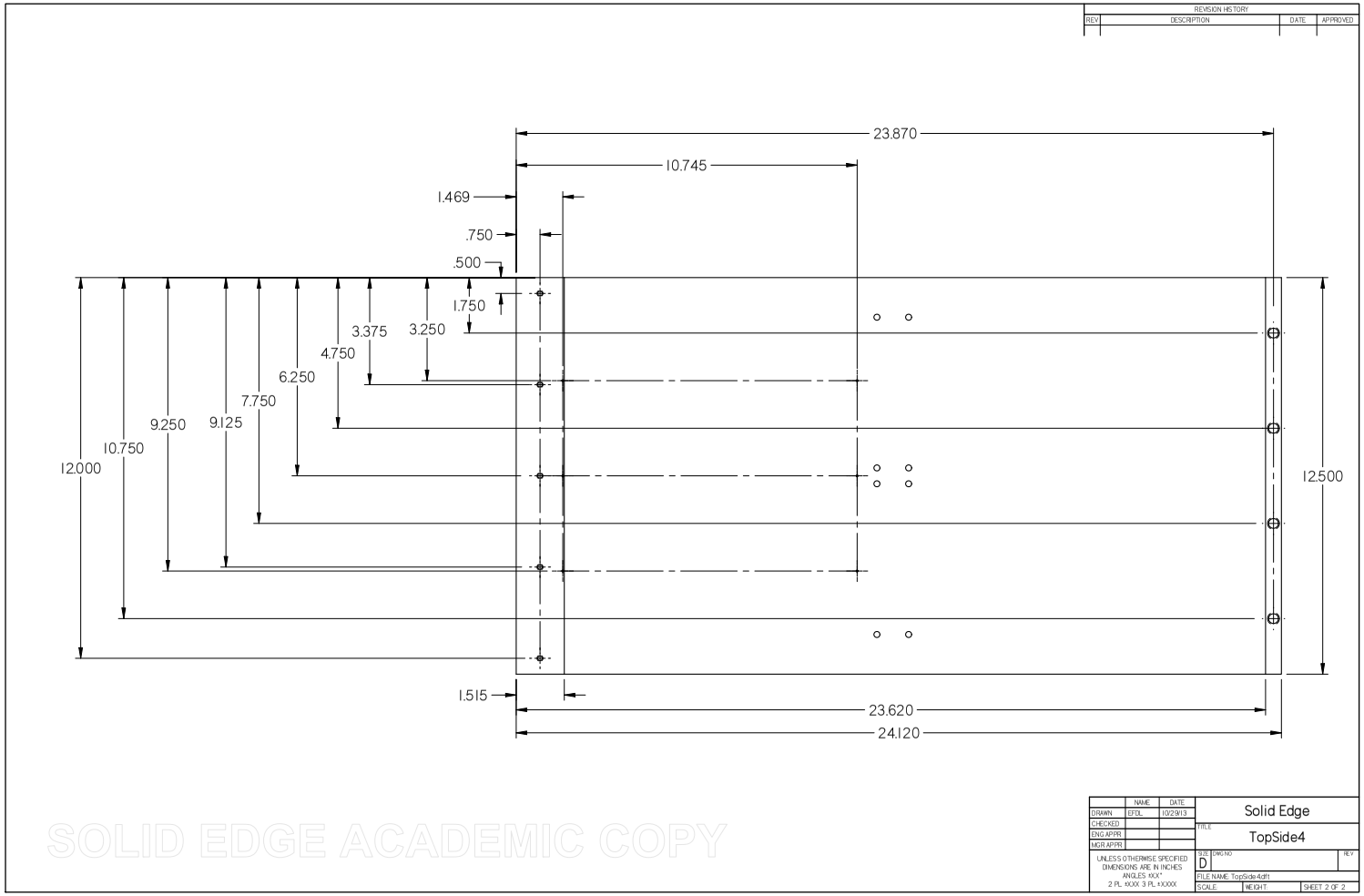
REVISION HISTORY
REV
DESCRIPTION
DATE
APPROVED
23.870
10.745
1.469
.750
.500
1.750
3.375
3.250
4.750
6.250
7.750
9.250
9.125
10.750
12.000
12.500
1.515
23.620
24.120
SOLID EDGE ACADEMIC COPY
NAME
DATE
DRAWN
EFDL
10/29/13
CHECKED
ENG APPR.
MGR APPR.
UNLESS OTHERWISE SPECIFIED
DIMENSIONS ARE IN INCHES
ANGLES: ±0X°
2 PL: ±XXX 3 PL: ±XXXX
Solid Edge
TITLE
TopSide4
SIZE
D
DWG NO
REV
FILE NAME: TopSide4.dft
SCALE:
WEIGHT:
SHEET 2 OF 2

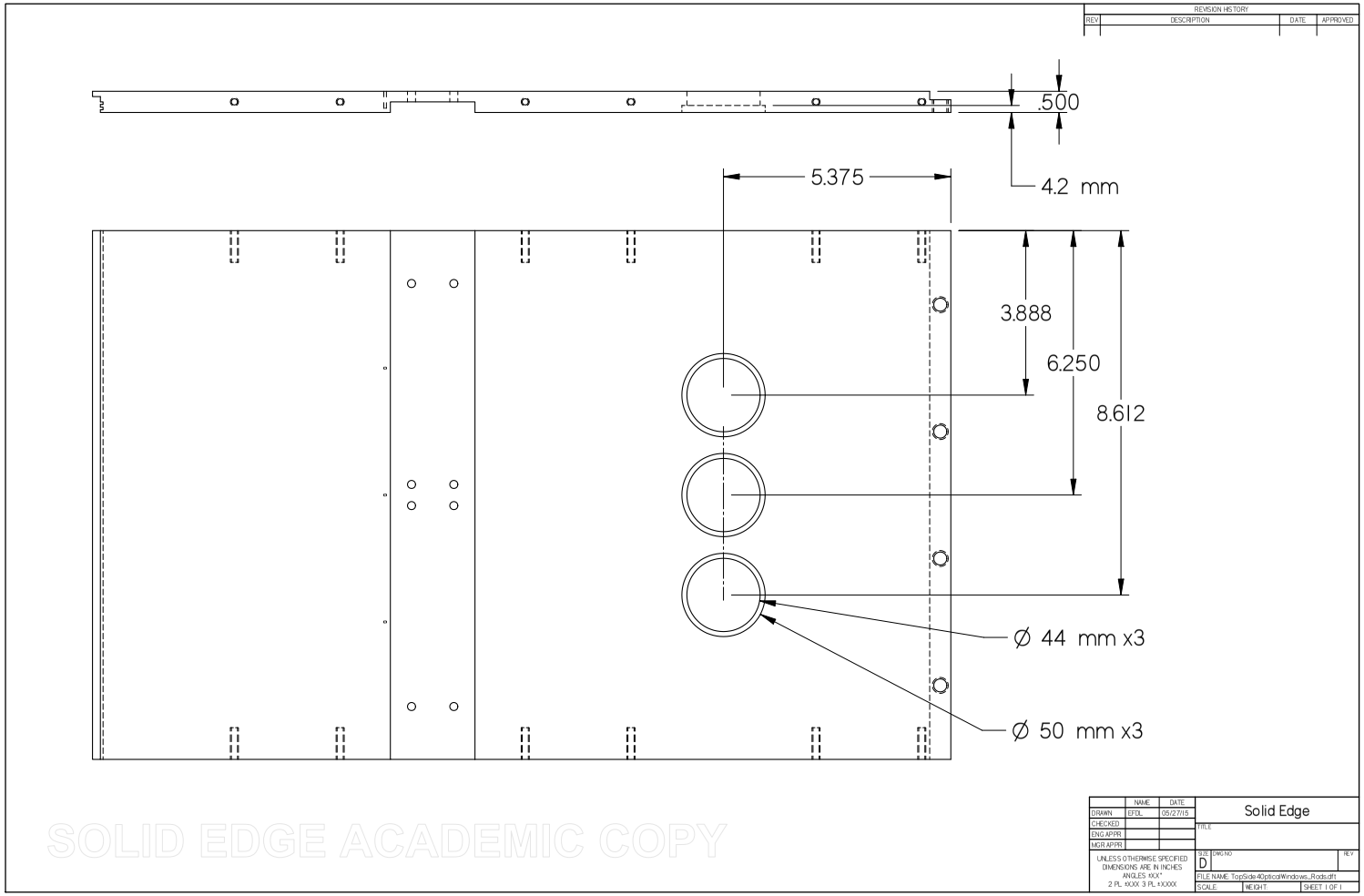

SOLID EDGE ACADEMIC COPY

CURRICULUM VITAE

Kyle L. **Jones**

Mechanical Engineer · Fluid Dynamics and Heat Transfer
1642 South 1150 West, Logan, UT 84321 USA
(435) 632 - 2773 | kyle.jones@aggiemail.usu.edu | mechengrkj

Education

Utah State University — *Logan, Utah*
PhD in Mechanical Engineering — *June 2016: 4.00 GPA*

Utah State University — *Logan, Utah*
M.S. in Mechanical Engineering — *December 2012: 3.66 GPA*

Utah State University — *Logan, Utah*
B.S. in Mechanical Engineering, Mathematics Minor — *December 2012: 3.64 GPA*

Dixie State College — *St. George, Utah*
Associates in Pre-Engineering — *May 2008: 3.74 GPA*

Experience

Experimental Fluid Dynamics Lab, Utah State University — *Logan, UT*
Graduate Research Assistant (PhD Candidate) — *August 2012 - Present*

- Designed and built a validation level experiment which simulates suspended nuclear fuel rods under pure naturally convective flow similar to dry cask storage of nuclear fuel rods. The research experiment was funded through an NEUP Award for Project 3374 entitled Validation Experiments for Spent-Fuel Dry-Cask In-Basket Convection.
- CFD validation level experiment including full instrumentation of the fuel rods and measurement of all boundary conditions as well as the acquisition of fluid velocity data using particle image velocimetry (PIV) measurement techniques.
- Measured boundary conditions used to construct 3D models of the wind tunnel and compute CFD simulations in Star-CCM+.
- Performed preliminary CFD simulations to guide experiment design and assist in placing instruments for measuring boundary conditions as inputs to the CFD models.

Experimental Fluid Dynamics Lab, Utah State University — *Logan, UT*
Graduate Research Assistant (Master's Student) — *January 2011 - August 2012*

- Assisted in validating a CFD model by developing a method to optically measure physical boundaries. This required writing a code to find the edges of objects in the images for reconstructing the model.
- Wrote a code for applying proper orthogonal decomposition (POD) to PIV data for a research group at Bettis Atomic Power Lab.
- Developed method for calculating the minimum random uncertainty for PIV measurements by generating artificially shifted PIV image pairs.

Electronics Assembly Lab, Space Dynamics Laboratory — *Logan, UT*
Laboratory Assistant, Statistician, and Quality Assurance — *April 2009 – August 2011*

- Assembled and reworked circuit boards and cable harnesses.
- Compiled quality, manufacturing, and financial statistics for the Electronics Assembly Lab.
- Developed thermal profiles of circuit boards for proper solder reflow.
- Performed calibrations for electrostatic dissipative (ESD) equipment and ESD workstations.

Undergraduate Heat Transfer, Utah State University *Logan, UT*

Graduate Teaching Assistant *January 2016 - May 2016*

- Held weekly recitation session to assist students in working out homework problems and to prepare for examinations.
- Assisted students one-on-one with homework problems.

Undergraduate Engineering Dynamics, Utah State University *Logan, UT*

Teaching Assistant *September 2010 - December 2010*

- Held daily help sessions for students as well as weekly recitation sessions.
- Graded homework assignments.

Technical Skills & Abilities

Programming	Fortran, Matlab, LabView, LaTeX
Technical Skills	Fluid Dynamics, Heat Transfer, Experimentation, Instrumentation, Computational Fluid Dynamics, Particle Image Velocimetry, Hotwire Anemometry
Computer Skills	DaVis 8, MathCAD, SolidEdge, Microsoft Office, Star-CCM+, Parallel/Cluster Computing, Photoshop, Illustrator, Paraview
Languages	English, Spanish

Training

Idaho National Laboratory *Idaho Falls, ID*

Modeling, Experimentation, and Validation (MeV) Summer School *July 2014*

- Attended a week long summer course design to expose students to the depth of investigation required in order to validate computer simulations.
- Lead the development and execution of group report and presentation for a topic assigned based on safety analysis, risk assesment and validation techniques in nuclear reactors.

Bill Oberkampf and Christopher Roy *Las Vegas, NV*

ASME Verification, Validation, and Uncertainty Quantification (VVUQ) Workshop *May 2015*

- Learned theory and best practices from two of the authors of the VVUQ standard practices guide for applications in fluid dynamics and heat transfer.

Leadership, Service & Honors

2008	**ASME Member**, Utah State University Student Chapter	*Logan, UT*
2013	**Communications Officer**, American Nuclear Society USU Student Chapter Leadership	*Logan, UT*
2011	**Engineering Undergraduate Research Program Award**, USU MAE Department Award	*Logan, UT*
2010	**Questar Scholarship in Engineering Recipient**, USU College of Engineering Award	*Logan, UT*
2008	**Academic Transfer Scholarship to USU**, Based on academic performance	*St. George, UT*
2008	**Outstanding Academic Award in Science/Engineering**, at Dixie State College	*St. George, UT*
2008	**Outstanding Academic Award in Mathematics**, at Dixie State College	*St. George, UT*
2008	**Cum Laude**, Graduated in top 7% of Class at Dixie State College	*St. George, UT*
2005-2007	**Spanish Speaking Volunteer**, 2 year service	*Veracruz, Mexico*
2004	**Senior Patrol Leader**, Timberline Boy Scout Leadership Training Camp	*St. George, UT*
2001	**Eagle Scout**, Boy Scouts of America	*St. George, UT*

Publications

Jones, K.L. *Benchmark Experiments for Natural Convection in Nuclear Fuel Rod Bundles*. PhD Dissertation. Utah State University, June 2016.

Jones, K.L., Smith, B.L. *Benchmark Experiments for Steady-State Natural Convection in Fuel Rod Bundles*. ASME Journal of Verification, Validation and Uncertainty Quantification. *Submited May 2016.*

Jones, K.L. *Investigation of the Noise Floor of the Standard PIV Cross-Correlation Algorithm*. Master's Report. Utah State University, July 2012.

Jones, K.L., Nani, D., and Smith, B.L. *Optical Measurement of Internal Geometry of a CFD Validation Experiment*. Proceedings of the ASME 2012 Fluids Engineering Division Summer Meeting 2012. July 2012. Rio Grande, Puerto Rico, USA.

Jones, K.L., and Smith, B.L. *Method to Determine the Minimum Random Uncertainty in PIV Based on Real Images*. American Physical Society Division of Fluid Dynamics Presentation. November 2012.

Harris, J.R., Nani, D., Jones, K.L., Kholdier, M., and Smith, B.L. *Investigation of the Uncertainty of a Validation Experiment due to Uncertainty in its Boundary Conditions*. The 14th International Topical Meeting on Nuclear Reactor Thermal Hydraulics, NURETH-14. Toronto, Ontario, Canada. September 2011.